

University of St Andrews



Full metadata for this thesis is available in
St Andrews Research Repository
at:

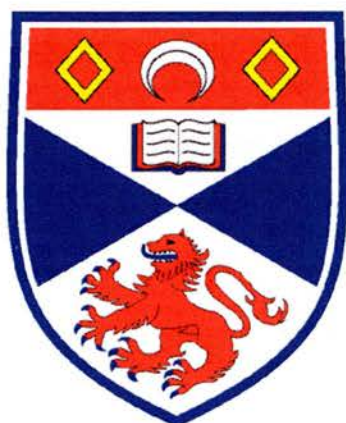
<http://research-repository.st-andrews.ac.uk/>

This thesis is protected by original copyright

Adsorption properties of porous organic-inorganic hybrid solids.

A thesis presented for the degree of
Doctor of Philosophy
in the faculty of science of the University of St. Andrews
by Jorge Gonzalez.

July 2005



University
of
St Andrews



Absorption properties of
porous organic-inorganic
hybrid solids.

A thesis presented for the degree of
Doctor of Philosophy
in the faculty of science of the University of Toronto
by
John J. Vignali

1999



University
of
Toronto



Declarations:

- (i) I, Jorge González González, hereby certify that this thesis, which is approximately 48,000 words in length, has been written by me, that it is the record of work carried out by me and that it has not been submitted in any previous application for a higher degree.

date 7.7.05 signature of candidate...

- (ii) I was admitted as a research student in November, 2001 and as a candidate for the degree of PhD in November, 2004; the higher study for which this is a record was carried out in the University of St Andrews between 2001 and 2005.

date 7.7.05 signature of candidate....

- (iii) I hereby certify that the candidate has fulfilled the conditions of the Resolution and Regulations appropriate for the degree of PhD in the University of St Andrews and that the candidate is qualified to submit this thesis in application for that degree.

date 10.7.05 signature of supervisor....

In submitting this thesis to the University of St Andrews I understand that I am giving permission for it to be made available for use in accordance with the regulations of the University Library for the time being in force, subject to any copyright vested in the work not being affected thereby. I also understand that the title and abstract will be published, and that a copy of the work may be made and supplied to any *bona fide* library or research worker.

date 7.7.05 signature of candidate...

Acknowledgements

Firstly, I would like to thank Dr. Paul A. Wright for giving me the opportunity to work under his supervision during the past three years. Without his expert advice and enthusiastic direction, this work would not be completed. I will always be in debt to him.

I am also grateful to the guys from Edinburgh involved in this project: Mr. Christian Schumacher, Dr. Manuel Pérez Mendoza and Prof. Nigel Seaton. Thank you very much for your hard work!

I am also indebted to my NMR teacher, David P. Tunstall, for his patience and complete commitment in my scientific formation.

I also must acknowledge Mrs Sylvia Williamson for her training and help towards the collection of the adsorption isotherms, Dr. Nandini Radhamonyamma and Dr. Filip Wormald for their help during the collection of the ^2H NMR experiments, Dr. David Apperley at the EPSRC solid state NMR service, Dr. Paula Ferreira for supplying me with a sample of Ph-HMM, Dr. Jesus Canales for his help with the TEM, and Colin F. M. Smith for preparing the NMR tubes for the ^2H NMR experiments.

I had the opportunity to work in the laboratory with numerous great scientists during the last three years. All of them have contributed to my scientific development. I would like to express my gratitude to Dr. Alfonso García-Bennett, Dr. Mark Edgar, Dr. Nandini Radhamonyamma, Dr. Raquel García Salas and Dr. Humphrey Yiu for their help at the beginning of my thesis with the material synthesis. I am also grateful to Dr. Tim Coombs and Dr. Phillip Cheshire for their help during with the organic synthesis.

For all the good moments in and outside the chemistry department, I would like to thank Robbie, Jesus y Pili, Juan Carlos y Virginia, Alf, Raquel Fernandez, Nico, Nandini, Cristina, Raquel Garcia, Stuart Miller, Stewart Warrender, Filip Wormald, Ivan and all the rest of my friends.

Also thank you to the EPSRC for the financial support.

Finally, but the most important, I would like to thank all my family for their support during these three years. Thank to: my wife and daughter (Paty and Georgina), my parents (Manuel González Rodríguez and Carmen González Vilches, great scientists and teachers of chemistry- siempre estaré en deuda con vosotros), my dear uncle and scientific mentor Professor Ernesto Carmona (Tito, muchas gracias por todo), my brother (Carlos González González), Dr Jesus Muñiz and Patricia madre, my grandparents Paco y Juan (sois un ejemplo para mí y os llevo en el corazón a los dos), and all the rest of my family. I could never thank you enough.

Dedication

This thesis is dedicated to my wife and my daughter, Patricia and Georgina, whom I could never thank enough.

Muchas gracias a las dos.

Abstract

The aim of this thesis was to study the adsorption properties of hybrid organic-inorganic porous solids and compare them with those exhibited by inorganic porous solids. Two different approaches were taken:

Firstly, the pore surface of MCM-41, SBA-1 and SBA-2 mesoporous solids have been functionalised using phenyl- and aminopropyl-organo-siloxanes with the target of improving their selectivities in pressure swing processes. Solids were characterised using a variety of techniques (XRD, NMR, TGA, SEM and nitrogen adsorption). Their adsorption properties were studied through high pressure adsorption of ethane and carbon dioxide and low pressure adsorption of carbon dioxide, n-butane, isobutane and toluene. It has been found that phenyl-functionalisation enhances the affinity of MCM-41 for ethane and toluene, although this effect is subtle. On the other hand, aminopropyl-functionalisation exerts a strong influence upon the affinity of MCM-41 and SBA-1 for CO₂ without affecting the adsorption of ethane.

In addition, a family of silicate SBA-2 solids with tailored unit cell dimensions has been synthesised using calcination temperatures between 823 K and 1173 K. Solids were characterised by XRD, TEM, TGA and MAS ²⁹Si NMR. The effect of the thermal treatments upon the porosity of the solids has been investigated by means of nitrogen, carbon dioxide, n-butane and isobutane adsorption. It has been found that with specific control of the calcination temperature it is possible to introduce molecular sieving capabilities to SBA-2: e.g. solids heated at 1073 K adsorb 0.8 wt % of isobutane and 7.5 % of n-butane.

A hybrid organic-inorganic ethane-siloxane with SBA-2 type structure has been also synthesised and characterised via similar methods. This solid has a smaller unit cell and pore size than the pure inorganic silicate, and a stronger affinity for hydrocarbon adsorption.

The second approach used in this thesis involved the study of the dynamics of deuterated adsorbed molecules in crystalline organic-inorganic hybrids microporous solids through ²H NMR. The hybrid host frameworks used in this thesis have been the

aluminium methylphosphonates $-\alpha$ and $-\beta$. Dynamics studies on $\text{AlPO}_4\text{-5}$ allowed a comparison with an inorganic framework.

First, the dynamics of ethane, isobutane and methanol have been compared in these solids. It has been found that the mobility of these molecules is higher in $\text{AlMePO-}\beta$, which possesses cylindrical channels lined with rapid rotating methyl groups. Secondly, the dynamics of aromatic molecules (para-xylene, toluene and benzene) has been also analysed in these frameworks. The motion of para-xylene and toluene has been described using a model in which the long axis of the molecules undergoes a cone type of motion. From these models it is possible to estimate the accessible pore diameter in these solids (e.g. from para-xylene 7.45 Å, 6.47 Å and 8.2 Å for $\text{AlMePO-}\beta$, $-\alpha$ and $\text{AlPO}_4\text{-5}$ respectively). Further studies have found that benzene undergoes isotropic rotations in $\text{AlMePO-}\beta$ whereas it exhibits more constraint dynamics in $\text{AlMePO-}\alpha$ and $\text{AlPO}_4\text{-5}$.

Finally, the dynamics of the aromatic groups in the metal organic framework MOF-5 and its closely related solid MOCP-L have been monitored by $^2\text{H-NMR}$. In MOF-5 , the aromatic groups are static at room temperature and undergo π -flips at 373 K. In MOCP-L , there is a fraction of framework aromatic groups that undergo π -flips at 173 K. Adsorbed benzene, also studied by $^2\text{H NMR}$, seems to undergo isotropic rotations at 183 K whereas at 120 K undergoes in-plane rotations.

Publications:

“Experimental and theoretical investigations of the structure and synthesis of inorganic-organic hybrid solids”. P. Grewal, N. Radhamonyamma, J. Gonzalez, P. A. Wright, P. A. Cox. *Recent advances in the science and technology of zeolites and related materials, PTS A-C, Studies in surface science and catalysis.* 154: 1777-1783
Part A-C 2004

“Modelling and experiment towards the design of mesoporous organic-inorganic hybrid adsorbents”. C. Schumacher, J. Gonzalez, M. Pérez-Mendoza, P.A. Wright, N.A. Seaton. *Recent advances in the science and technology of zeolites and related materials, PTS A-C, Studies in surface science and catalysis.* 154: 386-393 Part A-C
2004

“Structural studies and computer simulation of the inclusion of aromatic hydrocarbons in a zinc 2, 6-Naphthalene dicarboxylate framework compound”. R. N. Devi, M. Edgar, J. Gonzalez, A. M. Z. Slawin, D. P. Tunstall, P. Grewal, P. A. Cox, P. A. Wright, *J. Phys. Chem. B.*, **2004**, 108, 535

“Elucidation of the pore structure of SBA-2 using Monte Carlo simulations to interpret experimental data for the adsorption of light hydrocarbons.” M. Pérez-Mendoza, J. Gonzalez, P. A. Wright, N. A. Seaton, *Langmuir*, **2004**, 20, 7653

“Structure of the mesoporous silica SBA-2, determined by a percolation analysis of adsorption”. M. Pérez-Mendoza, J. Gonzalez, P. A. Wright, N. A. Seaton, *Langmuir*, **2004**, 20, 9856

“Packing of adsorbed molecules in microporous polymorphs aluminium methylphosphonates α and β ”. C. Schumacher, J. Gonzalez, P. A. Wright, N. A. Seaton, *Phys. Chem. Chem. Phys.* **2005**, 7, 2351

“Deuterium NMR studies of framework and guest mobility in the metal-organic framework compound MOF-5, $Zn_4O(O_2CC_6H_4CO_2)_3$ ”. J. Gonzalez, R. N. Devi, D. P. Tunstall, P. A. Cox, P. A. Wright, *Microporous Mesoporous Mater.*, (in press)

“The motion of aromatic hydrocarbons in the microporous aluminium methylphosphonates AlMePO- α and AlMePO- β ” J. Gonzalez, R. N. Devi, P. A. Wright, D. P. Tunstall, P. A. Cox. *J. Phys. Chem. B.*, **2005**. Submitted for publication.

“Synthesis and structure of framework scandium methylphosphonates NaSc(MePO₃)₂ and ScF.H₂O.MePO₃.”

S. R. Miller, E. Lear, J. Gonzalez, A. M. Z. Slawin, P. A. Wright, N. Guillou, G. Ferey, *Dalton. Trans.*, **2005**, (in press).

Works in preparation:

“Adsorption properties of organically functionalised mesoporous solids”.

“Molecular sieve properties of mesoporous silicate SBA-2”.

Contents

Chapter 1. General introduction	1
Introduction to hybrid organic-inorganic porous solids	2
Zeolites	2
Microporous Aluminophosphates	3
Mesoporous solids	4
Synthesis of mesoporous solids	7
Mechanism of formation	9
Hybrid organic-inorganic mesoporous solids	10
MCM-41, SBA-1 and SBA-2 mesoporous solids	13
Microporous organic-inorganic materials	16
Aluminium methylphosphonates	16
Metal organic frameworks (MOFs)	19
Context, Structure and Aims of this thesis	21
Part I	21
Part II	23
Aims	24
References for chapter 1	25
Chapter 2. Characterisation techniques	29
XRD Powder Diffraction	30
Transmission Electron Microscopy	35
Gas and Vapour Adsorption	39
Nuclear Magnetic Resonance	48
Sample preparation for ^2H NMR experiments	58
MXQET and MXQET1 computer codes	64
References for chapter 2	70
Part I (Chapter 3 and 4)	71
Chapter 3. Adsorption studies on SBA-2 and related materials	72
3.1 Introduction	73
3.2 Molecular sieve properties of siliceous SBA-2 material	75
3.2.1 Experimental	75
3.2.2 Structural characterisation	75
3.2.3. Characterisation by gas adsorption	83
3.3 Synthesis of hybrid ethane-siloxane mesoporous material with SBA-2 type structure	92
3.3.1 Synthesis	92

3.3.2 Characterisation	92
3.4 Conclusions	99
3.5 Further work	100
References for chapter 3	101
Chapter 4. Synthesis, characterisation and adsorption properties of phenyl- and aminopropyl-functionalised mesoporous solids	102
	103
4.1. Introduction	
4.2.1. Synthesis of phenyl-functionalised mesoporous silicates	105
4.2.2. Characterisation of phenyl-functionalised mesoporous solids by XRD, SEM and CHN analysis.	108
4.2.3. NMR characterisation of phenyl-functionalised mesoporous solids	118
4.2.4. Nitrogen adsorption	122
4.2.5. Adsorption of light hydrocarbons and CO ₂ in phenyl-functionalised MCM-41	128
4.2.6. Adsorption of aromatic molecules in phenyl-functionalised MCM-41 mesoporous solids.	135
4.2.7. Characterisation of phenyl-functionalised SBA-1 and SBA-2 solids by gas and vapour adsorption	142
4.3. Synthesis and characterisation of aminopropyl-functionalised mesoporous solids	150
4.3.1. Synthesis of aminopropyl-functionalised mesoporous solids	150
-Characterisation	151
-High pressure CO ₂ and ethane adsorption	156
-Conclusions	161
4.4. General conclusions	161
4.5. Further work	161
References for chapter 4	162
Part II (chapter 5, 6 and 7)	163
Chapter 5. Synthesis, characterisation and adsorption of small molecules in aluminium methylphosphonates α and β	164
	165
5.1. Introduction	
5.2. Synthesis and characterisation of microporous organic-inorganic hybrid aluminium methylphosphonates α and β and microporous aluminophosphate AlPO ₄ -5	167
5.3. Dynamics of 1, 4-dioxane in aluminium methylphosphonates α and β	177
5.4. Dynamics of methanol, isobutane and ethane in AlMePO- α , AlMePO- β and AlPO ₄ -5	185
5.5. Conclusions	196

Chapter 6. Dynamics of aromatic molecules in AlMePO- α , AlMePO- β and AlPO₄-5

6.1. Introduction	198
6.2. Experimental	200
6.3. d ₃ , d ₃ -paraxylene as guest in AlMePO- β	203
6.4. d ₃ , d ₃ -paraxylene as guest in AlMePO- α	204
6.5. d ₃ , d ₃ -paraxylene as guest in AlPO ₄ -5	205
6.6. Summary of the motion of para-xylene in AlMePO- β , - α and AlPO ₄ -5	207
6.7. Toluene as a guest in AlMePO- β	209
6.8. Toluene as a guest in AlMePO- α	216
6.9. Summary of toluene in AlMePOs	226
6.10. d ₆ -benzene in AlMePO- β	228
6.11. d ₆ -benzene in AlMePO- α	237
6.12. d ₆ -benzene in AlPO ₄ -5	245
6.13. Summary of the motion of benzene in the AlMePOs	247
6.14. General conclusions	248

Chapter 7. Synthesis and ²H NMR studies of the metal organic framework MOF-5

7.1. Introduction	253
7.2. Synthesis of metal organic frameworks	254
7.3. Characterisation of metal organic frameworks MOF-5 and MOCP-L	255
7.4. NMR sample preparation	260
7.5. ² H NMR studies on the framework	261
7.6. Mobility of adsorbed d ₆ -benzene	263
7.7. Conclusions	266

Chapter 1.

General introduction

Introduction to hybrid organic-inorganic porous solids

Porous materials have attracted the attention of chemists and material scientists over many years, due to commercial interest in their applications in adsorption and catalysis. Today, adsorption is a widely used technology for the separation and purification of gases and gas storage. The relevance of adsorbent materials is growing rapidly and covers a variety of industries, process objectives and scales of operations: for example, separation of linear and isoalkanes in refineries; purification of feed streams; removal of volatile organic compounds (V.O.C.); adsorptive storage of natural gas as an automotive fuel; and oxygen production from air at both industrial scale and for medical purposes. The domain of porous solids is currently experiencing rapid expansion, due to the new preparative approaches to porous solids that have been described during the last 20 years.

Zeolites [1, 2, 3]

The most widely known molecular sieves are the microporous aluminosilicate zeolites and their silica polymorphs, with general formula $xM_{2/n}O \cdot xAl_2O_3 \cdot ySiO_2$ in which M is a cation and n the cation valence.

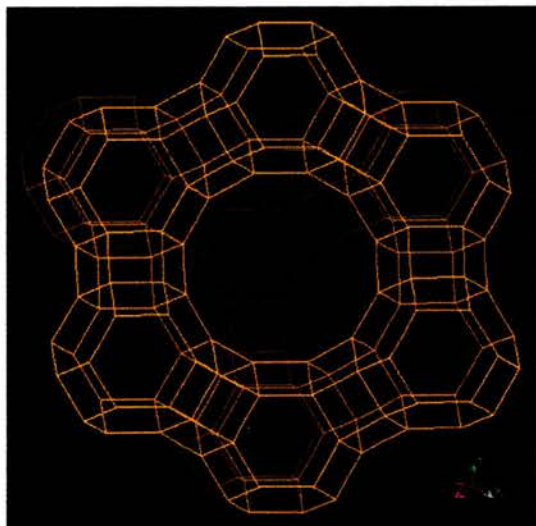


Figure 1.1. An example of zeolite architecture. (Faujasite) A node represents a tetrahedrally coordinated cation while a line portrays an oxygen bridge.

Their inorganic framework contains a pore space which may be composed of channels or cages. Entrances to the pore space are restricted by pore windows that may be from 4 Å to ca. 10 Å across. Zeolites therefore have high adsorption capacity and internal surface area. By controlling their composition by inclusion of aluminium (and therefore including negative charge into their framework) and charge balancing cations in extra-framework positions it is possible to change their character from hydrophobic to hydrophilic. It is also possible to generate acid sites within their framework. Taken together, these properties make zeolites extremely useful in catalysis and they are widely used for oil refining, petrochemistry and organic synthesis in the production of fine and speciality chemicals. They are also used for ion exchange (water softening and purification) and in gas separation processes (O₂ air enrichment for example using the cation induced quadrupole and dipole interactions of N₂ vs. O₂). Zeolites do have limitations, however, particularly concerning the maximum size of their pores and, for some adsorption processes they adsorbed too strongly at room temperature.

Microporous Aluminophosphates

In the early 1980s aluminophosphate were reported as the first family of framework oxide molecular sieves without silica. Some of these materials are microporous and have similar properties to zeolites but they exhibit less affinity for H₂O than the hydrophilic zeolites such as types A and X. The figure below represents the structure of AlPO₄-5, a solid that has been used in this thesis as a host framework for NMR studies.

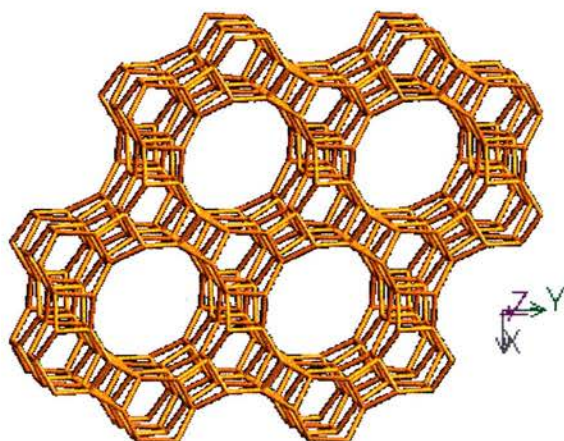


Figure 1.2. AlPO₄-5 structure.

Approaches are therefore being sought to produce porous solids with variable pore sizes and also with the pore walls lined by organic moieties. These would introduce new and readily variable adsorption properties to molecular sieves. Two routes were envisaged for this project: the first involves the modification of mesoporous silica by organic groups, the second the direct crystallisation of mixed organic-inorganic hybrid frameworks. These families of porous solids are introduced below.

Mesoporous solids

The search for new methods to prepare porous solids with pores larger than those of zeolites yielded, in the early 90s, a major breakthrough: the discovery of ordered mesoporous silicas, templated around surfactant micelles. This synthetic route allowed the synthesis of porous solids with tailored mesopores in the range of 30 to 100 Å.

They were discovered almost at the same time by two independent research groups. Koruda, from Waseda University, reported a family of solids, FSM-n (folded sheet materials), proposing as a synthesis mechanism the intercalation of surfactant molecules between the sheets of the layered silicate kanemite [4]. Practically at the same time, researchers from Mobil Company published the synthesis of MCM-41, MCM-48 and MCM-50 by using surfactants and a solubilised silica source [5,6].

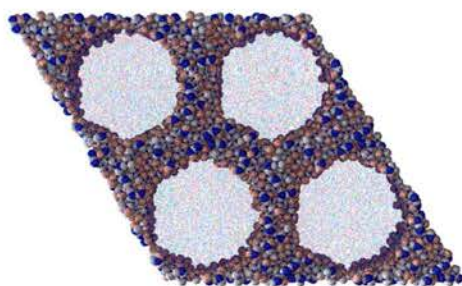


Figure 1.3. Representation of MCM-41 structure. Image supplied by C. Schumacher.

Removal of the surfactant by calcination yielded a solid with a unique structure: An ordered pore system (described in the space group $p6mm$ for MCM-41 and $Ia\bar{3}d$ for MCM-48) with a narrow pore size distribution, high surface areas ($\sim 1000 \text{ m}^2/\text{g}$) and thermal robustness ($\sim 900 \text{ }^\circ\text{C}$). In addition to these properties, the pore size of these

silicate solids could be tailored using surfactants with alkyl chains of different lengths, including swelling agents during synthesis (i.e. trimethylbenzene) or changing synthesis conditions (e.g. pH and temperature)

The discovery of these materials attracted the attention of numerous research groups who investigated the use of other surfactants as templates for the condensation of silica. As a result of this research, many mesoporous solids with different pore sizes and pore network geometries¹ are available. The research performed by Stucky and co-workers must be highlighted here for the large number of different solids they have prepared (SBA-n series) [7,8]. These solids include cage-containing silicates with pore openings on the 5-10 Å scale and also solids templated by block copolymers that have unit cells and pore sizes that offer unprecedented applications, like enzyme immobilisation [9]. Another family of mesoporous solids of interest is the FDU-series developed by Zhao and co-workers. This family includes mesoporous FDU-1, FDU-2, FDU-5 and FDU-12 [10-13]. R. Ryoo *et al.* have built on this work by using mesoporous silicate solids as “hard templates” to replicate carbon frameworks, producing a new family of materials with novel properties [14- 19].

Since the discovery of this type of solids the field has experienced a tremendous development and, many different potential applications for these solids have been reported: Remediation of heavy metal ions by thiol functionalisation [20], Fiber lasers [21], catalysis over silica-alumina-MCM-41 (Propene oligomerisation – gasoline and middle distillates production: C₉ and C₁₂ hydrocarbon selectivity) [22], catalysis over Ti-containing silica – (selective oxidation) [23,24], chiral catalysis [25,26], bimetallic hydrogenation [27,28]; computer microchip supports [29] and drug delivery [30]. In addition, Mobil, very recently, have commercialised and scaled-up the synthesis of MCM-41 for an undisclosed application [31].

¹ The author of this thesis recommends to read “Mesoporous Crystals and related nano-structured materials, *Studies in surface science and catalysis*, **2004**, 148”. This conference proceeding summarises some of the main developments of the field.

Mesoporous solids also have potential in gas separation processes. In this thesis, (chapter 3) the ability of silicate SBA-2 to act as a true molecular sieve for gas separation is demonstrated. Mesoporous solids also exhibit potential as adsorbents in pressure swing processes. This is clearly seen in Figure 1.4 where high pressure CO₂ isotherms of MCM-41 and SBA-2 mesoporous solids are compared with those of silicalite (a zeolite) and an activated carbon (Manuel Pérez-Mendoza, unpublished results). The high uptake of CO₂ between the two black lines, the pressure range of interest in pressure swing processes, indicates that these solids offer important benefits for CO₂ separation over the other solids.

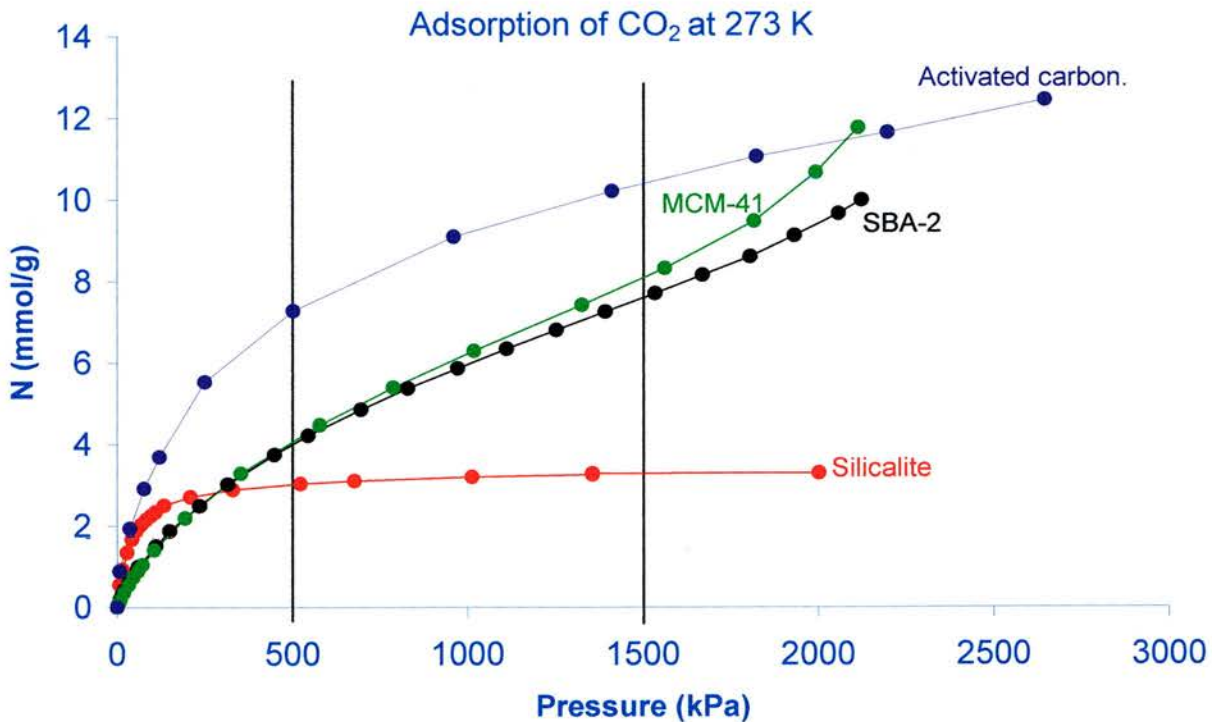


Figure 1.4. High pressure CO₂ isotherms in different solids [Manuel Pérez-Mendoza, unpublished result].

Synthesis of mesoporous solids

The role of the surfactant molecules is critical during the synthesis of mesoporous solids because they organize in micelles that act as structure directing agents of the silica solid. Surfactants are organic molecules that possess a hydrophobic and hydrophilic part. i.e. Hexadecyltriethyl ammonium bromide molecule:

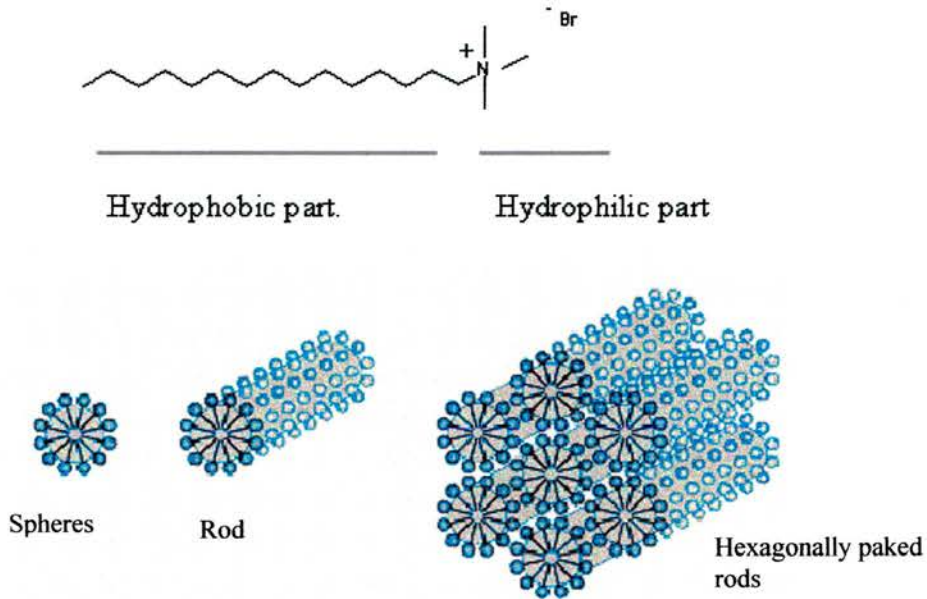


Figure 1.5. Representation of an hexagonal micellar system.

At low concentration, these molecules exist as discrete entities but above a certain concentration (the critical micelle concentration) they aggregate into micelles [32]. The hydrophobic parts of the surfactant pack to reduce their contact with water and the aggregation is limited by the electrostatic repulsion between the hydrophilic head-groups of the molecule. Depending on the surfactant structure, different forms of micellar packing are obtained [7].

The description of surfactant organization is typically rationalised by reference to the local effective surfactant packing parameter, $g=V/a_0l$, where V is the total volume of the surfactant chains, a_0 is the effective head group area at the micelle surface and l is the

length of the hydrocarbon chain. Phase transitions are thought to occur due to variations in g , where the expected mesophase changes as a function of g [7,32]:

g	Mesophase
$1/3$	Cubic ($Pm\bar{3}n$)
$1/2$	Hexagonal ($p6mm$)
$1/2-2/3$	Cubic ($Ia\bar{3}d$)
1	Lamellar

Surfactant molecules can constantly leave and join the micelles due to their dynamic nature. Thus, small changes in concentration, temperature, pH or electrolyte concentration can have a strong effect on the structure of the mesophase. This is clearly seen in the phase diagram of cetyltrimethylammonium bromide (CTAB), which shows changes from cubic to hexagonal to lamellar structures upon discrete changes in temperature and surfactant concentration [33].

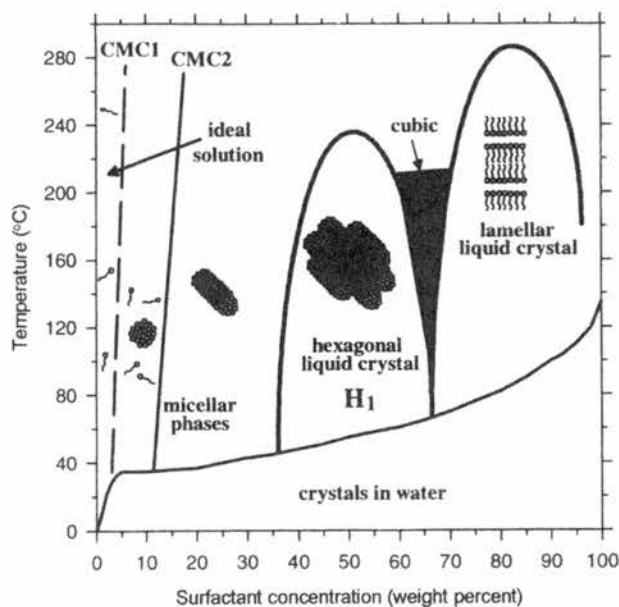


Figure 1.6. Phase diagram for the micellar packing of the surfactant cetyltrimethylammonium bromide changing with respect to temperature and surfactant concentration [33].

Mechanism of formation

The mechanism proposed by C. T. Kresge *et al.*, of Mobil company, involves the interaction of the positively charged quaternary ammonium salt and the negatively charged silicate ions [5,6]. Two different routes were proposed. First, a true liquid crystal template mechanism, in which the surfactant molecules already in a liquid crystal form before the addition of the silica source, act as a structure directing agent for the polymerisation of silica (route 1 in Figure 1.7). The second synthesis pathway proposed by C. T. Kresge involved a cooperative mechanism in which the surfactant and the silica co-assemble to form an organic-inorganic liquid crystal (route 2 in Figure 1.7).

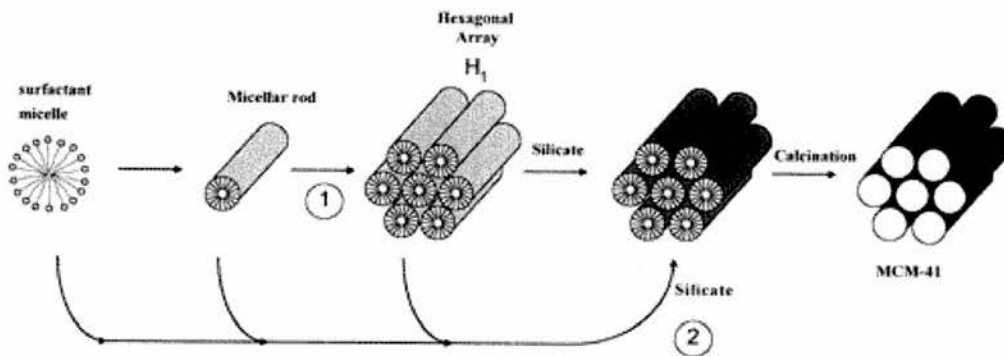


Figure 1.7. Liquid crystal template mechanism proposed by C.T. Kresge *et al* for the synthesis of MCM-41 [6].

The second mechanism is supported by the work of Davis and co-workers who refute the concept of ordered hexagonal arrays of micelles before the onset of silica condensation, mainly through ^{14}N MAS NMR studies [34]. In addition, Stucky *et al.* proposed a co-operative formation mechanism whereby multicharged inorganic species in an aqueous medium interact with the surfactant species and co-operatively form a liquid crystalline arrangement minimising the overall charge effects before silica condensation occurs [35,36]. It is also important to highlight the work of Anderson concerning the interaction of silica structures with micelles in an acidic solution and how the silica surface wraps around the micelles. In this work, water-coating of micelles is proposed to play a key role determining in the formation of mesoporous solid SBA-1 [37,38].

In this thesis, mesoporous solids have been synthesised using a sol-gel route. The method involves two stages, a hydrolysis step followed by a condensation step. The silica source is a silicon alkoxide. The hydrolysis of this silica precursor could be acid or base catalysed. During the hydrolysis, charged silica species interact with the surfactant molecules via the following mechanism:

S^+I^-	S^+ denotes the cationic surfactant and I^- the condensed silica
$S^+X^-I^-$	X^- , a counter-ion of appropriate charge balancing the charges of the cationic surfactant and ionic species when working in acidic media below the isoelectric point of silica (pH < 2) where the silica species is protonated
$N^0H^+X^-I^-$	Non-ionic surfactants (such as PEO-PPO-PEO) protonated under acidic conditions with N^0 denoting the neutral surfactant

The removal of the template, necessary to achieve porous solids, may be conducted by calcination at temperatures in the region of (400 – 550 °C), by template removal by microwave heating or by extraction with an appropriate solvent under reflux conditions.

Hybrid organic-inorganic mesoporous solids

Organic functionalisation of these materials permits the tuning of surface properties (e.g., hydrophilicity, hydrophobicity, binding to guest molecules), alteration of the surface reactivity, protection of the surface from attack, and modification of the bulk properties of the materials, and at the same time stabilizes the material towards hydrolysis. For example, mesoporous silica having thiol groups on the pore surface showed high adsorption efficiency for heavy metals such as Hg, Ag and Cr ion [20,39]. Sulphonic acid groups grafted mesoporous materials exhibited high catalytic for selective formation of bulky organic molecules [40].

These hybrid materials are generally synthesised via two methods [41]. The first is the post-synthesis grafting method in which the pore wall surface of the pre-fabricated inorganic mesoporous materials is modified with organosilane compounds after the surfactant removal. The original structure of the mesoporous support is usually maintained after grafting. Another method is the direct co-condensation *in situ*

functionalisation of a tetraalkoxysilane and one or more organo-trialkoxysilane with Si-C bonds.

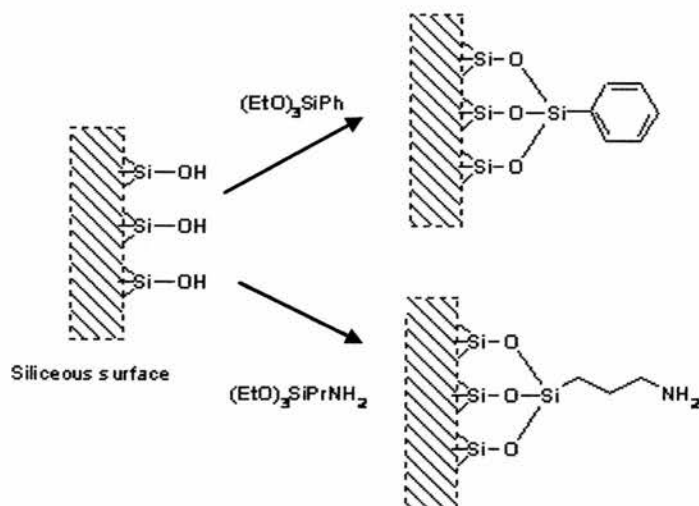


Figure 1.8. Post-synthesis functionalisation with organo-trialkoxysilanes.

Each of the two functionalisation methods has certain advantages. If uniform surface coverage with organic groups is desirable in a single step, the direct method may be the first choice. It also provides better control over the amount of organic groups incorporated in the structure. However, products obtained by post-synthetic grafting are often structurally better defined and hydrolytically more stable. Removal of the surfactant from samples functionalised *in situ* is performed by solvent extraction, normally using EtOH, because calcination processes decomposed the functional group. Sometimes it is not possible to incorporate the target organic molecule *in situ* due to the chemistry of the functional group in question. For example, SBA-1 cannot be synthesised *in situ* with amino groups because, in the highly acidic conditions required for the condensation of this framework, the amine protonates and transforms to a salt.

Many examples of functionalised mesoporous solids can be found in the literature in which the organic groups, pendant in the pores, modified the properties of these solids. A different kind of functionalisation can be achieved if molecules of the type $(\text{EtO})_3\text{-Si-R-Si-(OEt)}_3$ are used as a silica source [42-45]. This synthetic route yield solids that possess the organic groups (-R-) within the walls. Shinji Inagaki, from Toyota Central R&D Labs, is probably one of the most successful researchers in this field. He has reported numerous materials with many different organic groups included within the

walls that offer novel applications in catalysis. One of these solids, the Ph-HMM (Hybrid Mesoporous Material) solid, is of particular interest to this thesis [46]. This material possesses a unique crystal-like structure of aromatic groups arranged within the walls (Figure 1.9). A sample of this material was kindly supplied by Dr. Paula Ferreira (Universidade de Aveiro, Portugal).

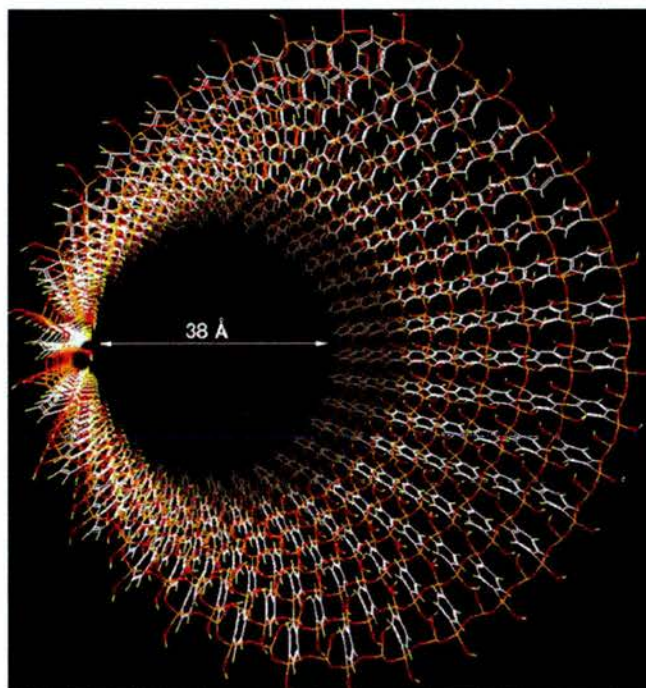


Figure 1.9. Reported pore structure of Ph-HMM solid [46].

MCM-41, SBA-1 and SBA-2 mesoporous solids

One of the aims of this project was to design and manufacture functionalised mesoporous solids for gas separations. The mesoporous solids chosen as starting points for this work are MCM-41 due to its readily modelled structure and, SBA-1 and SBA-2, due to the presence of small cages in their structure.

MCM-41 is the first ordered mesoporous reported by Mobil [5,6] and therefore is the most widely characterised mesoporous solid. It possesses one dimensional channels that can be described in the space group $p6mm$. A typical pore size obtained with the surfactant used in this work (CTAB) is $\sim 33 \text{ \AA}$ in diameter. MCM-41 is easily made in basic conditions at room temperature. Figure 1.10 shows two TEM micrographs of MCM-41.

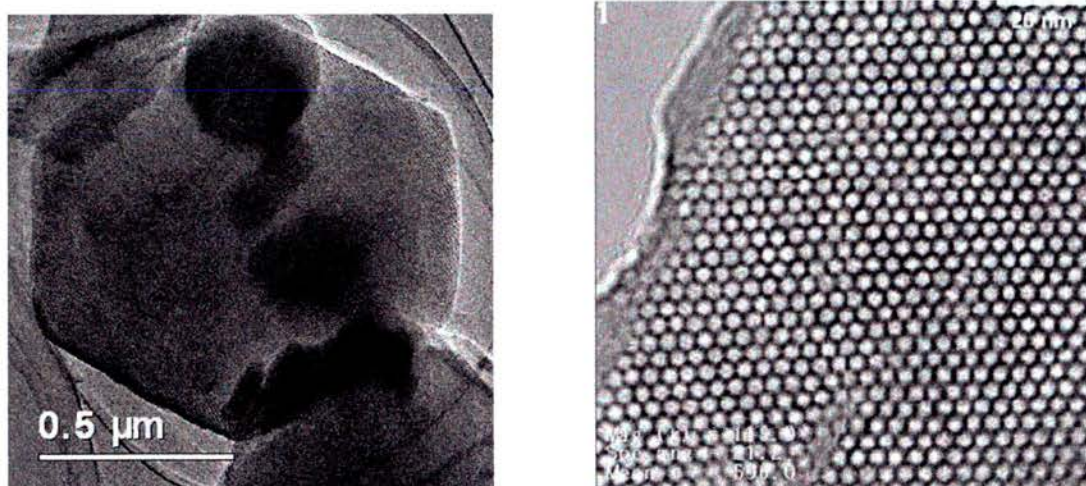


Figure 1.10. TEM micrographs of MCM-41 at different magnifications, right [47].

SBA-1 is the first mesoporous solid of the family reported by Stucky [35]. Sakamoto *et al.* elucidated its structure by means of TEM [48]. In this work, the SBA-1 structure was described as a bimodal cage-type system arranged in A₃B type, where the smallest B cages have a pore diameter of about 33 Å and large A-cages have a pore diameter of about 40 Å.

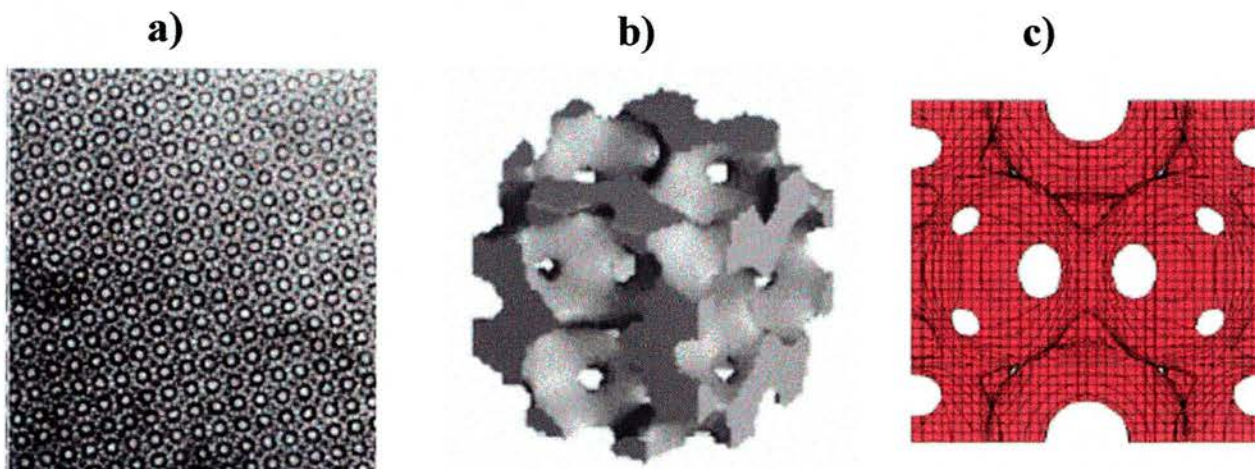


Figure 1.11. a) TEM micrograph of SBA-1 and b) 3D structure of SBA-6 (isostructural to SBA-1) obtained from the electrostatic potential map through TEM [48]. c) Surface enveloping the micellar templating agent for SBA-1 [38].

The synthesis of SBA-1 is carried out in highly acidic conditions and is strongly favoured by low temperatures. It has been reported that the mechanism of formation of this solid is via the formation of S^+XT^+ entities, where cationic silicate species, I^+ , interact with positive charge surfactant molecules, S^+ , through counter ions, X^- . The high concentration of HCl in the starting mixture that causes an increase in the head-to-tail volume ratio for the S^+XT^+ micelle results in a transition from hexagonal to cubic micelles [49].

Very recently, M.W. Anderson *et al.* (UMIST, Manchester University), performing *in-situ* NMR and diffraction experiments have questioned the latter pathway for the synthesis of this solid and have proposed a new model to describe the structure and mechanism of formation [37]. In this new picture of the structure, SBA-1 appears as a low curvature surface formed from a high curvature surfactant micelle mesophase. They also proposed that water plays an important role during the condensation of the silica as the condensation takes place around water coated micelles. The silica is excluded from the region between the micelles by the water coating and so, the sizes of the cavities and connecting windows depend on the size, shape and contact angle between the micelles.

SBA-2, the second ordered mesoporous solid reported by Stucky [7], also attracted the attention of the scientific community due to its unusual structure. Its pore system consists of large spherical cages, of about 40 Å, that are connected by narrow windows. Initially, it was described in the space group $P6_3/mmc$ but, after the work performed by Zhou *et al.* [50] it seems more convenient to describe its structure as being built up by spherical cages arranged in either hexagonal or cubic close packing. The connectivity of the pore network of this solid is an interesting issue that has been the object of publications by Pérez-Mendoza, a co-worker in this project [51, 52]. In this work, the pore structure of SBA-2 is considered by a collection of supercages connected by micropores, both described by a pore size distribution. It is also interesting that, due to the small diameter of the micropores, molecules with slightly different size, like nitrogen and ethane, exhibit very different permeability through the network. In this thesis, experimental data are presented that are compatible with this picture of the SBA-2 structure.

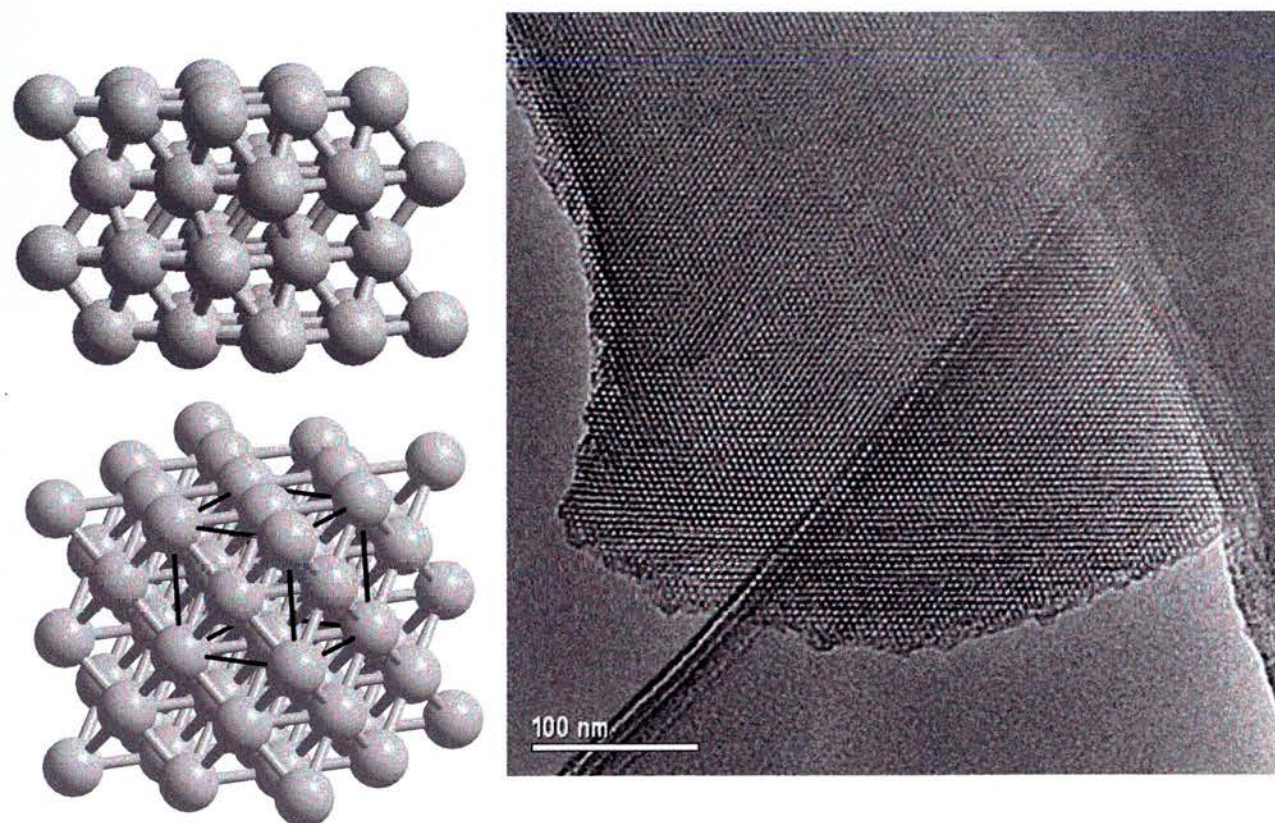


Figure 1.12. (Left), idealised representations of SBA-2 structure with micropores connecting big supercages, above, hexagonal $P6_3/mmc$; below, cubic $Fm\bar{3}m$. (Right), TEM micrograph of SBA-2.

The results of the study on these three mesoporous solids are presented in Part I of the experimental part of this thesis. In the Part II, the adsorption properties of microporous organic-inorganic hybrids are discussed.

Microporous organic-inorganic materials

The adsorption properties of microporous solids are controlled by the character of the channels and therefore organic modification of the pore chemistry leads to solids with novel adsorption properties. Several divalent metal organophosphonates (i.e. materials containing R-PO₃ units where R is an organic group) have been reported showing a wide range of architectures. The majority are layered, like Zn₃(O₃P(CH₂)₂CO₂)₂ [53], but there are some examples in the literature of microporous materials, like β-Cu(CH₃PO₃) [54] and, indeed, the functional organic groups lining the inside of these microporous solids provides them with a greatly different hydrophobicity than would a wholly inorganic analogue.

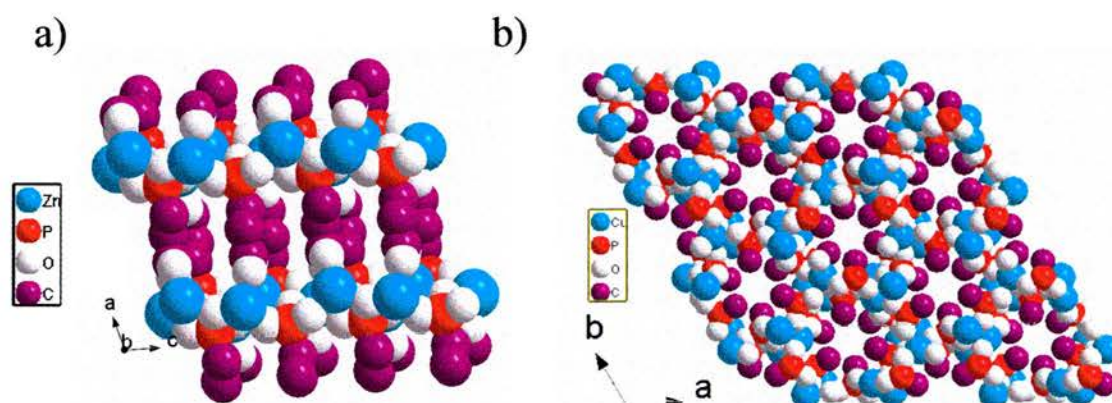


Figure 1.13. a) Layered structure of Zn(II) phosphonate, Zn₃(O₃P(CH₂)₂CO₂)₂. b) Microporous Copper (II) Phosphonate, β-Cu(CH₃PO₃).

Aluminium methylphosphonates.

A breakthrough in aluminium phosphonates was made by Maeda and co-workers who synthesised two crystalline microporous aluminium methylphosphonate materials,

AlMePO- α and AlMePO- β , with pore sizes in the same range as medium pore zeolites such as ZSM-5 [55,56, 57]. The phases are polymorphs of composition $\text{Al}_2(\text{PO}_3\text{CH}_3)_3$, and possess hexagonal arrays of one dimensional pores, with free diameter of around 6.5 Å, that are lined with methyl groups. AlMePO- β crystallizes in the space group R3c with a unit cell $a = 24.650$ Å and $c = 25.299$ Å. AlMePO- α is conventionally described in the trigonal space group P31c with unit cell $a = 13.995$ Å and $c = 8.531$ Å but the structure can be described in the space group R3c with $a' = \sqrt{3}a = 24.240$ Å and $c' = 3c = 25.293$ Å [58].

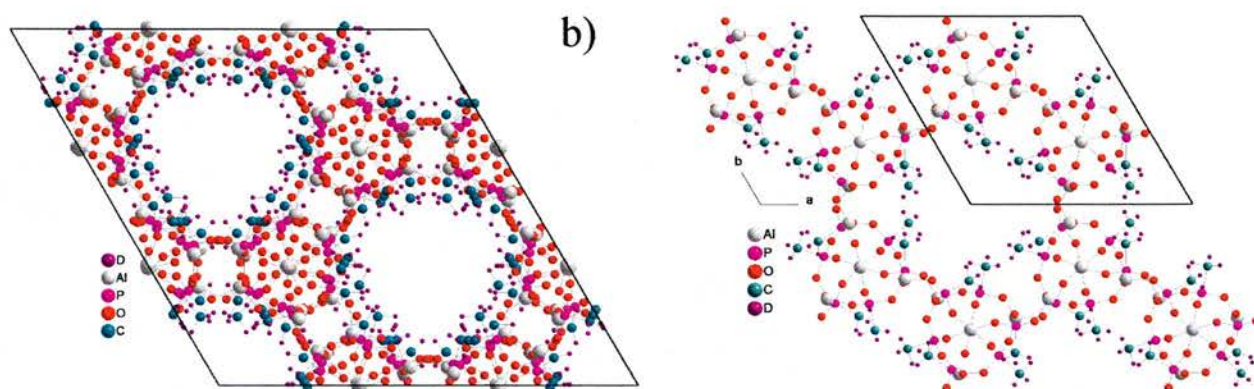


Figure 1.14 a) AlMePO- β and b) AlMePO- α view down the channels.

The hydrothermal synthesis of AlMePO- β is strongly favoured in the presence of 1, 4-dioxane, which can be removed from the pores after synthesis by thermal treatment. On the other hand, AlMePO- α , which is the more stable polymorph, is difficult to synthesise in bulk quantities from hydrothermal methods, but can be produced if AlMePO- β is heated in the presence of water molecules. The unusual role that 1, 4-dioxane plays stabilising AlMePO- β against AlMePO- α has been proposed by P. Grewal *et al.* [59] to be due to a blocking effect exerted by this organic agent on the formation of AlMePO- α , rather than a direct templating of the β framework.

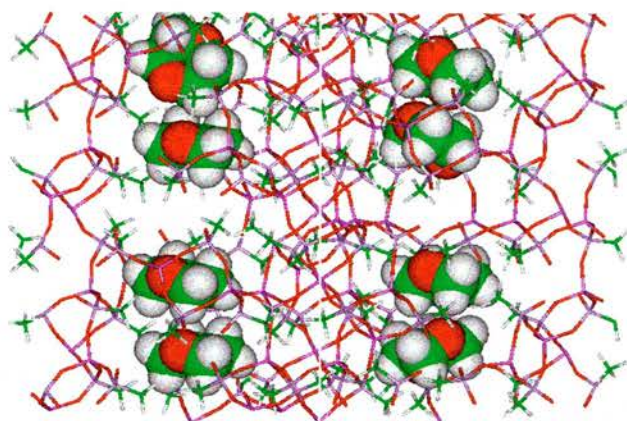


Figure 1.15. Computational model of AlMePO- β shows the minimal energy location of dioxane in the unit cell (Dr Paul Cox, Portsmouth University).

The unusual architecture and chemistry of these solids has been the object of thorough analysis: their structure has been further refined by neutron diffraction (High Resolution Powder Diffraction) and the position of the protons has been located [60,61]. The dynamics of the methyl groups of the β polymorph have been also analysed by ^2H NMR [62].

These solids exhibit unusual adsorption properties different from those of conventional inorganic zeolites. Due to the methyl groups lining the pores both polymorphs are highly hydrophobic and they exhibit little water adsorption at low relative pressures [57]. Nevertheless, the water adsorption capacity of AlMePO- β at high relative pressures increases to higher value than for AlMePO- α . Both phases present a type I nitrogen isotherm but AlMePO- α has two plateaus in the low-pressure region. This unusual property, attributed to a change in the packing of nitrogen molecules, has been the object of extensive work performed by C. Schumacher (project co-worker, currently a PhD student in the School of Chemical Engineering at Edinburgh University) who has studied this phenomenon by means of Monte Carlo simulations [61]. After all this, it can be said that these solids are among the most thoroughly structural characterised microporous organic-inorganic material, and they were therefore chosen as model systems for studying hydrocarbon adsorption, particularly in comparison with the purely inorganic $\text{AlPO}_4\text{-5}$ (see page 3).

Metal Organic Frameworks (MOFs) [62, 63]

Whereas the AlMePOs are members of a class of hybrid solids that consist of an inorganic framework decorated with organic groups, a far larger and rapidly growing class is made up by the so called metal organic frameworks, or MOFs, in which metalocentred 'nodes' are connected by organic 'linkers'. The framework of these hybrids porous solids is built up from both organic and inorganic species strongly connected by covalent bonds. MOFs, due to their organic nature, cannot compete in stability with conventional inorganic zeolites, but due to the degree of rational design that is possible, a sort of "lego" chemistry, they promise widespread applications in separations and gas storage.

There are known many different materials today. Some of them can be described, for example, as layered structures (i.e. zinc or copper carboxylates) with pillaring molecules in the interlayer region (i.e. triethylenediamine). Expanding the length of these units it is possible to modulate the dimension of the channels and tailor the adsorption properties of the solid. K. Seki, W. Mori and co-workers, with several publications [64], have shown the high potential that this family of solid presents for i.e. methane storage.

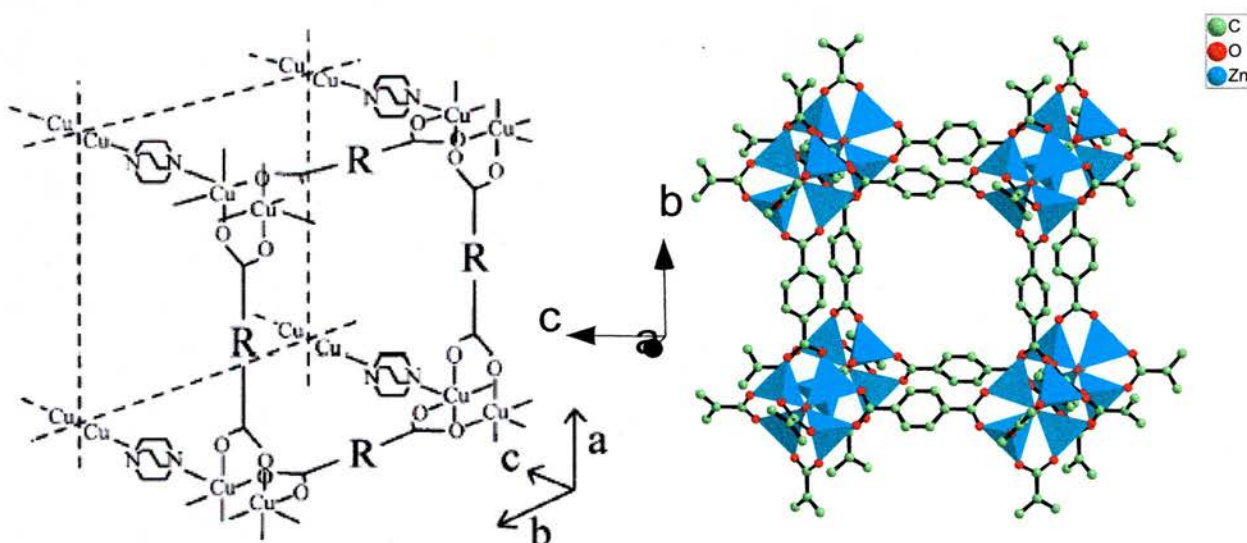


Figure 1.16. Left, basic structure for a family of amine copper dicarboxylate coordination polymer proposed by K. Seki [64]. Right, Representation of MOF-5 structure.

The family of zinc carboxylates solids reported by Yaghi and co-workers [62] is probably the best known in the context of MOFs. The frameworks of this family of materials can be described as large cubic cavities, with Zn_4O units at each of the cube's corners, linked by dicarboxylate units. The inorganic 'nodes' can be considered as four ZnO_4 tetrahedra, all sharing a central oxygen, with tetrahedral symmetry and composition Zn_4O_{13} . Such is the interest of the scientific community for this family of solids that, in the last years, they have been the object of numerous works including several publications in Nature and Science [65-69].

The prototypical MOF is the simplest material of the family. This solid, called MOF-5 [65] by Yaghi and co-workers (Figure 1.16), may be crystallised successfully from dilute solution, for example from the solvents dimethylformamide [65] or diethylformamide [67], either at room temperature or solvothermally. These routes give crystalline samples, the individual crystals possessing well defined cubic morphologies. More recently, a synthetic route has been reported whereby microcrystalline powders of the same composition and similar structure can be prepared rapidly by mixing at room temperature (MOCP-L of Huang *et al*) [70]. In the as-synthesised forms of these solids the pores are full of solvent molecules (DMF, DEF). Upon heating, however, the solvent molecules can be removed to leave the solid with accessible pore volume of around $1.04 \text{ cm}^3/\text{g}$. In chapter 7, the synthesis dynamic and adsorption properties of these materials are studied in detail.

Context, Structure and Aims of this thesis

This thesis has two parts: Part I concerns the study of the adsorption properties of hybrids organic-inorganic mesoporous solids. Part II addresses the dynamics of adsorbed molecules in microporous hybrid solids. The work reported here makes up part of an EPSRC project, performed in parallel with computer simulations carried out in the department of Chemical Engineering at Edinburgh University by Mr. Christian Schumacher (PhD student), Dr. Manuel Pérez Mendoza and Professor Nigel Seaton.

Part I.

It was previously highlighted that the surface of mesoporous solids can be organically modified and that such solids exhibit potential for gas separation processes. The target of the project was to design, manufacture and evaluate a family of hybrid organic-inorganic solids with tailored pore geometry and surface chemistry and to evaluate them as adsorbents with the target of improved selectivities (e.g. hydrocarbons and CO₂ separations). The project design is summarised in the block diagram presented below.

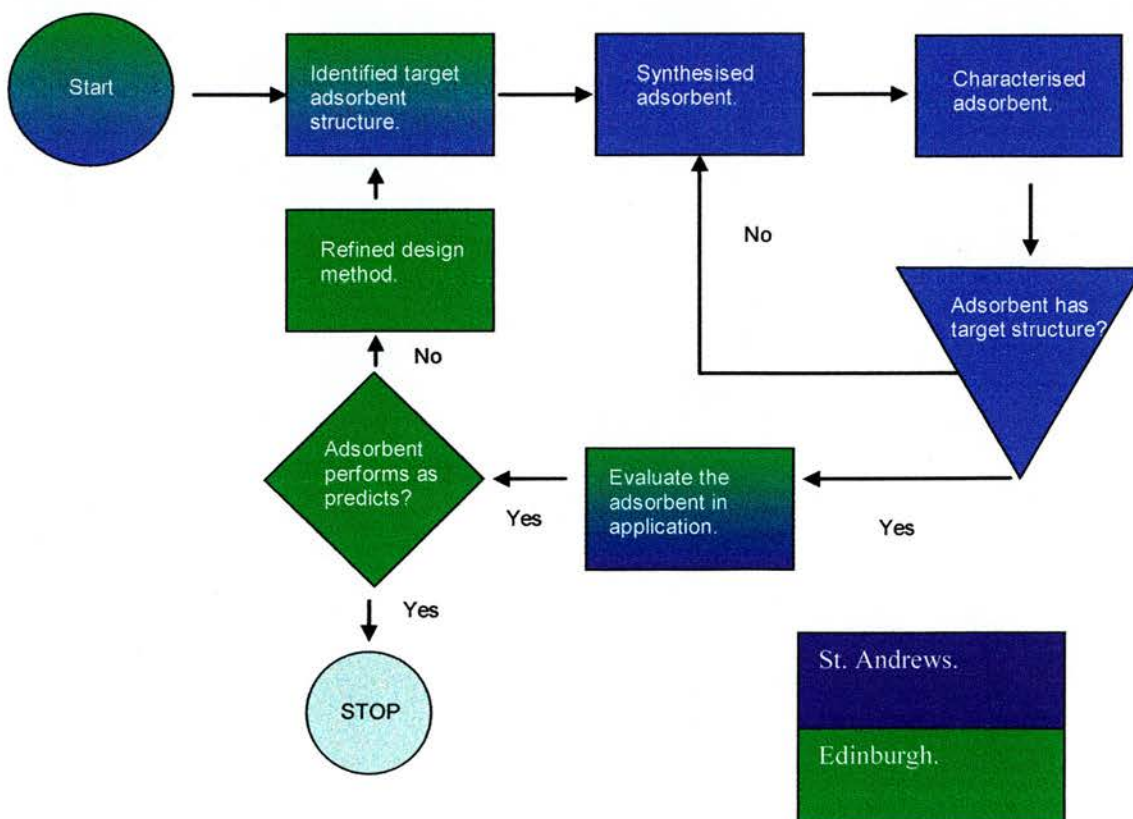


Figure 1.17. Project block diagram.

The adsorbents identified as possible solids with improved selectivities in gas separation have been phenyl- and aminopropyl-functionalised MCM-41, SBA-1 and SBA-2. Phenyl is a non-polar group that could favour the adsorption of hydrocarbons and, aminopropyl groups are expected to interact strongly with CO₂ molecules.

As shown in the project flow diagram, this thesis is concerned with the synthesis, characterisation and evaluation of gas adsorption properties of these solids.

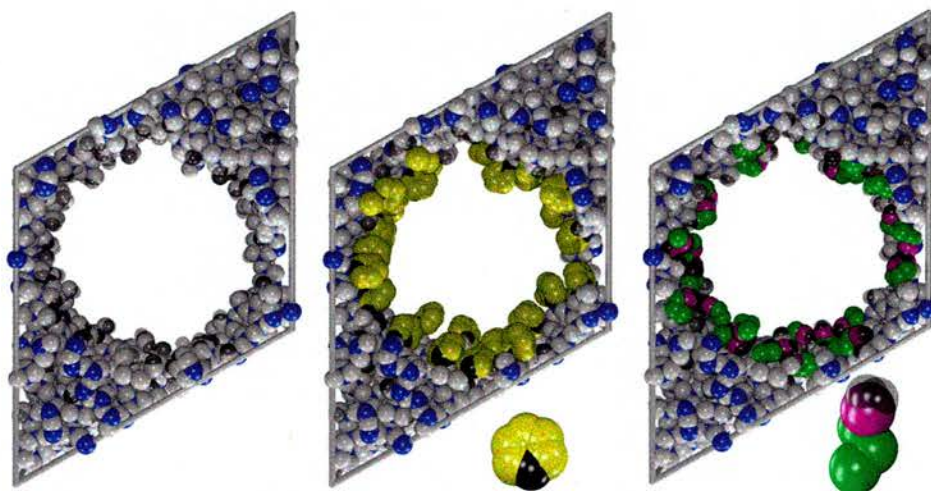


Figure 1.18. Model of pure silica MCM-41, phenyl functionalised MCM-41 and aminopropyl functionalised MCM-41. Images supplied by C. Schumacher.

Our co-workers at Edinburgh University, by means of Grand Canonical Monte Carlo Simulations, have simulated the synthesis and modelled the structures of these functionalised solids, and according to their models, have simulated their adsorption behaviour. These simulations should provide a powerful tool to understand the adsorption processes in mesoporous solids. The models of MCM-41 presented in Figure 1.18, obtained by C. Schumacher, are presented as an example of results yielded by the joint project. These models not only allow the simulation and prediction of gas adsorption by these solids, they also provide a picture of the intrapore structure of these materials, difficult to obtain by conventional diffraction techniques due to the amorphous nature of these solids. One aim of this thesis was to synthesise and characterise functionalised MCM-41 solids to provide experimental data against which the models could be tested and refined.

In addition, the mesoporous solids SBA-1 and SBA-2 were investigated as parent solids for functionalisation. Although these are complex structures, and have not yet been simulated computationally at the same level as been possible for MCM-41, Pérez-

Mendoza proposed a simplified model for the silicate [51,52]. In this thesis details about the SBA-2 structure and its organically-functionalised derivatives have been examined, as have details of organically-functionalised SBA-1.

Part II.

The dynamics of molecules adsorbed within porous solids is important in catalytic and adsorption applications. This has recently been emphasized by for example Denayer *et al.* [71] who has identified an entropy-based principle for molecular separations based on differences in molecular rotation in cage-like zeolites.

In the second part of this thesis, the dynamics of adsorbed molecules in microporous hybrid organic-inorganic solids have been studied by ^2H NMR. The well defined polymorphs AlMePO- α and - β were chosen as model sorbents. AlPO₄-5 was studied for comparison with an inorganic solid. The selected adsorbates are small molecules of a range of polarities (1, 4-dioxane, isobutane, ethane and methanol) and aromatic hydrocarbons (para-xylene, toluene and benzene).

The dynamics of the aromatic framework groups and adsorbed benzene in microporous zinc terephthalate MOF-5 synthesised via two different methods (slow solvothermal crystallisation and fast precipitation) have also been studied.

The dynamics of some of the molecules of interests adsorbed within the AlMePOs has been analysed independently by P. A. Cox and P. Grewal (Portsmouth University) by Molecular Dynamics Simulations. Their results will be compared with those obtained in this thesis through NMR.

Aims

Part I

-To establish details of the structure of mesoporous silicate SBA-2 through gas adsorption.

-The synthesis, characterisation and measurements of the gas adsorption properties of phenyl- and aminopropyl-functionalised MCM-41, SBA-1 and SBA-2 mesoporous solids.

Part II:

-To study the dynamics of guest molecules in AlMePO- α and - β and compare them with dynamics of the same molecules in AlPO₄-5.

-To study the dynamics of the framework groups and of adsorbed benzene in MOF-5.

References for Chapter 1.

- [1] M. E. Davis, *Nature*, **2002**, 417, 813
- [2] A. Corma, *Chem. Rev.*, **1995**, 95, 559
- [3] A. Corma, *Chem. Rev.*, **1997**, 97, 2373
- [4] T. Yanagisawa, T. Shimizu, K. Kuroda, C. Kato, *Bull. Chem. Soc. Jpn.*, **1990**, 63, 988
- [5] C.T. Kresge, M.E. Leonowicz, W.J. Roth, J.C. Vartuli, J.S. Beck, *Nature*, **1992**, 359, 710
- [6] J.S. Beck, J.C. Vartuli, W.J. Roth, M.E. Leonowicz, C.T. Kresge, K.D. Schmitt, C.T.-W. Chu, D.H. Olson, E.W. Sheppard, S.B. McCullen, J.B. Higgins, J.L. Schlenker, *J. Am. Chem. Soc.*, **1992**, 114, 10834
- [7] Q. Huo, R. Leon, P.M. Petroff, G.D. Stucky, *Science*, **1995**, 268, 1324
- [8] D. Zhao, Q. Huo, J. Feng, B.F. Chmelka, G.D. Stucky, *J. Am. Chem. Soc.*, **1998**, 120, 6024
- [9] H. H. P. Yiu, P. A. Wright, N. P. Botting, *J. Molecular Catalysis B: Enzymatic*, **2001**, 15, 81
- [10] C. Yu, Y. Yu, D. Zhao, *Chem. Commun.*, **2000**, 7, 575
- [11] S. Shen, Y. Li, Z. Zhang, J. Fan, B. Tu, W. Zhou, *Chem. Commun.*, **2002**, 19, 2212
- [12] X. Liu, B. Tian, C. Yu, F. Gao, S. Xie, B. Tu, R. Che, L. Peng, D. Zhao, *Angew. Chem. Int. Ed.*, **2002**, 41, 3876
- [13] J. Fan, C. Yu, F. Gao, J. Lei, B. Tian, C. Wang, Q. Luo, B. Tu, W. Zhou, D. Zhao, *Angew. Chem. Int. Ed.*, **2003**, 115, 3254
- [14] R. Ryoo, S.H. Joo, S. Jun, *J. Phys. Chem. B*, **1999**, 103, 7743
- [15] R. Ryoo, S.H. Joo, S. Jun, T. Tsubakiyama, O. Terasaki, *Stud. Surf. Sci. Catal.*, **2001**, 135, 150 – see also *Adv Mater.*, **2001**, 13, 677
- [16] S. Jun, S.H. Joo, R. Ryoo, M. Kruk, M. Jaroniec, Z. Liu, T. Ohsuna, O. Terasaki, *J. Am. Chem. Soc.*, **2000**, 122, 10712
- [17] S.H. Joo, R. Ryoo, *J. Phys. Chem. B*, **2002**, 106, 1256
- [18] S.H. Joo, S.J. Choi, I. Oh, J. Kwak, Z. Liu, O. Terasaki, R. Ryoo, *Nature*, **2001**, 412, 169
- [19] F. Kleitz, S.H. Choi, R. Ryoo, *Chem. Commun.*, **2003**, 17, 2136

- [20] X. Feng, G.E. Fryxell, L.Q. Wang, A.Y. Kim, J. Lui, K.M. Kemmer, *Science*, **1997**, 276, 923
- [21] F. Marlow, M.D. McGehee, D. Zhao, B.F. Chmelka, G.D. Stucky, *Adv. Mater.*, **1999**, 11, 632
- [22] G. Bellussi, C. Perego, A. Carati, S. Peratello, E.P. Massara, G. Perego, *Stud. Surf. Sci. Catal.*, **1994**, 84, 85
- [23] J.M. Thomas, *Nature*, **1994**, 368, 289
- [24] T. Maschmeyer, R. Rey, G. Sankar, J.M. Thomas, *Nature*, **1995**, 378, 159.
- [25] J.M. Thomas, *Angew. Chem. Int. Ed. Engl.*, **1999**, 38, 3588
- [26] M.D. Jones, R. Raja, J.M. Thomas, B.F.G. Johnson, D.W. Lewis, J. Rouzard, K.D.M. Harris, *Angew. Chem. Int. Ed. Engl.*, **2003**, 42, 4326
- [27] D.S. Shephard, T. Maschmeyer, J.M. Thomas, B.F.G. Johnson, G. Sankar, D. Ozkaya, W. Zhou, R.D. Oldroyd, R.G. Bell, *Angew. Chem. Int. Ed. Engl.*, **1997**, 36, 2242
- [28] J.M. Thomas, R. Raja, B.F.G. Johnson, T.J. O'Connell, G. Sankar, T. Khimyak, *J. Chem. Soc. Chem. Commun.*, **2003**, 10, 1126. See also *Science*, **2003**, 300, 867
- [29] R.D. Miller, *Science*, **1999**, 286, 421
- [30] M. Vallet-Regi, A. Ramila, R. P. del Real, J. Perez-Pariente, *Chem. Mater.*, **2001**, 13(2), 308; B. Munoz, A. Ramila, J. Perez-Pariente, I. Diaz, M. Vallet-Regi, *Chem. Mater.*, **2003**, 15(2), 500
- [31] C.T. Kresge, J.C. Vartuli, W.J. Roth, M.E. Leonovich, *Stud. Surf. Sci. Catal.*, **2004**, 148, 53
- [32] Q. Huo, D.I. Margolese, G.D. Stucky, *Chem. Mater.*, **1996**, 8, 1147
- [33] N.K. Raman, M.T. Anderson, C.J. Brinker, *Chem. Mater.*, **1996**, 8, 1682
- [34] C. Y. Chen, S.L. Burkett, H.L. Li, M.E. Davis, *Microporous Mater.*, **1993**, 2, 27
- [35] Q. Huo, D. Margolese, U. Ciesla, D. Demuth, P. Feng, T. Gier, P. Sieger, A. Firouzi, B. Chmelka, F. Schüth, G.D. Stucky, *Chem. Mater.*, **1994**, 6, 1176
- [36] A. Monnier, F. Schüth, Q. Huo, D. Kumar, D. Margolese, R.S. Maxwell, G. Stucky, M. Krishnamurty, P. Petroff, A. Firouzi, M. Janicke, B. Chmelka, *Science*, **1993**, 261, 1299
- [37] C. C. Egger, M. W. Anderson, G. J. T. Tiddy, J. L. Casci, *Phys. Chem. Chem. Phys.*, **2005**, 7, 1845
- [38] M. W. Anderson, C. C. Egger, G. J. T. Tiddy, J. L. Casci, K. A. Brakke, *Angew. Chem. Int. Ed.*, **2005**, 44, 2

- [39] L. Mercier, T. J. Pinnavaia, *Adv. Mater.*, **1997**, 9, 500
- [40] W. M. V. Rhijn, D. E. D. Vos, B. F. Sels, W. D. Bossaert, *Chem. Commun.*, **1998**, 3, 317
- [41] A. Stein, B. J. Melde, R. C. Schroden, *Adv. Mater.*, **2000**, 12, 1403
- [42] S. Inagaki, S. Guan, Y. Fukushima, T. Ohsuna, O. Terasaki, *J. Am. Chem. Soc.*, **1999**, 121, 9611
- [43] B. J. Melde, B. T. Holland, C. F. Blanford, A. Stein, *Chem. Mater.*, **1999**, 11, 3302
- [44] T. Asefa, M. J. MacLachlan, N. Coombs, G. A. Ozin, *Nature*, **1999**, 402, 867
- [45] S. Guan, S. Inagaki, T. Oshuna, O. Terasaki, *Microporous Mesoporous Mater.*, **2001**, 44-45, 165
- [46] S. Inagaki, S. Guan, T. Ohsuna, O. Terasaki, *Nature*, **2002**, 416, 304
- [47] K.P. de Jong, A. J. Koster, *Chem. Phys. Chem.*, **2002**, 3, 776
- [48] Y. Sakamoto, M. Kaneda, O. Terasaki, D. Y. Zhao, J. M. Kim, G. Stucky, H. J. Shin, R. Ryoo, *Nature*, **2000**, 408, 449
- [49] M. J. Kim, R. Ryoo, *Chem. Mater.*, **1999**, 11, 487
- [50] W. Zhou, H. M. A. Hunter, P. A. Wright, Q. Ge, J. M. Thomas, *J. Phys. Chem. B.*, **1998**, 102, 6933
- [51] M. Pérez-Mendoza, J. Gonzalez, P. A. Wright, N. A. Seaton, *Langmuir*, **2004**, 20, 7653
- [52] M. Pérez-Mendoza, J. Gonzalez, P. A. Wright, N. A. Seaton, *Langmuir*, **2004**, 20, 9856
- [53] S. Drumel, P. Janvier, P. Barboux, M. Bujoli-Doeuff, B. Bujoli, *Inorg. Chem.*, **1995**, 34, 148
- [54] J. L. Bideau, C. Payen, P. Palvadeau, B. Bujoli, *Inorg. Chem.*, **1994**, 22, 4885
- [55] K. Maeda, J. Akimoto, Y. Kiyozumi, F. Mizukami, *Angew. Chem. Int. Ed.* **1995**, 34, 1199
- [56] K. Maeda, J. Akimoto, Y. Kiyozumi, F. Mizukami, *J. Chem. Soc. Chem. Commun.*, **1995**, 1033
- [57] K. Maeda, Y. Kiyozumi, F. Mizukami, *J. Phys. Chem. B.*, **1997**, 101, 4402
- [58] V. J. Carter, P. A. Wright, J. D. Gale, R. E. Morris, E. Sastre, J. Perez-Pariente. *J. Mater. Chem.*, **1997**, 11, 2287
- [59] P. Grewal, N. Radhamonyamma, J. Gonzalez, P. A. Wright, P. A. Cox, *Stud. Surf. Sci. Cat.*, **2004**, 154, 1777

- [60] V. J. Carter, J. P. Kujanpää, F. G. Riddell, P. A. Wright, J. F. C. Turner, C. R. A. Catlow, K. S. Knight. *Chem. Phys. Let.*, **1999**, 313, 505
- [61] C. Schumacher, J. Gonzalez, P. A. Wright, N. A. Seaton., *Phys. Chem. Chem Phys.*, **2005**, 7, 2351 (Details about Neutron diffraction studies on AlMePO- α (HRPD) are given as supplementary information in this publication)
- [62] J. L. C. Rowsell, O. M. Yaghi, *Microporous Mesoporous Mater.*, **2004**, 73, 3
- [63] W. Mori, S. Takamizawa, C. N. Kato, T. Ohmura, T. Sato, *Microporous Mesoporous Mater.*, 2004, 73, 31
- [64] K. Seki., *Chem. Commun.*, **2001**, 1496; K. Seki., *Phys. Chem. Chem. Phys.* **2002**, 4, 1968; K. Seki, W. Mori., *J. Phys. Chem. B.*, **2002**, 106, 1380; R. Kitaura, K. Seki, G. Akiyama, S. Kitagawa., *Angew. Chem. Int. Ed.* **2003**, 42, 428
- [65] H. Li, M. Eddaoudi, M. O'Keeffe, O. M. Yaghi, *Nature*, **1999**, 402, 276
- [66] N. L. Rosi, J. Eckert, M. Eddaoudi, D. T. Vodak, J. Kim, M. O'Keeffe, O. M. Yaghi, *Science*, **2003**, 300, 1127
- [67] M. Eddaoudi, J. Kim, N. Rosi, D. Vodak, J. Wachter, M. O'Keeffe, O. M. Yaghi, *Science*, **2002**, 295, 469
- [68] O. M. Yaghi, M. O'Keeffe, N. W. Ockwing, H. K. Chae, M. Eddaoudi, J. Kim, *Nature*, **2003**, 423, 705
- [69] B. Chen, M. Eddaoudi, S. T. Hyde, M. O'Keeffe, O. M. Yaghi, *Science*, **2001**, 291, 1021
- [70] L. Huang, H. Wang, J. Chen, Z. Wang, J. Sun, D. Zhao, Y. Yan, *Microporous Mesoporous Mater.*, **2003**, 58, 105
- [71] J. F. M. Denayer, R. A. Ocakoglu, I. C. Arik, C. E. A. Kirschhock, J. A. Martens, G. V. Baron, *Angew. Chem. Int. Ed.*, **2005**, 44, 400.

Chapter 2.

Characterisation techniques

2.1. X-ray Powder Diffraction (XRD) [1]

A crystalline structure can be described in terms of its simplest repeating unit, the unit cell, that is defined by three translations, a , b and c , and three angles α , β and γ . There are seven basic types of unit cell (see table 2.1.1). For crystallographic purposes, it is often convenient to refer to lattice planes that pass through lattice points (identical points in space) in the structure. The reciprocal of the intercepts of these lattice planes on the three axes (x , y , z) are known as the Miller indices (h , k , l) and describe the three dimensional lattice planes. The spacing between adjacent lattice planes, which has particular relevance in description of diffraction, is designated d_{hkl} .

Crystal system	Lattice parameters
Triclinic	$a \neq b \neq c; \alpha \neq \beta \neq \gamma$
Monoclinic	$a \neq b \neq c; \alpha = \gamma = 90^\circ; \beta \neq 90^\circ$
Orthorhombic	$a \neq b \neq c; \alpha = \beta = \gamma = 90^\circ$
Tetragonal	$a = b \neq c; \alpha = \beta = \gamma = 90^\circ$
Rhombohedral	$a = b = c; \alpha = \beta = \gamma \neq 90^\circ$
Hexagonal	$a = b \neq c; \alpha = \beta = 90^\circ; \gamma = 120^\circ$
Cubic	$a = b = c; \alpha = \beta = \gamma = 90^\circ$

Table 2.1.1. The seven crystal system with their defining lattice parameters.

The phenomenon of diffraction is the interference caused by an object in the path of waves, and the pattern of varying intensity that results is called the diffraction pattern. Diffraction occurs when the dimensions of the diffraction object are comparable to the wavelength of the radiation. X-rays have wavelengths comparable to bond lengths in molecules and the spacing of atoms in crystals (about 100 ppm) and by analysing of the x-ray diffraction pattern it is possible to obtain a detailed picture of the atomic structure in solids.

When a monochromatic beam of X-rays is incident on a crystalline sample, every atom in the crystal scatters the X-ray beam in all directions. Constructive interference of

scattered X-ray radiation will only take place if the arrangement of atoms satisfy the Laue equations. The position of the diffracted beams depends on the unit cell dimensions and shape of the crystal symmetry. The intensity of the reflections depends on the position of the atoms within the unit cell and the scattering power of the atoms. Heavier atoms, which have more electrons, scatter the x-rays more strongly.

Reflections only occur at certain values of θ , depending on the wavelength λ , of the incident X-rays and the spacing, d , between the planes in the crystal lattice (see Figure 2.1.1). This is expressed by the Bragg equation:

$$AB + BC = 2d_{hkl}\sin\theta$$

$$\lambda = 2d_{hkl}\sin\theta$$

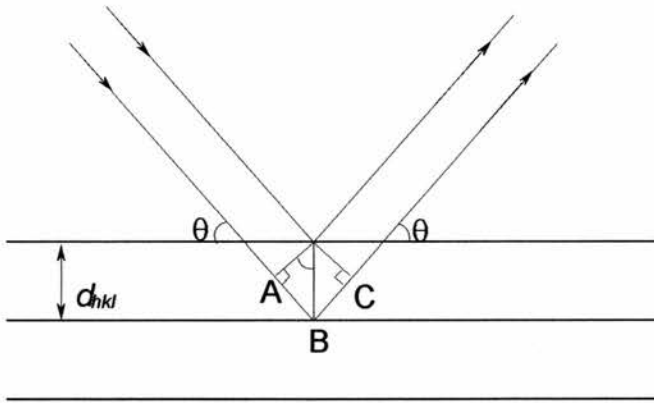


Figure 2.1.1. Bragg reflection from crystal planes of spacing d_{hkl} .

Powder XRD is a simple technique to obtain diffraction patterns. Here a finely divided polycrystalline powder with random orientations is used instead of single crystal. As the powdered sample contains a large number of crystallites there will be some Bragg reflection from each set of planes. When the X-ray beam with known wavelength λ , is at an incident angle θ the reflected beam from the powdered sample will make an angle 2θ with the incident beam. The sample and the detector are rotated during the measurement in order to collect all the 2θ angles. The intensity of the reflected beam is then measured by the detector. Reflections from sets of planes of the powdered interface

constructively when the Bragg condition is met and lead to high intensities measured at the detector. The set of d-spacing data can be obtained from the diffraction pattern based on the Bragg equation. If the values of h , k and l for the planes responsible for the reflections are known, the dimensions of the unit cell can be deduced. For example, for the mesoporous silicate structure SBA-1, the dimensions of the unit cell can be deduced on basis of the equation

$$\frac{1}{d_{hkl}^2} = \frac{(h^2 + k^2 + l^2)}{a^2},$$

that relates the Miller indices (hkl) and the lattice parameters for cubic symmetry. The figure below presents the XRD pattern of SBA-1 with some indexed reflections.

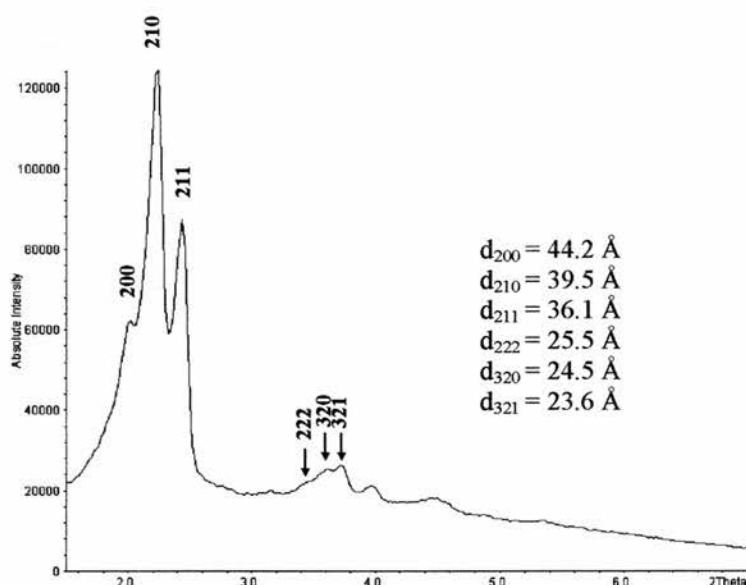


Figure 2.1.2. Indexed XRD pattern of SBA-1 mesoporous solid ($a = 88.4 \text{ \AA}$).

Mesoporous materials, due to their amorphous nature and the presence of long-range order exhibit only few diffraction features in the low angle region (below $10^\circ 2\theta$). It is plausible to calculate the unit cell parameters but, as they are not crystalline materials, the determination of atomic positions is not possible. In addition it can be difficult to determine phase purity due to the experimental error and broadness of the peaks. This concept is illustrated by the theoretical low angle peak positions for hexagonal and

cubic crystal systems, Figure 2.1.3. The figure also presents the XRD pattern of a SBA-2 solid calcined at 550 °C. The structure of this solid is built up by spherical supercages arranged in either hexagonal close packing or cubic close packing. Note that the pattern can be indexed according to both $P6_3/mmc$ or $Fm\bar{3}m$ symmetry.

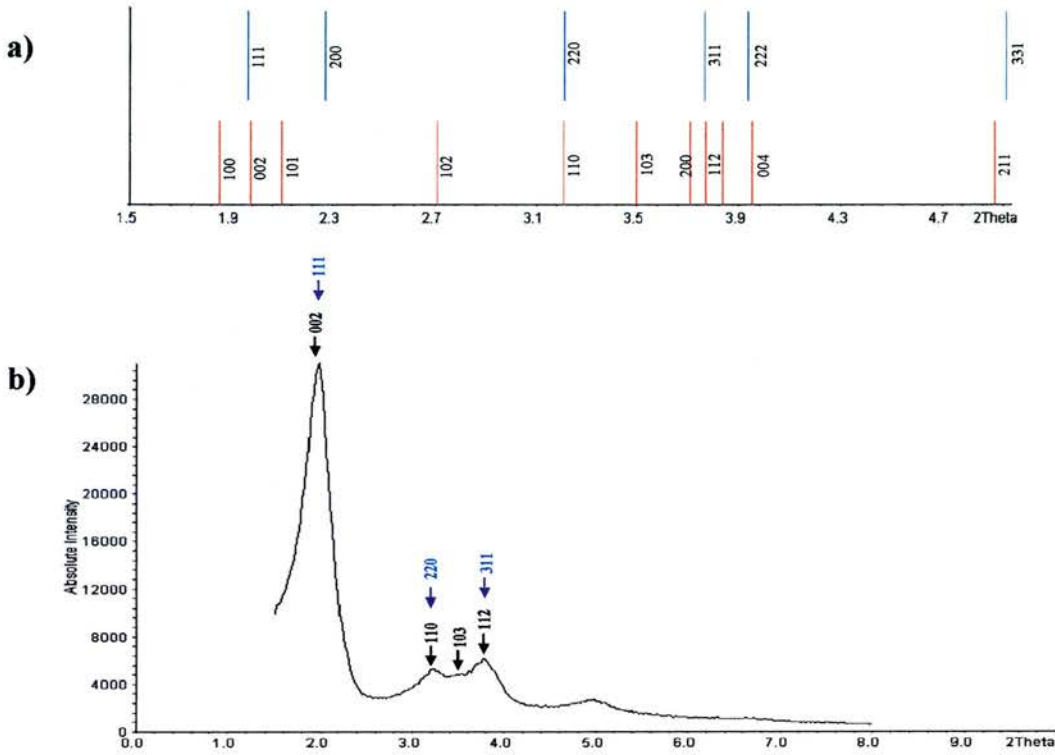


Figure 2.1.3 a) Theoretical XRD peak positions for the hcp ($a = 55.0 \text{ \AA}$, $c = 89.3 \text{ \AA}$) and ccp ($a = 77.7 \text{ \AA}$), indexed appropriately. Note that the hexagonal (103) peak does not have a cubic equivalent. b) SBA-2 XRD pattern diffraction indexed according to both $P6_3/mmc$ (black) and $Fm\bar{3}m$ symmetry (blue).



Figure 2.1.4 An X-ray diffractometer typically used to produce diffraction patterns of crystalline materials.

In this thesis XRD has been used for phase identification. Powder X-ray diffraction patterns were collected in transmission mode in the form of powder supported in 0.7 mm quartz glass capillaries. Measurements were made at ambient temperature using monochromated $\text{Cu K}_{\alpha 1}$ radiation, $\lambda = 1.54056 \text{ \AA}$, on a STOE Stadi/p diffractometer (an image of the diffractometer used in this work is shown above this paragraph).

2.2. Transmission Electron Microscopy [2]

Transmission electron microscopy is used to understand the local structure of a sample and in mesoporous solids high resolution TEM is used to elucidate the structure, together with XRD. In addition the mesoporous solids can be imaged at relatively low magnifications without any loss of information due to their large unit cells. There has therefore been extensive research on mesoporous solids using HRTEM to help solve their structures.

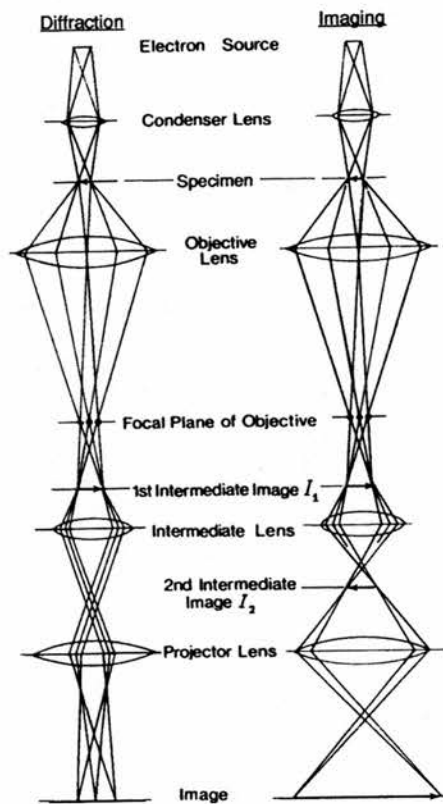


Figure 2.2.1. A diagrammatic view of the electron pathway within the evacuated column showing both the diffraction and imaging modes.

In transmission electron microscope, electrons are produced from a heated source (e.g. lanthanum hexaboride (LaB_6) crystal or a tungsten filament). Electrons are accelerated in an electric field generating a high energy beam of kinetic energy:

$$eV = \frac{m_0 v^2}{2}$$

This leads to the relationship between the electron wavelength, λ and the accelerating voltage of the electron microscope, V :

$$\lambda = \frac{h}{(2m_0 eV)^{1/2}}$$

where m_0 and e are the mass and charge of the electron respectively and h is Planck's constant. The smallest distance that can be resolved, according to the Rayleigh equation is:

$$\delta = \frac{0.61\lambda}{\mu \sin \beta}$$

with λ equalling the wavelength of radiation, μ the refractive index of the viewing medium and β the semi-angle of collection of the magnifying lens. μ and β are approximately unity so the resolution is equal to about half the wavelength of light. The wavelength of the electrons is related to their energy, E . de Broglie's equation approximates:

$$\lambda = \frac{1.22}{E^{1/2}}$$

with E in electron volts (eV) and λ in nm. So for a 200 keV electron microscope the theoretical wavelength is about 3 pm (0.003 nm), much smaller than the diameter of the atom, although electron microscopes do not achieve such theoretical resolutions due to imperfections in the magnetic lenses. A series of lenses are required in order to focus and magnify the beam through the microscope. Since an electron has a charge the path

of the beam can be altered by magnetic fields. A schematic representation of an electron microscope from the electron source to the image was shown in Figure 2.2.1.



Figure 2.2.2. High resolution transmission electron microscope equipped with EDX operating at 200 keV at St. Andrews University.

In this thesis, like XRD, TEM has been used for phase identification purposes. Micrographs were taken using a JEOL-JEM 2011 electron microscope equipped with a CCD Gatan digital camera operating at 200 keV. Samples were ground before being dispersed in acetone then deposited onto a holey carbon film, supported on a Cu grid. The objective lens parameters, $C_s = 0.50$ nm and $C_c = 1.10$ nm gave a point resolution of ca. 1.94 \AA .

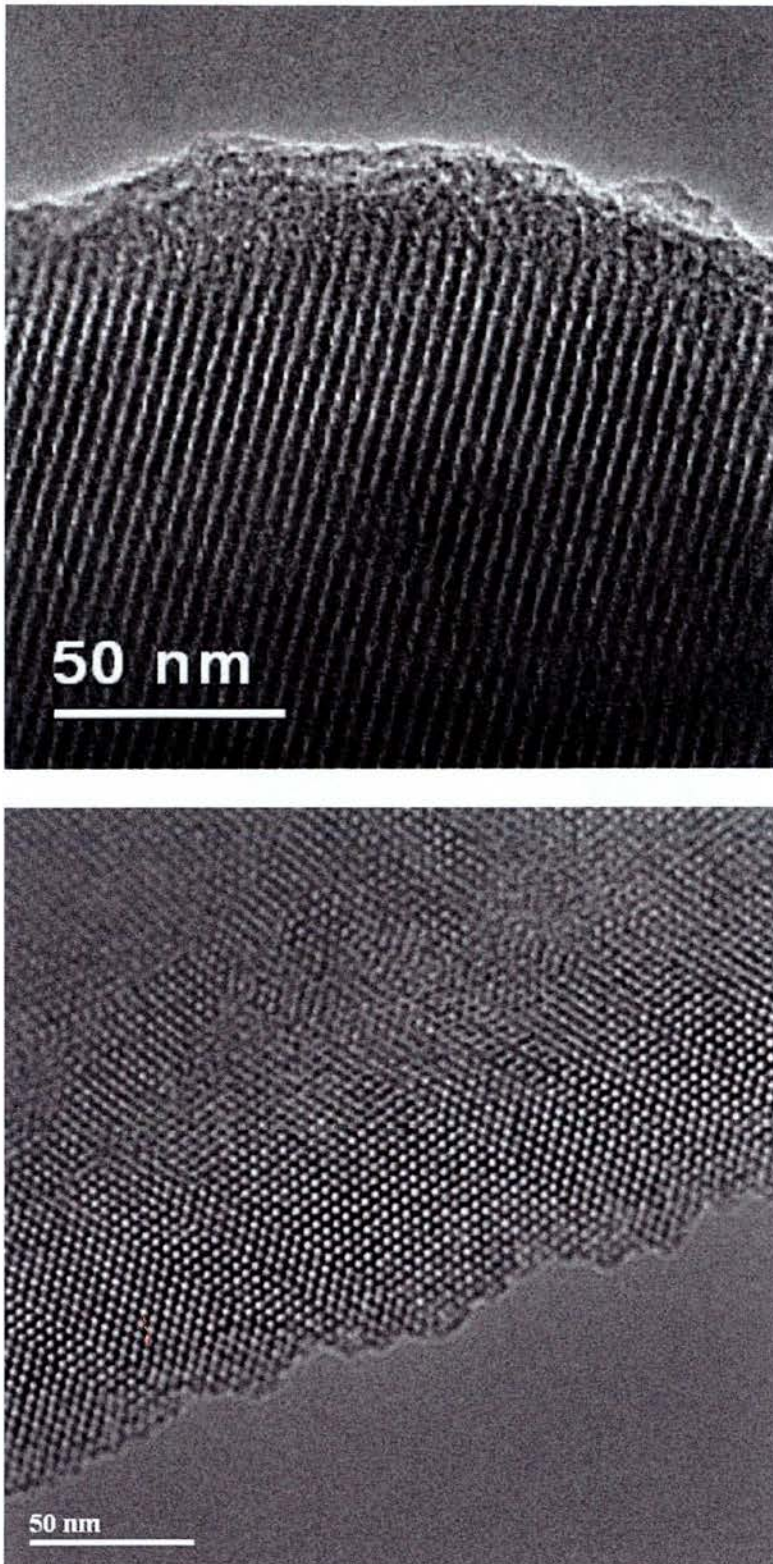


Figure 1.2.3. Examples of TEM micrographs of mesoporous solids. Top, of post-synthesis phenyl-functionalised MCM-41. Bottom, ethane-siloxane SBA-2

2.3. Gas and Vapour Adsorption.

The measurements of adsorption (and desorption) of gases and vapours are widely used to determine surface area, pore volume and pore size distribution of porous solids. Using selected probe molecules can also provide information about pore connectivity and surface chemistry (i.e. surface polarity).

Typically the gas (adsorbate) uptake is measured, at a constant temperature as the pressure of the adsorbate is varied. The uptake can be measured volumetrically or gravimetrically, the later method being employed more frequently in this thesis. Typically, both adsorption and desorption are measured. The uptake of gas, which can be expressed as an equivalent volume at standard pressure, as a true volume or mass or moles per g, is plotted against the equilibrium pressure at constant temperature (isotherm). According to the Brunauer classification [3], there are five basic types of isotherms (See figure below).

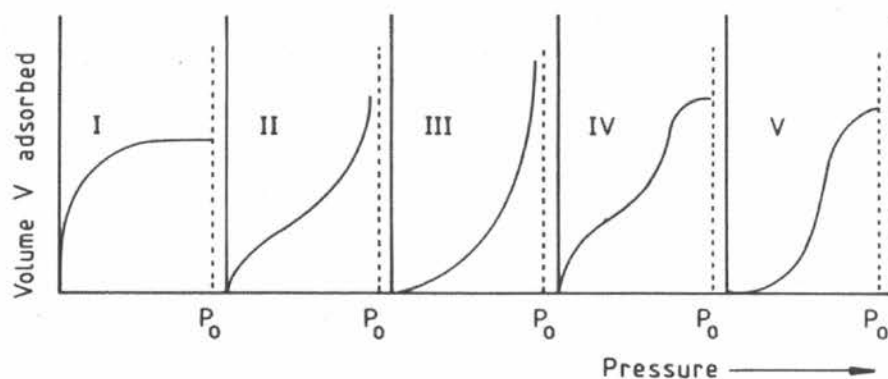


Figure 2.3.1. The Brunauer classification of the five types of adsorption isotherms [3].

Type I isotherms are typical of microporous solids. They are characterised by a rapid rise in the volume adsorbed at low pressures corresponding to pore filling followed by a plateau governed by total pore volume. Any gradual increase in adsorption at high partial pressures, therefore, is attributable to multilayer coverage of the external surfaces.

Mesoporous solids normally exhibit type IV isotherms (see Figure 2.3.2 for examples). The initial monolayer coverage is built upon by multilayer adsorption at higher

adsorbate pressures, in an exactly similar way to that observed in type II isotherm, which are typical of open surfaces. At higher relative pressures a steeper upward slope forms as a direct result of capillary condensation. The internal surface and free pore volume decrease upon multilayer adsorption and a critical pressure is reached at which capillary condensation occurs to fill the remaining volume preferentially over any larger diameter pores. There is a significant increase in uptake over a narrow pressure region and the type IV isotherm – now distinguished from type II isotherm –reaches a plateau upon pore filling with the upper limit of adsorption governed by the total pore volume.

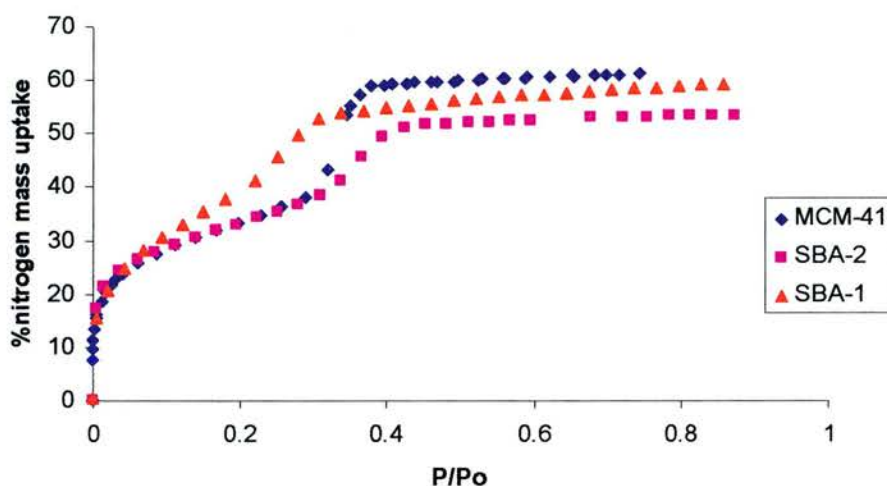


Figure 2.2.2. Experimental N₂ adsorption isotherms at 77 K in MCM-41, SBA-2 and SBA-1 silicate mesoporous solids.

On larger pore mesoporous solids, like SBA-15, where the capillary condensation occurs at higher P/P_o (~ 0.8), desorption from the pores takes place at lower relative pressures than the adsorption. This hysteresis loop in the mesoporous region, occurs as a result of adsorption of a metastable multilayer, which remains on the pore wall before the onset of capillary condensation. On the other hand, desorption takes place over a concave surface at lower pressures. This condensation pressure drop or increase depends also on the shape of the pore surface (spheres, cylinders etc).

The most common method of obtaining data on the specific surface area of samples from adsorption data, is the use of the Brunauer-Emmett-Teller (BET) equation [4]. The equation is applicable to multilayer adsorption reflected in type II isotherms and also the lower pressure regions of type IV isotherms displayed by mesoporous solids.

BET theory - an extension of the Langmuir theory - allows for the formation of multilayers to form on top of the initial monolayer. There are however assumptions made in order to derive such a theory: (i) the heats of adsorption for the monolayer is independent of surface coverage, and (ii) the heats of formation of the second and third layer etc (the multilayers) are all assumed to be the same, and different from that of the monolayer. The predominant interactions in the multilayers are adsorbate-adsorbate so that their formation is similar to the heat of condensation. The monolayer involves interactions of gas molecule - surface site which will be different from gas-gas interactions and probably significantly larger. The BET equation can be expressed as

$$\frac{P}{V(P_0 - P)} = \frac{c-1}{V_m c} * \frac{P}{P_0} + \frac{1}{V_m c},$$

where V is the volume of gas adsorbed (corrected to STP) at a specific value of P an equilibrium pressure with the constant c

$$c \sim \exp \frac{\Delta H_{liquid} - \Delta H_{monolayer}}{RT}.$$

In practice the assumptions on which the derivation of the BET equation is derived are such that the above equation is only applicable up to P/P₀ values of about 0.03 → 0.4.

In order to obtain a straight line from the above equation - which in turn shows the data from the experiment obeying the BET model - a plot of P/P₀ as x and P/[V(P₀-P)] as y is plotted, with gradient and intercept (equations 2.3.3 and 2.3.4 respectively);

$$gradient = \frac{c-1}{V_m c}$$

$$intercept = \frac{1}{V_m c}$$

In many cases the gradient is much larger than the intercept (equivalent to c >>1) and thus the equation for the volume of the monolayer simplifies to

$$V_m = \frac{1}{\text{gradient}}$$

V_m can be converted into moles and hence the specific surface area (S_g , m^2/g) can be derived using, for example, molecular area of a nitrogen molecule (16.2 \AA^2 at 77K).

$$S_g = \frac{V_m}{0.0224} \times 6.023 \times 10^{23} \times A$$

In the capillary condensation region, the pore size distribution can be derived using the Barrett-Jayner and Halenda (BJH), which is based on the Kelvin equation [5]

$$RT \ln\left(\frac{P}{P_0}\right) = \frac{2\gamma V_m}{r}$$

where γ = surface tension; V_m = molar volume and r = radius of curvature of condensed gas assuming 0° contact angle of liquid nitrogen with pores.

The applicability of the BJH method for the calculation of pore size distribution in mesoporous solids is controversial and it has been shown to underestimate the pore size in many cases. Non Local Density Functional Theory software, NLDFIT, (the most recent method to determine pore sizes of spherical connected pores [5]) was not available for this thesis. BET surface area and BJH pore size distribution calculations were performed using IGA-2 gravimetric analyser software. In the case of mesoporous solids, like SBA-1 and SBA-2, these values should only be used for comparative purposes, as the models are not strictly applicable.

Quantifying the strength of adsorption:*Heats of adsorption:*

In Part I of this thesis, the adsorption properties of phenyl-functionalised mesoporous solids are studied. This aromatic functionalisation is expected to enhance the interaction of aromatic molecules, like toluene, with the solids. This effect has been analysed through measurements of the isosteric heats of adsorption. These were measured using the Clausius-Clayperon equation:

$$\frac{d \ln P}{dT} = \frac{\Delta H_{\text{ads}}}{RT^2}$$

On basis of this equation, for a fixed gas uptake by the solid, a plot of $\ln P$ vs $1/T$ is a straight line with slope $\frac{\Delta H_{\text{ads}}}{R}$.

Henry constant:

In an adsorption isotherm, as $P \rightarrow 0$, the amount adsorbed follows a linear relation with the pressure that can be defined by the equation

$$\text{Amount adsorbed} = K_H * P,$$

where K is an empirical temperature-dependent constant called Henry's constant.

Henry's constant measures of the strength of the interaction between the gas and the solid because in the low pressure region in which the equation is applicable adsorbate-adsorbate interactions are negligible.

Experimental:

Nitrogen adsorption isotherms (0-1 bar) were obtained gravimetrically using an IGA-II series automated gravimetric analyser (see figure below). Typically between 10 – 25 mg of sample are used in each isotherm run. Samples were degassed at 383 K for 3 h (typical heat ramp rate of 5 °C/ min). The sample is then cooled down (typically 308 K)

before the dry mass is set. The sample is immersed in liquid nitrogen and data collection started at typically 173 K. The isotherm run followed a program consisting of an adsorption branch followed by a desorption branch.

Low pressure CO₂, butane, isobutane and toluene adsorption experiments were performed using similar procedures using a thermostatted water bath to control the temperatures. Low temperature experiments of CO₂ were carried out using a dry ice/EtOH bath.

The equilibrium adsorption values were those calculated by mathematical analysis of the asymptotic increase or decrease of weight within a 1 h time period.



Figure 2.3.3. A Hiden IGA (Intelligent Gravimetric Analyser) used to measure N₂ isotherms at 77 K.

High pressure adsorption experiments.

Selected samples were analysed by means of high pressure adsorption experiments of ethane and CO₂. These experiments allowed the study of the adsorption properties of these solids in conditions similar to those used in pressure swing separation processes.

Experiments were performed on a high pressure adsorption rig at the School of Chemical Engineering, Edinburgh University (in the laboratory of Prof. N. Seaton) in collaboration with Christian Schumacher and Manuel Pérez Mendoza, co-workers in this project (see figure below, a description of the rig can be found in ref [6]).

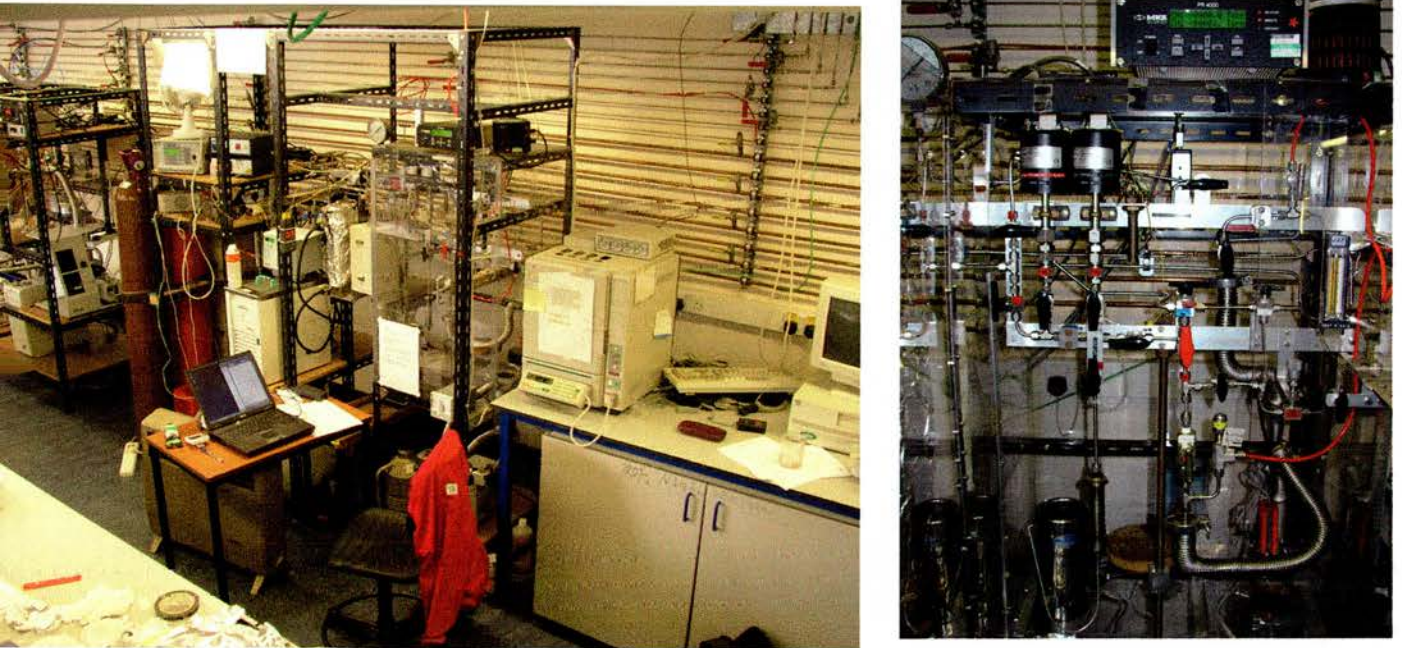


Figure 2.3.4. High pressure adsorption rig at the School of Chemical Engineering at Edinburgh University. A description of this apparatus can be found in ref [6]

Typically, 10g of sample were dried for 6~8 h at 110 °C in an oven before measuring the dry weight of the solid. After this, the solid was placed on the adsorption chamber of the rig, and the sample was outgassed for 4 hours at 110 °C using an oil pump.

After cooling the sample to room temperature, it was necessary to check the absence of leaks in the system. For this, helium was introduced onto the system at a pressure of 20 atmospheres and the rig was isolated. Constant pressure reading during 2 hours indicated that no leaks were present.

After the calibration of the void volume within the adsorption chamber with helium, this was removed from the system with the help of the vacuum pump at room temperature, and the adsorption chamber was cooled to the desired temperature using a thermostatted bath.

High pressure adsorption experiments were performed manually using small pressure steps. The different points of the isotherms were taken after equilibration of the pressure

and temperature of the sample (measured with a thermocouple). After initial adsorption experiments the sample was slowly degassed, at 110 ° C, and a second experiment performed. Overlapping of the two sets of isotherms was taken to indicate reliable data. During this thesis, it was necessary to make an important modification of the adsorption rig. Calcined silicate mesoporous solids (at least SBA-1, SBA-2 and MCM-41) are readily compacted into pellets by application of very small pressures that do not induce any damage or modification into their structure or adsorption properties. Compacting of the sample into big particles is critical in order to retain the solid in the adsorption chamber and avoid contamination of the high pressure adsorption rig. However, phenyl- and aminopropyl-functionalised SBA-1, SBA-2 and MCM-41 cannot be compacted into larger particles without using a pressure so high that they affect their structure and therefore their adsorption properties. Many attempts to achieve a sample with suitable characteristics were unsuccessful, since the particles do not cohere.

To collect the high pressure isotherms it was necessary to place the sample inside a “cigarette” built with a membrane¹ that allows the diffusion of the gas (see Figures 2.3.5 and Figure 2.3.6). The membrane was glued into two metal pieces at the top and at the bottom of the “cigarette”. The sample was loaded through a hole that was closed before the experiments using a screw.



Figure 2.3.5. Special “membrane cigarette” device to measured high pressure adsorption experiments on fine grained powder solids.

¹ The membrane was obtained from MEMBRANA Underlining Performance. (MicroPres®). (<http://www.membrana.de/industrial/center.htm>)

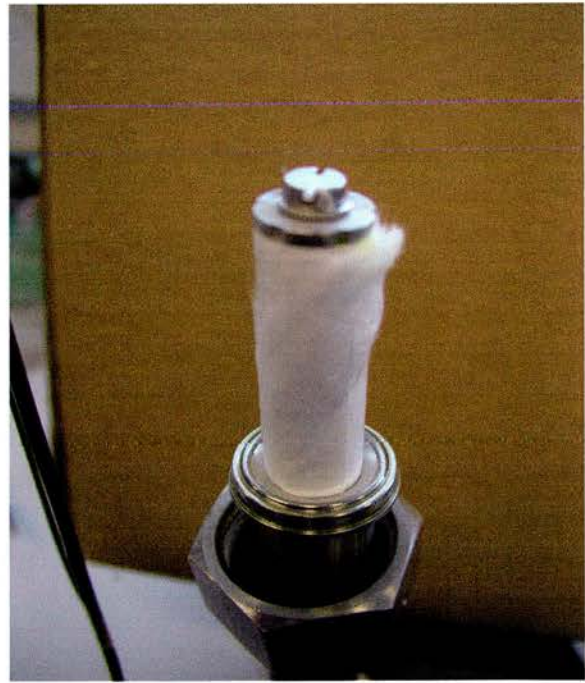
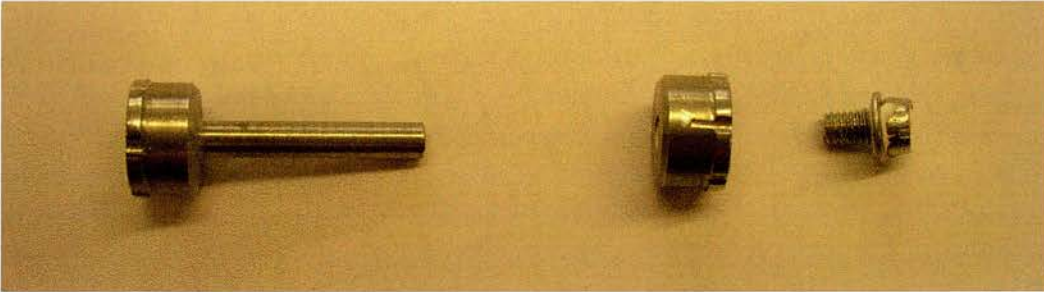


Figure 2.3.6. Top, components of the “membrane cigarette” device to measured high pressure adsorption experiments on fine grained powder solids. Bottom, High pressure adsorption chamber.

2.4. NMR introduction: [7, 8, 9, 10]

Nuclear magnetic resonance is arguably the most powerful spectroscopic technique available to the chemist for combined structural characterisation and study of dynamic processes. In Part I of this thesis NMR has been used to characterise both silicate and organic modified mesoporous solids. In Part II, ^2H NMR has been used to study the dynamics of adsorbed molecules and framework groups of microporous organic-inorganic hybrids.

In this section the background theory of the technique is briefly outlined. First, NMR the vector model of NMR is described, because it is of help in understanding the generation of the NMR signal. Secondly, the main interactions experienced by the nucleus are summarised. The quadrupolar interaction of the deuterium nucleus is of special interest because it is the source of the valuable information that ^2H NMR provides about dynamics. It is therefore treated in slightly more detail. A more detailed description of the basics of the theory behind this technique can be found in ref [7, 8, 9 and 10].

This section also includes:

- (i) A description of the method used to load porous solids with deuterated molecules.
- (ii) A summary of the techniques used in this thesis for the collection of the NMR signals.
- (iii) A description of the two computer codes used for the simulations of the ^2H NMR spectra, MXQET and MXQET1 [11].

The vector model of NMR.

Magnetic active nuclei, i.e. nuclei with spin number $I \neq 0$, have a magnetic moment, $\vec{\mu}$, related to the spin number by

$$\vec{\mu} = \gamma \vec{I}$$

where γ is the gyromagnetic ratio, a constant for each nucleus. In a strong magnetic field, nuclei behave like “little magnets” and adopt energetically favoured positions orientating themselves within the magnetic field. The overall magnetisation of a sample,

\vec{M} , is defined as the vectorial sum of all the individual magnetic moments associated with all the nuclei. Thus the overall magnetisation of the sample can be expressed as

$$\vec{M} = \gamma \vec{J}$$

where \vec{J} is the spin angular momentum of the sample giving rise to the magnetization.

If nuclei are placed in a uniform magnetic field \vec{B} , a torque \vec{T} is exerted on the magnetization vector:

$$\vec{T} = \frac{d}{dt} \vec{J}; \quad \vec{T} = \vec{M} \times \vec{B}$$

Combining the two previous equations, it is possible to write,

$$\frac{d\vec{M}}{dt} = \gamma \vec{M} \times \vec{B},$$

the expression that describes the motion of the bulk magnetization vector \vec{M} around \vec{B} .

It can be shown that the last equation predicts that \vec{M} precesses about \vec{B} at a constant rate $\omega = \gamma B$. This frequency is called the Larmor frequency.

A radiofrequency electromagnetic wave (rf) has associated with it an oscillating magnetic field. In an NMR experiment, this rf is arranged so that its magnetic field oscillates perpendicularly to the \vec{B} direction. This oscillating magnetic field can be thought as two vectors rotating about \vec{B} in opposite senses. It can be shown that only the component that rotates in the same direction as the above precession has an effect on \vec{M} .

The effect of this oscillating magnetic field, \vec{B}_1 , is most easily seen by transforming the whole problem into a reference frame that rotates at frequency ω_{rf} around \vec{B} . In this "rotating frame", \vec{B}_1 appears static. It was said before that in the laboratory frame and in the absence of any radiofrequency, the bulk magnetisation vector \vec{M} precesses around \vec{B}_1 at a frequency ω_0 . If the pulse is on resonance, $\omega_0 = \omega_{rf}$, and so in the rotating frame \vec{M} appears stationary. In the presence of an on resonance rf, the only magnetic field present in the rotating frame is \vec{B}_1 . Therefore, during the application of this field, the macroscopic magnetization precesses around \vec{B}_1 at a frequency $\gamma \vec{B}_1$.

An important concept in NMR is the phase of the pulse which is defined as the angle that \vec{B}_1 makes to the x axis of the rotating frame. The flip angle is the angle, θ_{rf} , that the pulse field B_1 turns the magnetization during a time τ_{rf} :

$$\theta_{rf} = \gamma B_1 \tau_{rf}$$

Rotations, by definition, are anticlockwise around an axis. So, for example, a 90°_x pulse is a pulse that flips the angle of the magnetization by $\pi/2$ radians around x , leaving the \vec{M} vector lying on $-y$.

This transverse magnetisation precessing at ω_0 , induces an oscillating magnetic flux density and therefore, a voltage in the coil.

After the pulse, the M_z returns to its equilibrium position about the magnetic field. This process, spin lattice relaxation, is characterised by a spin-lattice relaxation time constant, T_1 , defined as

$$\frac{dM_z}{dt} = -\frac{M_z - M_0}{T_1}$$

When the radiofrequency pulse is turned off, the transverse component of the magnetization, which is precessing at many frequencies, dephases on the xy plane until it is lost. This dephasing is due to the exchange in energy between the nuclei in the sample. This evolution of the magnetization in the transverse plane, spin-spin relaxation or transverse relaxation, is characterised through another time constant, T_2 .

Interaction experience by the nuclei. NMR and energy levels.

Zeeman interaction.

Nuclei with spin number $I \neq 0$ possess a spin angular momentum \vec{I} with modulus $|\vec{I}| = \hbar \sqrt{I(I+1)}$ where I is the spin quantum number and $\hbar = h/2\pi$. All magnetically active nuclei have nuclear magnetic dipole moment $\vec{\mu} = \gamma \vec{I}$ coaxial with \vec{I} . When a magnetic field is applied, by convention in the z direction, this interacts with the magnetic moment. The corresponding Hamiltonian is:

$$\hat{H}_z = -\hat{\mu} \cdot \vec{B} = -\gamma \hat{I}_z B_0$$

The value of the z component of the spin angular momentum, is defined as $\hat{I}_z = \hbar m$ where the magnetic quantum number $m = (-I, -I+1, \dots, I, I-1)$ has $2I+1$ possible values corresponding to $2I+1$ energy states. Therefore a nucleus with spin number $I=1/2$ possesses two degenerate energy levels. In the presence of a magnetic field, these levels split into two different states. The difference in energy between the states is linear with the magnetic field and equal to

$$\Delta E = \gamma B_0 \hbar = \hbar \omega_0,$$

The energy transition between the states corresponds to a radiofrequency ν_0 :

$$\nu_0 = \omega_0 / 2\pi = \Delta E / h.$$

When an rf is applied on resonance with ν_0 , the Larmor frequency, transitions between the energy levels take place.

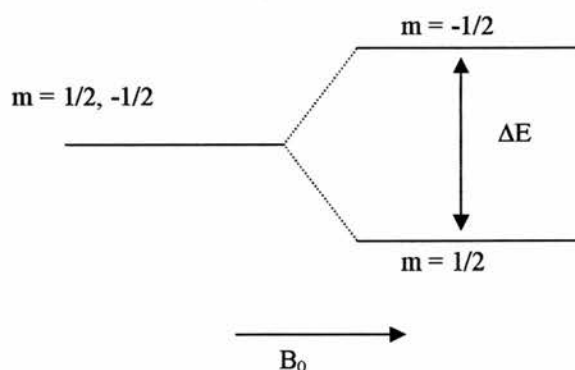


Figure 2.4.1. Zeeman splitting of the energy levels of a spin $\frac{1}{2}$ in a B_0 magnetic field.

The population difference between the energy levels is a function of the temperature and is given by the Boltzmann distribution:

$$\frac{N_\alpha}{N_\beta} = \exp\left(\frac{-\Delta E}{kT}\right)$$

If the Zeeman interaction were the only existing interaction, NMR would not provide any information about the structure or dynamics of the system under study. The origin of this information comes from other interactions experienced by the nuclei. These interactions are the chemical shielding, the dipolar coupling, the spin-spin coupling and

the quadrupolar coupling. A general hamiltonian can be written to describe the combination of the sum of all these interactions:

$$H_{\text{Total}} = H_z + H_{\text{CS}} + H_{\text{D}} + H_{\text{SS}} + H_{\text{Q}}.$$

All these interactions are magnetic field orientation dependent and therefore have an anisotropic component.

Chemical Shift interaction.

The magnetic field experienced by a particular nucleus in a sample does not depend only on B_0 . Chemical structure around the nuclei has an influence on this magnetic field, in particular the electrons surrounding the nuclei. This interaction, B_0 dependent, causes a change in the Larmor frequency of the nuclei. The values of the chemical shift are measured by the frequency difference from a reference material and it is expressed in parts per million (ppm).

$$\delta = \frac{10^6 (\nu_{\text{sample}} - \nu_{\text{ref}})}{\nu_{\text{ref}}}$$

Since the electron distribution in general is not spherical, the shift depends on the orientation of the molecules with respect to the external magnetic field B_0 . The anisotropy of the chemical shift causes a broadening of the NMR signals of solids samples. In liquids, the chemical shift anisotropy averages out by the molecular motion, leaving an isotropic chemical shift.

The Hamiltonian of the anisotropic chemical shift reads

$$\hat{H}_{\text{cs}} = \gamma \vec{I} \hat{\sigma} \vec{B}_0,$$

where the shielding tensor $\hat{\sigma}$ is a 3×3 matrix.

Dipolar interaction.

Since each nuclear spin is magnetic, it generates a magnetic field that interacts through space with the surrounding spins. The dipole-dipole Hamiltonian, H_{D} , between two spins reads,

$$\hat{H}_D = \gamma_1 \gamma_2 \hbar^2 \left\{ \frac{\vec{I}_1 \vec{I}_2}{r_{12}^3} - 3 \frac{(\vec{I}_1 \vec{r}_{12})(\vec{I}_2 \vec{r}_{12})}{r_{12}^5} \right\} \frac{\mu_0}{4\pi}$$

where μ_0 is the permeability constant, γ_1 and γ_2 are the gyromagnetic constants of the two spins, \vec{r}_{12} is a unitary vector parallel to the line joining the two spins and r_{12} is the distance between the two spins.

According to the previous equation, the dipole-dipole interaction between two nuclei is dependent on the gyromagnetic constant and the distance between the nuclei. Note also that the Hamiltonian is angular dependent because the vector \vec{r}_{12} changes direction as the molecules moves. In solution, this interaction averages out due to the fast molecular tumbling. On the other hand, in solids dipole couplings are the main cause of signal broadening and loss of spectral resolution. Techniques like MAS and high power decoupling are necessary to improve the spectral resolution. However, through sophisticated techniques, the dipole-dipole interaction can be exploited in order to obtain structural information (interatomic distances, etc).

Spin-spin coupling interaction.

The interaction arises from an indirect coupling of a pair of spins through the electron bonds. The hamiltonian of this interaction is given by:

$$\hat{H}_J = 2\pi \vec{I}_1 \hat{J} \vec{I}_2$$

where \hat{J} is the J-coupling tensor. This interaction, much smaller than the dipole-dipole interaction does not play an important role in NMR of solid samples.

Quadrupole interaction.

Magnetic nuclei with spin number $I \neq \frac{1}{2}$ posses an electric quadrupole moment, in addition to the magnetic dipole moment, that interacts with electric field gradients at the site of the nucleus. Quadrupole moments arise due to a non spherical distribution of charge of the nucleus. The electric field gradient that a nucleus feels depends on the immediate environment around the nucleus, i.e. the geometry of the bonds around the nucleus.

The general expression of the Hamiltonian describing the quadrupole interaction can be written as:

$$H_Q = \frac{eQ}{2I(2I-1)\hbar} \hat{V} \hat{I} \hat{I},$$

where \hat{V} is the electric field gradient at the nucleus, \hat{I} is the nuclear spin vector and Q is the nuclear quadrupole moment.

It is conventional to define the parameters

$$eq = V_{zz}^{PAS} \quad \eta_Q = \frac{V_{xx}^{PAS} - V_{yy}^{PAS}}{V_{zz}^{PAS}}$$

to describe the electric field gradient tensor at the nucleus site. η_Q is the asymmetry parameter and eq is the expression of the structure dependent value of the principal value of the electric field gradient tensor in the principal axis system (PAS), reference frame in which the tensor is diagonal.

For nuclei with $\eta_Q = 0$, on basis of a first order perturbation the Hamiltonian can be rewritten as

$$\hat{H}_Q = \frac{e^2 q Q}{4I(2I-1)\hbar} \cdot \left(\frac{1}{2} (3\cos^2\theta - 1) (3\hat{I}_z^2 - \hat{I}^2) \right)$$

The angle θ defines the orientation of the magnetic field respect to the PAS. It is usual to express the strength of the quadrupolar coupling defining a quadrupolar coupling

constant
$$\chi = \frac{e^2 q Q}{\hbar}.$$

Due to the angular dependency of the Hamiltonian, this interaction leads also to a powder pattern. The width and shape of the powder pattern are dependent on χ and η_Q .

Quadrupole interaction for ^2H nucleus.

Deuterium is a quadrupolar nucleus which has a relatively small quadrupole moment. In C-D bonds, the electric field gradient tensor is approximately axially symmetric, $\eta_Q=0$.

Due to these two properties, the deuterium NMR is particularly well suited to study molecular motion of organic molecules, since it is in principle possible to follow motions occurring on timescales of between 10 MHz and 1 Hz by a combination of wide-line spectroscopy and relaxation time measurements

^2H possesses a spin number $I = 1$. In the presence of a magnetic field, the Zeeman interaction influences the energy levels in a way that all the $m-1 \rightarrow m$ transitions are equally spaced. This situation corresponds to an unique resonance frequency and would generate an isotropic peak shape. The quadrupole interaction experience at the nucleus site shifts the energy levels and the corresponding NMR signal results in a doublet symmetric to the Larmor frequency, ν_0 , with a splitting

$$\Delta\nu_Q = 3/4\chi(3\cos^2\theta - 1),$$

where θ is the angle between the principal axis of the electric field gradient tensor and the applied magnetic field.

In a powder sample, there are many crystallites with different angles (θ) between the C-D bond, the principal axis of the electric field tensor, and the applied magnetic field. This results in a powder pattern that, in the absence of any motion, exhibit $3/4\chi$ splitting between the sharp singularities.

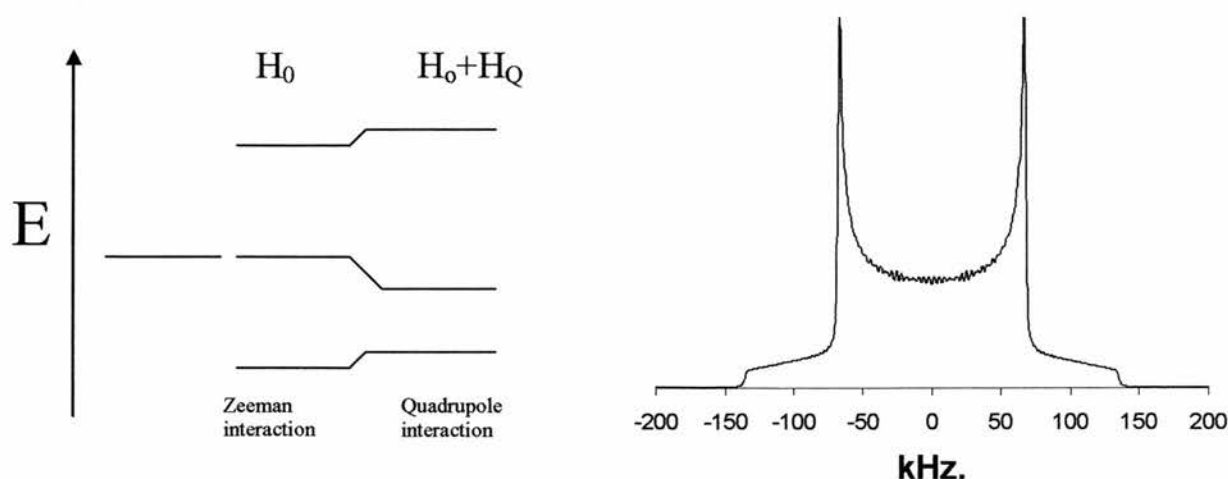


Figure 3.4.2. Energy level diagram for ^2H , $I = 1$, in the presence of magnetic field (left) and simulated powder pattern spectra for a static C-D bond (right).

In the presence of molecular motion the shape of the NMR signal will change. If this motion is rapid on the time scale defined by the inverse width of the spectra in the absence of motion (fast limit motion $\sim 10^7$ Hz), the effective electric field gradient tensor experienced by the nucleus will be the average of all the tensor positions occupied during the motion.

The average frequency, expressed in terms of the average tensor, would be

$$\bar{\omega}(\theta_a, \phi_a) = \bar{\delta} \frac{1}{2} (3 \cos^2 \theta_a - 1 - \bar{\eta} \sin^2 \theta_a \cos 2\phi_a),$$

where (θ_a, ϕ_a) are the polar coordinates of B_0 in the PAS of the average tensor.

The orientation of the principal axis system of the average tensor will be related to the symmetry of the molecular motion, i.e. for C-D rotations about an axis between N sites, with $N \geq 3$, the average tensor would be axially symmetric, $\bar{\eta}_Q = 0$, and

$$\bar{\delta} = \delta \frac{1}{2} (3 \cos^2 \beta_p - 1 - \eta \sin^2 \beta_p \cos 2\alpha_p),$$

where β_p and α_p are the Euler angles that expresses the orientation of the original tensor in the rotation axis and $\delta = \frac{3}{4} \chi$ [9].

It is possible to deduce the main features of the ^2H NMR spectra of several simple fast molecular motions by means of these equations and other published mathematical expressions [12].

When the motion of the C-D bonds is slower, 10^6 - 10^3 Hz, the NMR spectra becomes very characteristic and sensitive to subtle changes in angle orientations to the magnetic field or exchange rate (see Figure 3 for an example). In this motional regime, called the intermediate exchange rate, the frequencies are not the average anymore and the spectra become complex.

Calculations of the average tensor and NMR spectra are time consuming subjects that involves multiple rotations and diagonalisation of complex matrices. The mathematical methodology necessary to performed this calculations is explained in [9,13]. In this thesis, all the simulated spectra have been calculated with the computer codes MXQET and MXQET1 [11].

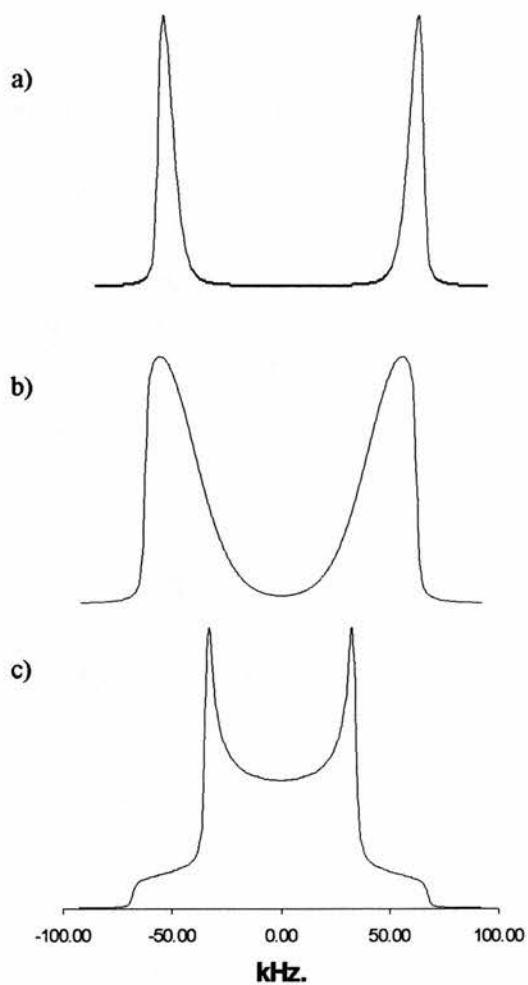


Figure 2.4.3. Simulated MXQET powder patterns spectra for a benzene ring undergoing in-plane rotations at $1.0 \text{ E}7$, $1.0\text{E}6$ and $1.0\text{E}5 \text{ S}^{-1}$. The benzene ring was described using a 6 site model. The time between the quadrupole pulses was $100 \mu\text{s}$.

Sample preparation for ^2H NMR experiments

^2H NMR has been used in this thesis to monitor the dynamics of adsorbed molecules in hybrid-microporous frameworks. The methodology use to dose the solids with the perdeuterated guest molecules is described below:

Solid were placed into specially adapted glassware consisting of a Pyrex NMR tube (5 mm in diameter) attached to a Schlenk tube. The samples were degassed under vacuum on a glass line at 423 K, conditions sufficient to remove all water molecules. A known amount of the deuterated organic molecule was dosed onto the solid from the vapour phase, with the constraint that all of the adsorbate would be within the pores. The sample tubes were partially immersed in liquid nitrogen to ensure no organic vapour pressure was present before sealing the other end of the glass tube with a flame. Photographs of a typical sample tube used for the ^2H NMR experiments and the vacuum line used for the experiments are shown below.

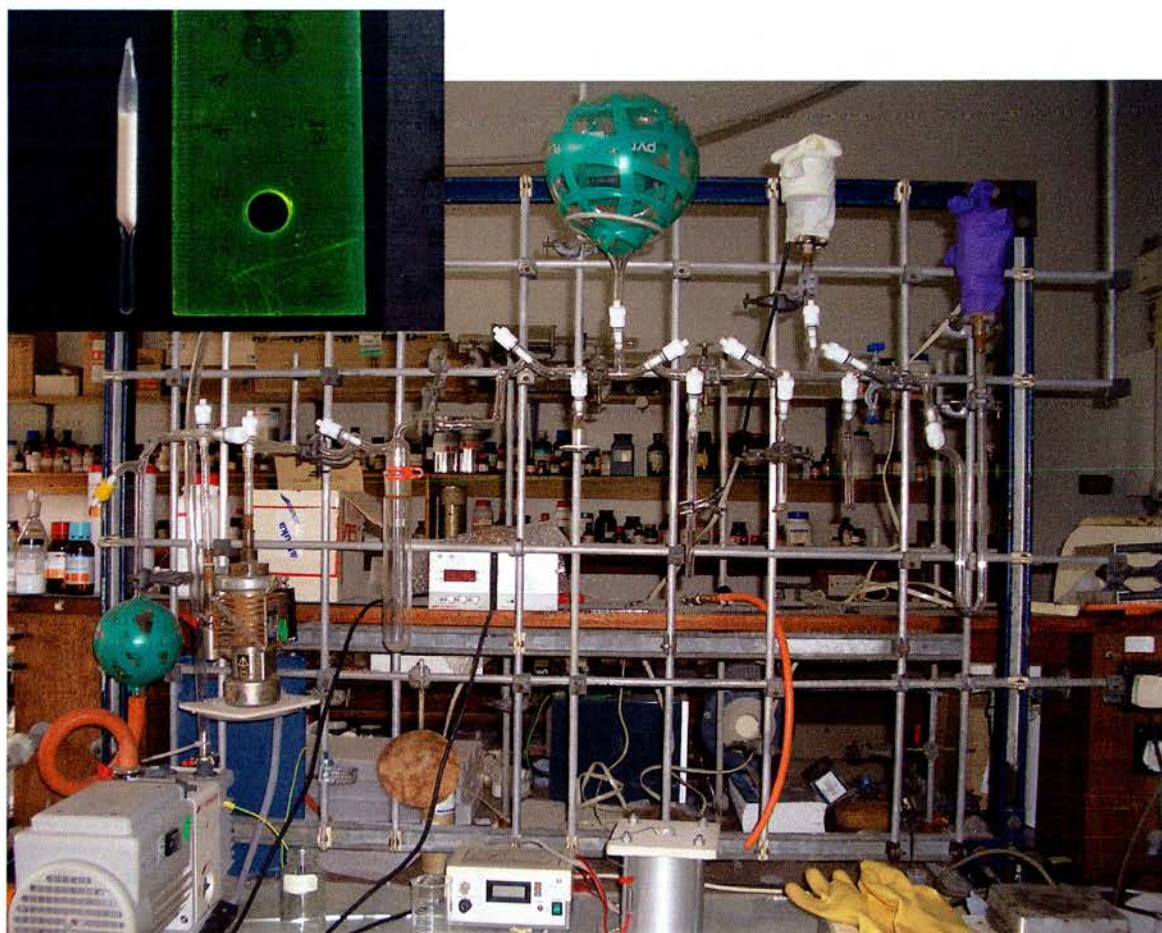


Figure 2.4.4. The bottom image is a picture of the vacuum line setup used to prepare the samples for the ^2H NMR experiments. The image at the top is a typical Pyrex tube use for these experiments.

NMR techniques used during this thesis.

Quadrupole solid echo.

Solid echo pulse sequence is the NMR technique used for the acquisition of the ^2H NMR signal in this PhD thesis. The actual pulse sequence is $90^\circ_x\text{-}\tau\text{-}90^\circ_y\text{-}\tau\text{-echo}$. This pulse sequence refocuses the transverse magnetization at a time τ after the application of the refocusing pulse. One of the main advantages of this technique is that the line shapes observed after Fourier transform of the FID are not distorted due to lost signal during the dead time of the receiver detector.

In the intermediate exchange rate, the line shapes are sensitive to the quadrupole delay, τ , and so, this technique can be exploited to obtain information about dynamical processes in this regime.

T_1 measurements through saturation recovery pulse sequence.

In this thesis T_1 relaxation time constants have been measured using a standard T_1 saturation- recovery pulse sequence coupled to a solid echo pulse sequence used for detection of the signals, i.e. $(90^\circ)_n\text{-delay-}90^\circ_x\text{-}\tau\text{-}90^\circ_y\text{-}\tau\text{-echo}$, $n \geq 40$. The n pulses of the initial saturation sequence, $(90^\circ)_n$, are equally spaced by a time greater than the transverse magnetisation decay.

The evolution of the growing magnetization was fitted to an exponential equation using the SPINSIGHT software.

High power decoupling.

This technique is used to enhance the resolution of the spectra, especially in those signals broadened by heteronuclear dipolar coupling, like $^{13}\text{C}\text{-}^1\text{H}$ dipolar coupling. The method consists of the application of continuous very high power radiofrequency (100-1000 watts) at the resonance frequency of the nuclei that needs to be decoupled.

Magic angle spinning.

It was mentioned before that the molecular motion in solution averages out the dipolar and the chemical shift anisotropy. This motion causing the averaging of the interactions can be mimicked in solid state NMR by spinning the sample at a certain angle with respect to the magnetic field.

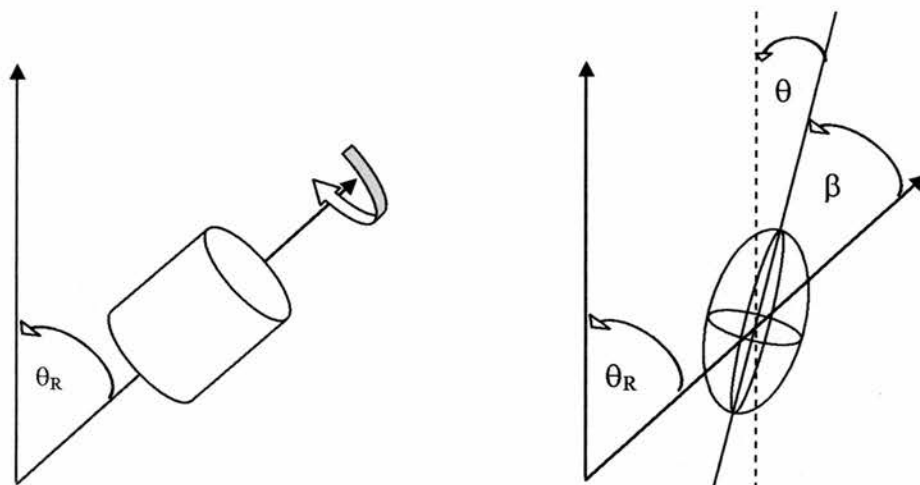


Figure 2.4.5. Representation of rotor spinning about an angle θ_R with respect to the magnetic field and a chemical shielding tensor rotating with the sample.

In powder samples there are many crystallites randomly oriented with respect to the magnetic field. If the sample is spun about an angle θ_R with respect to the magnetic field, then θ varies with the time and the orientation becomes time dependence and its orientation becomes:

$$\langle 3\cos^2\theta - 1 \rangle = \frac{1}{2} (3\cos^2\theta_R - 1)(3\cos^2\beta - 1),$$

where β is the angle between the principal z axis of the shielding tensor and the spinning axis. For $\theta_R = 54.74^\circ$, $(3\cos^2\theta_R - 1) = 0$, and so the average $\langle 3\cos^2\theta - 1 \rangle = 0$ as well.

Magic angle spinning is widely used in solid state NMR to removed chemical shift anisotropies and dipolar interactions and so, enhance the resolution of the spectra.

Cross Polarisation.

Acquisitions of the NMR signal of dilute spins, e.g. ^{13}C , is difficult because of the low intensity of the signal. Another factor that makes the NMR of dilute spins difficult is the large relaxation time that these nuclei sometimes exhibit.

These two problems can be solved using cross-polarisation techniques, which make use of the interaction of dilute spins (i.e. ^{13}C) with high abundance nuclei (i.e. ^1H), enhancing the signal to noise ratio and decreasing the relaxation time of the nuclei under study which allows a faster acquisition time between pulse sequences.

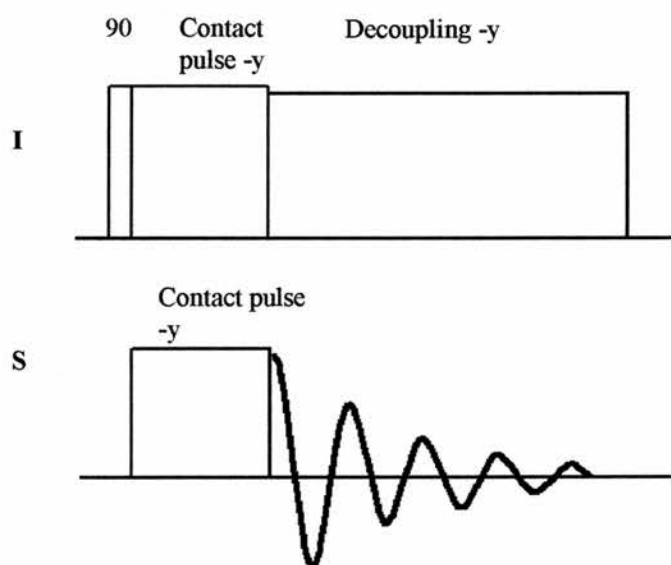


Figure 2.4.6. Cross-polarisation pulse sequence diagram.

Figure 2.4.6 represents the pulse sequence for the cross-polarisation transfer between abundant spins I and dilute spins S. An initial 90_x pulse applied at I frequency flips the magnetization to $-y$ axis (on the rotating frame). Then this magnetisation is spin locked at this axis with a contact pulse. Simultaneously, a contact pulse is applied at the resonance frequency of S. If the two fields applied at I and S frequency are adjusted so that the Hartmann-Hahn condition, $\gamma_I B_I = \gamma_S B_S$ is satisfied, the transfer of resonance energy would take place between the two spin systems. The increase of magnetisation corresponds to a factor γ_I/γ_S . At the end of the contact pulse, a FID is collected. Cross polarisation is normally combined with high power decoupling, and MAS to enhance

the resolution of the spectra. A further FID can be collected after a repetition of the cycle, with the time between the repetitions controlled by the, usually, shorter relaxation time of the I spins.

Experimental details.

The solid state apparatus used in this thesis was a Varian Infinityplus triple channel Solid State NMR operating at 500.156 MHz for ^1H , 76.78 MHz for ^2H , 125.76 MHz for ^{13}C , 99.355 MHz for ^{29}Si and 122.606 MHz for ^{27}Al . The spectrometer was controlled from a Silicon Graphics workstation, running the Chemagnetics Spinsight software.

All the MAS experiments presented were collected on a Chemagnetics HXY 4 mm MAS probe using 4 mm zirconium oxide rotor (including Vespél drive tips and Teflon end-caps).

Typical pulse widths used to record the direct polarisation MAS ^{27}Al , MAS ^{31}P and MAS ^{29}Si spectra were 2.20 μs , 3.0 μs and 3.0 μs respectively. The recycle delays used for these experiments were 1 s, 20 s and 300 s for MAS ^{27}Al , MAS ^{31}P and MAS ^{29}Si respectively. MAS CP $^1\text{H}\rightarrow^{13}\text{C}$ were recorded at 5 kHz spinning rate using a 2.0 μs ^1H 90° pulse followed by a typical contact time of 2 ms with a recycle delay of 3s.

Direct polarisation MAS ^{29}Si spectra presented in figure 3.2.3.7 (page 81, chapter 3) were performed by Dr. D. Apperley at the EPSRC Solid-State NMR Service (University of Durham) in a 300 MHz solid state apparatus operating at 59.557 MHz for ^{29}Si using 7.5 mm rotor at 5 kHz spinning rate with a recycle delay of 240 s. The deconvolution analyses of these spectra, kindly supplied by Dr. A. Apperley, are presented in the appendix.

Static ^2H NMR experiments were performed on a static solenoid Bruker probe. A typical 90° pulse width was 3.6 μs . The recycle delay used to acquire these experiments was variable between 1~5 s depending on T_1 (recycle delay must be $\sim 5 T_1$ to record fully relaxed spectra). Low temperature experiments were performed using cold nitrogen gas produced by evaporating liquid nitrogen from a tank connected to the probe and controlling the temperature of the sample with a thermocouple on the sample chamber of the probe.



Figure 2.4.7. Images of the magnet and probe used for the ^2H NMR work.

^2H NMR simulation. MXQET and MXQET1 computer codes and examples of simulated spectra.

Most of the simulations have been performed with the MXQET computer code, kindly supplied by Professor Robert Vold, which allows the calculation of ^2H NMR spectra of molecules performing complicated motion by using multiple frames in which deuterium atoms can interchange independently. The Quadrupole Coupling Constant (QCC) used for the simulations were 168 kHz for aliphatic deuterons and 193 kHz for aromatic ones according to ref [14] and [15]

Some MXQET simulated spectra (one single frame mode, fast motion limit) for characteristics motional modes of the guest molecules studied in this work are presented below. Static line shape is also shown for comparison.

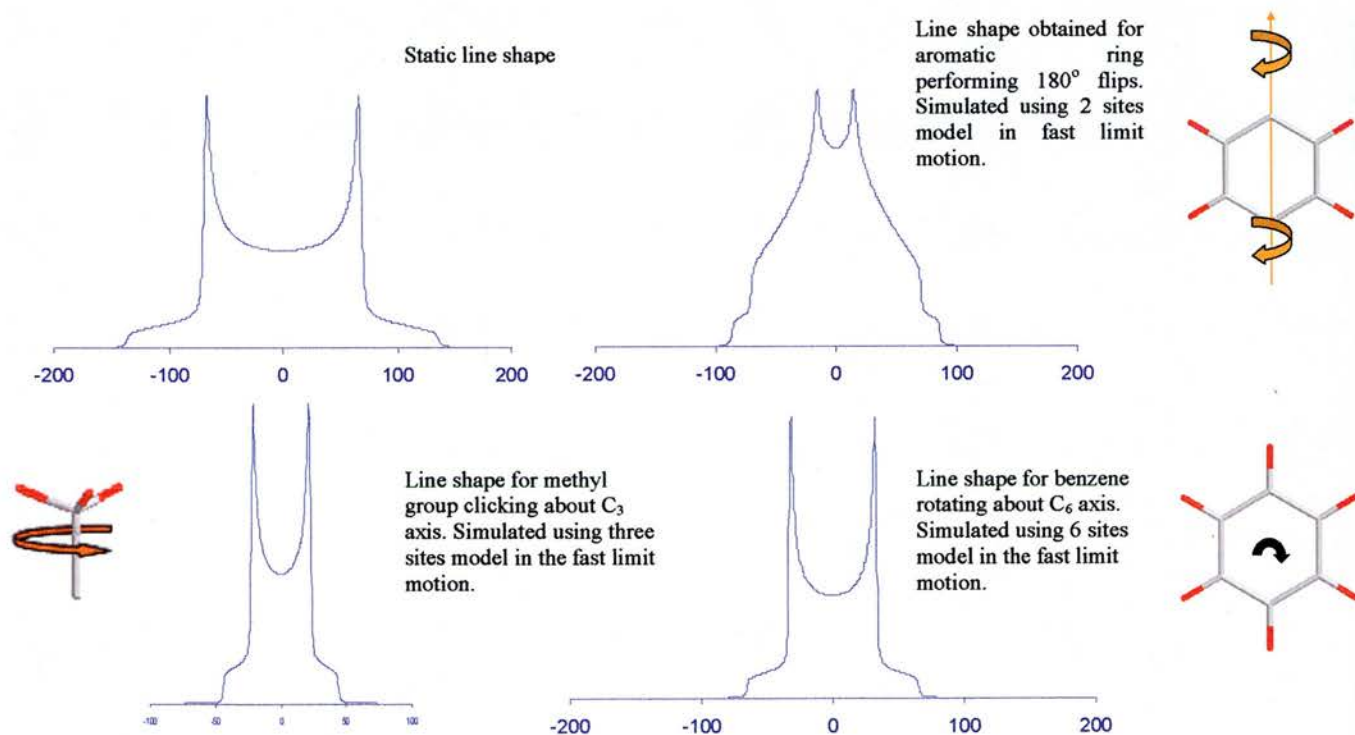


Figure 2.4.8. Simulated MXQET ^2H spectra for a static C-D bond (top left), a deuterated phenyl group performing π -flips about its para axis (top right), a methyl groups spinning about its C_3 axis (bottom left) and a benzene ring undergoing in-plane rotation about its C_6 axis (bottom right)

According to the MXQET simulations, fast aromatic π -flips produces a spectra with features at ± 17 , ± 67 and ± 84 kHz, fast in-plane rotation of a benzene ring produces a spectra 72 kHz broad (half of the static value) and a fast rotating methyl group produces a spectra 42 kHz broad (one third of the rigid value). These results agree with reported spectra [9,11].

The figure (below) shows solid quadrupole echo spectra simulated by MXQET for a methyl group undergoing a fast cone type of motion (with half cone angle ϕ) as well as a rapid rotation around its C_3 axis.

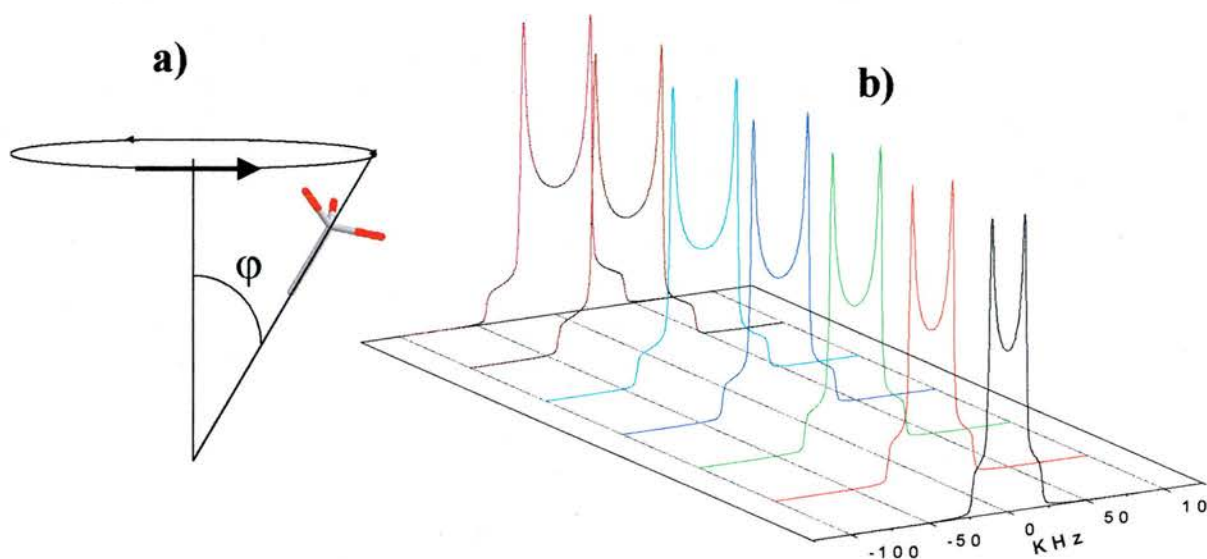


Figure 2.4.9. a) Representation of a methyl group reorientating its C_3 axis in a cone of angle ϕ . b) Library of solid quadrupole echo spectra simulated using MXQET computer code for methyl group jumping fast ($1E9\text{ s}^{-1}$ exchange rate) in a cone of three sites with different cone angles. The QCC for rigid C-D bonds used in these simulations was 168 kHz.

In Figure the widths of these spectra are plotted as a function of the half cone angle. These simulations results are independent of the number of sites used for the description of the cone (for cone with number of sites $n \geq 3$). This simulations show that, for example, it is easy to follow the cone angle describe by the long axis of a toluene molecule undergoing this rotational mode by measuring the width of the methyl signal.

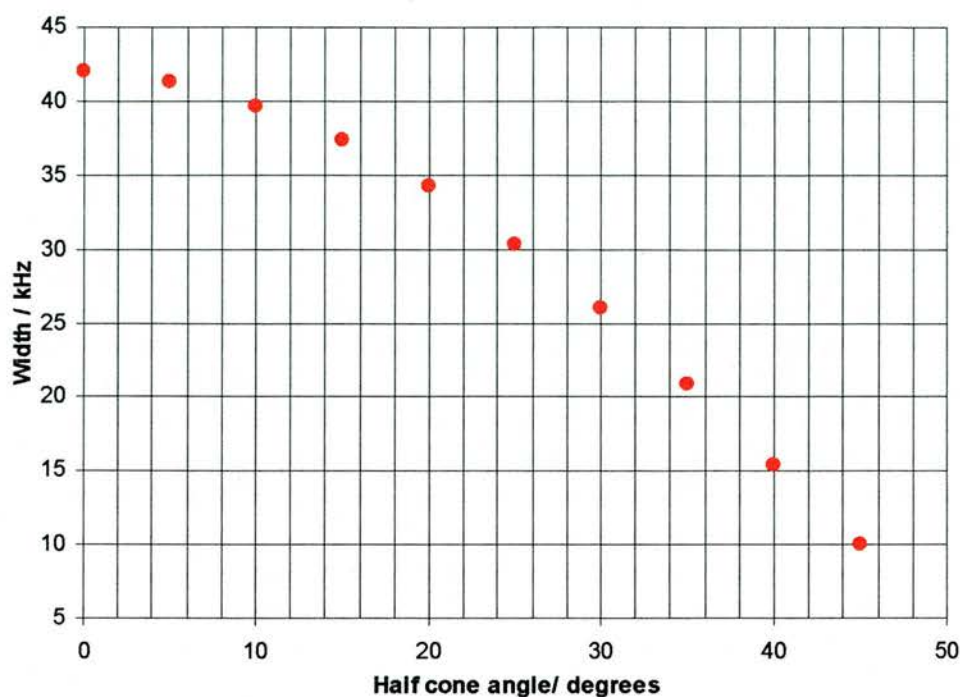


Figure 2.4.10. Width of the methyl signal as a function of the half cone angle.

The next figure shows the simulated spectra corresponding to a rapid rotating methyl which also undergoes jumps between two discrete sites separated by an angle of 60° . It can be seen that the line shape obtained now is different for those presented in figure 3 for a cone type of motion. This result also agrees with the literature [11].

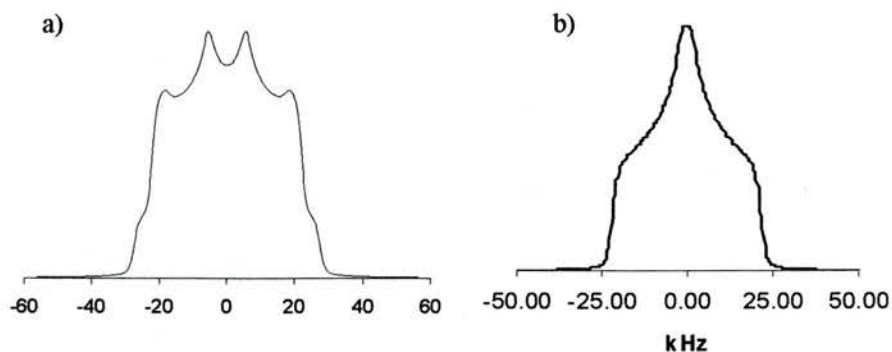


Figure 2.4.11. ^2H NMR spectra of a methyl group spinning fast around its C_3 axis and jumping between two sites separated by an angle of a) 60° and b) 109.5° .

The other program used during this thesis is MXQET1. Very similar to MXQET, it offers the possibility of using independent QCC values for the different deuterium sites. One example of the advantages that it offers is the calculation of the ^2H NMR spectra of molecules with constrained dynamics that exchange with isotropic molecules within the NMR time scale (see Chapter 6).

This sort of motional model has proved useful reproducing the dynamics of d_6 -benzene in KL zeolite [15]. Figure 2.4.12 presents a simulation performed with MXQET1 according to the motional regime proposed by T. Sato *et al.* to describe the dynamics of benzene in KL zeolite at 293 K. In this simulation, in-plane rotating benzene molecules, located on the K^+ ions, exchange with isotropic benzene molecules, at the centre of the cavities, with an exchange rate of $5.0\text{E}4 \text{ s}^{-1}$. The simulated spectra presented in the figure below also agree with the published results [14].

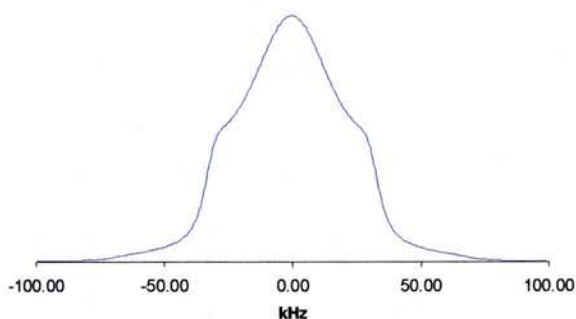


Figure 2.4.12. ^2H NMR spectra calculated with MXQET1 computer code corresponding to the dynamic model proposed by T. Sato *et al.* [15] for benzene in KL zeolite at 293 K.

The MXQET programs have been applied successfully to adsorption in zeolites [15], inclusion in hybrid solids [16] and also in problems of biological relevance [17]. They are indeed very powerful programs that allow the calculation of spectra associated with many complicated motions.

A typical input file for MXQET is given below. In this case, it is the input file used to simulate the spectrum of a methyl group whose long axis is jumping between two sites 60° apart (shown in Figure 2.4.11):

```

DO MATRIX TESTS? ->N
# SPECTRA TO BE CALCULATED ->1
OUTPUT FILE ( NO EXT. ) ->SIMDATA/methyl_two_sites
# OF AXES ->2
PARAMETERS FOR AXIS 1:
# EXCHANGE SITES -> 2
SITE 2: THETA -> 30.0000 PHI -> 0.0000 RHO -> 0.0000
SITE 2: THETA -> 30.0000 PHI ->180.0000 RHO -> 0.0000
MODEL: ALL SITES EXCHANGE=1, NEAREST NEIGHBOR=2, OTHER=3 ->2
USE HARD COLLISION MODEL? ->N
EXCHANGE RATE (1/sec) -> 1.00000E+07
EQUAL A PRIORI PROBABILITIES? ->Y
PARAMETERS FOR AXIS 3:
# EXCHANGE SITES -> 3
SITE 1: THETA ->109.5000 PHI -> 30.0000 RHO -> 90.0000
SITE 2: THETA ->109.5000 PHI ->150.0000 RHO -> 90.0000
SITE 3: THETA ->109.5000 PHI ->270.0000 RHO -> 90.0000
MODEL: ALL SITES EXCHANGE=1, NEAREST NEIGHBOR=2, OTHER=3 ->2
EXCHANGE RATE (1/sec) ->2.0E7
EQUAL A PRIORI PROBABILITIES? ->Y
SITE SYMMETRY (Cn), n->3
90 DEGREE PULSE LENGTH (us) ->3.6
COMPOSITE PULSE? ->N
PULSE SPACING (us) ->20.0
SPECTRAL WIDTH (kHz) ->200.0
# POWDER INCREMENTS ->400
# POINTS OF FID CALCULATED ->512
# REAL POINTS IN SPECTRUM ->1024
QCC (kHz) ->168.00
STATIC ASYMMETRY PARAMETER ->0.0
LORENTZIAN BROADENING (kHz) ->0.2
GAUSSIAN BROADENING (kHz) ->0.2
CALCULATE VIRTUAL FID? ->Y
SPECIAL SCALING FACTOR? ->N      SCALING FACTOR ->2000.0

```

The program makes use of Euler angles to describe orientations of the PAS of the different deuterium sites and the frames in which the molecule is further reorientated.

The Euler angles are generally labeled (α , β , γ) and they are defined as follow [8]:

The rotation of the frame (X, Y, Z) into (x, y, z) is described by a rotation of a frame coincident with (X, Y, Z) by an angle γ about Z, taking this frame into (X₂, Y₂, Z₂).

There then follows a rotation of (X₂, Y₂, Z₂) by an angle β about Y, i.e. the original axis frame Y axis, taking the (X₂, Y₂, Z₂) frame into (X₃, Y₃, Z₃). Finally, a rotation of α about Z, i.e. the original axis frame Z axis, takes (X₃, Y₃, Z₃) into (x, y, z).

In the program the angles (α , β , γ) correspond to (PHI, THETA, RHO).

In the input file, the set of Euler angles in blue correspond to the angles used to describe the orientations C-D bonds of the methyl group where the main axis of the PAS, in which the tensor is diagonal, is coincident with the Z axis of each frame, described by

one of the three sets of Euler angles respect to an original reference frame. Note that with the angles used for the methyl group description (blue angles), the C-D bonds (Z axis) would be at a 109.5° of the Z axis of the initial reference frame.

The set of angles in red, correspond to a set of intermediate frames in which the original frame, used to describe the methyl group, can be rotated. Note that the Z axis of two intermediate frames are separated by a total angle of $30^\circ + 30^\circ = 60^\circ$. Note also that each set of angles has its own exchange rate.

The input file also includes two experimental parameters, 90 DEGREE PULSE LENGTH, PULSE SPACING (us), that should agree with the number used for the acquisition of the NMR signals. It also includes the QCC and the asymmetry parameter needed for the calculation of the spectra. The QCC used were 168 and 193 for aliphatic and aromatic C-D respectively. The asymmetry parameter, according to Spiess [9], was taken as zero in all the calculations. The typical Lorentzian and Gaussian broadening of the spectra were 1.0 kHz. The hard collision model and the composite pulse option were never used during this work.

Once the calculation is complete, the program generates an ascii file of one single column corresponding to NMR signal intensities. The number of points of the spectra and the spectral width, both in the MXQET input file, are required to plot the simulated spectra with its X axis in kHz.

The aromatic QCC, 193 kHz, was taken from the literature [15]. The aliphatic QCC, 168 kHz, was deduced from the spectra observed in a deuterated sample of sodium scandium methylphosphonate [14]. The spectrum observed in this solid was 42 kHz broad (below).

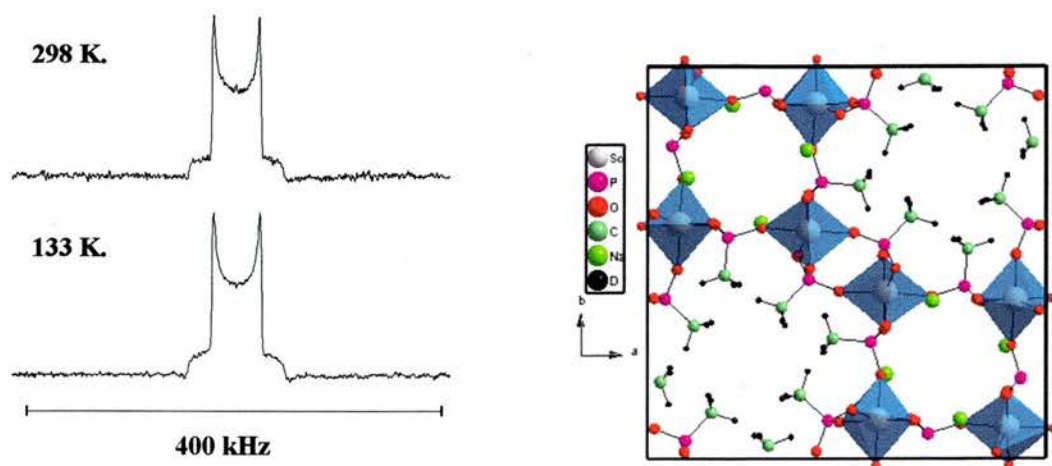


Figure 2.4.13. Structure of sodium scandium methylphosphonate refined from high resolution neutron diffraction [14] and ^2H NMR spectra of the solid.

References for chapter 2

- [1] Métodos de difracción de rayos-x. Joaquín Bermúdez-Polonio, Ediciones Pirámide, S.A.-Madrid
- [2] D.B. Williams, C.B. Carter, *Transmission Electron Microscopy*, 1996, Plenum Press, New York
- [3] J. M. Thomas, W. J. Thomas, *Principles and practice of heterogeneous catalysis*, 1997, VCH, Weinheim, Germany.
- [4] S. Brunauer, P.H. Emmett, E. Teller, *J. Am. Chem. Soc.*, **1938**, 60, 309
- [5] P. I. Ravikovitch, G. L. Haller, A. V. Neimark, *Advances in colloid and interface science*, **1998**, 76-77, 203
- [6] J-H. Yun, T. Düren, F. J. Keil, N. A. Seaton, *Langmuir*, **2002**, 18, 2693
- [7] M. H. Levitt. Spin Dynamics, *Basics of Nuclear Magnetic Resonance*, (Wiley), **2001**
- [8] M. Duer, *Solid State NMR spectroscopy*, (Blackwell), **2001**
- [9] K. Schmidt-Rohr, W. Spiess, *Multidimensional Solid-State NMR and Polymers*. (Academic Press), **1994**
- [10] J. Keeler, *Understanding NMR spectroscopy*. (Online course: http://www.spectroscopynow.com/Spy/basehtml/SpyH/1,1181,5-14-9-0-0-education_dets-0-1839,00.htm), **2002**
- [11] M.S. Greenfield, A. D. Ronemus, R. L. Vold, R. R. Vold, P. D. Ellis, T. E. Raidy, *J. Mag. Res.*, **1987**, 72, 89; J. H. Ok, R. R. Vold, R. L. Vold, M. C. Etter, *J. Phys. Chem.*, **1989**, 93, 7618
- [12] I. Kustanovich, H. M. Vieth, Z. Luz, S. Vega, *J. Phys. Chem.*, **1989**, 93, 7427; I. Kustanovich, D. Fraenkel, Z. Luz, S. Vega, H. Zimmerman. *J. Phys. Chem.*, **1988**, 92, 4134
- [13] Shin-Ichi Nishikiori. *Journal of inclusion phenomena and macrocyclic chemistry*. **1999**, 34, 331
- [14] S. R. Miller, E. Lear, J. Gonzalez, A. M. Z. Slawin, P. A. Wright, N. Guillou, G. Ferey, *Dalton. Trans.*, **2005**, (in press).
- [15] T. Sato, K. Kunimori, S. Hayashi, *Phys. Chem. Chem. Phys.* **1999**, 1, 3839
- [16] J. Gonzalez, R. N. Devi, D. P. Tunstall, P. A. Cox, P. A. Wright. *Microporous Mesoporous Mater.*, (in press)
- [17] A. R. Jude, D. V. Greathouse, M.C. Leister, R. E. Koeppe, *Biophys. J.*, **1999**, 77, 1927

Part I

One of the aims this project was to evaluate the adsorption properties of organically-modified MCM-41, SBA-1 and SBA-2 mesoporous solid with the target of improved selectivities in pressure swing processes for gas separation.

First, in chapter 3, the adsorption properties of a family of inorganic SBA-2 mesoporous solid with tailored unit cell are analysed by means of nitrogen adsorption at 77 K, CO₂ adsorption at 196 K and butane and isobutane adsorption at 268 K. Details about the structure of SBA-2 have been established through these adsorption experiments. Chapter 3 also includes the synthesis, characterisation and adsorption properties of a hybrid ethane-siloxane mesoporous material with SBA-2 type structure.

Chapter 4 concerns the synthesis and characterisation of phenyl- and aminopropyl-functionalised MCM-41, SBA-1 and SBA-2 mesoporous solids. The adsorption properties of these solids were evaluated through high pressure adsorption of ethane and CO₂ and low pressure adsorption of toluene, CO₂, n-butane and isobutane.

Chapter 3.

Adsorption studies on SBA- 2 and related materials.

3.1 Introduction

Although SBA-2 was first reported in 1995 [1], its structure is still not as well understood as other mesoporous solids, such as MCM-41[2], MCM-48 [3] and SBA-1 [4]. Initially indexed as possessing hexagonal symmetry, $P6_3/mmc$, it was described as silica condensed around a hexagonally close packed (hcp) arrangement of spherical micelles. Subsequent studies [5,6] suggest that it is typically silica condensed around a mixture of hexagonal and cubic close packed (ccp) micelle arrays, with a pore window size that can be very small (see Figure 3.1.1). However, relatively little was known about the detailed pore size distribution, or its response to extraction or calcination of the solid, prior to this thesis. Since SBA-2 has a potentially useful pore structure for sieving, and because one of the original aims of the project was to investigate the adsorption properties of organic-inorganic hybrids so called “meso-cage” structures, such as SBA-1 and SBA-2 (see Chapter 4), it was first necessary to establish details of the structure of inorganic SBA-2.

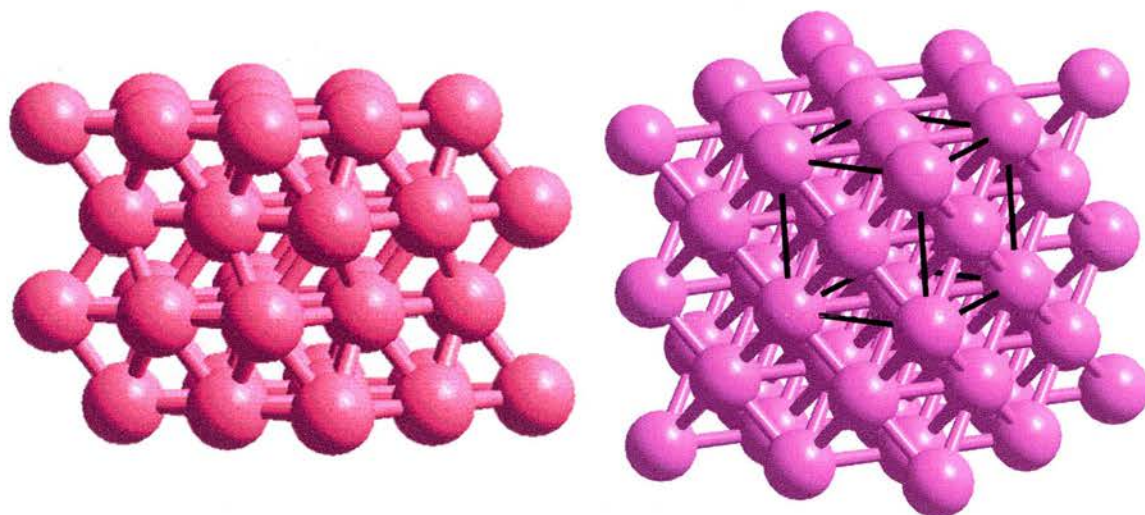


Figure 3.1.1. Representation of hexagonal (left) and cubic (right) close packed arrays of supercages connected by micropores.

In parallel to this work, Pérez-Mendoza [7,8] has proposed a description of the pore network of SBA-2 using a pore size distribution for both the supercages and the micropores of the solid. In this work, the different porosities that the solid exhibits for ethane and nitrogen is explained through the existence of cages that are not accessible to

ethane due to the small size of their interconnecting windows (Figure 3.1.2). Pérez-Mendoza found that different uptakes could only be explained by connectivities much less than the maximum 12.

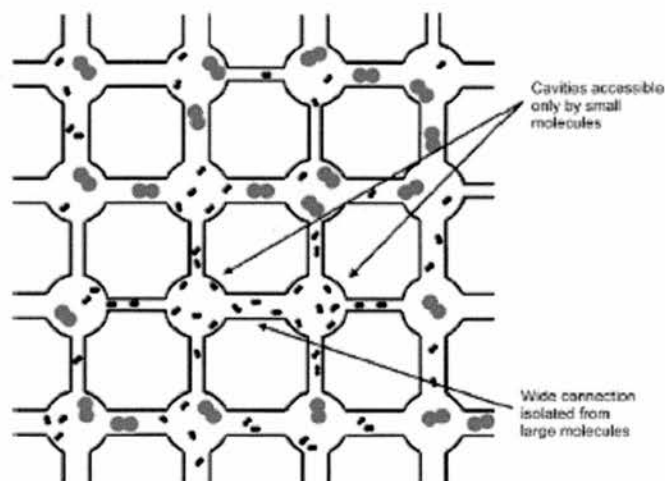


Figure 3.1.2. Schematic diagram showing the connectivity in a 2D lattice for large (ethane) and small (nitrogen) molecules. The relative size of the cavities, channels and molecules have been modified for the sake of clarity. Picture adapted from ref [8].

In this chapter the effects on the porosity of a range of post-synthesis treatments of inorganic SBA-2 silicate are reported. The adsorption of N_2 , CO_2 , butane and isobutane is measured on samples from which the template has been removed by extraction and calcination at temperatures between 550 °C and 900 °C. It is well known [9] that the unit cell of silicate mesoporous materials shrink during calcination due to an increase of the condensation of the framework. The micropores that connect the supercages of SBA-2 are expected to shrink with the unit cell when the material is heated. Studying the adsorption properties of solids with systematic differences in pore/window size provides interesting information about network connectivity and highlights the possible molecular sieving properties of the solid.

In addition, the synthesis and characterisation of a periodic mesoporous organosilica with the SBA-2 structure is reported. The solid is prepared by condensation of bis(triethoxysilyl)ethane. The adsorption properties of this material are compared with those of inorganic SBA-2.

3.2 Molecular sieve properties of siliceous SBA-2 type material

3.2.1. Experimental.

According to published procedures [5,6], siliceous SBA-2 solids were synthesised mixing TEOS (Aldrich 98%), tetramethyl ammonium hydroxide (25% w/w aqueous solution), water and gemini surfactant C₁₆₋₃₋₁ in molar ratios 1: 0.3: 75: 0.04. After 4h stirring at room temperature, a white solid was filtered, washed with water and dried in air at 100 °C for 10h. The template was extracted under reflux conditions for 3h using a solvent mixture of EtOH/HCl. After the removal of the template the solid was dried in air at 60°C overnight. All the solids studied were synthesised using this method.

Apart from the extracted sample, other materials were prepared by heating batches of extracted SBA-2 at different temperatures of 550 °C, 700 °C, 800 °C, 900 °C and 1000 °C. Each calcination was performed under flowing oxygen for 8 h. All samples were characterised by low angle XRD powder diffraction after calcination. All samples other than that calcined at 1000 °C retain long order structure according to XRD and were characterised further by TGA, ²⁹Si MAS NMR, TEM, nitrogen adsorption at 77 K, CO₂ adsorption at 196 K and butane and isobutane adsorption at 268 K.

Results and discussion:

3.2.3. Structural characterisation:

The XRD patterns of all the solids are typical of SBA-2 type materials (Figure 3.2.3.1). The absence of any well defined (103)_{hex} reflection, which is expected for the hcp array but not for ccp stacking, indicates few regions of ordered hcp structure.

The diffraction maxima shift progressively to higher angles with the increase in calcination temperature, indicating a systematic contraction of the unit cell. Indexing the patterns according to the cubic (Fm $\bar{3}$ m) structure, the unit cell parameter, a , changes from 81.5 Å for the extracted sample, to 70 Å for the sample calcined at 900 °C, a 14 % contraction. A summary of the XRD analyses is presented in table 3.2.3.1. Note that the decrease of the a_{cub} is almost linear with the calcination temperature (Figure 3.2.3.2).

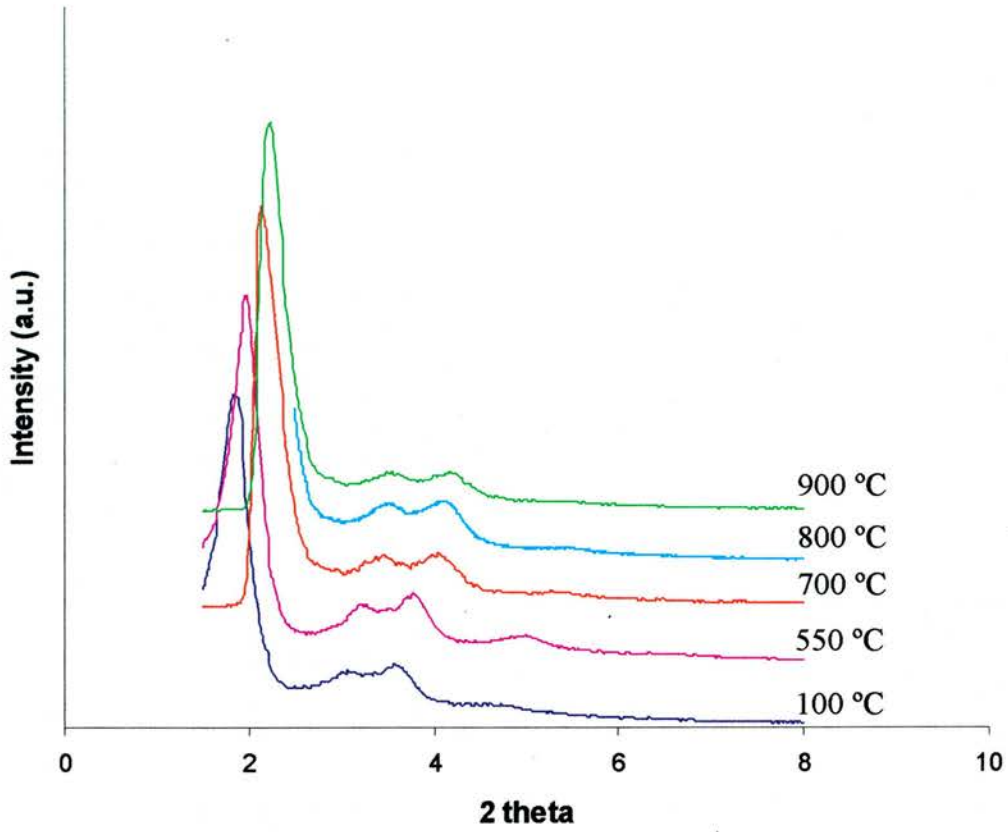


Figure 3.2.3.1. XRD patterns of silicate SBA-2 type materials heated at different temperatures.

Temperature of calcination /°C	ccp		
	$d_{220}/\text{\AA}$	$d_{311}/\text{\AA}$	$a_{\text{cub}}/\text{\AA}$
100	28.8	24.6	81.5
550	27.4	23.5	77.7
700	25.8	21.9	72.8
800	25.2	21.7	71.6
900	24.8	21.1	70.0

Table 3.2.3.1. Summary of the analyses of the XRD patterns of silicate SBA-2 heated at different temperatures.

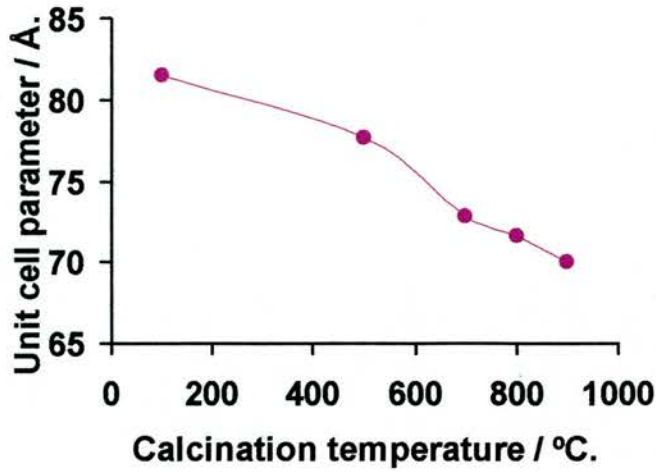


Figure 3.2.3.2. Graph summary of the dependence of the calcination temperature and the unit cell parameters found from XRD on the basis of a ccp.

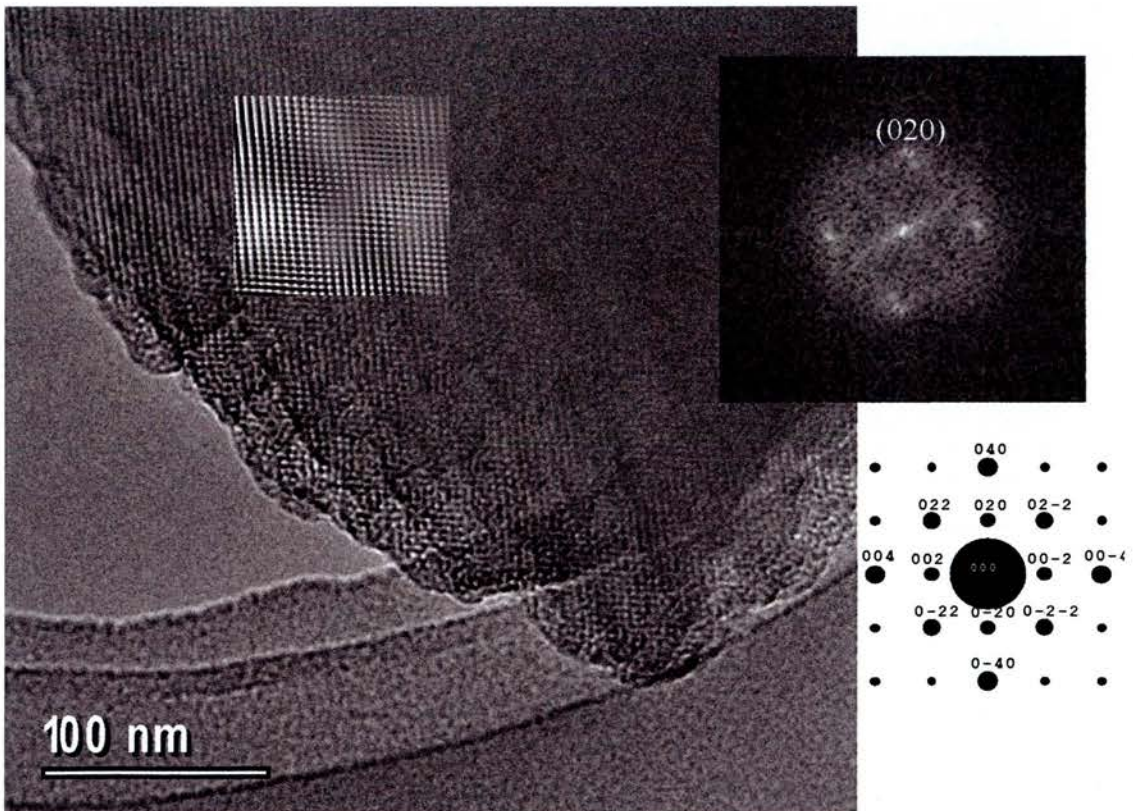


Figure 3.2.3.3. TEM image of silicate SBA-2 calcined at 900 °C looking down [100] of cubic 'crystal'.

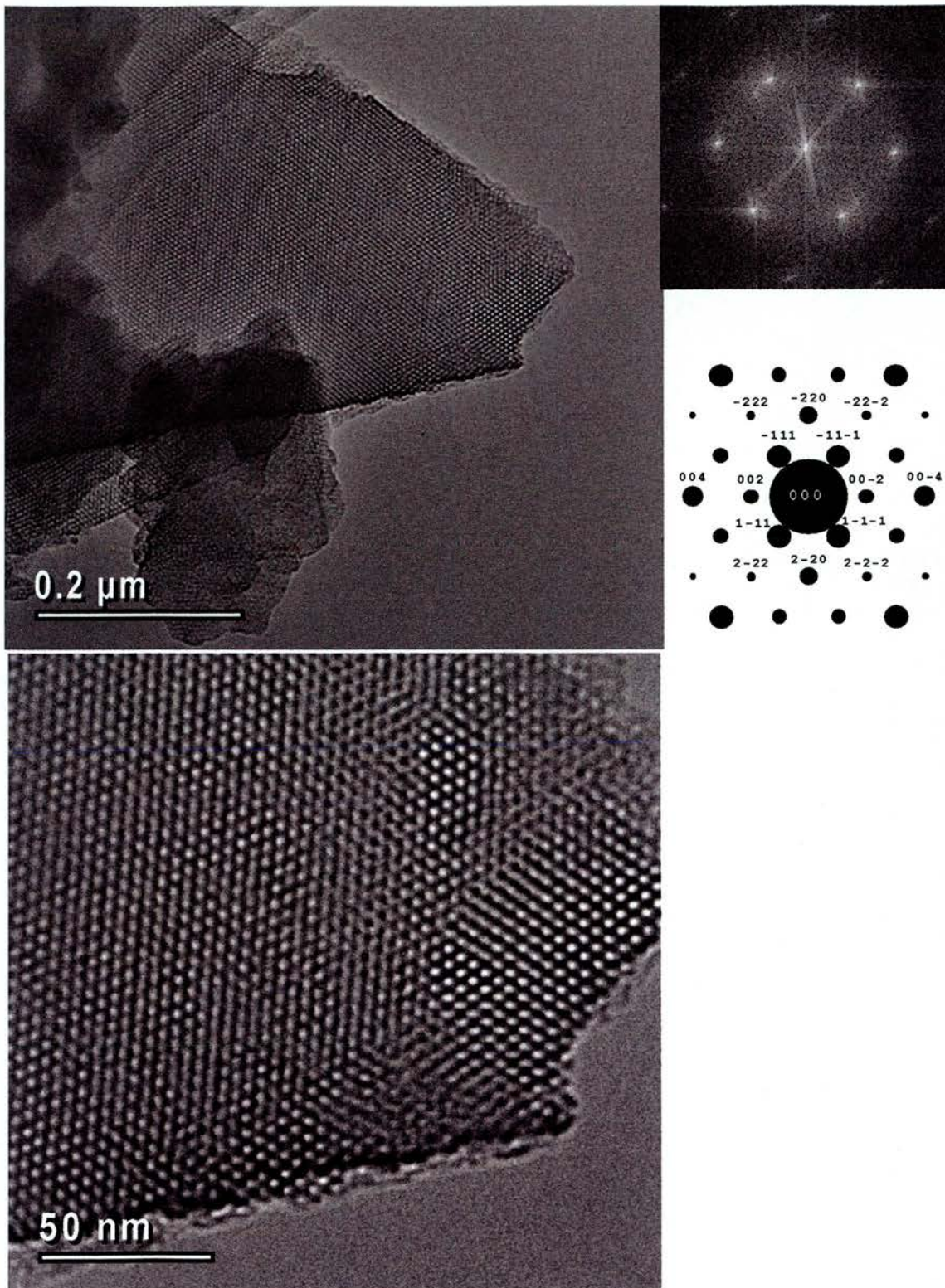


Figure 3.2.3.4. TEM images of silicate SBA-2 calcined at 900 °C looking down the [110] zone axis of a cubic region at different magnifications. The indexed FFT-ED patterns and theoretical ED are shown.

The structure of the SBA-2 type of solid calcined at 900 °C was studied by means of TEM. Figure 3.2.3.3 shows an image of SBA-2 with FFT-ED looking down $[100]_{\text{cub}}$. Figure 3.2.3.4 presents two micrographs of the same sample with their corresponding FFT-ED patterns, viewed down the $[110]$ direction of a cubic unit cell. The images show the typical ...ABCABCABC...stacking corresponding to an ccp array of supercages, represented in Figure 3.2.3.5. From the FFT-DP it is possible to measure directly the $d_{(111)}$ reflection and derive the unit cell parameter $a_{\text{cub}} = 70.6 \text{ \AA}$, similar value to the value calculated from XRD ($a_{\text{cub}} = 77.0 \text{ \AA}$).

It was reported by Huo *et al.* [1] that silicate SBA-2 material was thermally stable up to 800 °C. It is clear from the XRD and TEM analysis that the stability of this cage-like solid is even higher, up to 900 °C.

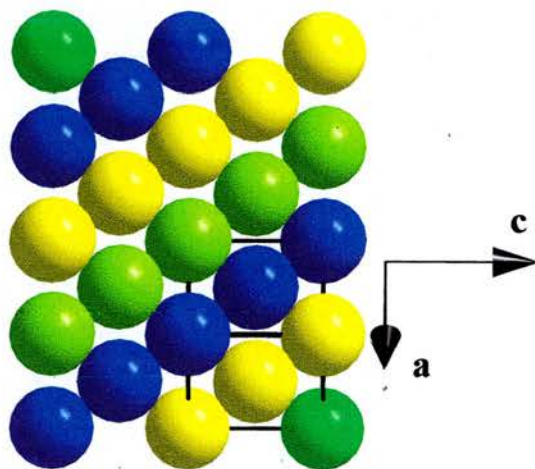


Figure 3.2.3.5. Representation of an ccp of spheres looking down the $[110]$ zone axis. A single unit cell is highlighted in black. The layers of spheres forming the ccp array are plotted in different colours.

Elemental analysis of the extracted SBA-2 gave C, H and N contents of 1.78 wt %, 1.96 wt % and 0.04 wt %. From the nitrogen content, taking into account the composition of the gemini surfactant, the residual mass of surfactant after the extraction is just 0.5 wt %. This corresponds to a 0.41 wt% of carbon and 0.08 wt% of hydrogen associated to residual surfactant not removed during the solvent extraction process. The bulk of carbon excess not associated with the surfactant, 1.37 wt % is due to ethoxy groups chemically bonded to the silica walls.

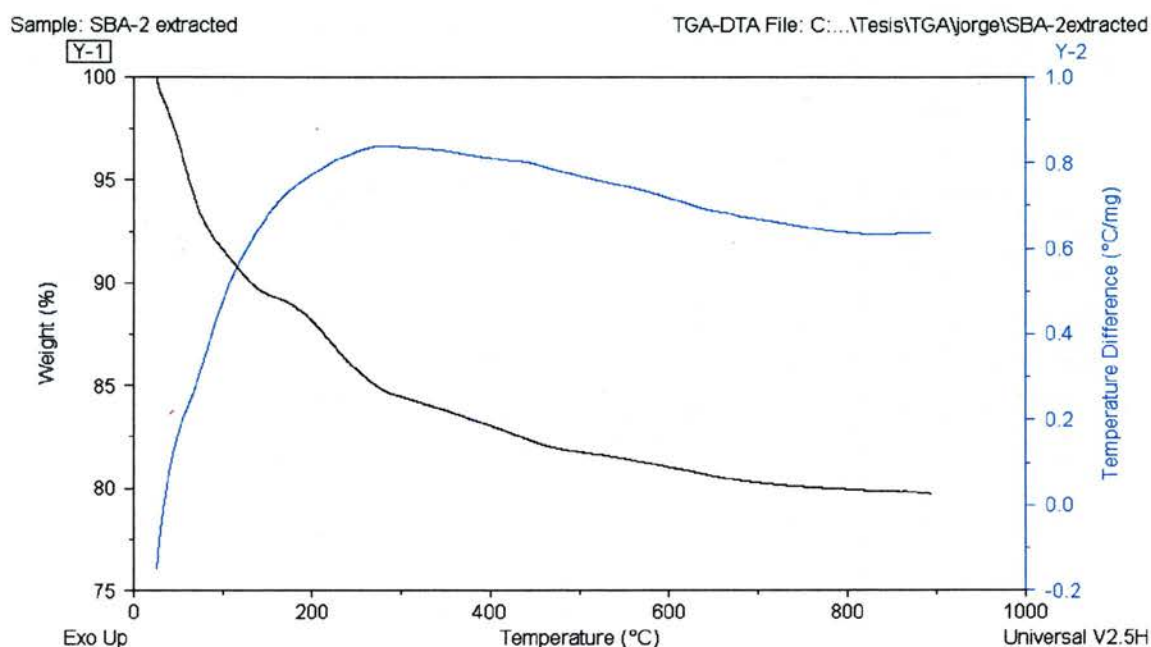


Figure 3.2.3.6. TGA-DTA under O₂ of siliceous SBA-2 type of solid solvent extracted.

TGA of the extracted sample is shown in Figure 3.2.3.6. The loss of weight presented low temperatures (10 wt% between rt and 150 °C) is probably related to the presence of traces of EtOH, surfactant and atmospheric water, adsorbed by the solid. The solid continues to lose weight until 800 °C, even at temperatures where the pores will be free of surfactant and physisorbed species. This, together with the XRD analysis, demonstrates that the removal of hydroxyl groups and therefore, the increase of condensation within the silica walls is a gradual process that takes place over a large temperature range.

The progressive condensation of the amorphous walls with increasing calcination temperature has been analysed in detail by ^{29}Si NMR (Figure 3.2.3.7). In this experiment, the ratio of the different silicon type units, Q_2 , Q_3 and Q_4 , has been measured by deconvolution of the signals (see appendix A). The results are summarised in Figure 3.2.3.8 and table 3.2.3.2. It can be seen that the as-synthesised solid, dried in air, presents a low degree of condensation with 50% of the Si atoms in Q_3 form. This solid was found to suffer loss of order and porosity during the surfactant extraction. After the thermal treatment at 100°C for 10h and solvent extraction the number of Q_2 silicons decreases to 7% and the Q_4 silicons increases to 47%.

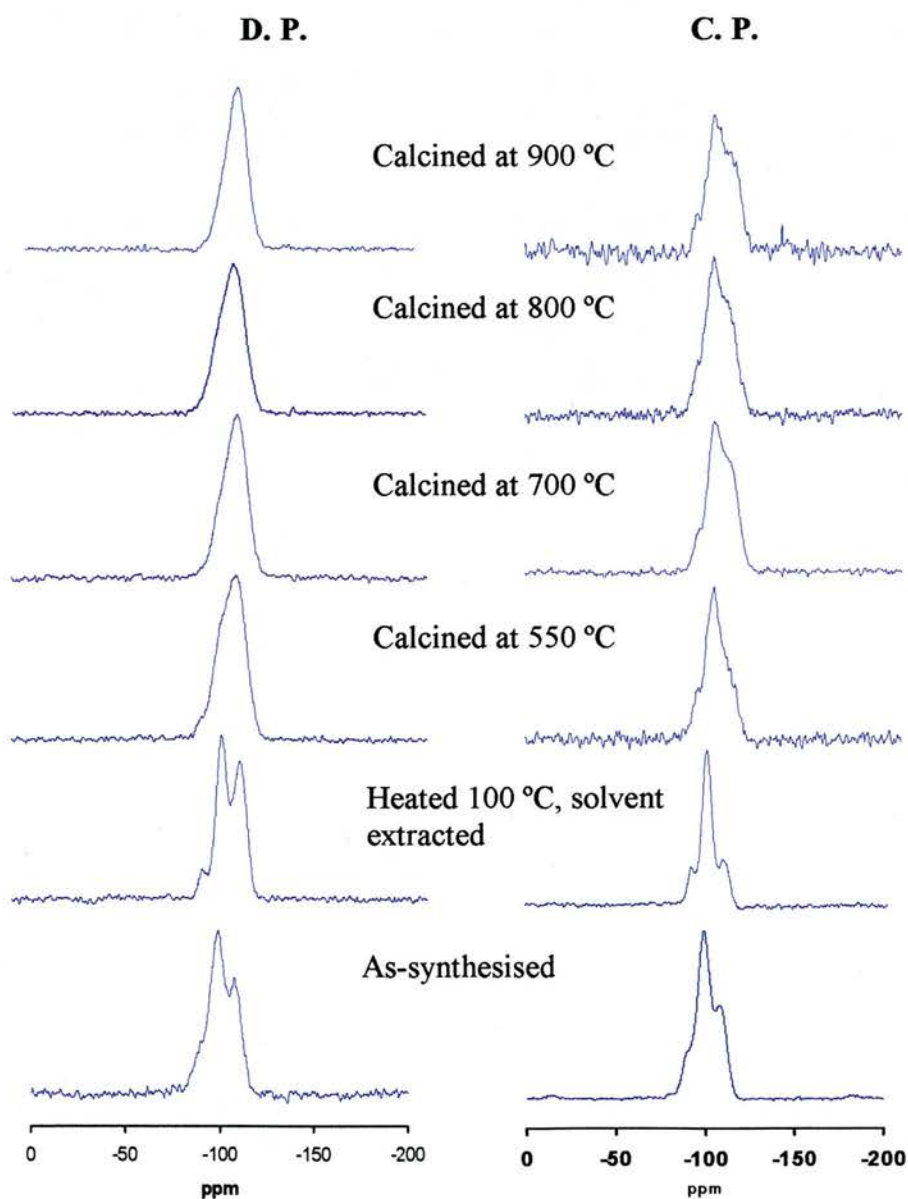


Figure 3.2.3.7. Direct polarisation ^{29}Si and cross polarisation $^1\text{H}\rightarrow^{29}\text{Si}$ NMR experiments performed on silicate SBA-2 type materials heated at different temperatures under O_2 . It is also included the analysis of one solid as-synthesised, with the C_{16-3-1} surfactant fulfilling the pores, dry on air at 60°C overnight.

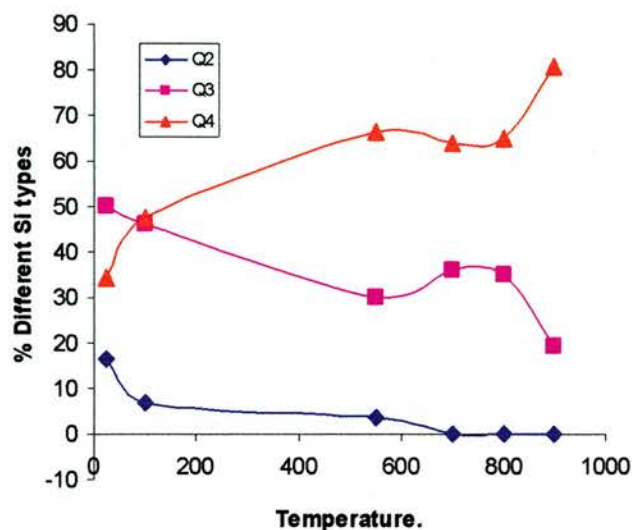


Figure 3.2.3.7. Evolution of the different silica types Q_2 , Q_3 and Q_4 with the increase in temperature. Data obtained from deconvolution of spectra presented in figure 3.2.3.6. (see Appendix A).

Calcination temperature / °C	$Q_2\%$	$Q_3\%$	$Q_4\%$	Q_4/Q_3
Solid as-synthesised	16.4	49.9	34.3	0.69
100	6.7	45.9	47.4	1.03
550	3.5	29.9	66.6	2.23
700	0	35.9	64.1	1.79
800	0	35.1	64.9	1.85
900	0	19.4	80.6	4.15

Table 1. Results of the deconvolution analysis performed on the spectra presented in Figure 3.2.3.7. See appendix A for deconvoluted spectra.

XRD of the extracted solid heated at 100 °C (Figure 3.2.3.1) presents well resolved reflections in the low angle region indicating that the structure of the material was retained after the solvent extraction. After the removal of the surfactant, calcination of the material produces extra condensation of the framework. The Q_4/Q_3 ratios found at different temperatures were 2.2, 1.78, 1.84 and 4.2 at 550, 700, 800 and 900 °C. According to this, it seems that the thermal treatment at 100°C for 10 h is a key step in order to stabilise the material prior the aggressive solvent extraction with HCl/EtOH.

3.2.4. Characterisation by gas adsorption

The porosity of the series of SBA-2 of solids has been studied by N₂ adsorption at 77 K, CO₂ adsorption at 196 K and butane and isobutane adsorption at 268 K. (According to the literature [10] N₂ and CO₂ have kinetic diameters equals to 3.64 and 3.3 Å at 200 °C). CO₂ and N₂ adsorption isotherms are presented in Figure 3.2.4.1 and Figure 3.2.4.2. Butane and isobutane isotherms are presented in Figure 3.2.4.4 and Figure 3.2.4.5. A summary of these experiments is given in table 3.2.4.1, in page 90.

CO₂ adsorption

The adsorption capacity of the different solids (at 1000 mbars, P/Po= 0.5) for CO₂, (Figure 3.2.4.1), decreases with the increase in heating temperature from 63.9 wt % for the extracted sample to 49.7 wt % for the solid heated at 900 °C, which corresponds to a 21.8 % decrease. This gradual decrease of the adsorption capacity is expected, due to the unit cell contraction, resulting from the thermal treatment. The rapid increase in adsorption that all the experiments present between 600 and 800 mbar, associated with a capillary condensation of CO₂ within the cages, is shifted to lower pressures with the increase in calcination temperature due to a decrease of the average pore-cage diameter accessible to CO₂ molecules (see Figure 3.2.4.1 b) for a clearer representation).

The affinity of the different solids for CO₂ at pressures below 0.1 P/Po seems to increase after the first thermal treatment at 550 °C and then to decrease with further rise of the calcination temperature. The reduction of the pore-cage size is expected to decrease the diameter of the microchannels interconnecting the supercages, enhancing the microporous character of the network. On the other hand, the calcination produces a gradual elimination of hydroxyl groups and therefore a decrease of the wall polarity. The adsorption behaviour observed at low pressures is probably due to a combination of these two factors.

The pore network of the SBA-2 type solids studied therefore presents a very high accessibility to CO₂, even after calcination of the material at 900 °C.

N₂ adsorption

The N₂ adsorption isotherms of the SBA-2 solids are shown in Figure 3.2.4.2. The decrease of the nitrogen capacity is remarkable. The solid heated at 900 °C only adsorbs 17.7 wt % of nitrogen at 0.8 P/P₀, a reduction of 66.7% compared to the solid heated at 550 °C. In Figure 3.2.4.3 b) the adsorption isotherms are scaled for a clear comparison of the capillary condensation step. It is clear that heating temperatures up to 700 °C produce a gradual shift of the capillary condensation to lower pressures. Further increase of the calcination temperature does not seem to affect the partial pressure of capillary condensation and, as can be seen in table 3.2.4.1 (page 90), the BJH¹ pore size values of the solids heated at 700, 800 and 900 °C are very similar.

Although the BET surface area model is of limited validity in materials with cage-like structure, it can be used for comparative purpose within the solids under study due to their similar structure. The BET values (table 3.2.4.1, page 90) for the samples extracted and heated at 550 and 700 °C are larger than those reported for silicate SBA-2 in ref [1], ~600 m²/g. The BET surface area of the samples calcined at 800 and 900 °C decrease by 35 and 59 % with respect to the sample calcined at 700 °C. Similarly, the adsorption capacity of the solids calcined at 800 and 900 °C is reduced by 31 and 56 % with respect to the capacity of the sample heated at 700 °C. This result, together with that from the capillary condensation pressures, suggests that the diameter of the supercages accessible to nitrogen molecules in the solids calcined at 700, 800 and 900 °C should be roughly the same although the number of cages accessible to nitrogen molecules decreases with the increase of calcination temperature

The large difference in accessibility that N₂ and CO₂ present in these solids can be related to different molecular size and temperature of the adsorption experiments (77 K vs 196 K) The N₂ molecules have less kinetic energy to overcome diffusional barriers and get through the microchannels.

Pérez-Mendoza *et al* [7,8], described the SBA-2 structure as a collection of supercages and micropores of variable diameter (both defined by a pore size distribution) and explained the different accessibility that ethane (273 K) and nitrogen (77 K) exhibit to the SBA-2 network in terms of a percolation phenomenon.

¹ BJH model underestimate the real cage size of SBA-2 because it assumes a cylindrical geometry for the pores. The values presented in table 2 are for comparative purposes. Several studies suggest that the real cage size of SBA-2 solid calcined at 550 °C (synthesised from surfactant C₁₆₋₃₋₁) is about of 44 Å in diameter [e.g. 11].

In their picture of the structure, some of the cages of the pore system were not accessible to the large ethane molecules due to small size of the micropores. According to this structural model, it is likely that with the increase in calcination temperature, the unit cell contraction would produce a gradual reduction of the mean sizes of the connecting windows between the supercages. The reduction of a micropore diameter should be related to the shrinking of the cages connected by the micropore. So the micropores connecting small cages should be smaller than those connecting larger cages.

The different accessibility that CO₂ and N₂ isotherms have to the SBA-2 type of solids under study seem to agree with the structural model propose by Pérez-Mendoza *et al* [3]. The solid calcined at 550 °C (15 Å N₂ BJH pore radius) shows large accessibility to both CO₂ and N₂ because most of the micropores in the network are big enough to allow the diffusion of both gases to the supercages. Increasing the calcination temperature up to 700 °C decreases the pore radius of the supercages to 13 Å. Nevertheless, the similar BET surface area values that the solids calcined at 550 and 700 °C present suggests that the number of cages accessible to nitrogen is similar for both. According to this, the N₂ and CO₂ accessibility of the pore network is not affected by the thermal treatment at 700 °C.

Calcination up to 800 and 900 °C produces a progressive reduction of the CO₂ uptake due to a smaller overall size of the supercages (as seen from the P/P₀ values of the capillary condensation step). In the case of N₂, the decrease of the uptake is more drastic because, apart of the reduction of the cage size, now the accessibility starts to play an important role: the contraction of the channels during the calcination hinders the access of nitrogen molecules to certain parts of the network. It is interesting that, although the number of cages accessible to nitrogen decreases substantially, their pore size seems to remain constant. This is contrary to what CO₂ isotherms suggest (these show continuous decrease of the capillary condensation pressure). This can be explained in the shrinking of the micropores associated with that of the cages, as commented above, reaching a critical size below which nitrogen cannot gain access to the cages. According to this analysis, the supercages and micropore diameters cannot be the same through the entire pore network. This is in agreement with the cited structural model, which suggests a pore size distribution for both micropores and cages.

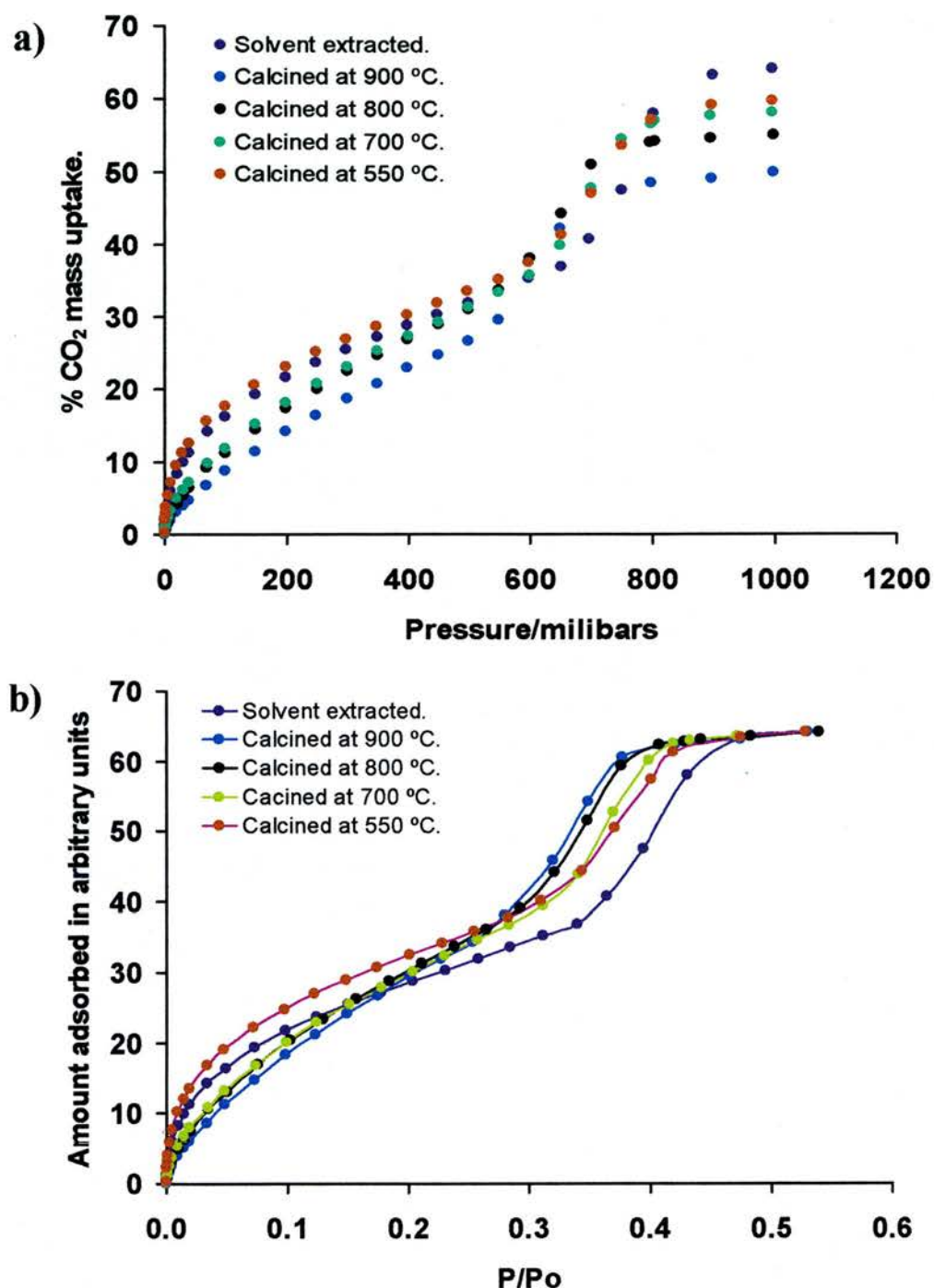


Figure 3.2.4.1. (a) Experimental adsorption isotherms of CO₂ at 196 K in siliceous SBA-2 type of solids heated at different temperatures after the removal of the surfactant with HCl/EtOH under reflux conditions. Prior the solvent extraction the as-synthesised solid was heated at 100 °C in air for 10 h.

In (b), the different CO₂ isotherms have been scaled by appropriated mathematical factors so all the experiments reach the same uptake at $P/P_0 = 0.5$. Note that the step associated with the capillary condensation of CO₂ with the cages is shifted to lower pressures with the increase of calcination temperature of the different solids. This experimental fact suggested that the cages of the SBA-2 pore network that are accessible to CO₂ at 196 K decrease in size with the calcination temperature.

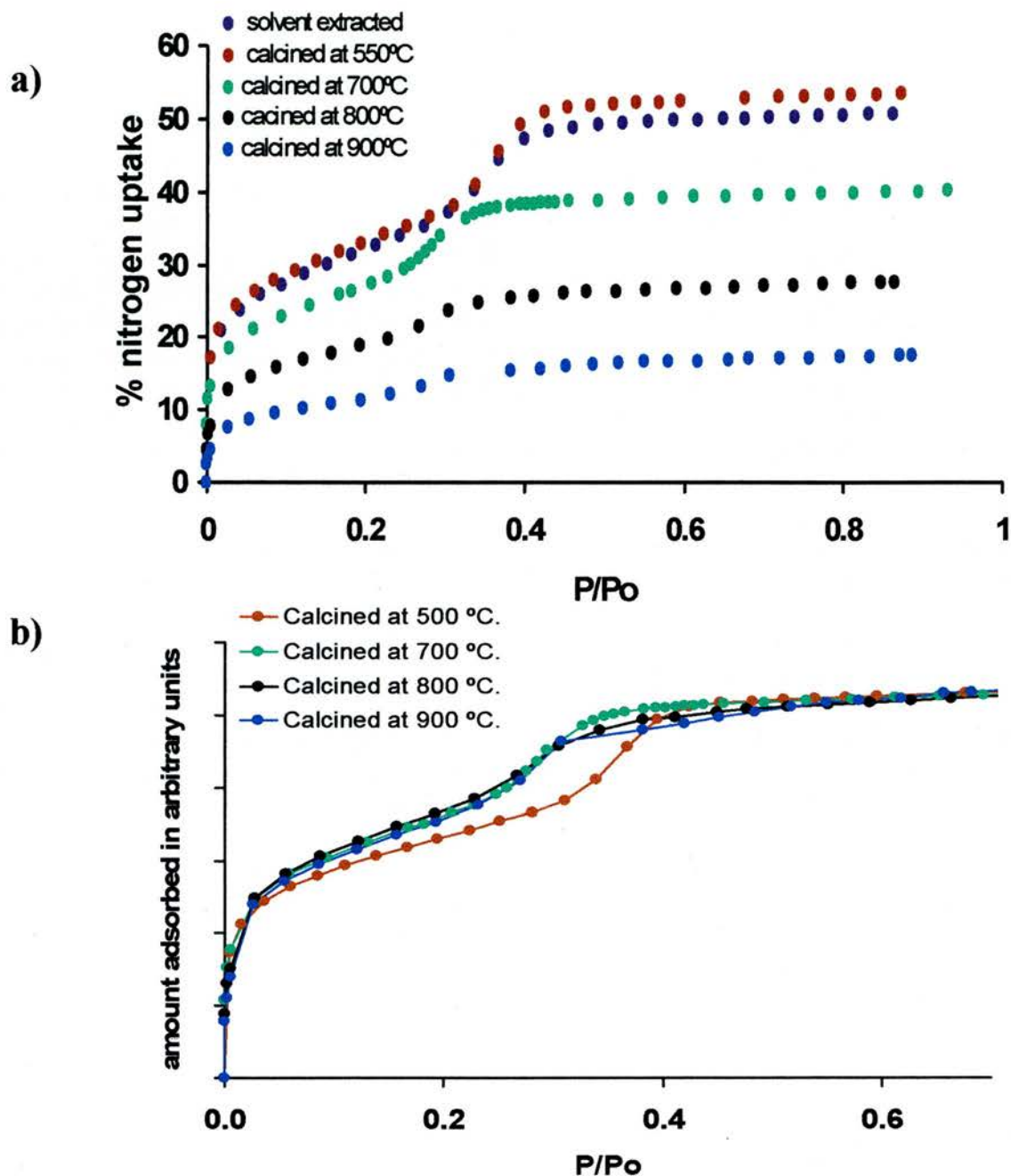


Figure 3.2.4.2. (a) Experimental adsorption isotherms of N_2 at 77 K in siliceous SBA-2 heated at different temperatures after the removal of the surfactant with HCl/EtOH. Prior to the solvent extraction the as-synthesised solid was heated at 100 °C in air for 10 h. In (b), the experiments have been scaled by appropriated mathematical factors so all the experiments reach the same uptake at $P/P_0 = 0.6$. Note that the capillary condensation of the samples heated at 700 °C, 800 °C and 900 °C occurs at the same partial pressure. This suggests that in these three different solids, nitrogen gains access to cages of similar diameter.

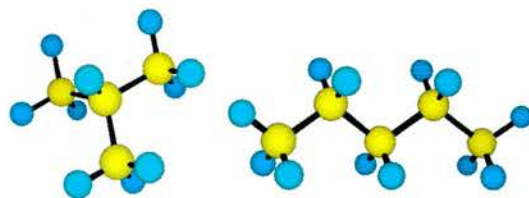


Figure 3.2.4.3. representation of isobutane (left) and *n*-butane (right) molecules.

The different permeability that SBA-2 displays for N_2 and CO_2 suggested that this material could act as a molecular sieve and would be able to separate gases of different size. Separation of isobutane and butane, represented in Figure 3.2.4.4, could therefore be of interest. The similar physico-chemical properties of these gases make difficult their separation by other methods.

Experimental isotherms of isobutane and butane at 268 K in SBA-2 heated at different temperatures, Figure 3.2.4.3., show a remarkable decrease in the accessibility of the gases with the increase in calcination temperature (table 3.2.4.1), but the change does not follow the same trend for the two gases:

The experiments performed with isobutane show that calcination at 550, 700, 800 and 900 °C produced a change in capacity of 32, 85, 96 and 98 % respectively with respect to the extracted sample. On the other hand, the changes in porosity for *n*-butane are 7, 67, 77 and 96 % for the solids calcined at 550, 700, 800 and 900 °C respectively respect to the solvent-extracted sample. The solid heated at 800 °C adsorbs 0.8 wt % of isobutane but 7.5 wt % of *n*-butane. This result makes SBA-2 a potential substrate for the separation of the two hydrocarbons in a pressure swing process.

In figure 3.2.4.5 the wt % uptake of all the gases studied are plotted as a function of the calcination temperature. The solid calcined at 900 °C adsorbed a 60 wt % CO_2 , < 20 wt % N_2 and almost no butane and isobutane. (This result does not necessarily mean that the solid could separate CO_2 and N_2 because the different accessibilities of CO_2 and N_2 are at least partly due to a temperature effect. High pressure adsorption experiments at the same temperature are required in order to investigate the possible ability of these solids to separate N_2 and CO_2).

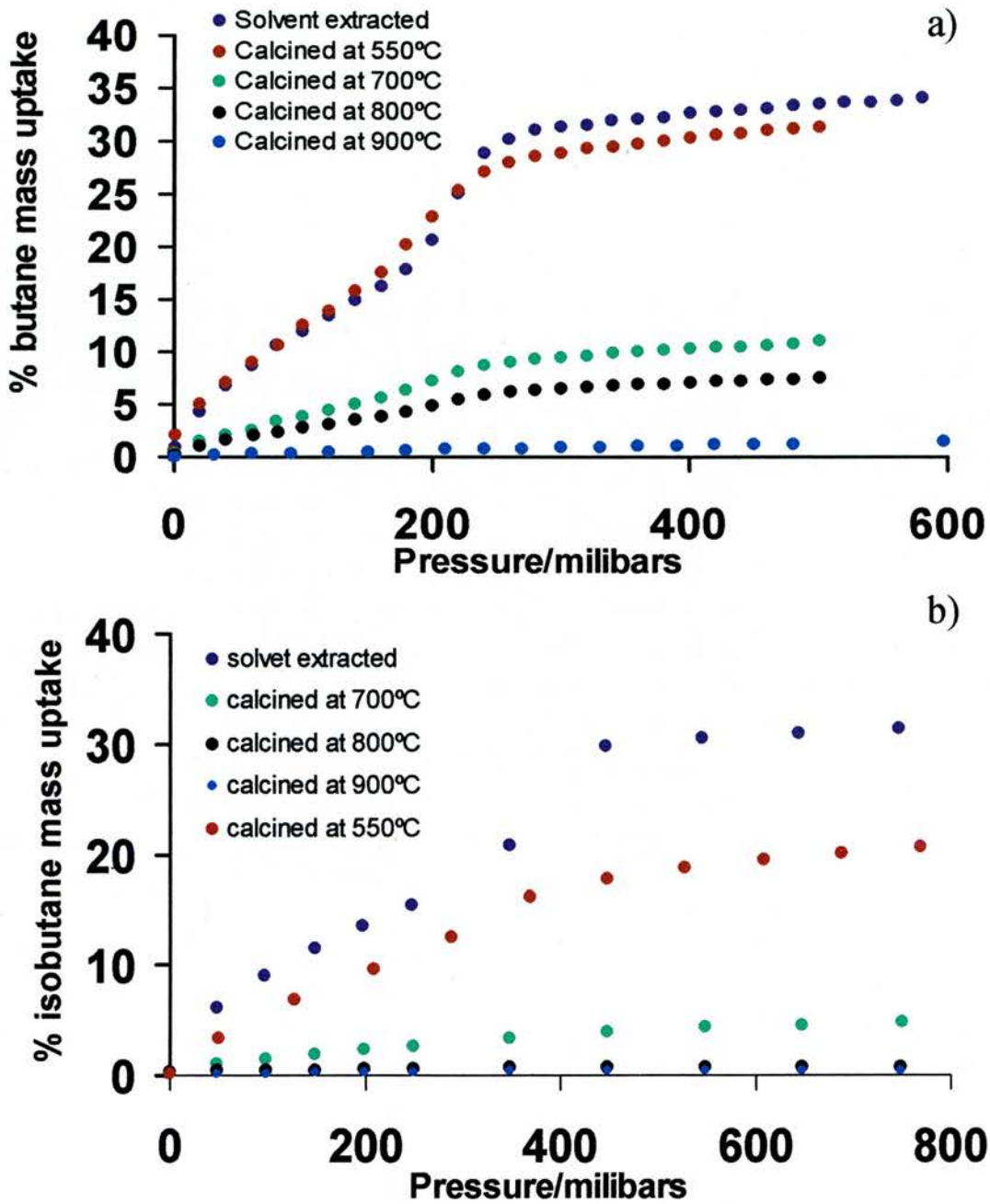


Figure 3.2.4.4. Adsorption isotherms of butane (a) and isobutane (b) at 268 K in siliceous SBA-2 type of solids heated at different temperatures after the removal of the surfactant under reflux. Prior to solvent extraction the as-synthesised solid was heated at 100 °C in air for 10 h. Note that the isobutane adsorption isotherms of the solids calcined at 800 °C and 900 °C overlap.

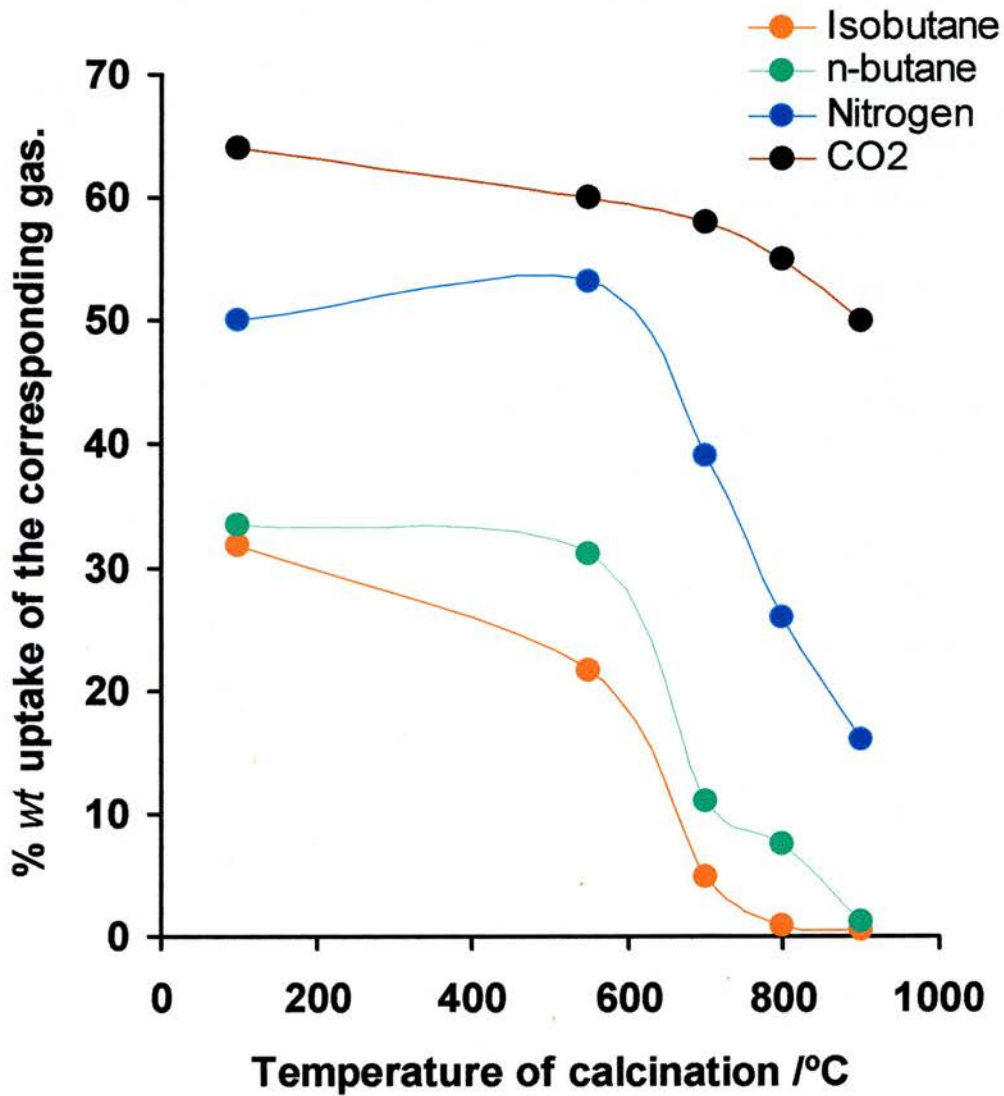


Figure 3.2.4.5. Representation of the wt % uptake of different gases as a function of the calcination temperature. The N₂ value is that measured at 0.8 P/P₀. CO₂, n-butane and isobutane were taken at to 1000, 700 and 500 mbar respectively.

	N₂ BET surface area (m²/g)	CO₂ BET surface area (m²/g)	BJH radius (de Boer) Å⁻¹	wt % N₂ uptake	wt % CO₂ uptake	wt % butane uptake	wt % isobutane uptake
Extracted	907±4	534±2	14.4	50.0	63.9	33.5	31.7
Calcined at 550 °C	922±6	557±4	14.9	53.2	59.6	31.1	21.6
Calcined at 700 °C	916±51	587±3	12.8	40.0	57.6	11.0	4.8
Calcined at 800 °C	595±20	593±5	12.3	27.8	55.2	7.5	0.8
Calcined at 900 °C	378±22	598±2	12.8	17.7	49.7	1.2	0.5

Table 3.2.4.1. Summary of the N₂ (77 K), CO₂ (196 K), *n*-butane and isobutane (both at 268 K) adsorption experiments performed on siliceous SBA-2 heated at different temperatures. BET surface and BJH pore size distribution were calculated from the N₂ adsorption experiment using the computer program IGASwin System Software. The % uptake measured at P/P₀= 0.8 for N₂, 1000 mbars for CO₂, 500 mbar for isobutane and 700 mbar for butane.

3.3. Synthesis of hybrid ethane-siloxane mesoporous material with SBA-2 type structure

3.3.1 Synthesis

The synthesis of hybrid ethane siloxane solid was conducted using the same procedure described for the synthesis of pure siliceous SBA-2 but adapting the silicon molar ratios according to the new silica source, 1,2-bis(triethoxysilyl)-ethane, $(\text{EtO})_3\text{-Si-CH}_2\text{-CH}_2\text{-Si-(OEt)}_3$, BTEE. Typically, BTEE, tetramethyl ammonium hydroxide, water and C_{16-3-1} surfactant, were mixed in the molar ratio 0.5:0.3:75:0.04. After 10h stirring at room temperature, a white solid was filtered and dried on an oven at 100 °C for 10 h. The template was removed by solvent extraction with a mixture of EtOH/HCl.

3.3.2. Characterisation

XRD patterns of the as-prepared and extracted solids are compared in Figure 3.3.2.1. Both patterns are similar to those reported for silicate SBA-2 although the reflections at high angle are not as strong as those from the pure silicate solid. Assuming that the main peak observed at low angle corresponds to the [111] reflection of the cubic $\text{Fm}\bar{3}m$, the unit cells of the extracted and as-prepared solid would be 71 and 75 Å, which are smaller than the unit cell observed for the pure silicate solid solvent extracted, 81 Å.

Elemental CHN analysis gave 12.06% C, 3.65% H and 0.08 %N. The low percent of nitrogen in the solid indicate that the removal of the template was efficient. TGA analysis of the extracted solid presented a weight loss of approximately 10% at 240 °C associated with a strong exothermic process (Figure 3.3.2.2.). This weight loss is probably due to the decomposition of the organic groups of the framework.

^{13}C NMR of the extracted solid presents a broad resonance signal at 6 ppm corresponding to the ethane groups of the framework (Figure 3.3.2.3). It also exhibits a signal of low intensity at 59 ppm due to ethoxy groups formed during the extraction of the surfactant. The shoulder observed at 12 ppm on the broad signal is probably due to these ethoxy groups as well. This spectrum is consistent with results published by Guan

et al [12], who synthesised a hybrid ethane-siloxane mesoporous solid with Pm3n symmetry. The absence of resonance signals associated with the surfactant confirms the effectiveness of the solvent extraction process.

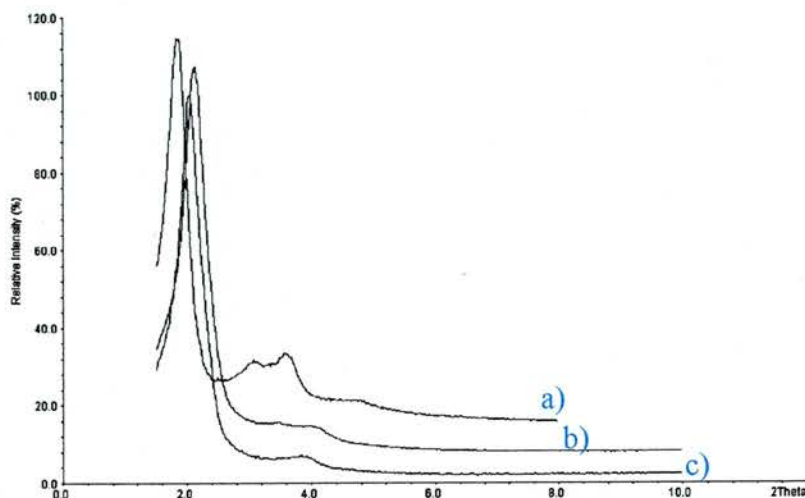


Figure 3.3.2.1. XRD diffraction pattern of a) extracted silicate SBA-2 solvent, b) ethane-siloxane extracted SBA-2 and c) as-prepared ethane-siloxane SBA-2

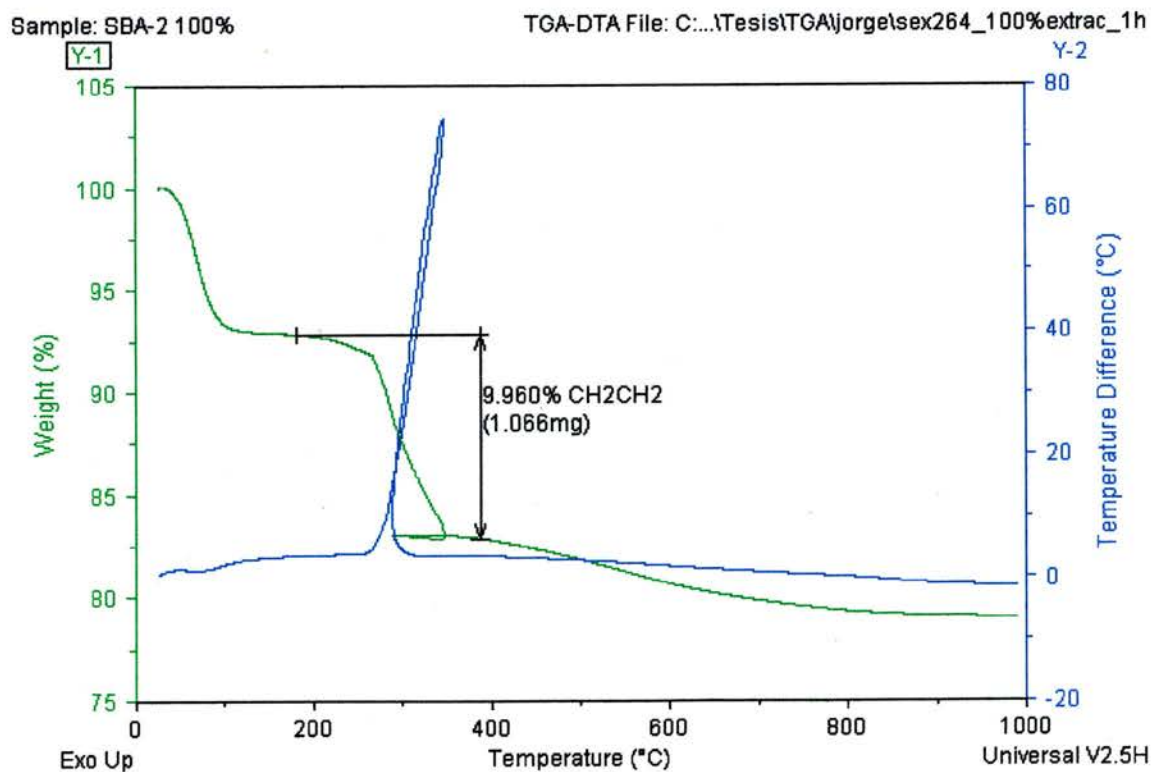


Figure 3.3.2.2. TGA analysis of ethane-siloxane SBA-2 solvent extracted (under O₂).

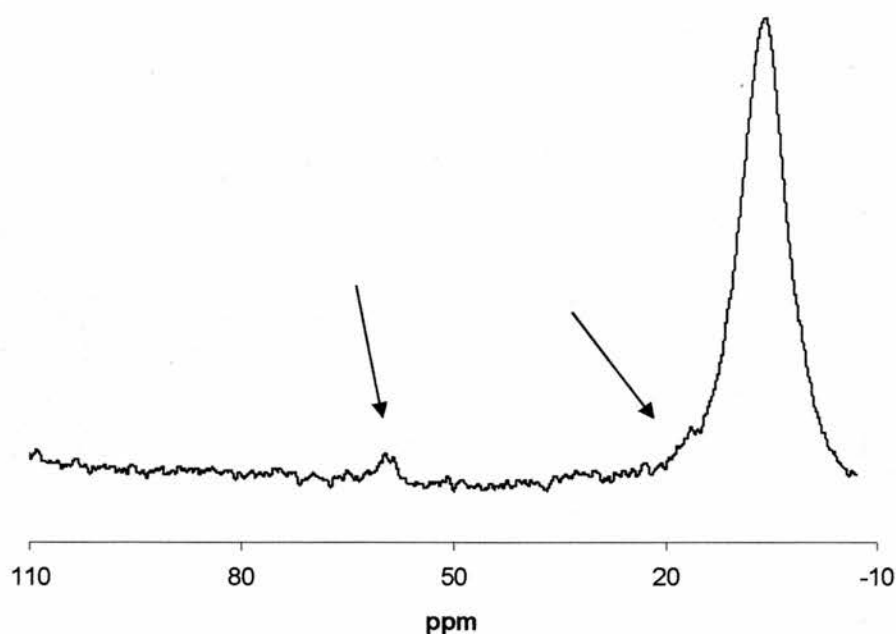


Figure 3.3.2.3. ^{13}C NMR spectra of ethane-siloxane SBA-2 solvent extracted. The black arrows indicate resonances associated with ethoxy groups.

The structure of the ethane-siloxane SBA-2 solvent extracted solid was examined under the TEM. Figure 3.3.2.4. shows two micrographs, at different magnifications, in which the presence of multiple twin planes can be observed.

Figure 3.3.2.5 shows another micrograph viewed down the [110] zone axis with its FFT-ED simulated pattern. Measurements of the contrast profile either in the image or in the FFT-ED patterns yield unit cell parameter of 70 Å, which agrees with the calculated value from the XRD.

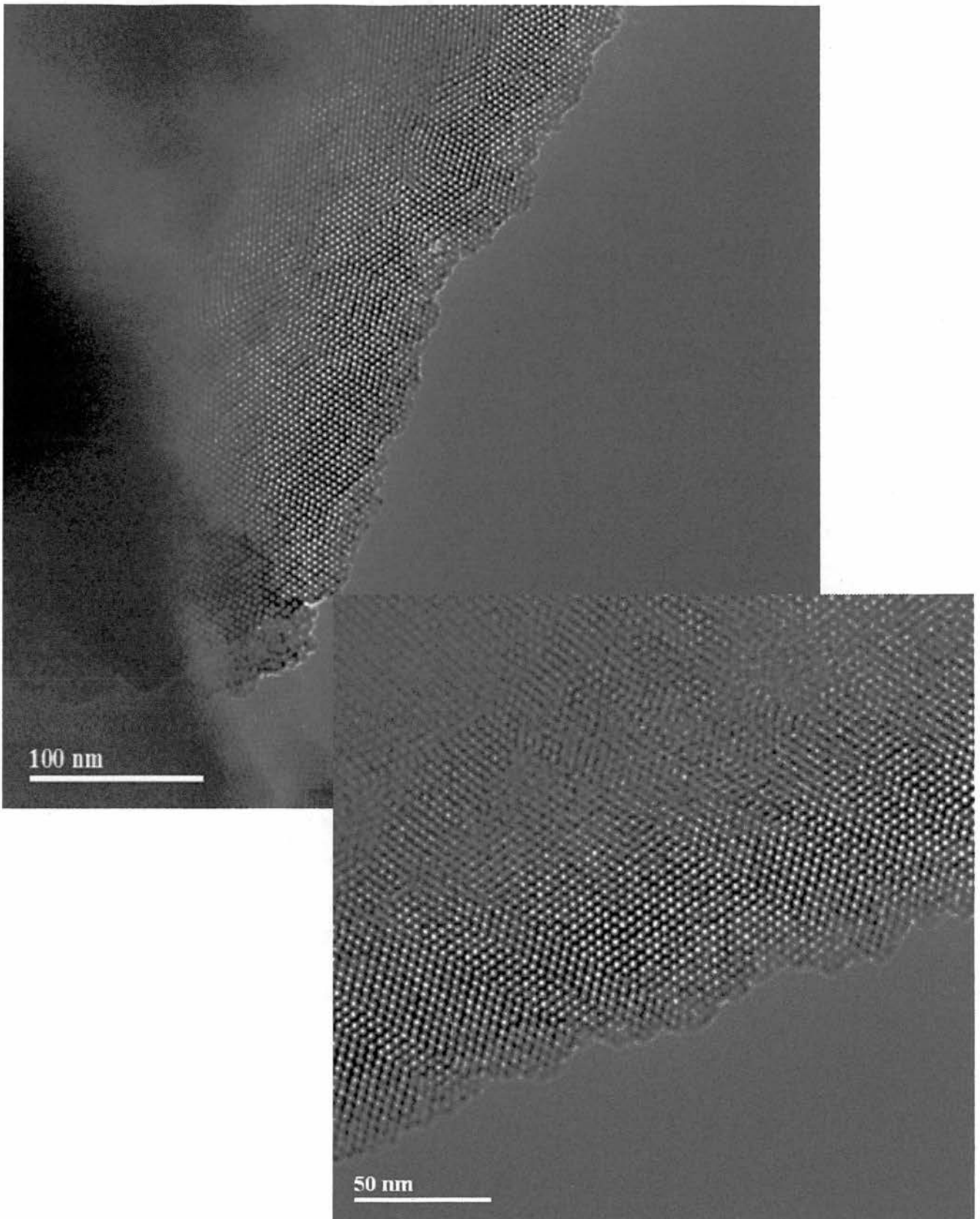


Figure 3.3.2.4. TEM micrographs of ethane-siloxane SBA-2 at different magnifications. Note the presence of multiple twin planes.

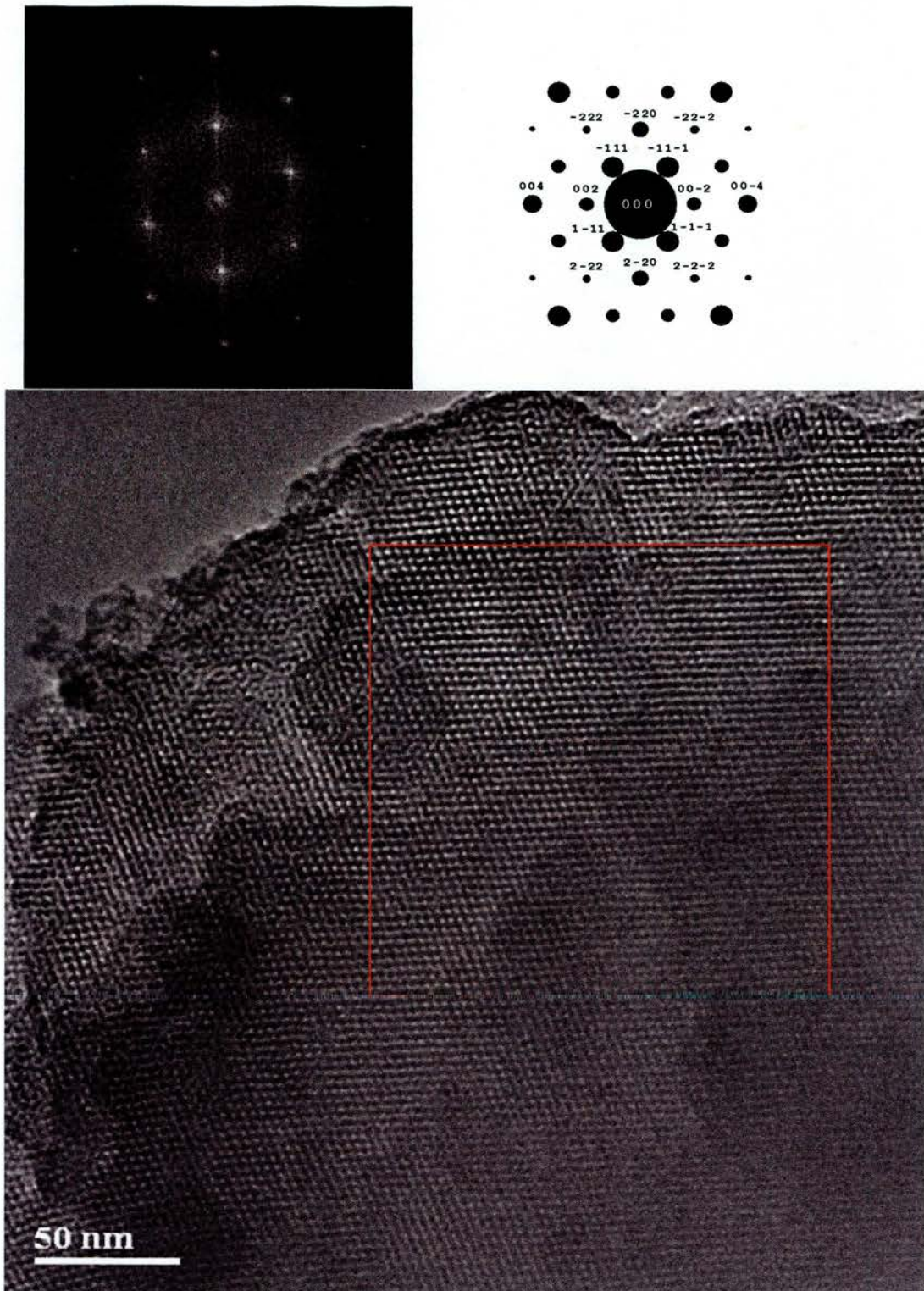


Figure 3.3.2.5. TEM micrograph of extracted ethane-siloxane SBA-2 solvent viewed down the [110] zone axis of a cubic region. The indexed FFT-ED and theoretical ED patterns are shown.

Figure 3.3.2.6 compares the N_2 adsorption isotherms at 77 K of the extracted ethane-siloxane SBA-2 with the isotherms of a pure siliceous extracted SBA-2. The shift to lower pressures of the capillary condensation indicates that the pore size of the hybrid solid is smaller. It is probably due to the lower density of the hybrid material that the adsorption capacity of the solids remains almost the same. BET surface areas are also similar for the two solids, 1142 ± 11 and 907 ± 7 m^2/g , although it has to be borne in mind that this model is not strictly applicable to cage-type porous solids. Note also that, despite the smaller cage-size exhibited by the ethane-siloxane SBA-2, there are no significant changes in adsorption at low pressures. This suggests that the size of the windows that connect the supercages of the solids are similar.

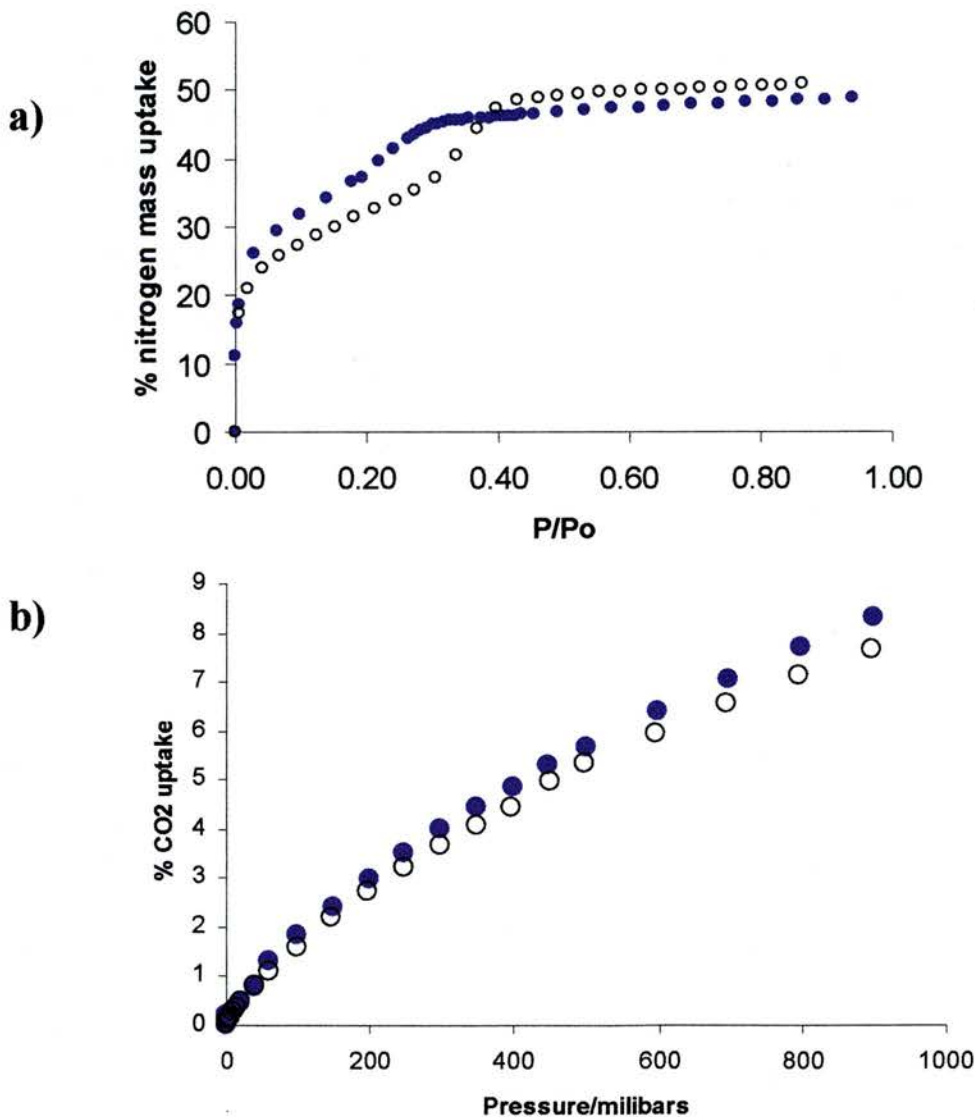


Figure 3.3.2.6. a) N_2 adsorption at 77 K and b) CO_2 adsorption at 268 K in extracted siliceous SBA-2 (open black symbols) and extracted ethane-siloxane SBA-2 (blue symbols).

Low pressure CO₂ adsorption isotherms at 268 K in these two solids are also compared in Figure 3.3.2.6. The two isotherms are similar, indicating that the ethane functionalisation of the framework does not have an important effect upon the polarity of the wall.

Butane and isobutane adsorption isotherms at 268 K in hybrid ethane-siloxane and siliceous SBA-2 materials are also compared in Figure 3.3.2.7. The adsorption isotherm of both gases is shifted to lower pressures due to the smaller pore size of the solids. At lower pressure, the affinity of the ethane-siloxane SBA-2 solid for two hydrocarbons is also stronger. Note also that the adsorption capacity of isobutane, a relative large molecule, is comparable for the two extracted solids.

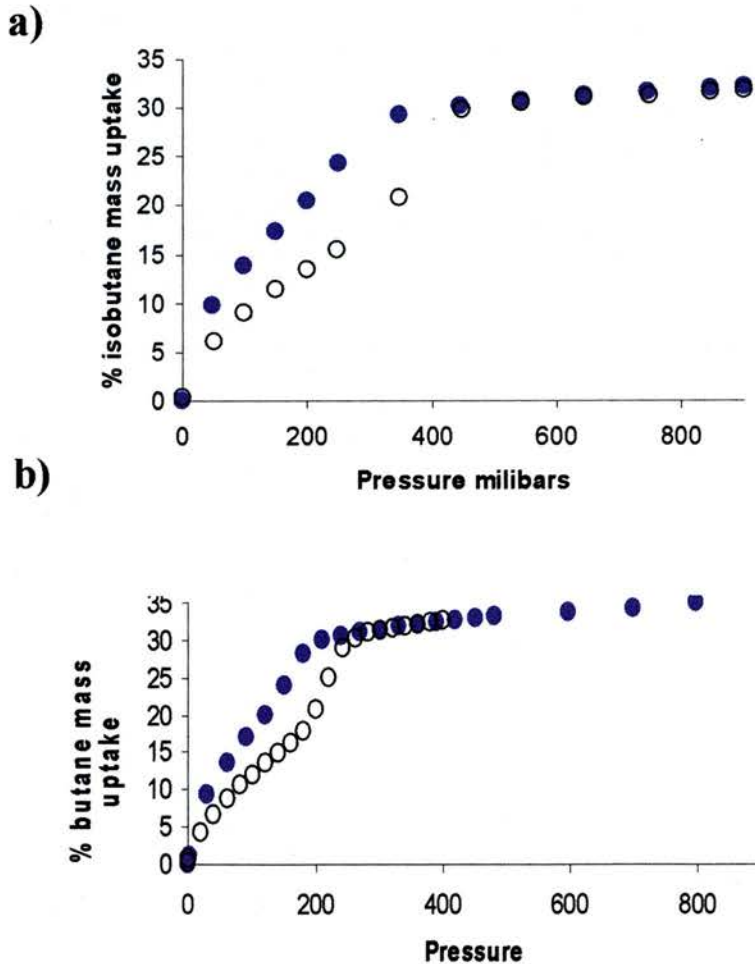


Figure 3.3.2.7. a) butane and b) isobutane adsorption experiments in extracted siliceous SBA-2 (open black symbols) and extracted ethane-siloxane SBA-2 (blue symbols).

3.4 Conclusions

Siliceous SBA-2 has been prepared according to an established procedure and the template has successfully been extracted. Batches of the extracted solid have been heated at 100 °C, 550 °C, 700 °C, 800 °C, 900 °C and 1000 °C. The resultant solids have been shown by XRD and TEM to be predominantly of face centred cubic symmetry ($Fm\bar{3}m$) related to a cubic close packed arrangement of mesocages. The solid is robust up to 900 °C. The unit cell decreases from 85 Å to 70 Å as the calcination temperature is increased, in parallel with an increase in the silicate condensation.

Adsorption studies of the series of solids have been performed using gases of molecules with different kinetic diameters. Thermal treatment of the SBA-2 silica results in a decrease of the adsorption capacity. This is slight for CO₂ (21.8 % at 900 °C) but progressively more marked for N₂ (66.7 % at 900 °C), *n*-butane (96.4% at 900 °C) and isobutane (98 % at 900°C). This is consistent with a structural model in which mesocages are linked by micropore-dimension windows that have a distribution of sizes. As the window size distribution is shifted to smaller sizes, the accessibility of the larger pores to adsorbate molecules is decreased. By controlling the calcination conditions, it is possible to introduce molecular sieving capabilities to SBA-2. After calcination at 800 °C, for example, the solid adsorbs 0.8 wt % of isobutane but a 7.5 wt % of *n*-butane. This makes SBA-2 a potential substrate for the separation of these two hydrocarbons in a pressure swing process. To the knowledge of the author, this is the first time that an ordered mesoporous solid has been described as a molecular sieve able to separate small hydrocarbons.

The pore size of SBA-2 can also be tailored by incorporation of ethane moieties within the framework. The gas adsorption properties of this hybrid ethane-siloxane solid are different to the pure silicate solid. The hybrid solid has a smaller cage size and interacts strongly with butane and isobutane while the CO₂ adsorption is only slightly increased due to the smaller cage size.

3.5. Further work

The molecular sieve properties of SBA-2 could be further investigated in many different directions:

It will be of interest to perform high pressure experiments of CO₂ and N₂ in the solid calcined at 900 °C to check if it is able to separate these gases. High pressure adsorption experiments of O₂ would be interesting as well.

It is likely to think that with the appropriate thermal treatment it should be possible to synthesise a solid able to separate species like para-xylene from ortho-xylene, benzene from cyclohexane etc.

Increasing the length of the hydrocarbon tail of the surfactant could lead to solids with higher adsorption capacity and therefore to optimize the performance of separations like *n*-butane from isobutane.

Large cage-like solids with micropores connections, like FDU-12, should be also studied due to their possible sieve properties.

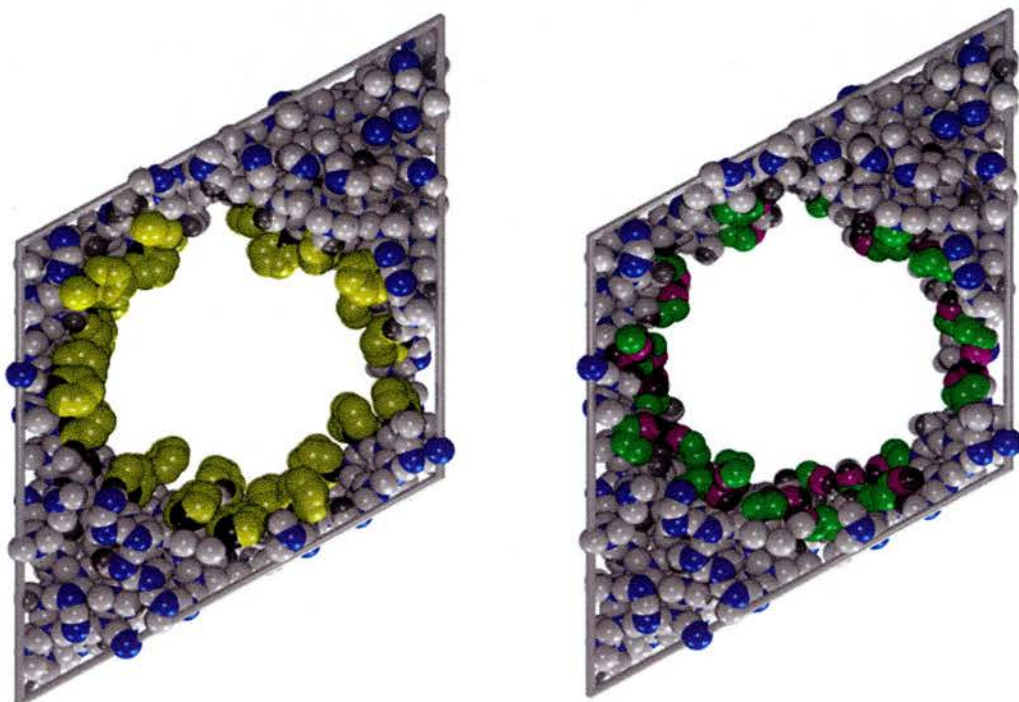
Due to the apparent stronger interaction of hydrocarbons with the hybrid ethane-siloxane solid, it would be of interest to performed high pressure adsorption experiments of methane and ethane. Also high pressure adsorption experiments of CO₂ would be interesting, as it seems not to be strongly affected by the smaller size of the cages.

References for chapter 3.

- [1] Q. Huo, R. Leon, P. M. Petroff, G. D. Stucky, *Science*, **1995**, 268, 1324.
- [2] M. Kruk, M. Jaroniec, Y. Sakamoto, O. Terasaki, R. Ryoo, C. H. Ko, *J. Phys. Chem. B.*, **2000**, 104, 292.
- [3] M. Kaneda, T. Tsubakiyama, A. Carlsson, Y. Sakamoto, T. Ohsuna, O. Terasaki, *J. Phys. Chem.*, **2002**, 106, 1256.
- [4] Y. Sakamoto, M. Kaneda, O. Terasaki, D. Y. Zhao, J. M. Kim, G. Stucky, H. J. Shin, R. Ryoo, *Nature*, **2000**, 408, 449.
- [5] W. Zhou, H. M. A. Hunter, P. A. Wright, Q. Ge, J. M. Thomas, *J. Phys. Chem. B.*, **1998**, 102, 6933.
- [6] H. M. A. Hunter, A. E. Garcia-Bennett, I. J. Shannon, W. Zhou, P. A. Wright., *J. Mater. Chem.*, **2002**, 12, 10.
- [7] M. Pérez-Mendoza, J. Gonzalez, P. A. Wright, N. A. Seaton, *Langmuir*, **2004**, 20, 7653.
- [8] M. Pérez-Mendoza, J. Gonzalez, P. A. Wright, N. A. Seaton, *Langmuir*, **2004**, 20, 9856.
- [9] F. Kleitz, W. Schmidt, F. Schüth, *Microporous Mesoporous Mater.*, **2003**, 65, 1.
- [10] R. M. de Vos, H. Verweij, *Science*, **1998**, 279, 1710.
- [11] P. I. Ravikovitch, A. V. Neimark, *Langmuir*, **2002**, 18, 1550.
- [12] S. Guan, S. Inaganki, T. Ohsuna, O. Terasaki, *Microporous Mesoporous Mater.*, **2001**. 165.

Chapter 4.

Synthesis, characterisation and adsorption properties of phenyl- and aminopropyl- functionalised mesoporous solids



4.1. Introduction.

One of the objectives of the EPSRC project developed in close collaboration with chemical engineers at Edinburgh University was to design and manufacture a new family of hybrid organic-inorganic adsorbents with tailored pore surface chemistry, and evaluate them as adsorbents with the target of improved selectivities (e.g. in separations involving ethane and CO₂). For selective adsorption processes applications, the pores of the adsorbent must ideally be of the same order of the adsorbate molecules (i.e. micropore region, < 20 Å). The performance of the adsorbent depends intimately on the pore structure. The main variables are (i) the pore geometry (i.e. shape and size of the pores), and (ii) the surface chemistry. For pores that are only slightly larger than the adsorbate molecules molecular sieving can occur (i.e. butane/isobutane in SBA-2, chapter 3). For larger pores, the effect of the pore geometry on the adsorbate is more subtle.

The mesoporous solids of interest during this thesis have been SBA-1 [1], SBA-2[2] and MCM-41[3]. Whereas SBA-1 and SBA-2 have a remarkable microporous character that is expected to lead to a strong interaction with adsorbate molecules, MCM-41, with one dimensional cylindrical pores, was easier to model for our co-workers, and therefore presents itself as better model solid to understand the effects of changes of surface chemistry on adsorption in mesoporous solids.

The surface of mesoporous silicates can be functionalised by incorporating functionalised siloxanes during synthesis or through the grafting of these agents post-synthesis [4]. By means of the organic modification of the surface specific interactions should be made possible that will be able to distinguish between gases of different nature (i.e. polarity or size).

Phenyl-functionalised mesoporous solids have been of interest to this project (Section 4.2). Phenyl is a bulky organic group that should have an important effect upon the pore size and the surface heterogeneity of the solids. Also, due to its non-polar nature, its inclusion is expected to enhance the selectivity for adsorption of hydrocarbons. These assumptions were supported by initial computer calculations performed by the group at

Edinburgh University, in which phenyl-functionalised mesoporous solids were identified as possible adsorbates for hydrocarbon purification in mixtures of these and polar gases like CO₂.

Aminopropyl modification of the pore surface has also been of interest in this work. It has been reported that, in mesoporous solids MCM-41 and SBA-1, aminopropyl moieties improves the affinity of these solids for heavy metals [5]. In addition, during the course of the thesis, it was shown that functionalising SBA-15 with aminopropyl groups produces strong adsorption sites for CO₂ [6]. This experimental evidence make aminopropyl moieties a potential agent to improve the CO₂ adsorption selectivity in mixtures of CO₂ and ethane or other small hydrocarbons of low polarity.

In this chapter (section 4.2) the synthesis and characterisation of phenyl-functionalised MCM-41, SBA-1 and SBA-2 mesoporous solids are discussed. The adsorption properties of these solids have been studied by means of ethane, CO₂, toluene and isobutane adsorption experiments. Section 4.3 discusses the synthesis, characterisation and adsorption properties of aminopropyl-functionalised MCM-41 and SBA-1 solids. (Synthesis of porous aminopropyl-SBA-2 was not successful).

The adsorption data presented in this thesis has been analysed through Monte Carlo Simulations by Christian Schumacher (Edinburgh). Preliminary results of this collaboration were presented at the 14th International Zeolite Conference, Cape Town , South Africa [7]. Publications in which the molecular mechanism of gas adsorption of these solids is discussed, are in preparation.

4.2.1 Phenyl-functionalised mesoporous silicates

Synthesis of MCM-41 and phenyl-functionalised MCM-41

MCM-41 materials were synthesised according to published procedures [8] using tetramethylorthosilicate (TEOS, 98% from Aldrich), phenyltriethoxysilane (Ph-TEOS, Aldrich), hexadecyltrimethylammonium bromide (CTMABr, Aldrich) as a surfactant, sodium hydroxide (Aldrich), acetic acid and water. The mother gel composition was $(1-x)$ TEOS: x Ph-TEOS: 0.7 NaOH: 0.12 CTMABr: 589 H₂O, where x is the fraction of Ph-TEOS in the silica source. Four solids were prepared with $x = 0, 0.05, 0.1$ and 0.2 . Silicate MCM-41 was synthesised as follows: 1.38 g of NaOH were dissolved in a plastic beaker with 475 ml of water and 2g of CTMABr. To this clear and homogeneous solution 9.34 g of TEOS were added dropwise under high stirring conditions, turning it white in few minutes. After 20 h stirring at room temperature the pH was adjusted to 8.5 with acetic acid and the reaction medium was placed in an autoclave at 100 °C. After 24 hours the solid was filtered and dried at 60⁰C in air for 24 h. The surfactant extraction was performed by refluxing 1g of dry material in a mixture of 15 cm³ of HCl (37%) and 185 cm³ of ethanol for 1 hour or by calcination at 550 °C under flowing nitrogen for 5 h and another extra 5 h under oxygen. Phenyl-functionalised MCM-41 materials were synthesised following the same route but using as the silica source a mixture of Ph-TEOS and TEOS with $x = 0.05, 0.1$ and 0.2 .

Synthesis of SBA-1 and phenyl-functionalised SBA-1 using CTEABr (low acid concentrations and low temperature)

The particle size of SBA-1 mesoporous solid can be controlled via the gel composition and the temperature of the reaction [9]. Due to the nature of the high adsorption pressure rig, large particles are desired in order to avoid contamination of the system. Therefore, the method of S. Che *et al.* [9], which yields larger particles, was chosen as a starting point for the synthesis of the phenyl-functionalised solids.

Accordingly to [9], surfactant C₁₆TEABr, distilled water and hydrochloric acid (37%, Fisher Chemicals) were combined in the following molar ratio; 0.13 C₁₆TEABr: 2.5 HCl : 125 H₂O, to give a homogeneous solution. The solution was stirred for 30 minutes prior to the dropwise addition of 1 mol of TEOS (98%, Aldrich) The reaction mixture was stirred for three minutes and then kept at -5 °C under static conditions for four days. After this, a white precipitate is filtered and dried at 60°C. The surfactant was removed in two different ways from the pure silica material: by successive calcination in nitrogen and oxygen at 550 °C and by solvent extraction. Before the extraction the sample was heated for one hour at 100 °C and thirty minutes at 160 °C to stabilise the framework by condensation.

Phenyl-functionalised solids were prepared following the same methodology using a mixture of Phenyl-TEOS/(Ph-TEOS+TEOS) in molar ratio 0.1 as a silica source. The concentration of acid in the gel for the synthesis of the hybrids SBA-1 solids was higher than for the silicate solid. A typical gel composition was, in molar ratios, 1 Si(OR)₄: 0.13 C₁₆TEABr: 5 HCl : 125 H₂O.

Attempts to synthesise SBA-1 solids with a higher degree of phenyl functionalisation via the method [9] were not successful. However, it was found that under the conditions reported by M. J. Kim *et al.* [10], solids with SBA-1 type structure were obtained using a mixture of Phenyl-TEOS/(Ph-TEOS+TEOS) in molar ratio 0.26 as a silica source.

On basis of this procedure [10], 26% phenyl-functionalised SBA-1 solid was synthesised at low temperatures as follows: Surfactant C₁₆TEABr, distilled water and hydrochloric acid (37%, Fisher Chemicals) were combined in the following molar ratios; 0.2 C₁₆TEABr: 56 HCl: 600 H₂O, obtaining a homogeneous solution. The solution was stirred for 30 minutes prior to the drop wise addition of 1 mol of pre-cooled silica source: TEOS (98%, Aldrich) and Phenyl-TEOS (98%, Aldrich). The reaction mixture was stirred until condensation is observed and then kept at -5 °C for three days, filtered and dried at room temperature. The surfactant extraction was carried out with a solution of HCl 10% (v/v). The phenyl-TEOS/(Ph-TEOS+TEOS) molar ratio used for the synthesis was 0.26.

Synthesis of silicate and phenyl-functionalised SBA-2.

On the basis of published procedures [11], pure silica SBA-2 was synthesised in basic conditions at room temperature. In a typical synthesis TEOS (Aldrich 98%), tetramethyl ammonium hydroxide (25% w/w aqueous solution), water and gemini surfactant C₁₆₋₃₋₁ are mixed in the molar ratio 1: 0.3 : 75: 0.04. First the surfactant was added to the water with the base and left stirring for half an hour until the surfactant was completely dissolved. After that the TEOS was added to the solution drop-wise and the reaction mixture left stirring for 4 hours. The product was recovered by filtration, dried in air at 60°C and calcined at 550°C overnight under nitrogen and oxygen. The material was characterised by XRD showing the typical diffraction pattern for SBA-2.

Phenyl-functionalised SBA-2 solids were prepared with of Ph-TEOS / (Ph-TEOS+TEOS) molar ratios of 0.05, 0.1 and 0.2 using the same procedure as that described above. Removal of the surfactant was performed by refluxing the material in a solution of 10% (v/v) HCl in EtOH for three hours.

4.2.2. Characterisation of phenyl-functionalised mesoporous solids by XRD, SEM and elemental CHN analysis

Phenyl- MCM-41

The synthesis of phenyl-functionalised MCM-41 was based on a published procedure [8]. In this work, highly ordered pure silica MCM-41 was synthesised from a gel with the molar ratio TEOS: CTMABr: NaOH: H₂O of 1: 0.13: 0.32: 615 respectively. However, these synthetic conditions gave poor quality MCM-41 when Ph-TEOS was incorporated in the reaction mixture. In order to achieve higher quality Ph-MCM-41 material it was necessary to increase the pH during the condensation of the silica in solution at room temperature.

Figure 4.2.1 presents the XRD patterns of some 10% phenyl-functionalised MCM-41 type solids synthesised with different Si: NaOH molar ratios. These correspond to solids filtered and dried at 60° C in air overnight after 20 h stirring at room temperature without any other thermal treatment. Note the low quality diffraction pattern of the hybrid solid synthesised using 0.32 NaOH: 615 H₂O molar ratio (blue) and the decrease in unit cell with the increase in NaOH in the reaction mixture.

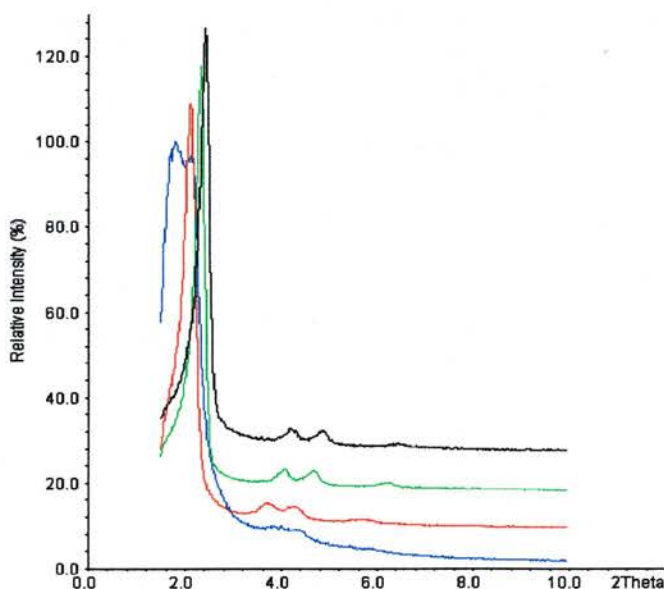


Figure 4.2.1 XRD patterns of MCM-41 type materials. Red and blue correspond to a pure silica and 10% phenyl-functionalised MCM-41 respectively, synthesised using the Si: NaOH molar ratios reported in ref [7] Green and black lines correspond to 10% phenyl-functionalised MCM-41 synthesised with 0.67 NaOH: 615 H₂O and 0.9 NaOH: 615 H₂O added in the synthesis, respectively.

Solids dried at 60°C after stirring for 20 h at room temperature became amorphous after the solvent extraction with HCl/EtOH due to the low condensation of the silica achieved at room temperature. In order to stabilise the solid it was necessary to heat the reaction mixture for 24 h at 100°C in an autoclave after correction of the pH to ~9 with acetic acid. This pH correction was found to be critical in order to obtain a good quality solid. After the 24h in the autoclave, the solids were filtered and dried at 60 °C overnight in air prior to the surfactant extraction.

It has been reported [12] that, due to the high thermal stability of the phenyl groups, it is possible to remove the template by calcination at low temperatures without affecting the aromatic groups. The high thermal stability of the phenyl groups has been confirmed during this thesis. However, attempts to remove the surfactant using low temperature calcination gave carbon deposits.

According to these procedures, MCM-41 materials were prepared with different degrees of phenyl-functionalisation. Figure 4.2.2 presents the XRD patterns of phenyl-functionalised MCM-41 type materials which are shifted to higher angles with increasing functionalisation.

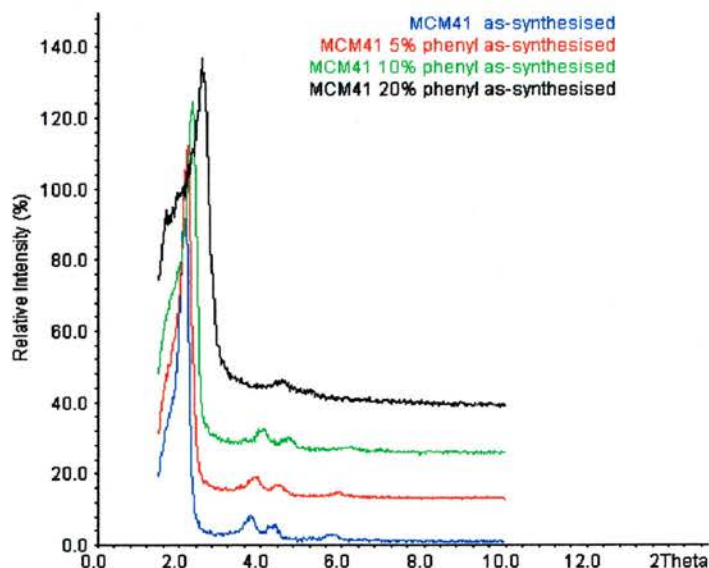


Figure 4.2.2. XRD of as-synthesised MCM-41 type materials. The pattern in blue corresponds to pure siliceous sample. Red, green and black patterns correspond to 5, 10 and 20% phenyl- functionalised solids.

After the removal of the surfactant the solids retained their structure (Figure 4.2.3.) Table 4.2.1 summarises the unit cell parameters calculated for these solids on the basis of $p6mm$ symmetry.

The adsorption properties of Ph-MCM-41 have been of special interest in this project. As functionalisation *in situ* could result in some of the phenyl moieties in the walls rather than in the pores, the question arose, of the effect of removal of the organic moieties by calcination upon the structural order and adsorption properties of the phenyl-functionalised MCM-41 type solids. XRD of solids calcined in O_2 at $550\text{ }^\circ\text{C}$ are presented in Figure 4.2.3. Analyses of these XRD patterns are summarised in Table 4.2.1. Nitrogen adsorption isotherms of the calcined solids are shown later.

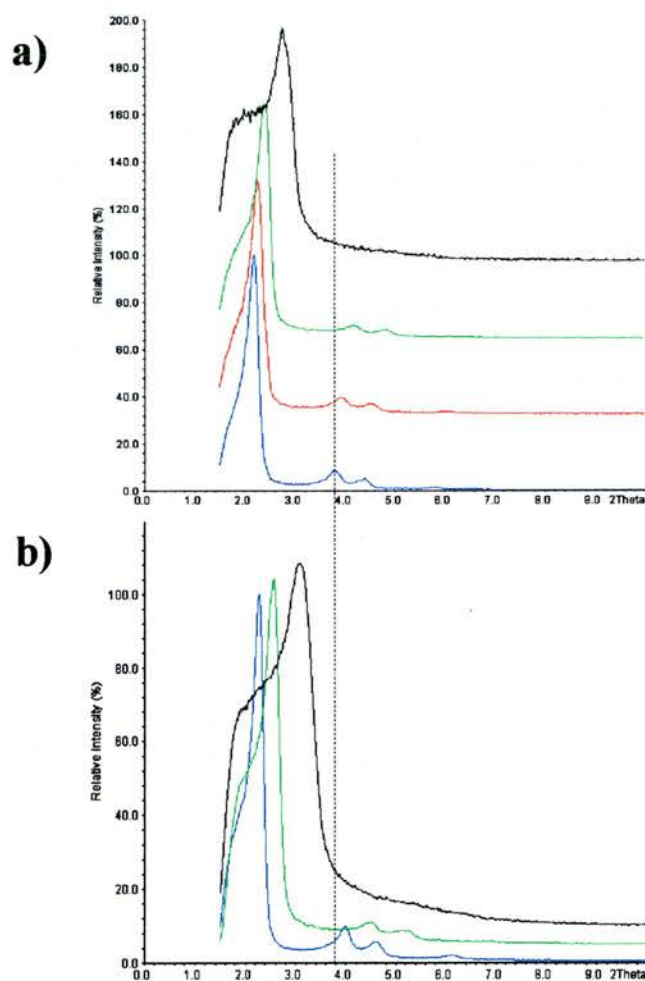


Figure 4.2.3. a) XRD of MCM-41 type materials after the removal of the surfactant by solvent extraction and b) XRD patterns of MCM-41 type solids calcined at $550\text{ }^\circ\text{C}$ under O_2 . In both graphs, blue corresponds to pure siliceous solid. Red, green and black correspond to 5, 10 and 20% functionalised solids. The black line at $d=23.8\text{ \AA}$ has been drawn to facilitate comparison between of the high angle reflections in both diagrams.

	As-synthesised.				Solvent extracted.				Calcined at 550 °C under O ₂ .			
	<i>d</i> ₁₀₀ / Å	<i>d</i> ₁₁₀ / Å	<i>d</i> ₂₀₀ / Å	<i>a</i> / Å	<i>d</i> ₁₀₀ / Å	<i>d</i> ₁₁₀ / Å	<i>d</i> ₂₀₀ / Å	<i>a</i> / Å	<i>d</i> ₁₀₀ / Å	<i>d</i> ₁₁₀ / Å	<i>d</i> ₂₀₀ / Å	<i>a</i> / Å
Pure SiO ₂	41.1	23.5	20.6	47.4	40.3	23.5	20.3	47.1	38.5	22.0	19.0	44.1
5% phenyl.	39.7	22.9	19.9	45.9	39.9	22.9	19.9	45.9	-----	-----	-----	-----
10% phenyl.	38.1	21.7	18.9	43.7	37.0	21.3	18.4	42.6	34.5	19.8	17.2	39.7
20% phenyl.	34.3	-----	-----	39.6	32.3	-----	-----	37.4	28.8	-----	-----	33.3

Table 4.2.1. Summary of the interplanar distances and *a* unit cell parameter for the different MCM-41 type solids on the basis of the space group p6 m (0.5 Å error). Note that the *d*₁₁₀ and *d*₂₀₀ reflection are not well resolved in the XRD patterns of the sample 20% phenyl-functionalised sample and are not included in the table.

- The XRD pattern of the post-synthesis phenyl-functionalised MCM-41 was the same as that observed for the extracted pure siliceous MCM-41 extracted used as a starting material.

Phenyl-SBA-1 XRD characterisation

As mentioned in the characterisation techniques chapter, due to the nature of the multi-component high pressure adsorption apparatus at Edinburgh University, large particles sizes are preferred so as not to contaminate the apparatus. According to the literature [9], synthesise of SBA-1 at low temperatures and low acidic media, leads to solids with well defined morphologies and better long range order. These synthetic conditions were used to prepare phenyl-SBA-1 solids in order to achieve control over the particle morphology. XRD patterns of calcined and extracted pure silicate SBA-1 (Figure 4.2.4) prepared according to the method of S. Che *et al.* [9] agree with previous results [1]. Both patterns present several diffraction peaks with well defined (210) and (211) reflections. Table 4.2.2 summarises the results found on the basis of the XRD analysis.

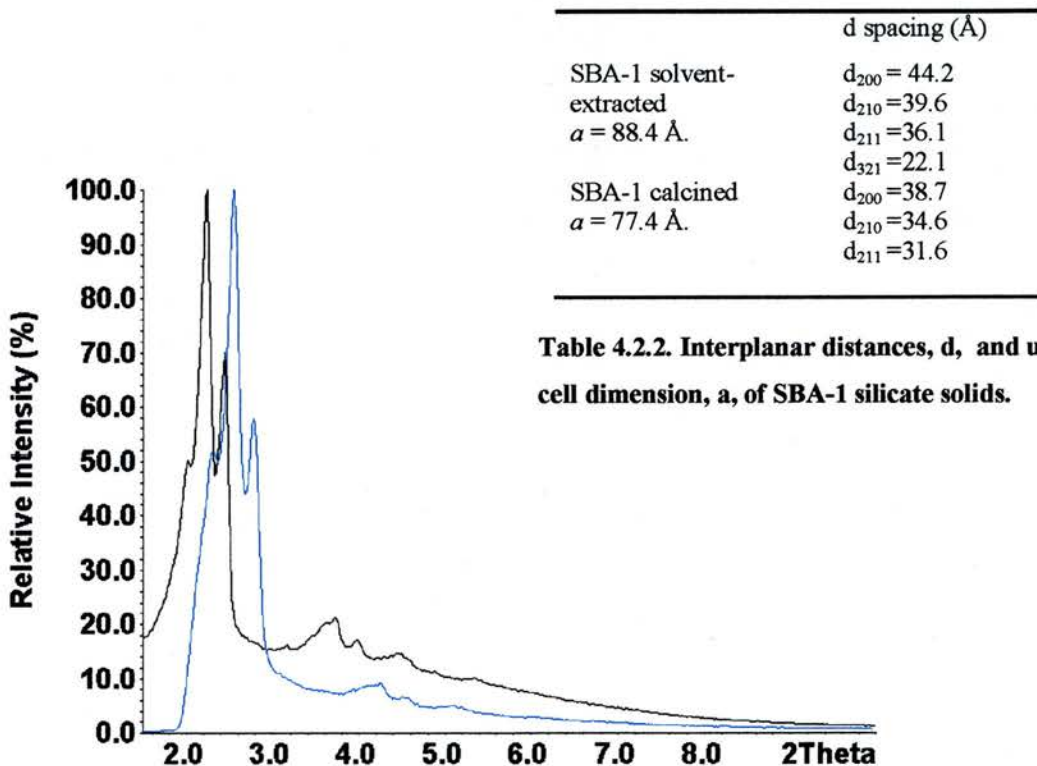
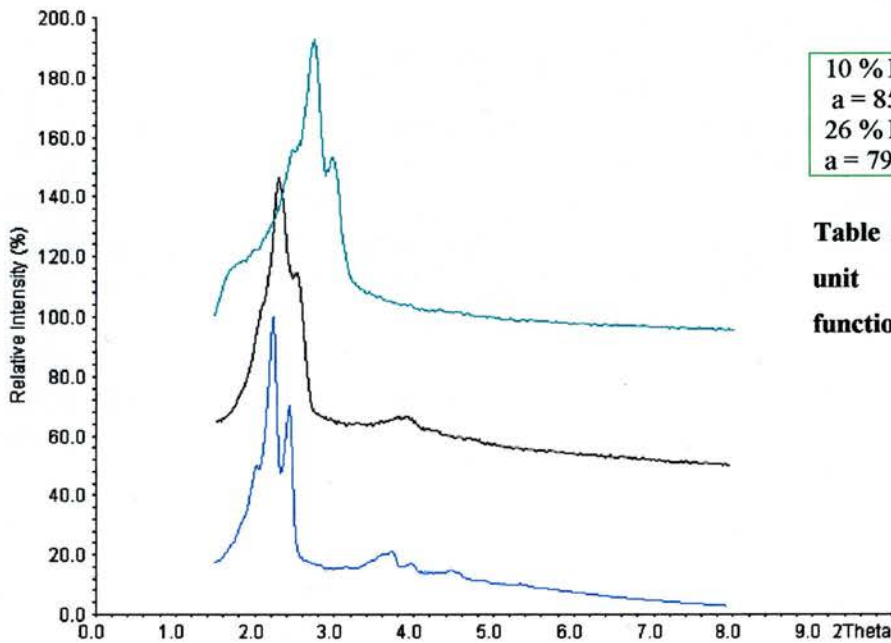


Table 4.2.2. Interplanar distances, d , and unit cell dimension, a , of SBA-1 silicate solids.

Figure 4.2.4. XRD patterns of SBA-1 calcined (blue) and solvent extracted (black).

Attempts to synthesised phenyl-functionalised solids via these low temperature, low acid concentrations conditions [9] were unsuccessful. To synthesise well defined Ph-SBA-1 it was necessary to increase the acid concentration in the reaction mixture up to 5 HCl: 125 H₂O when Ph-TEOS/(Ph-TEOS+TEOS) was 0.1. In figure 4.2.5 the XRD patterns of extracted 10% phenyl-functionalised and silicate SBA-1 are compared. After functionalisation the XRD pattern is not as well resolved as the pure silicate solid, but it remains characteristic of SBA-1. Table 4.2.3 presents the summary of the XRD. To achieve higher degrees of phenyl-functionalisation it was necessary to further increase the acidic concentration. Using the molar ratios 1 Silica source: 0.2 C16TEABr: 56 HCl : 600 H₂O [10] it was possible to synthesised a 26 % phenyl-functionalised SBA-1 solid (using Ph-TEOS/(Ph-TEOS+TEOS) in ratio 0.26 as the silica source).



	d spacing (Å)
10 % Phe-SBA-1	d ₂₁₀ = 38.3
a = 85.5 Å	d ₂₁₁ = 34.9
26 % Phe-SBA-1	d ₂₁₀ = 29.5
a = 79.1 Å	d ₂₁₁ = 32.3

Table 4.2.3. Interplanar distances, d, and unit cell dimension, a, of phenyl functionalised SBA-1 silicate solids.

Figure 4.2.5. XRD patterns of 26 % phenyl functionalised (green), 10 % phenyl-SBA-1 (black) and silicate SBA-1 solvent extracted (blue).

SEM micrographs of phenyl-functionalised SBA-1 are shown in Figure 4.2.6. Note that the particle size of the 10 % phenyl-functionalised SBA-1, synthesised at lower acidic conditions is larger. Similar behaviour has been observed for silicate SBA-1 solid [8].

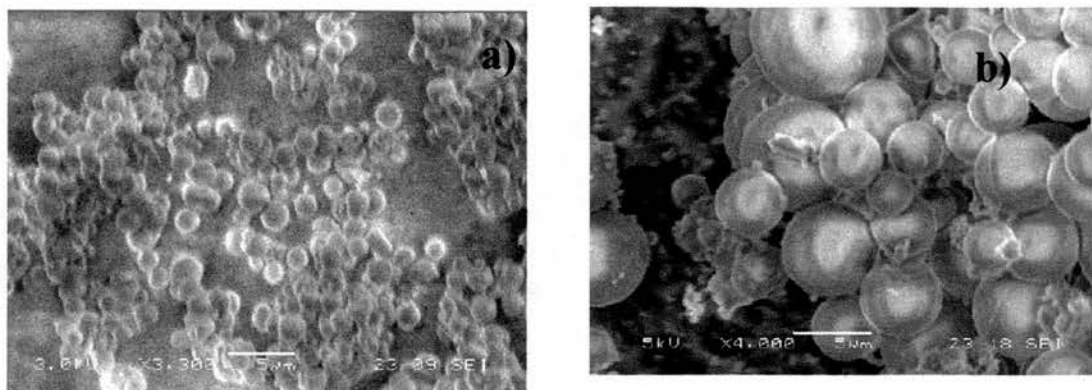


Figure 4.2.6. SEM micrographs of 26% phenyl-functionalised SBA-1 and 10% phenyl-functionalised SBA-1.

SBA-2 XRD characterisation.

The synthesis of phenyl-functionalised SBA-2 was performed according to published procedures [11]. XRD results are shown in Figure 4.2.7. The product of the syntheses using surfactant C_{16-3-1} was the hexagonal phase SBA-2 for all the Ph-TEOS/TEOS ratios used in the gels (These solids, unlike those observed in chapter 3, show the $(103)_{\text{hex}}$ reflection and have therefore been indexed on the basis of a hexagonal symmetry, $P6_3/mmc$). Peaks corresponding to (002), (110), (112) and (210) are observed in all the patterns but the relative intensity of (110) decreases on increasing functionalisation. Also it seems that with the increase of functionalisation there is a slight increase of the (103) reflection intensity, indicating a larger proportion of the hexagonal intergrowth. All the XRD patterns could be indexed on basis of the space group $P6_3/mmc$ with unit cell parameters $a=57.8 \text{ \AA}$ and $b=95.4 \text{ \AA}$ for the materials after the surfactant extraction and $a=54.6 \text{ \AA}$ and $c=89.1 \text{ \AA}$ for pure silicate SBA-2 calcined at $550 \text{ }^\circ\text{C}$. No significant changes in the unit cell parameter were observed for solids with different degrees of functionalisation. All these materials were stable to the surfactant extraction after the thermal treatment at $100 \text{ }^\circ\text{C}$. The morphology observed for a 20% phenyl-functionalised sample (Figure 4.2.8), flat-sheets, is also characteristic of SBA-2 [11].

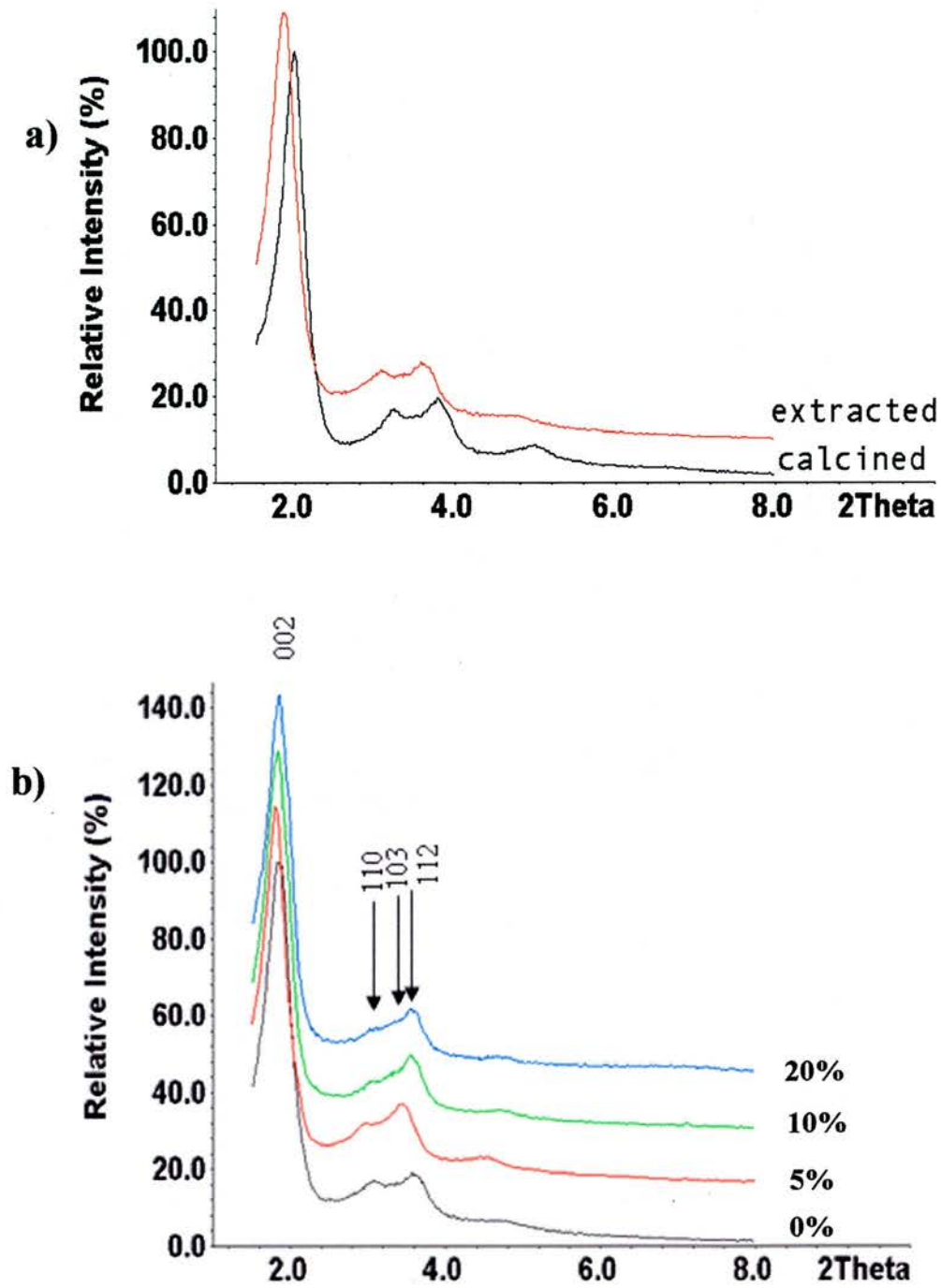


Figure 4.2.7. XRD patterns of a) silicate SBA-2 calcined and solvent extracted and b) extracted phenyl-functionalised solids. The degree of functionalisation is indicated in the graph.

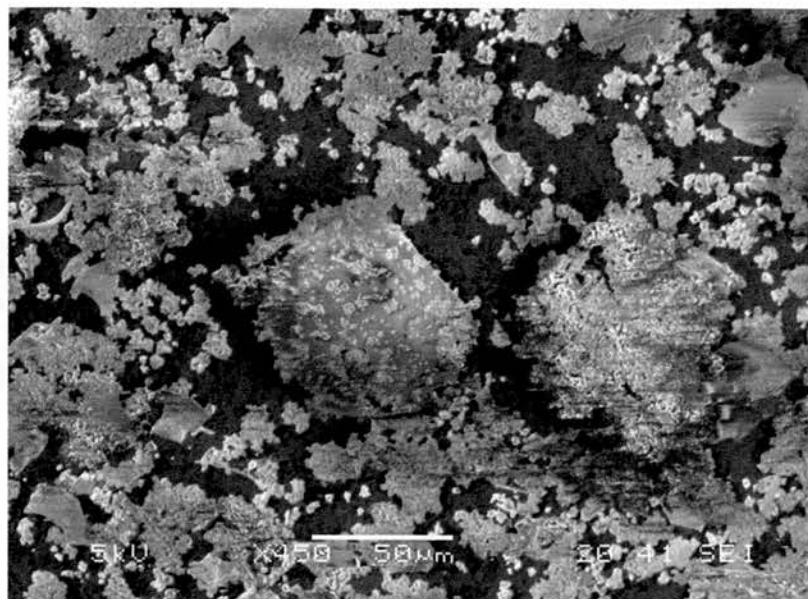


Figure 4.2. 8. SEM micrograph of 20% phenyl- functionalised SBA-2 solid after removal of the surfactant by solvent extraction.

Elemental analysis:

The elemental content of carbon, hydrogen and nitrogen of the different phenyl functionalised mesoporous materials after the removal of the surfactant by solvent extraction was:

For MCM-41:

Pure silica extracted 2.60% C, 1.37%H, 0.04% N.

5% functionalised: 7.32% C, 1.58%H, 0.02%N.

10% functionalised: 11.06%C, 1.78%H 0.05%N.

20% functionalised: 19.67%C,2.05%H,0.05%N.

Functionalised post-synthesis: 12.06%C, 1.25%H, 0.17%N.

For SBA-1 (synthesised at low temperature and low acidic conditions):

10% functionalised 11.21% C, 2.16% H, 0.02% N.

26% functionalised 16.74% C, 2.56% H, 0.05% N.

For SBA-2:

Pure silica extracted: 1.78% C, 1.96% H, 0.04% N.

5% functionalised: 5.26% C, 2.27% H, 0.10% N.

10% functionalised: 11.57% C, 2.29% H, 0.11 % N.

20% functionalised: 20.75% C, 2.73% H, 0.17% N.

In addition, a sample of Ph-HMM solid [13] was kindly supplied by Dr. Paula Ferreira (Universidade de Aveiro, Portugal). This solid, first reported by S. Inagaki and co-workers, possesses a unique hybrid organic-inorganic “crystal-like structure” of aromatic phenylene groups in its framework. The XRD pattern of the solid is presented in figure 4.2.9, showing reflections at $d = 7.6$, 3.8 and 2.5 Å, consistent with the reported diffraction pattern.

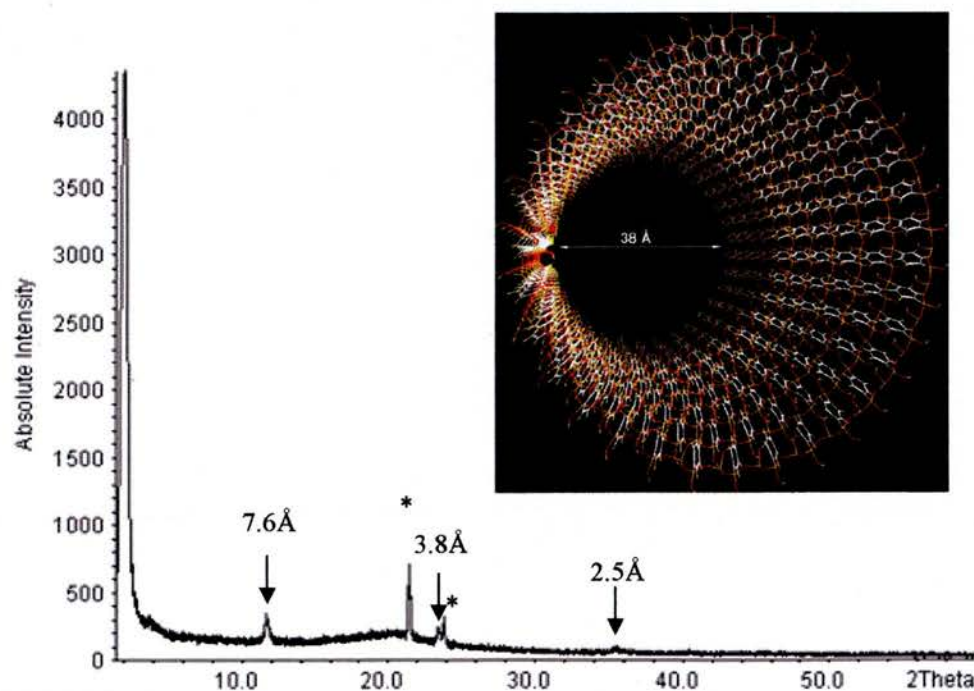


Figure 4.2.9. XRD pattern of Ph-HMM and representation of the structure [13]. (Sample supplied by Dr. Paula Ferreira, Universidade de Aveiro). This XRD pattern was collected using a disk sample holder. Vaseline peaks are asterisked.

4.2.3. NMR characterisation of phenyl-functionalised mesoporous solids

CP $^1\text{H}\rightarrow^{13}\text{C}$ MAS NMR was used to verify the presence of phenyl groups in the solids functionalised *in situ*. Figure 4.2.10 and 4.2.11 are examples of spectra recorded on phenyl-functionalised materials before and after the removal of the surfactant by solvent extraction. As-synthesised solids exhibit well defined resonances at 135 and 125 ppm corresponding to aromatic carbons of the phenyl groups and several other resonances between 60 and 5 ppm due to the surfactant molecules. The signals at 130 ppm associated with the phenyl groups, are more clearly observed in all the solids after extraction. It can also be seen that the method used to remove the template was very effective. Note that the main resonance of the hydrocarbon chain at ~ 39 ppm is drastically reduced in all the solids after the solvent extraction of the surfactant. Samples treated under reflux in HCl/EtOH present resonances at ~ 58 and ~ 16 ppm which were not observed in the as-synthesised solids. These signals are attributed to ethoxy groups ($-\text{OCH}_2\text{CH}_3$) tethered to the surface of the solids as a result of the solvent extraction process. These groups, like the phenyl moieties, exhibit high thermal stability, remaining within the material after heating at 300°C under N_2 .

^{13}C NMR spectra of the solid functionalised post-synthesis was analogous to the spectra depicted in Figure 4.2.12, indicating that the solid was successfully grafted with phenyl groups and also showed resonance signals corresponding to ethoxy groups.

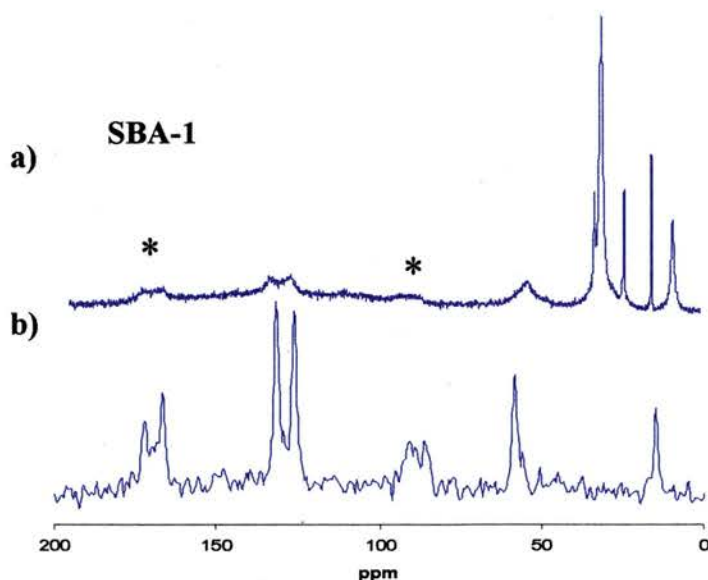


Figure 4.2.10. CP $^1\text{H}\rightarrow^{13}\text{C}$ MAS NMR of a) as-synthesised and b) surfactant-free, solvent-extracted, 10% phenyl SBA-1. Spinning side bands are asterisked.

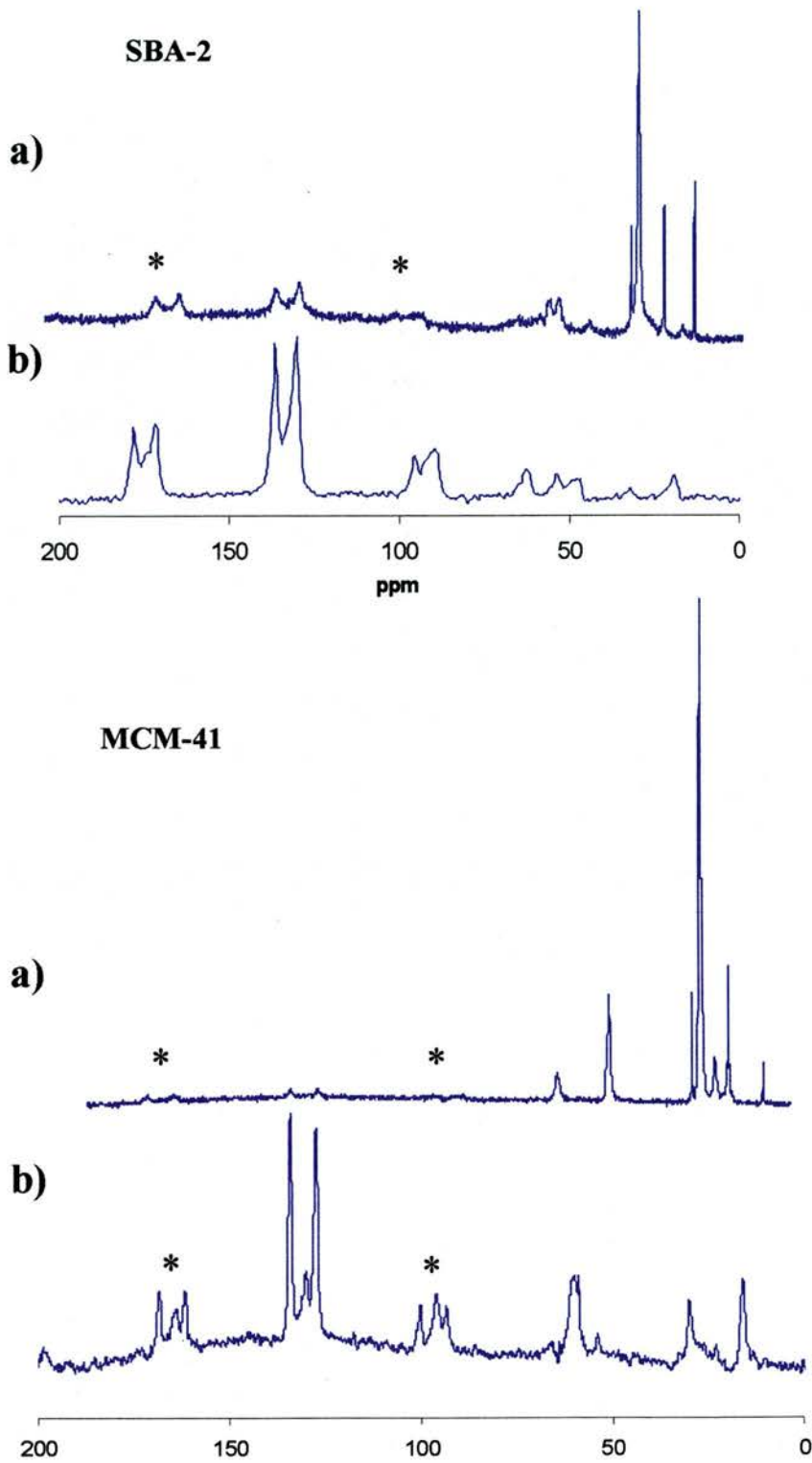


Figure 4.2.11. MAS CP $^1\text{H} \rightarrow ^{13}\text{C}$ NMR of a) as-synthesised and b) surfactant-free, solvent-extracted, 10% phenyl functionalised mesoporous solids. Spinning side bands are asterisked.

^{29}Si MAS NMR is used to determine the degree of polymerisation and concentration of silanol species present (Figure 4.2.12). Relatively broad resonances arise because the silicon occupies a range of environments in the structure. In figure 4.2.13, ^{29}Si NMR spectra of MCM-41 type materials functionalised *in situ* and post-synthesis are compared. The elemental carbon content found in these two samples was similar. Both spectra show two clear signals at -110 and -101 ppm corresponding to Q_4 and Q_3 silica units. The ratios Q_4/Q_3 found by deconvolution of the signals were 1.6 and 1.4 for the solids functionalised post-synthesis and *in situ* respectively. These values indicate similar degree of condensation for pure inorganic and *in situ* phenyl-functionalised frameworks. The spectra also show signals between -50 and -90 ppm corresponding to three types of Si bond bonded to carbon.

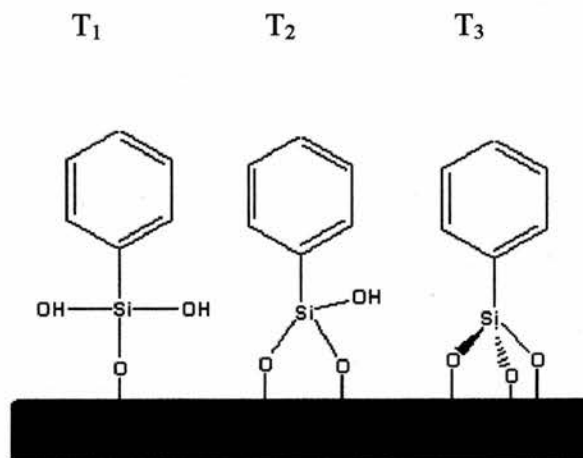


Figure 4.2.12. Representation of the three types of Si environments associated with the T type signals.

These signals, T₁, T₂ and T₃, correspond to $\text{C}_6\text{H}_5\text{-Si}$ units respectively bonded to one, two or three SiO entities (Figure 4.2.12). It can be seen that the sample functionalised *in situ* exhibits a larger proportion of T₃ signal than the sample functionalised post-synthesis, which shows a predominant resonances at T₂ and T₁ frequencies. It can be concluded from these experiments that *in situ* functionalisation produces a more condensed framework around the functional group.

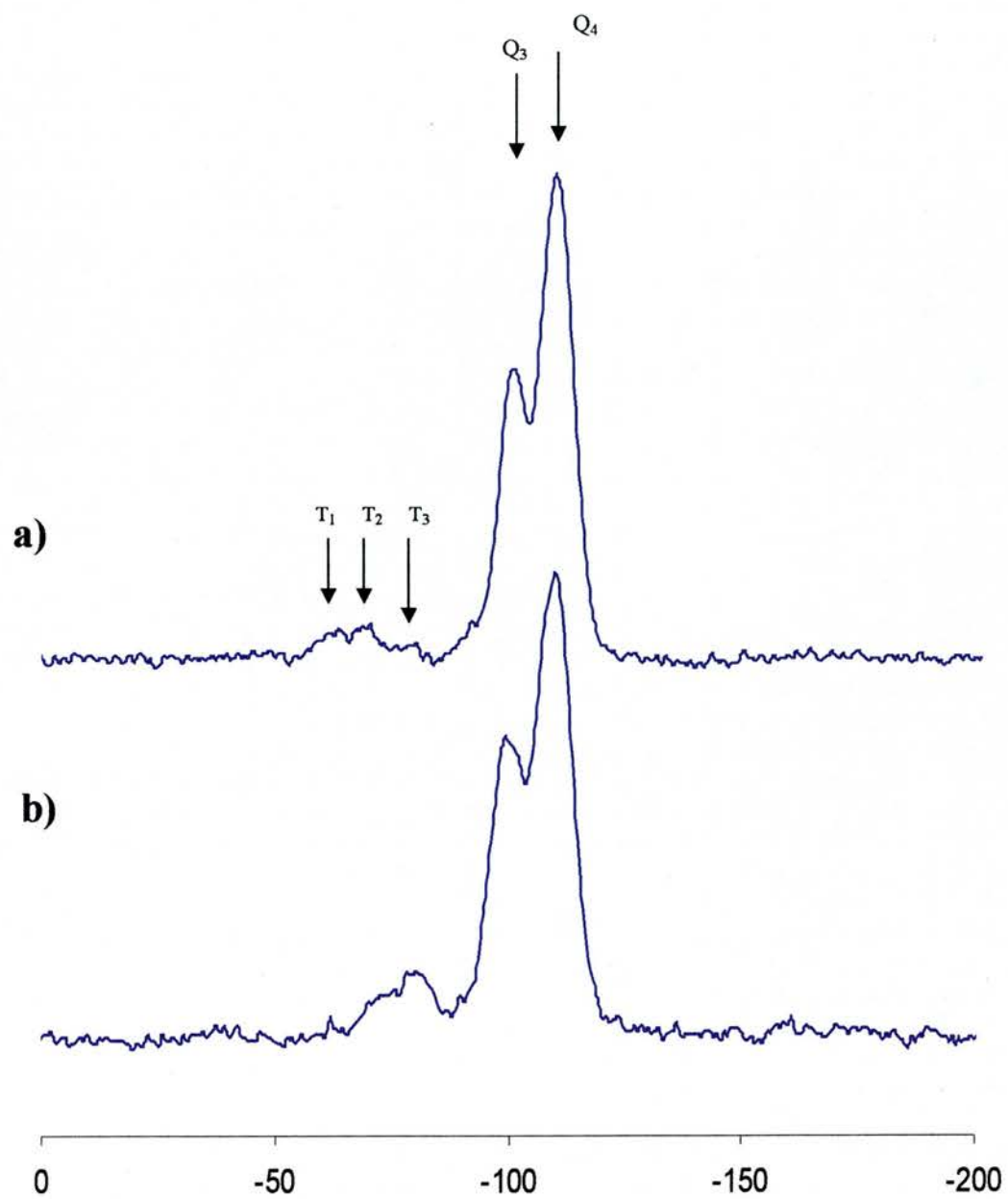


Figure 4.2.13. ^{29}Si NMR experiments of phenyl-functionalised MCM-41 a) post-synthesis and b) *in situ*.

4.2.4. Nitrogen adsorption

Phenyl-functionalised MCM-41 solids were characterised by means of N_2 adsorption at 77 K and compared with pure silicate MCM-41 (Figure 4.2.14). All the isotherms are type IV, with well defined capillary condensation steps, except the isotherm of the 20% phenyl-functionalised solid which is type I. (The XRD pattern presents no (110) or (200) reflections and probably this solid is not well ordered). With the increase of the degree of functionalisation the pore volume decreases and the P/P_0 value at which capillary condensation takes place is shifted to lower pressures as is expected from the presence of phenyl moieties in the channels. This agrees with a decrease in pore size due to the presence of aromatic groups within the pores.

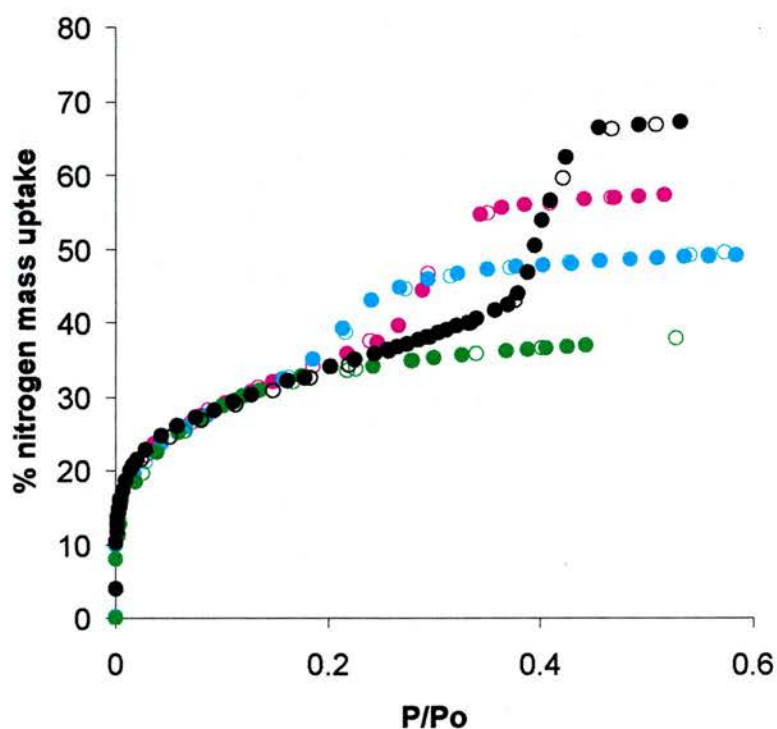


Figure 4.2.14. Nitrogen adsorption isotherms at 77 K of silicate MCM-41 (back symbols) and 5, 10 and 20 % in situ phenyl-functionalised (pink, blue and green, respectively). Solid and open symbols correspond to adsorption and desorption. All the solids were extracted to remove the surfactant.

As a result of the *in situ* phenyl functionalisation some of the phenyl groups could in principle be “trapped” between the inorganic silica walls and might not be accessible to adsorbed molecules. If an important amount of these “trapped” groups are present in the solid, the removal of the organic groups by high temperature calcination should create microporosity detectable by nitrogen adsorption. Figure 4.2.15 compares the N_2 isotherms at 77 K of MCM-41 pure silica, 10% phenyl and 20% phenyl functionalised before and after the calcination of these materials at 550 °C under O_2 .

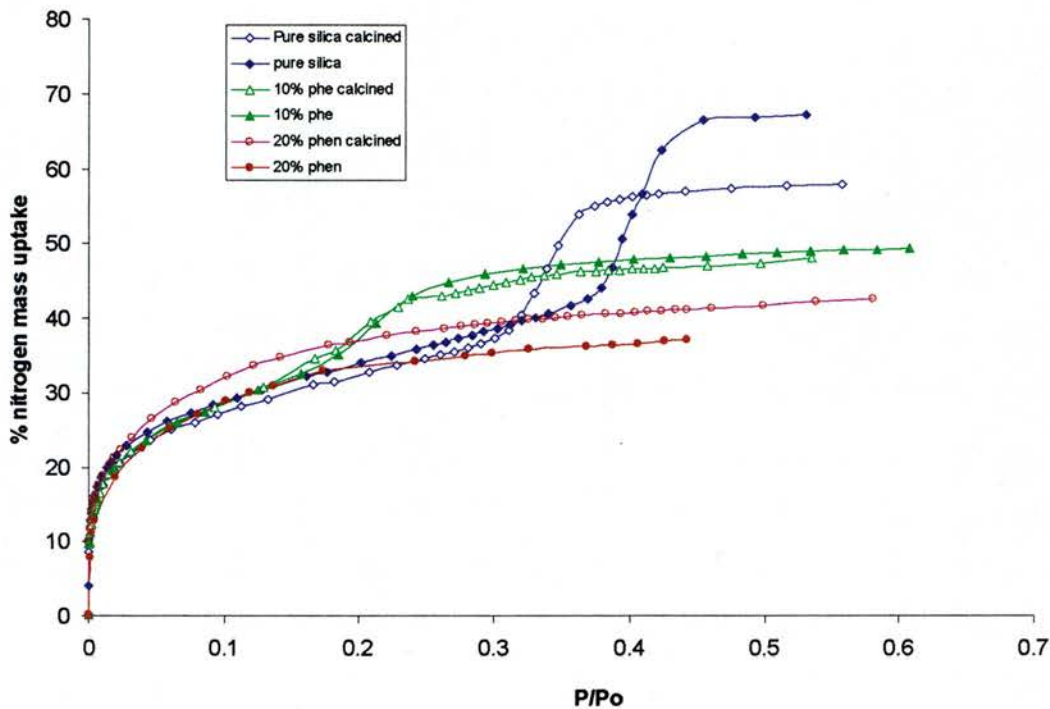


Figure 4.2.15. Nitrogen adsorption isotherms of solvent-extracted MCM-41 solids before and after calcination at 550 °C. Blue, green and red correspond to pure silica, 10% and 20% phenyl functionalised. Solid and open symbols correspond to solids solvent-extracted and solids solvent-extracted calcined at 550 °C.

The calcination process affects the pore volume of the pure siliceous sample which is reduced by 10 %. This is related to the 5% unit cell contraction induced by the thermal treatment (see table 4.2.1 -XRD analysis, or table 4.2.4.). Note as well the shift to lower pressures of the capillary condensation. On the other hand, the sample 10% phenyl-functionalised sample does not seem to change its apparent pore size and pore volume

during the calcination despite the 7 % unit cell contraction detected by XRD. The pore volume exhibited by the 20 % phenyl functionalised sample increases by 12 % upon calcination and the BET surface area is also higher (see table 4.2.4) despite of the 11 % unit cell contraction.

This behaviour can only be compatible with the presence of phenyl groups in the pores rather than in the walls. Calcination is expected to produce two effects: unit cell contraction, which decreases the pore volume, and removal of organic groups which increases the pore volume. The changes in nitrogen adsorption are due to a combination of these two factors. Note that there are not changes in the low pressure region of the adsorption experiments indicating that there were not important amounts of phenyl moieties “trapped” within the walls of the solids that, upon removal, would be expected to leave microporosity.

The N_2 isotherm of the phenyl MCM-41 functionalised post-synthesis is shown in the Figure 4.2.16. with the isotherm of the MCM-41 starting material. The pore volume reduction and the decrease to lower pressures of the capillary condensation are also compatible with the presence of phenyl groups within the pores.

(The carbon content found in post-synthesis and in the *in situ* functionalised solids are comparable).

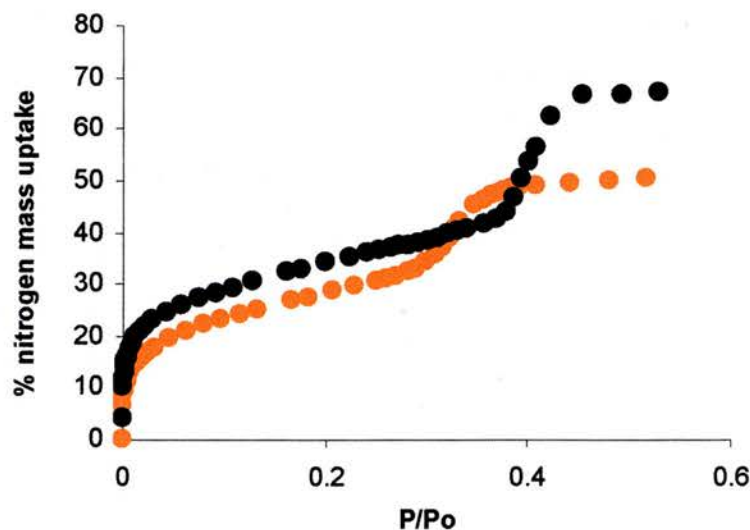


Figure 4.2.16. Nitrogen isotherms of extracted MCM-41 (black) and post-synthesis phenyl-functionalised MCM-41 (orange).

The following table summarises the % nitrogen uptake and BET surface areas found for the phenyl-MCM-41 solids. Note that the BET surface areas of the solids increases after phenyl-functionalisation. This suggests a larger surface heterogeneity and increased surface roughness due to the presence of the bulky organic groups.

MCM-41 type solid.	Unit cell a parameter (Å)	BET surface area (m ² /g)	% wt of N ₂ adsorption capacity. (at P/P ₀ 0.5)	P/P ₀ capillary condensation step
Silicate solvent-extracted	47.1	944	66.8	0.40
5 % phenyl in situ	45.9	1024	57.2	0.30
10% phenyl in situ	42.6	1250	48.7	0.21
20% phenyl in situ	37.4	1014	36.5	----
Calcined.	44.2	966	59.8	0.33
Silicate solvent extracted, calcined.	44.1	924	57.0	0.33
10 % phenyl in situ, calcined.	39.7	1180	47.3	----
20 % phenyl in situ, calcined.	33.3	1065	41.7	----
Phenyl functionalised post-synthesis.	47.0	841	50.0	0.32

Table 4.2.4. Summary of nitrogen adsorption results in phenyl-MCM-41 solids. Unit cell parameters derived from XRD are also included.

N₂ adsorption on a sample of Ph-HMM is compared with MCM-41 samples in Figure 4.2.17. The BET surface area of the solid, 881 m²/g, agrees with reported values [13].

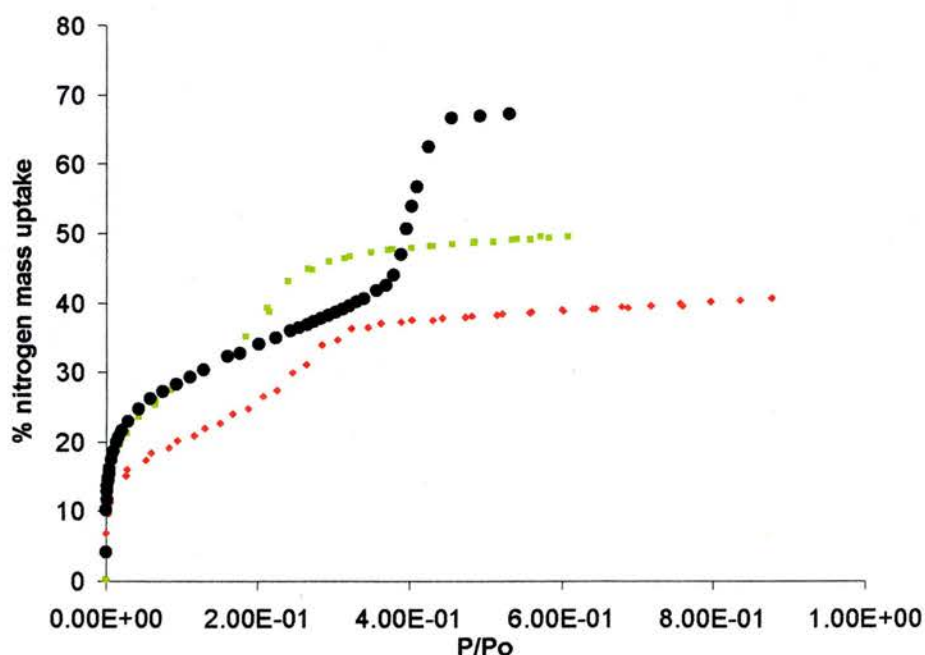


Figure 4.2.17. Nitrogen adsorption experiments in MCM-41 extracted (black), 10 % phenyl-MCM-41 (green) and Ph-HMM (red).

Nitrogen adsorption in phenyl SBA-1 type of solids.

Figure 4.2.18 presents nitrogen adsorption experiments performed on SBA-1 materials. The % nitrogen mass uptake was 52 wt %, 59 wt % and 40 wt % for calcined pure silica SBA-1, extracted SBA-1 and 10% extracted phenyl-functionalised SBA-1, respectively. The difference between the adsorption capacity of calcined and extracted pure silicate SBA-1 can be explained due to the smaller unit cell of the calcined material. 10% phenyl-functionalised SBA-1 adsorbs 27% less nitrogen than the calcined pure silica material due to the presence of bulky phenyl groups in the pores. The 26% phenyl-functionalised solid exhibits a total nitrogen uptake of 18 wt % and no signs of mesoporosity. This low adsorption capacity suggests that probably some of the phenyl groups block the accessibility of nitrogen to some parts of the solid.

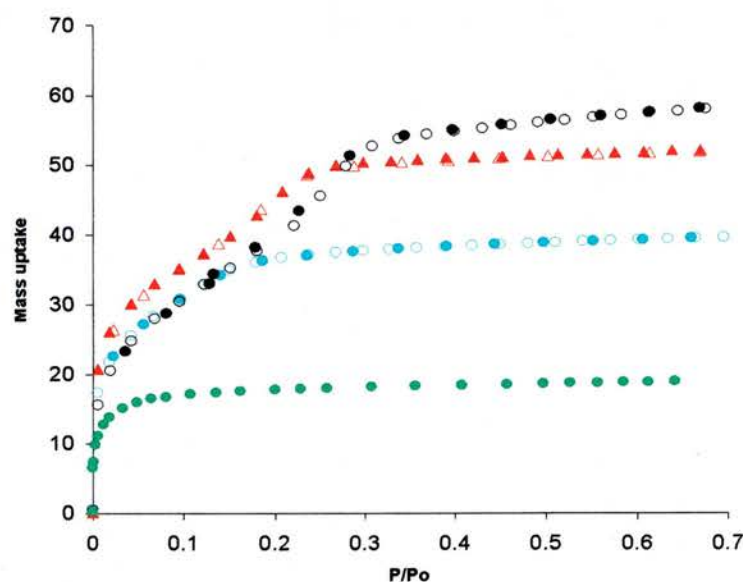


Figure 4.2.18. Nitrogen adsorption isotherms at 77K of extracted and calcined pure silica SBA-1, 10% and 26 % functionalised SBA-1 materials.

	Calcined	Pure silica extracted	10% phenyl	26% phenyl
BET m ² /g	1325±24	1456±41	1030±25	505±7
%wt N ₂ uptake	52	59	40	18

Table 4.2.5. BET surface area and wt % of nitrogen mass uptake of extracted and calcined pure silica SBA-1 and 10% and 26% phenyl-functionalised SBA-1.

Figure 4.2.19 presents N_2 adsorption experiments performed on SBA-2 type materials. The porosity of the phenyl-functionalised SBA-2 type solids follows the same trend as MCM-41 and SBA-1 i.e. the adsorption capacity decreases with the increase in functionalisation due to the volume occupied by the phenyl groups. Also the capillary condensation progressively shifts to lower pressures.

The N_2 % mass uptakes for SBA-2 materials are summarised in Table 4.2.6. The decrease in the adsorption capacity of the extracted pure silica material compared with the calcined form could be related to the presence of traces of surfactant in the extracted solid. The solid retains a relative high adsorption capacity even after 20 % phenyl-functionalisation. This points to the absence of phenyl groups at the micropore windows where they would cause reduction of porosity.

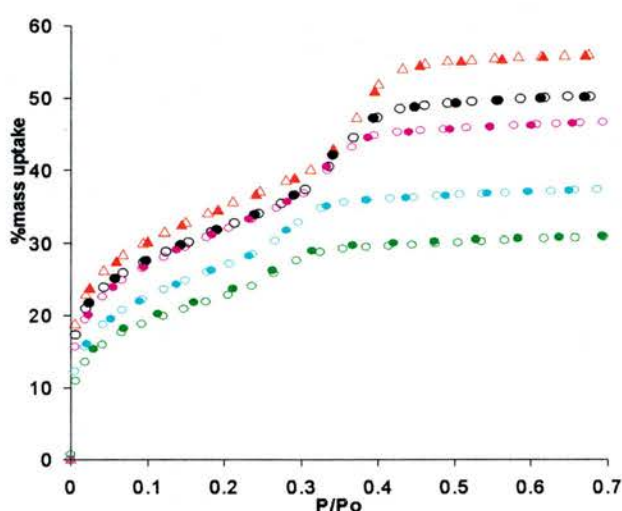


Figure 4.2.19. N_2 adsorption experiments in phenyl-SBA-2 solids. Calcined (red), extracted siliceous (black), 5 % phenyl (pink), 10% phenyl (blue) and 20% phenyl (green) SBA-2.

	Calcined	Pure silica extracted	5% phenyl	10% phenyl	20% phenyl
BET m^2/g	1039±10	1007±4	967±15	817±4	672±12
% wt N_2 uptake	57	51	56	35	30

Table 4.2 6. N_2 adsorption data for phenyl-functionalised SBA-2 solids.

4.2.5 Adsorption of light hydrocarbons and CO₂ in phenyl-functionalised MCM-41.

In this section the adsorption properties of phenyl-functionalised mesoporous solids have been characterised by means of ethane, CO₂ and isobutane adsorption experiments. The high pressure adsorption experiments presented in this section were collected by the author of this thesis in collaboration with Christian Schumacher and Manuel Pérez Mendoza (Edinburgh University). The method used to perform these experiments was explained in chapter 2. The high pressure adsorption experiments of the extracted and 10% phenyl-functionalised (*in situ*) MCM-41 were measured using compacted particles because modification that allows the study of fine powders (the “cigarette” of chapter 2) was not developed at the time of the experiments.

Effect of phenyl-functionalisation on CO₂ adsorption in MCM-41

High pressure CO₂ adsorption isotherms were collected at 263 K for calcined MCM-41, extracted MCM-41 and 10 % phenyl-functionalised MCM-41 samples prepared by both *in situ* and post-synthesis approaches. The low pressure region, in which the interactions of the gas molecules with the walls are dominant, has been expanded in Figure 4.2.21. This figure also shows low pressure adsorption experiments performed on the IGA apparatus (St. Andrews) at 268 K for comparison.

CO₂ isotherms at 263.15K on MCM-41 and phenyl-MCM-41

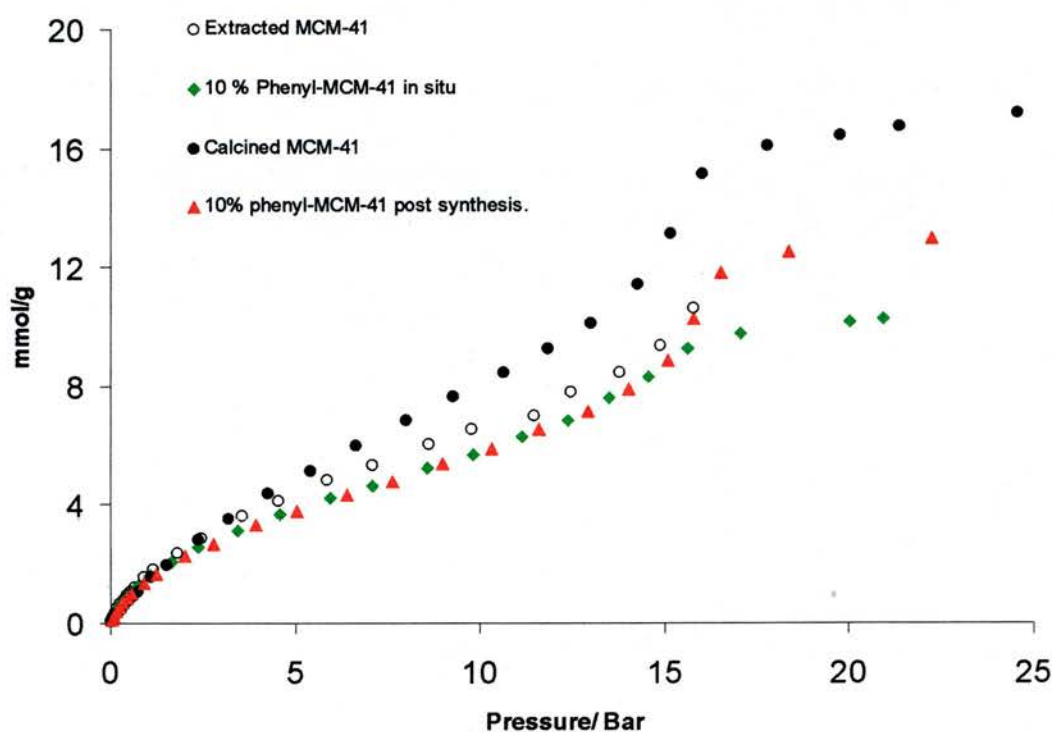
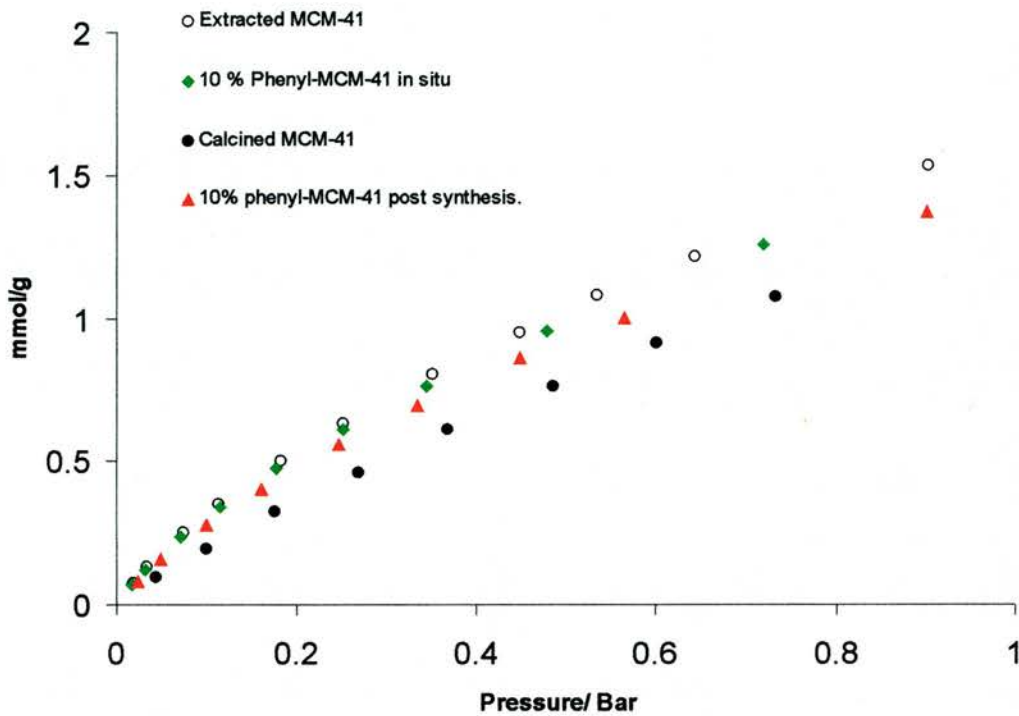


Figure 4.2.20. High pressure CO₂ isotherm at 263 K on MCM-41 materials.

(Edinburgh)

CO₂ isotherms at 263.15K on MCM-41 and phenyl-MCM-41

a)



(St. Andrews).

b)

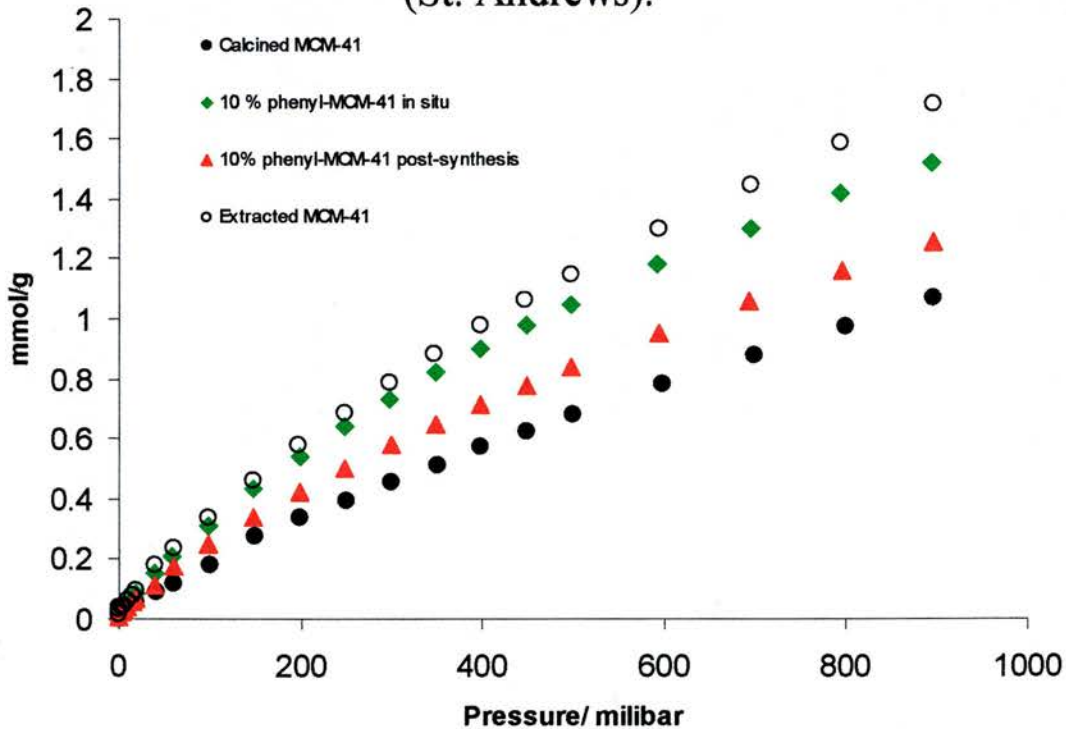


Figure 4.2.21. Low pressure adsorption isotherms of CO₂ in MCM-41 type materials. a) corresponds to the low pressure region of the high pressure isotherms at 263 K presented in Figure 4.2.20. b) are low pressure isotherms performed at 268 K on the IGA system (St. Andrews) on the same solids.

A close comparison between of the low pressure region of the experiments performed on the high pressure adsorption rig and in the IGA system suggests that, although the agreement of both set of experiments is good, some reduction in porosity occurred during pelletising the sample and the real adsorption capacity of the 10% phenyl-functionalised solid and extracted pure silica should be slightly larger.

Henry constants values can be estimated from the isotherms in Figure 4.2.21 b). The values found were (in $\text{mol kg}^{-1} \text{mbar}^{-1} * 10^3$): 1.8 for calcined solid, 2.3 for phenyl functionalised post-synthesis, 2.9 for 10% phenyl functionalised in situ and 3.2 for pure silica solvent-extracted solid.

The differences in adsorption at low pressures are relatively small, but the order of the adsorption strength is the same between the two sets of experiments. In each case the extracted sample has highest affinity and the calcined the lowest. This is expected to be because the surface of the extracted material has a higher density of hydroxyl groups, whereas calcination removes these from the surface by dehydroxylation. The phenyl-functionalised solids have intermediate affinities, probably because part of the effect of the surface hydroxyls is removed by partially covering by phenyl groups.

In the high pressure region, a step in adsorption is observed between 13~17 bars. This is due to a rapid pore filling of the pores with CO_2 . Note that the pore filling of the calcined sample occurs at lower pressures than the other solids due to its smaller pore size. In the solid functionalised at 10% in situ, this pore filling step is not clearly observed.

In Figure 4.2.22., high pressure ethane isotherms at 263 K performed on several materials are presented: calcined and extracted MCM-41, *in situ* 10 % phenyl-functionalised MCM-41 and post-synthesis phenyl-functionalised MCM-41. The low pressure region, in which the interaction of the gas molecules with the walls are dominant, has been expanded in Figure 4.2.23.

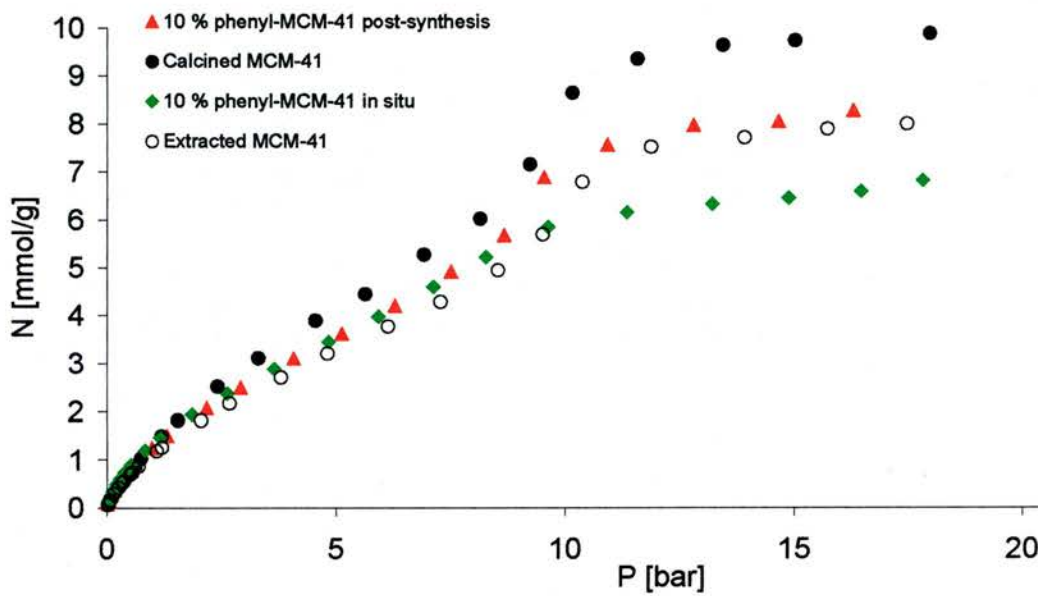


Figure 4.2.22. High pressure ethane adsorption isotherms performed on MCM-41 type of solids at 263 K.

It was mentioned before that the porosity of the solids MCM-41 pure silica extracted and 10% functionalised *in situ* was affected during the compacting of the solids. Looking to the uptake of ethane at high pressure, it seems that this effect is more marked for ethane. Note that the adsorption of ethane by the extracted pure silica MCM-41 is rather low.

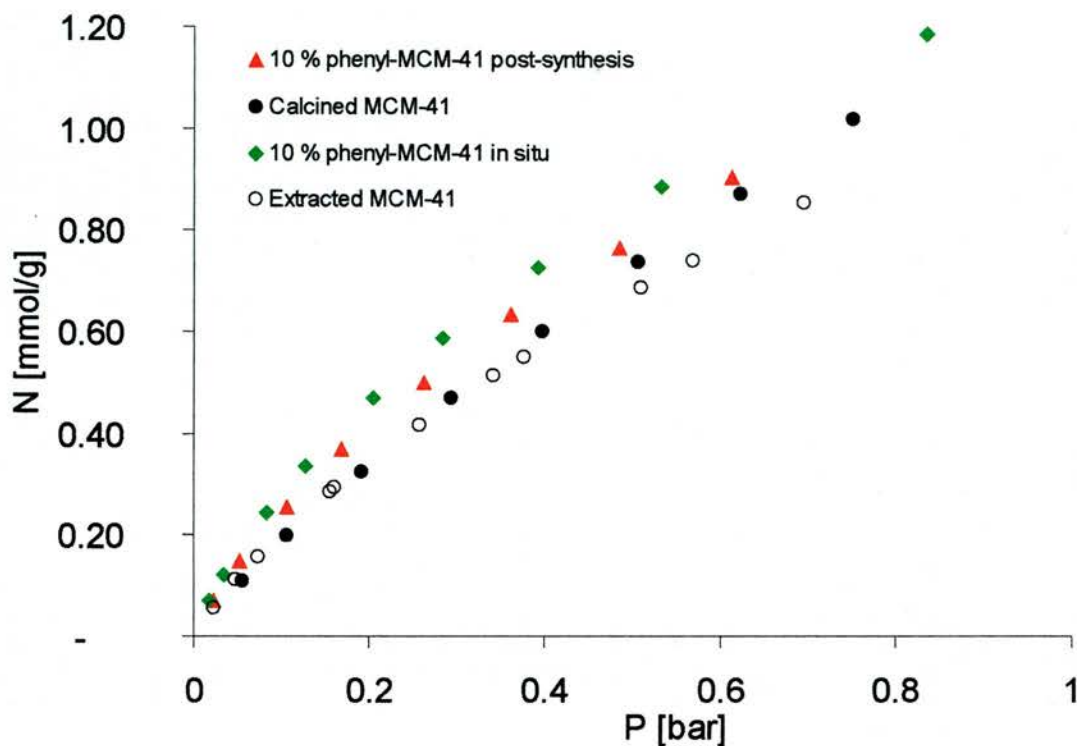


Figure 4.2.23. Low pressure region of the adsorption experiments presented in Figure 4.2.22.

It can be seen as well that the uptake of ethane by the solid 10% phenyl-functionalised (*in situ*) is higher than the uptake of the non-functionalised solids. Despite the problems arising due to the experimental difficulties on performing these experiments with compacted solids, it appears that the phenyl-functionalisation enhances the affinity of MCM-41 for ethane and, on the other hand, decreases the adsorption of CO₂. Therefore, this aromatic functionalisation would increase the selectivity for small organic non-polar gas molecules respect to polar ones like CO₂, although this effect is expected to be small.

Finally, the effect of phenyl-functionalisation upon the adsorption of isobutane was studied. Figure 4.2.24 presents isobutane adsorption experiments at 263 K performed on 10 % phenyl-functionalised, calcined MCM-41 and on the Ph-HMM sample.

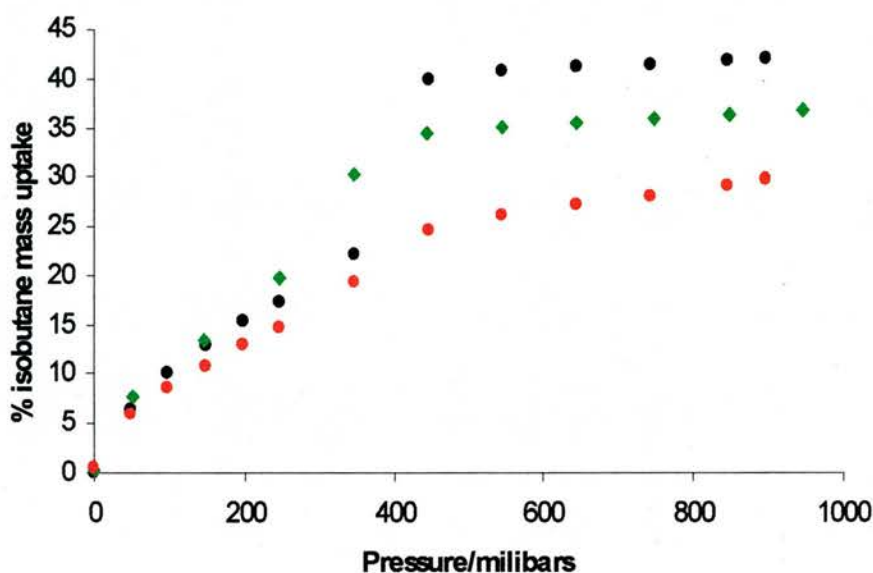


Figure 4.2.24. Isobutane adsorption experiments at 263 K on 10% phenyl functionalised MCM-41 *in situ* (green), calcined-MCM-41 (black) and Ph-HMM solid (red).

In the low pressure region, the adsorption isotherm of the sample calcined and 10 % phenyl-functionalised *in situ* are almost equal. According to this, the phenyl functionalisation exerts little effect upon the adsorption of isobutane. The different behaviour observed for ethane and isobutane suggests that the smaller ethane could find slightly stronger adsorption sites between the aromatic phenyl rings of the wall, whereas the larger isobutane cannot gain to these sites, and therefore interacts similarly with the phenyl-modified and the silicate solids.

4.2.6. Adsorption of aromatic molecules in phenyl-functionalised MCM-41 mesoporous solids

The aromatic modification of the pore surface is expected to enhance the interaction of aromatic molecules, like toluene or benzene, with these silicate frameworks. In order to quantify this effect, the solids have been studied by measurement of toluene isotherms at different temperatures which allows the determination of thermodynamic functions such as the heats of adsorption.

The adsorption apparatus, based on a gravimetric method, recorded the amount toluene adsorbed, in grams, at an equilibrium gas pressure. The dependence of the toluene mass uptake as a function of the experimental pressure was described for each individual isotherm using multiple polynomial equations. From these equations the equilibrium pressure was expressed as a function of the temperature at constant adsorbate uptake. Obtaining such relationships at different uptakes allows for a full description of sorption equilibria for a gas-sorbent system. According to fundamentals of physical sorption, sorption isosteres are assumed to be straight lines at a constant adsorbate concentration, (n), according to the *Clausius-Clayperon* equation, $\ln p$ vs. $1/T$. The slopes of isosteres allow the calculation of the concentration dependence of the isosteric molar sorption enthalpy, $-\Delta H(n)$.

Toluene adsorption isotherms at different temperatures and isosteres at several sorbate concentrations are presented in the next figures. In all the figures, dots represent experimental values and lines denote the mathematical equations used to describe the experimental points that have been used for the calculation of the different thermodynamic functions.

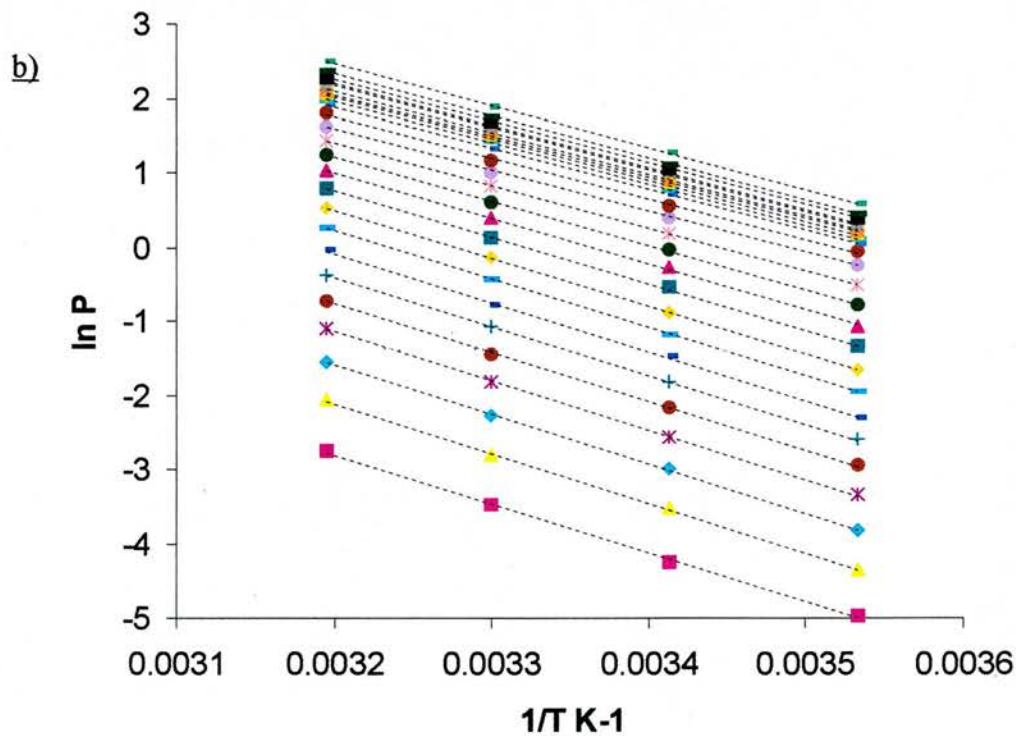
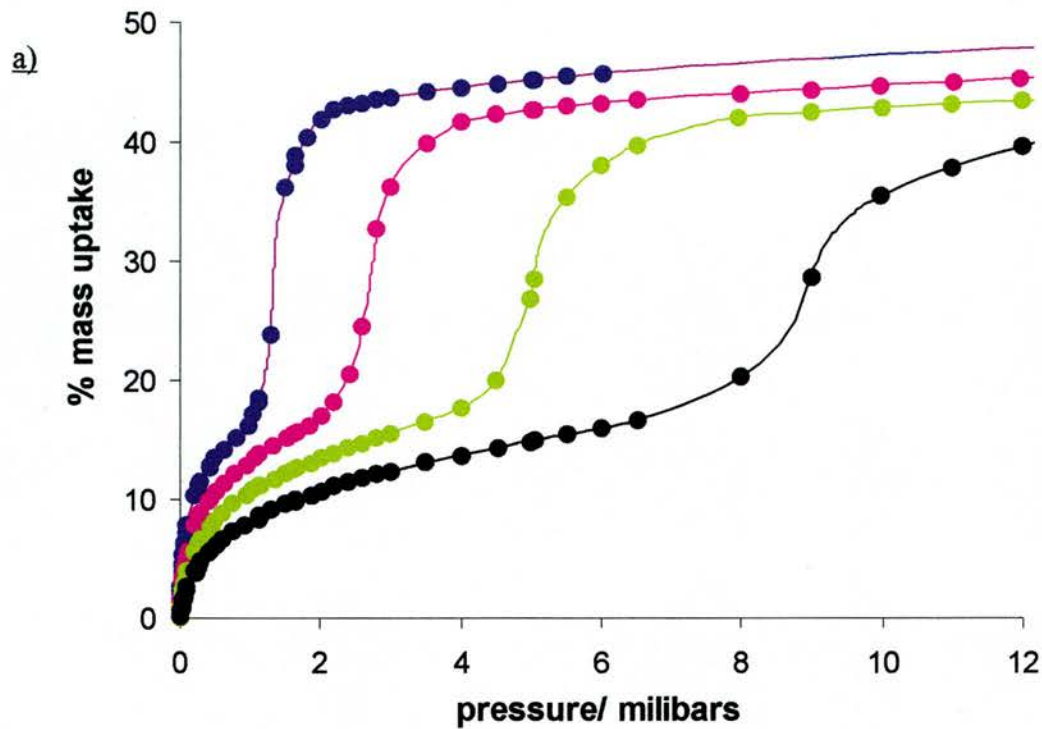


Figure 4.2.25. a) Toluene adsorption isotherms at different temperatures in 10% phenyl-functionalised MCM-41 *in situ*. Blue, pink, green and black correspond to experiments performed at 283, 293, 303 and 313 K respectively. Dots are experimental points and lines are the polynomial fits required to plot the isosteres presented in b). Isosteres were calculated between 0.5 and 40 wt % of toluene.

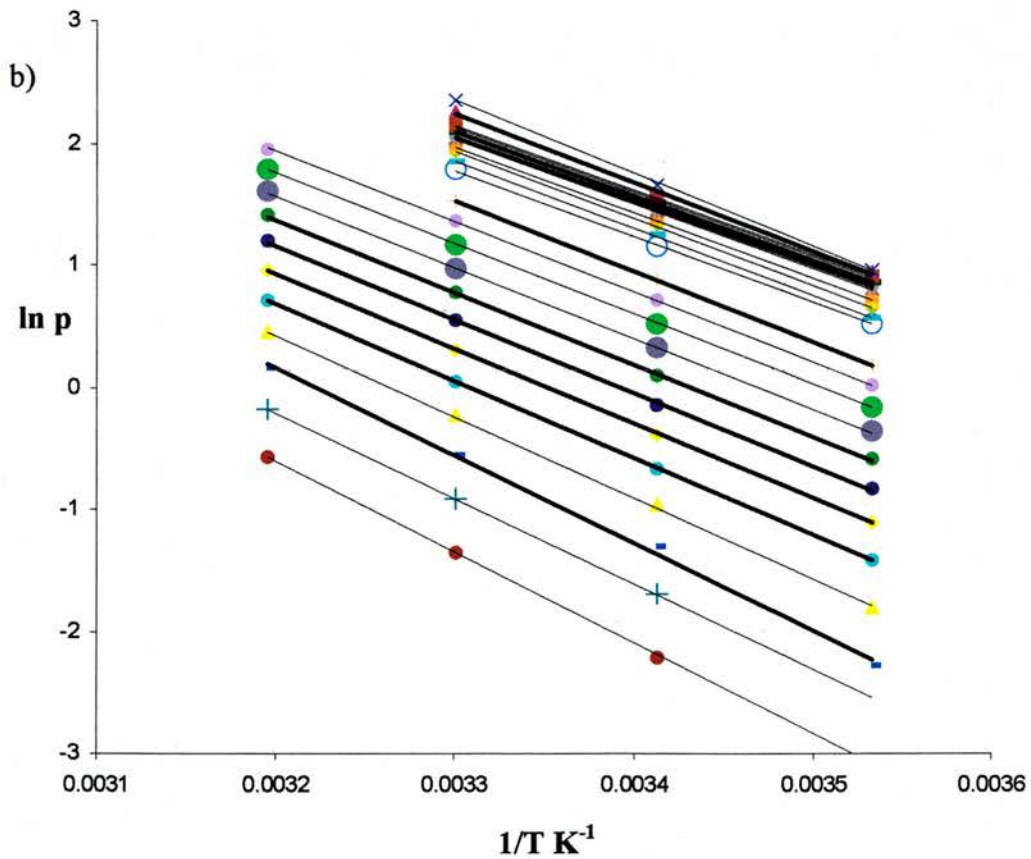
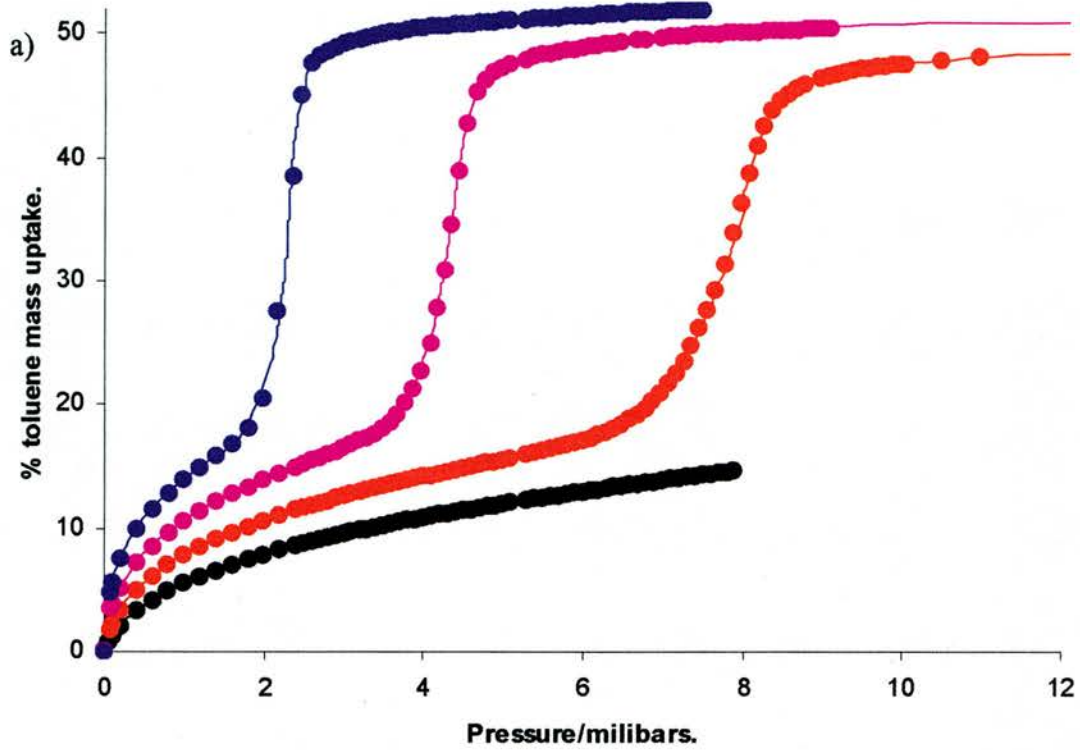


Figure 4.26. a) Toluene adsorption isotherms at different temperatures in phenyl-functionalised MCM-41 post-synthesis. Blue, pink, green and black correspond to experiments performed at 283, 293, 303 and 313 K respectively. Dots are experimental points and lines are the polynomial fits required to plot the isosteres presented in b). Isotheres were calculated between 0.5 and 40 wt % of toluene.

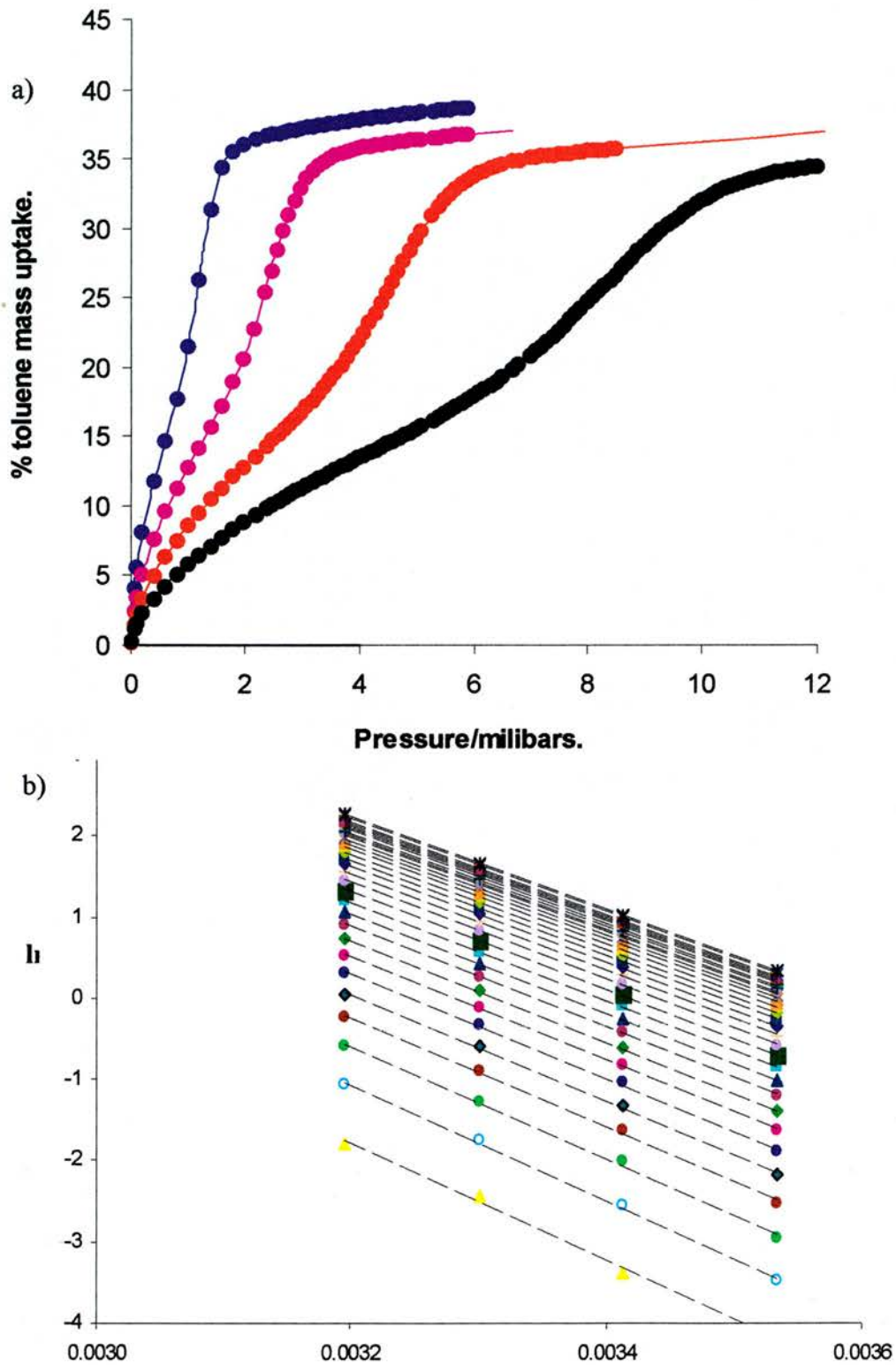


Figure 4.2.27. a) Toluene adsorption isotherms at different temperatures in Ph-HMM solid. Blue, pink, green and black correspond to experiments performed at 283, 293, 303 and 313 K respectively. Dots are experimental points and lines are the polynomial fits required to plot the isosteres presented in b). Isosteres were calculated between 0.5 and 35 wt % of toluene.

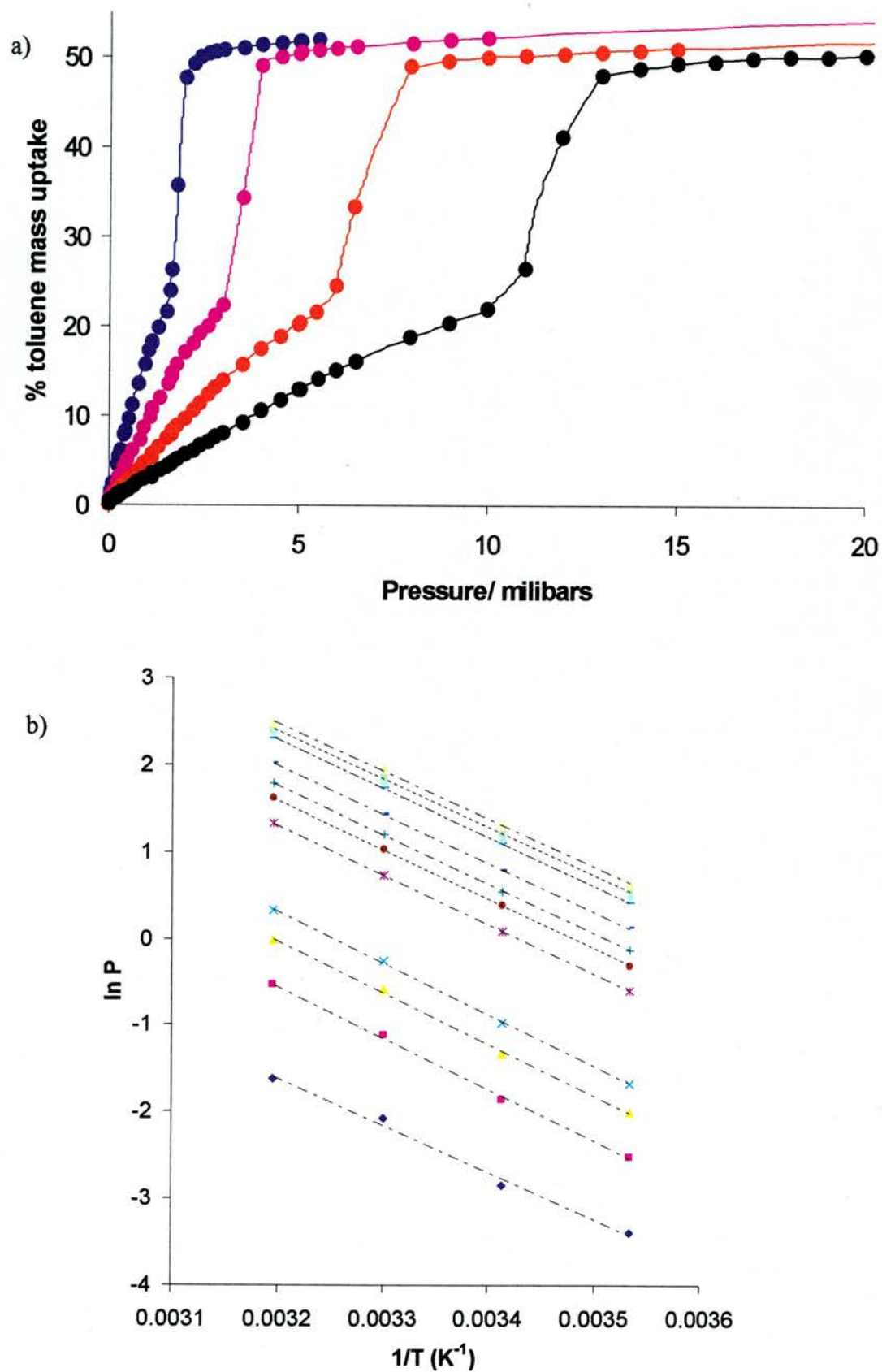


Figure 4.2.28. a) Toluene adsorption isotherms at different temperatures in calcined MCM-41. Blue, pink, green and black correspond to experiments performed at 283, 293, 303 and 313 K respectively. Dots are experimental points and lines are the polynomial fits required to plot the isotherms presented in b). Isotherms were calculated between 2 and 40 wt % of toluene.

In order to compare the strength of the interaction of toluene with the different phenyl functionalised solids, Henry Law constants have been estimated from the toluene adsorption experiments performed on the different solids at 293 K. Table 4.2.7 summarises the calculated values. Also has been calculated the isosteric heats of adsorption as a function of the toluene uptake for each sample. Figure 4.2.29 summarises the results of these calculations.

Solid	Henry constant (mol/Kg mbar ⁻¹)
MCM-41 calcined with no phenyl	2.1
MCM-41 10% phenyl (in situ)	17.2
Ph-HMM	4.5
MCM-41 phenyl post-synthesis	5.3

Table 4.2.7. Henry Law constants for toluene on phenyl-functionalised and calcined MCM-41.

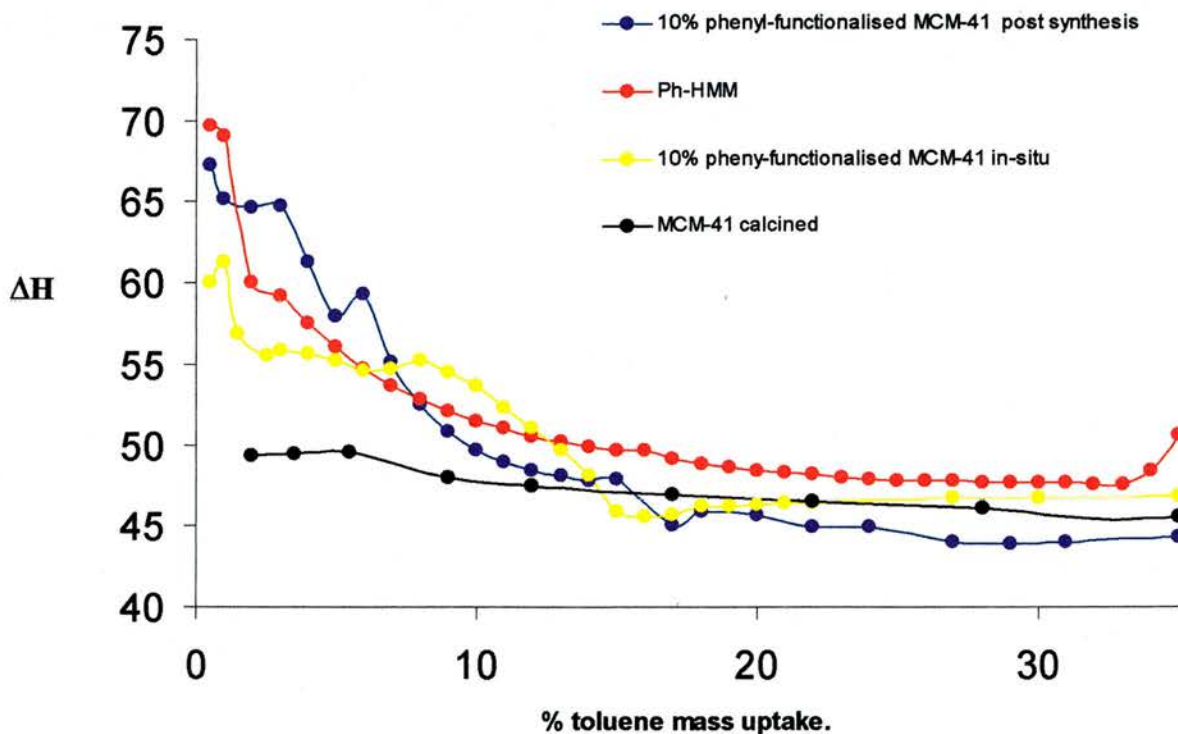


Figure 4.2.29. a) Comparative plot of toluene heats of adsorption in phenyl-functionalised solids (in situ and post synthesis), Ph-HMM solid and calcined MCM-41. The error of these measurements has been estimated as 2%.

The main conclusion from these experiments is that the heat of adsorption of toluene with phenyl-functionalised solids is higher than with the pure inorganic framework at low adsorbate concentration. At 5 % toluene uptake, this difference is from 5 to 10 kJmol^{-1} . Henry constant values presented in table 4.2.7 also point to higher interaction of toluene with the phenyl-functionalised MCM-41 type of solids. In addition, the heats of adsorption of the sample functionalised post-synthesis exhibit a plateau (at 5 % wt uptake) of almost constant value, $\sim 55 \text{ kJmol}^{-1}$, which is approximately 5 kJmol^{-1} larger than the heat of adsorption exhibited by the calcined MCM-41, suggesting that the phenyl-functionalisation provides multiple adsorption sites of similar energy. The heats of adsorption of the solid grafted with phenyl groups post-synthesis and the Ph-HMM solid are slightly higher at low pressures and decrease gradually with the increase of toluene concentration.

4.2.7. Characterisation of phenyl-functionalised SBA-1 and SBA-2 solids by gas and vapour adsorption

The experiments of 4.2.5 on phenyl-MCM-41 indicate that, although the phenyl functionalisation modifies the adsorption of ethane and CO₂, the effect was subtle. High pressure ethane and carbon dioxide experiments were therefore not performed on phenyl-functionalised SBA-1 and SBA-2, because these experiments are time-consuming and require large amounts of sample (~10 g.) Instead, the adsorption properties of functionalised SBA-1 and SBA-2 were investigated by low pressure adsorption of the hydrocarbons toluene, isobutane and butane, which appear to be controlled by the pore size rather than the surface modification.

The adsorption experiments presented in this section are:

Toluene adsorption at 283, 293, 303 and 303 K on *in situ* 10% phenyl-functionalised SBA-1, *in situ* 10% phenyl-functionalised SBA-2 and calcined SBA-1. (Heats of adsorption of toluene were calculated from these adsorption experiments).

Isobutane adsorption at 268 K on *in situ* 10% and 26 % phenyl-functionalised SBA-1 and extracted SBA-1. Also, isobutane adsorption at 268 K on *in situ* 10% and 20% phenyl-functionalised SBA-2 and extracted SBA-2.

Butane adsorption at 268 K on *in situ* 26% phenyl-functionalised SBA-1 and *in situ* 20% phenyl-functionalised SBA-2.

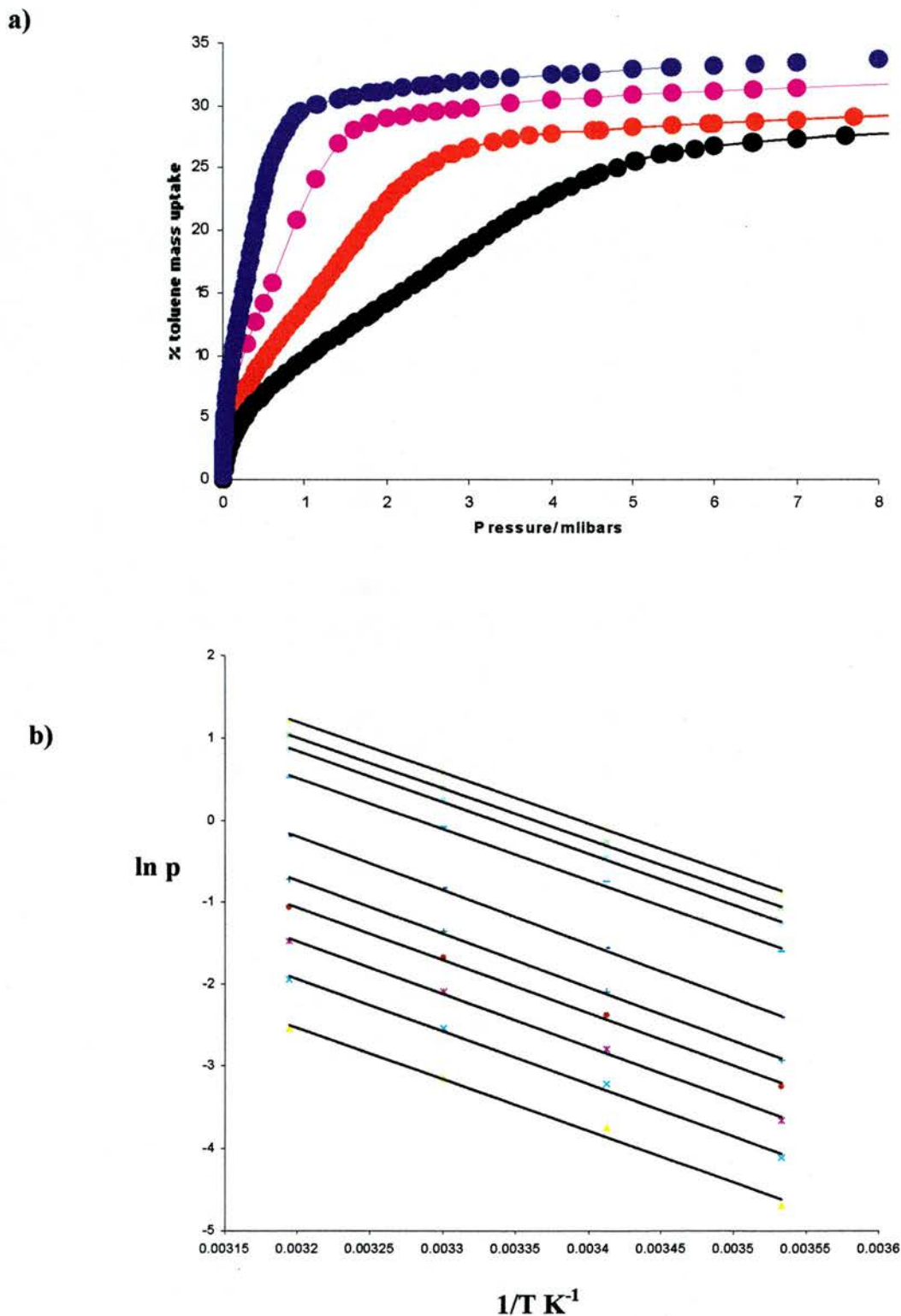


Figure 4.2.30. a) Toluene adsorption isotherms at different temperatures in 10% phenyl-functionalised SBA-1 in situ. Blue, pink, green and black correspond to experiments performed at 283, 293, 303 and 313 K respectively. Dots are experimental points and lines are the polynomial fits required to plot the isotheres presented in b). Isotheres were calculated between 2 and 40 wt % of toluene.

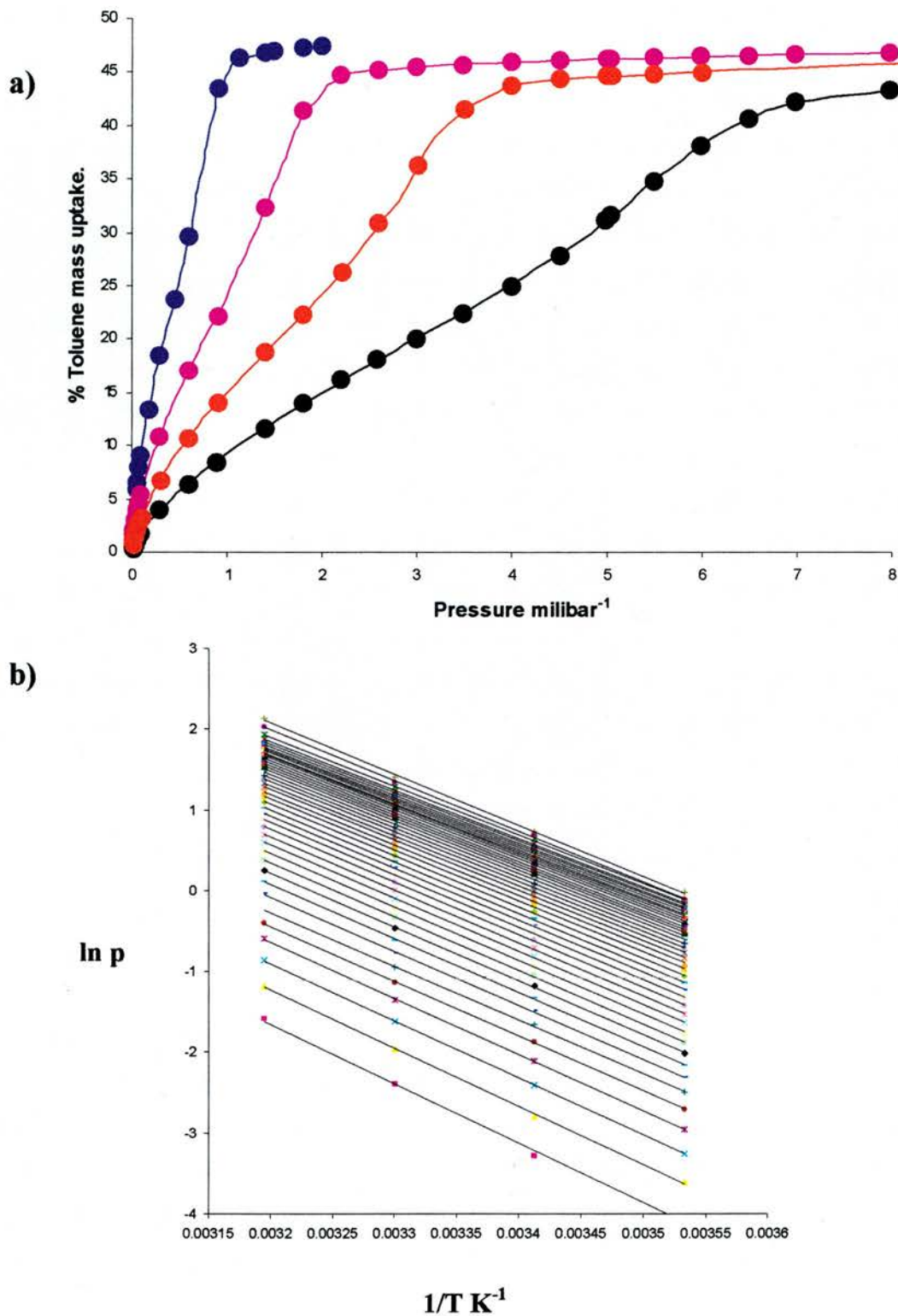


Figure 4.2.31. a) Toluene adsorption isotherms at different temperatures in calcined SBA-1 type of solid. Blue, pink, green and black correspond to experiments performed at 283, 293, 303 and 313 K respectively. Dots are experimental points and lines are the polynomial fits required to plot the isosteres presented in b). Isosteres were calculated between 2 and 40 wt % of toluene.

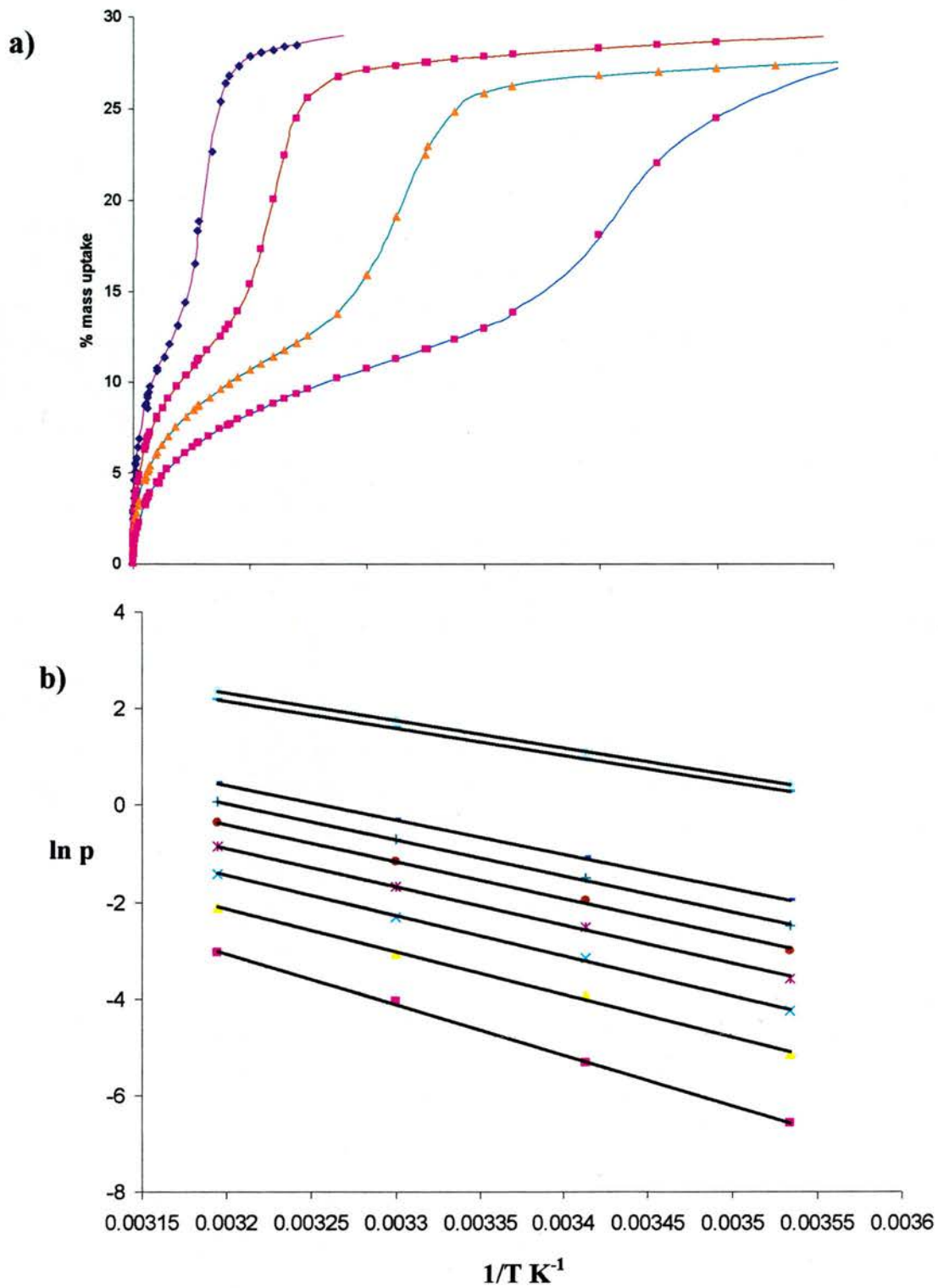


Figure 4.2.32. Toluene adsorption isotherms at different temperatures in 10 % phenyl functionalised SBA-2. Blue, pink, green and black correspond to experiments performed at 283, 293, 303 and 313 K respectively. Dots are experimental points and lines are the polynomial fits required to plot the isosteres presented in b). Isosteres were calculated between 2 and 40 wt % of toluene.

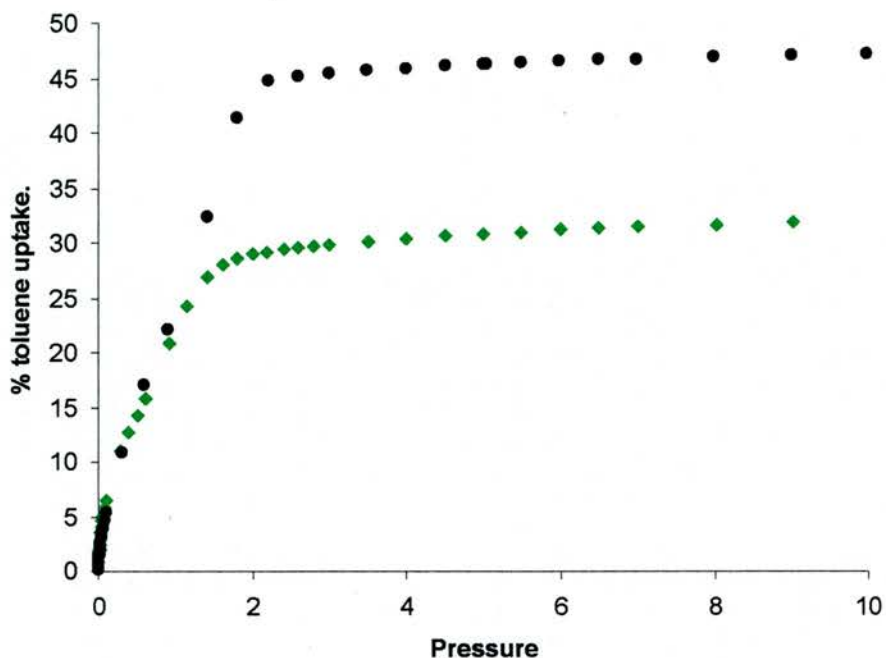


Figure 4.2.33. Toluene adsorption isotherms in silicate SBA-1 and 10% phenyl-functionalised SBA-1 *in situ* (black and green symbols).

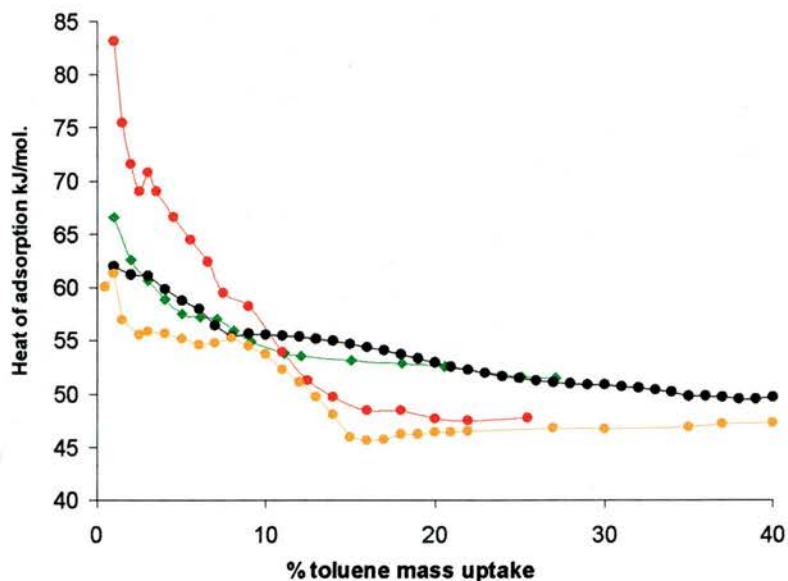


Figure 4.2.34. Toluene heats of adsorption in SBA-1 calcined (black), 10% phenyl-functionalised SBA-1 (green), 10% phenyl-functionalised SBA-2 (red) and 10% phenyl-functionalised MCM-41 *in situ* (orange). The estimated error of this measurements is ~2 %.

Toluene

Figure 4.2.33. presents toluene adsorption experiments performed at 293 K on silicate SBA-1 and 10 % phenyl functionalised SBA-1. All these solids were synthesised according to ref [9]. Low pressure adsorption indicates that the *in situ* phenyl-functionalised solid exhibits similar affinity for toluene to the calcined solid.

Figure 4.2.34 shows the heats of adsorption of toluene in calcined SBA-1, 10% phenyl-functionalised SBA-1, 10% phenyl-functionalised SBA-2 and 10% phenyl-functionalised MCM-41. Toluene isotherms used for the estimation of these thermodynamic values, using similar procedures as for MCM-41 type materials, are presented in Figures 4.2.30, 4.2.31 and 4.2.32.

At low toluene uptakes, the heats of adsorption on the 10 % phenyl-functionalised SBA-2 solid are higher than in the other solids. On the other hand, at high toluene uptake, the heats of adsorption are higher in the 10% phenyl-functionalised SBA-1 and calcined SBA-1. It is also observed that the heat of adsorption of toluene on the 10% phenyl-functionalised SBA-1 and on the calcined SBA-1 are similar for the whole uptake range.

The 10% phenyl-functionalised SBA-2 is thought to exhibit higher heats of adsorption at low pressures because its pore network possesses micropores (windows between the supercages) that act as high energy adsorption sites.

At high toluene uptake, the heat of adsorption in the SBA-1 solids is higher than in the 10 % phenyl-MCM-41 *in situ* and 10 % phenyl-SBA-2 due to the smaller average cage size of SBA-1. In this type of solid, the interaction of toluene is expected to be stronger than in MCM-41 which possesses cylindrical pores of larger diameters. Note that the heat of adsorption of toluene in SBA-1 at high toluene uptakes, ~ 55 kJ/mol, is the same as in the 10% phenyl-functionalised MCM-41 at low pressures. It seems that, in SBA-1, the effect exerted by the phenyl-functionalisation on the toluene heats of adsorption is much smaller than the effect of the pore structure.

Isobutane

The next figure presents isobutane adsorption experiments in phenyl-SBA-1 solids. As observed for MCM-41, no influence of the phenyl upon the adsorption of isobutane is observed. Increasing functionalisation decreases the adsorption capacity of the solids. Note also that the solid 20% functionalised does not seem to have any molecular sieve properties for butane and isobutane as their adsorption capacity are almost the same: the window size must be greater than the kinetic diameter of isobutane (5.6 Å).

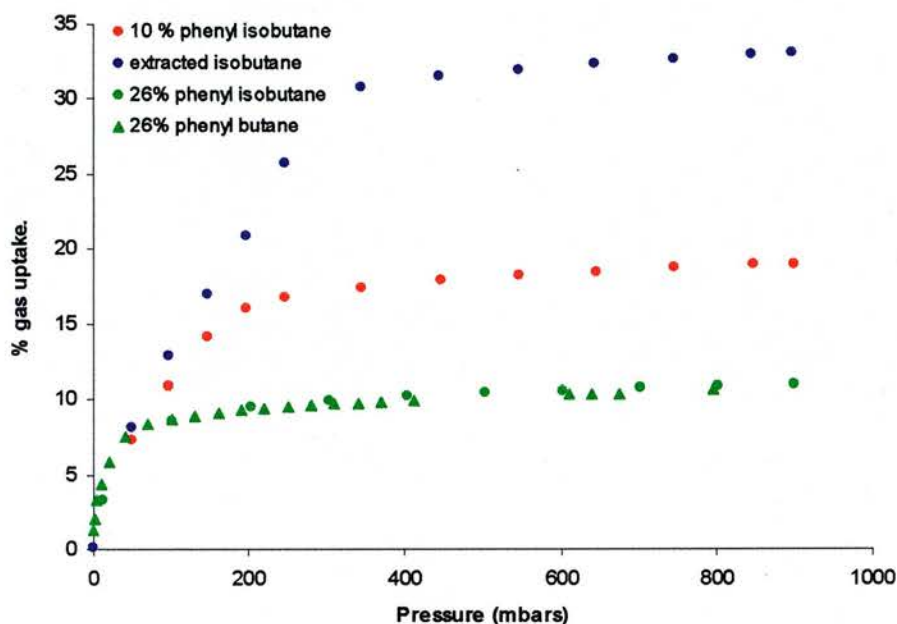


Figure 4.2.33. Isobutane adsorption experiments (round symbols) at in SBA-1 calcined (blue), 10% phenyl-functionalised SBA-1 (red), 20% phenyl functionalised SBA-1 (green). Also included butane adsorption experiment in 20% phenyl-functionalised for comparison, triangular green symbols

The same result is seen when isobutane is adsorbed in phenyl-SBA-2 solids. (See figure below) The adsorption capacity decreases and there are no signs of stronger affinity for the gas at low pressures when phenyl is incorporated in the solids.

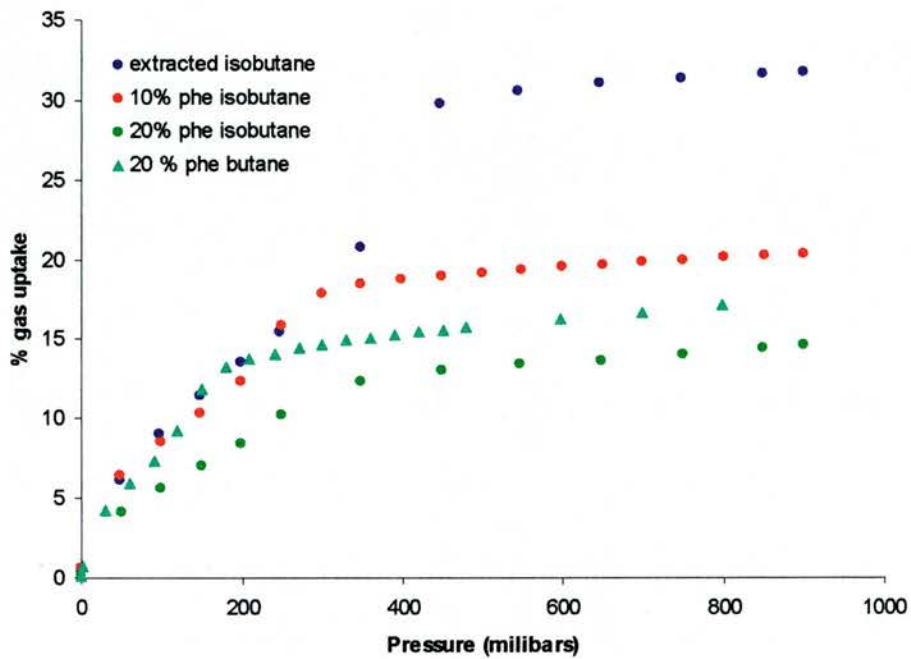


Figure 4.2.34. Isobutane adsorption experiments (round symbols) at in SBA-2 calcined (blue), 10% phenyl-functionalised SBA-2 (red), 20% phenyl-functionalised SBA-2 (green). Also included butane adsorption experiment in 20% phenyl-functionalised for comparison, triangular green symbols.

4.3. Synthesis and characterisation of aminopropyl-functionalised mesoporous solids

4.3.1 Synthesis of aminopropyl-functionalised mesoporous solids

The route chosen for the functionalisation of the solids was the post-synthesis method, where aminopropyl moieties are grafted at the surface of surfactant-free mesoporous solids. In this functionalisation route it is more difficult to control the amount of organic groups incorporated to the solid than via the *in situ* functionalisation, but it was preferred for several reasons: the amino group, $-NH_2$, reacts with hydrochloric acid to form the corresponding ammonium salt, NH_3Cl [5]. SBA-1 is made in acid conditions and MCM-41, synthesised in basic conditions, requires mixture of HCl/EtOH in order to remove the surfactant from the pores, so that post-synthesis functionalisation gives the best route to surface amine groups.

Synthesis of aminopropyl-functionalised MCM-41

Aminopropyl-functionalised MCM-41 was prepared via post-synthesis functionalisation of a siliceous MCM-41 (synthesised following the method of [8]) whose surfactant had been previously removed by solvent extraction. 8.03 g of extracted MCM-41 was placed on a Schlenk flask with approximately 60 cm³ of dried toluene and 15 cm³ aminopropyl triethoxysilane (Aldrich). The suspension of the solid was stirred under refluxed conditions for 4 h. The system was kept under dry nitrogen during this process. After this, the solid was quickly filtered and dried several times with a 50% mixture of dichloromethane and diethyl ether. Solids were dried under vacuum at 80 °C and were stored in closed vials before further use or characterisation.

Synthesis of aminopropyl functionalised SBA-1 type of solid:

The synthesis of this material was conducted by a similar method to the aminopropyl-functionalised MCM-41. Typically, 6 g of solvent-extracted pure silicate SBA-1¹ type of solid (synthesised in acid conditions from hexadecyltriethylammonium bromide at

¹ At the time of these studies, the special sample holder device to perform high pressure adsorption studies on non-compacted solids was available and therefore the control of the particle size was not a critical factor. Synthesis of silicate SBA-1 were conducted based on the method reported by M. J. Kim *et al* [10] rather than via the low temperature and low acidic conditions reported by S. Che *et al* [9] due to the higher yield obtained through this route.

low temperatures), was stirred under reflux conditions in a mixture of 60 ml of dry toluene and 8 ml of aminopropyltriethoxysilane. After a 4 h of reflux, the solid was filtered and washed several times with a mixture of 50% dichloromethane and 50% diethyl ether. The solid was dried under vacuum at 80 ° C and stored in a closed vial before further use or characterisation.

Synthesis of aminopropyl-functionalised SBA-2

Typically, 0.82 g of solvent-extracted pure silicate SBA-2 (synthesised according to [10]), was stirred under reflux conditions in a mixture of 50 ml of dry toluene and 2 ml of aminopropyltriethoxysilane. After a 4 h reflux, the solid was filtered and washed several times with a mixture of 50% dichloromethane and 50% diethyl ether. The solid was dried under vacuum at 80 ° C and was stored in a closed vial before further use or characterisation.

XRD characterisation

The diffraction patterns of MCM-41, SBA-1 and SBA-2, before and after the functionalisation are compared in Figure 4.3.1. These demonstrate that the materials retain their structure after grafting the organic groups. Table 4.3.1 summarises the *d* spacing for some reflections and the corresponding lattice parameters on basis of a cubic (SBA-1) or hexagonal (SBA-2 and MCM-41) unit cell.

Elemental CHN analyses

Elemental CHN analyses performed on the phenyl-functionalised MCM-41 gave 10.73% C, 1.92% H and 3.23% N. According to the nitrogen content, this corresponds to 2.3 mmols of aminopropyl groups per gram of solid.

The analysis of the aminopropyl-SBA-1 sample gave 9.73% C, 2.82% H and 3.29% N. This corresponds to 2.4 mmol/g of aminopropyl groups, according to the nitrogen content.

The analysis of the aminopropyl-SBA-2 sample gave 25.28% C, 3.42% H and 1.37% N.

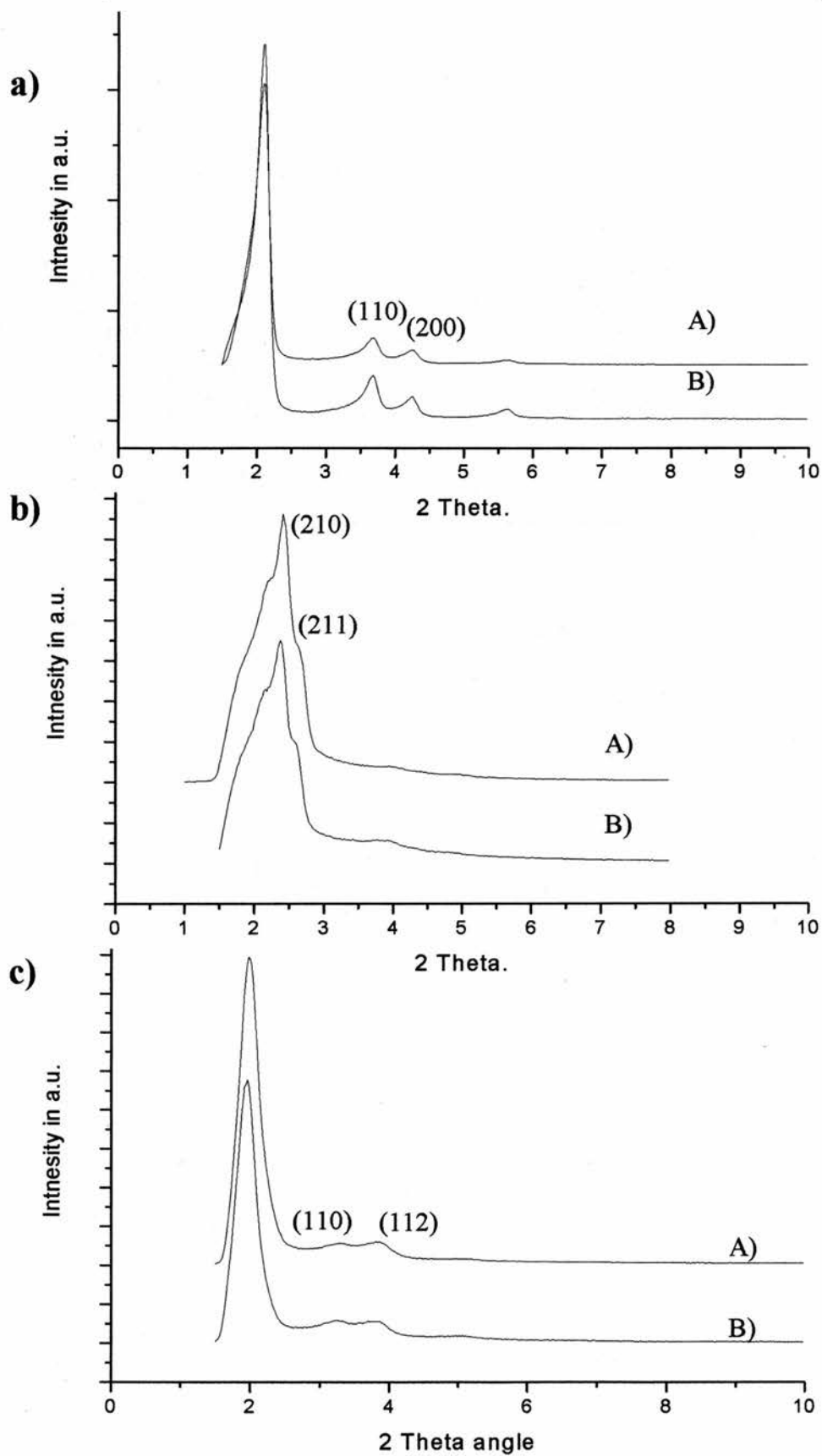


Figure 4.3.1. XRD patterns of aminopropyl-functionalised solids. a) MCM-41, b) SBA-1 and c) SBA-2. A) correspond to the functionalised solids and B) to the starting materials.

Solid.	Reflection/ d-spacing	Symmetry.
MCM-41	$d_{110} = 24.02$ $d_{200} = 20.74$	Hexagonal. $a = 47.9 \text{ \AA}$
SBA-1	$d_{210} = 36.42$ $d_{211} = 33.27$	Cubic. $a = 81.5 \text{ \AA}$
SBA-2	$d_{110} = 26.77$ $d_{112} = 23.09$	Hexagonal. $a = 53.54 \text{ \AA}$ $c = 91.3 \text{ \AA}$

Table 4.3.1. Summary of the XRD analyses performed on the aminopropyl-functionalised solids.

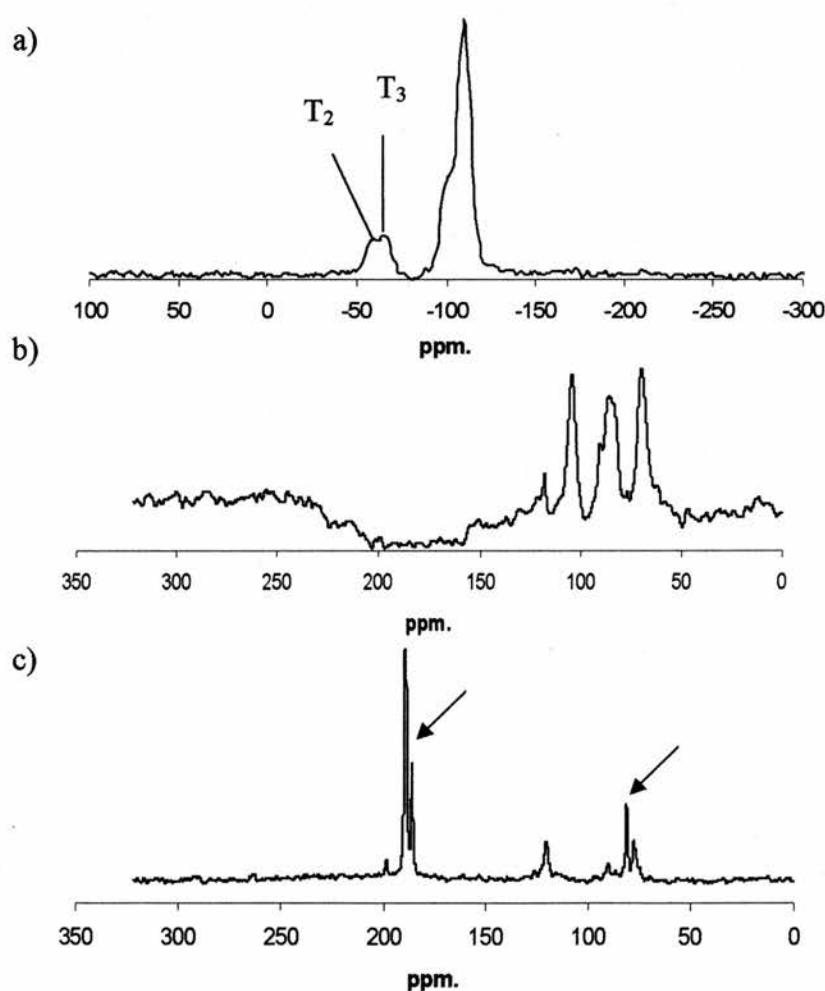


Figure 4.3.2. a) and b) MAS ^{29}Si and MAS ^{13}C NMR spectra of aminopropyl-MCM-41. c) ^{13}C MAS NMR of aminopropyl-SBA-2 (black arrows indicate the signals associated with toluene molecules trapped within the pores during the functionalisation).

MAS ^{29}Si NMR spectra of the aminopropyl-functionalised solid (Figure 4.3.2) exhibit two resonance signals, δ -59 and -65, which correspond to $(\text{OH})\text{RSi}(\text{OSi})_3$ (T_2) and $\text{RSi}(\text{OSi})_3$ (T_3) types of silicate environment as well as signals δ -100 and -110 due to Q_3 and Q_4 silica units. ^{13}C MAS NMR spectra shows three resonance signals δ 69, 85 and 103, associated with the three carbon types of the aminopropyl moieties. These spectra agree with previous work [5] in which similar methods were used to graft amines post-synthesis in MCM-41 and SBA-1 silicate materials.

MAS ^{13}C NMR spectra of the functionalised SBA-2 solid (Figure 4.3.2) shows the already mentioned signals due to the aminopropyl groups and also four intense signals, δ 81, 185, 188 and 189. These are due to toluene molecules trapped within the cages of SBA-2 during reaction with APTES. These signals are still present after heating at 150 °C under vacuum and suggest that the pore network of this solid was blocked by the functionalisation. This explains the high amount of carbon found in the sample by elemental CHN analysis.

Nitrogen adsorption studies of the original and functionalised starting materials are shown in Figure 4.3.3 and 4.3.4. The pore volume of the aminopropyl-MCM-41 is 0.47 cm^3/g and its calculated BET surface area is 657 m^2/g . These values are substantially decreased compared to those exhibited by the starting MCM-41 solid, 0.80 cm^3/g and 957 m^2/g for pore volume and BET surface area respectively. The capillary condensation step, at 0.4 P/Po in the original MCM-41, is shifted to lower pressures after coating the pores with aminopropyl groups. This is indication of a pore volume reduction as a consequence of the presence of aminopropyl groups grafted in the pore surface. BJH pore diameters for the aminopropyl-MCM-41 are 25.6, smaller than the starting MCM-41, 32 Å.

The pore volume and the surface area of the aminopropyl-SBA-1, 0.32 cm^3/g and 691.5 m^2/g respectively, are also lower than the values observed in the starting SBA-1, 0.73 cm^3/g and 1456 m^2/g . The capillary condensation step is also shifted to lower pressures as a result of the pore size reduction.

The nitrogen adsorption of the aminopropyl-SBA-2 (not shown) reveals a solid with almost no porosity. The total uptake of the sample, 1.8 % *wt* of nitrogen uptake, points to an almost totally blocked network as a result of the organic functionalisation. This agrees with the high amount of toluene found in the solid, probably trapped inside the cavities as the micropores were closed by aminopropyl triethoxysilane groups. Due to the lack of porosity of this solid, it was not further characterised.

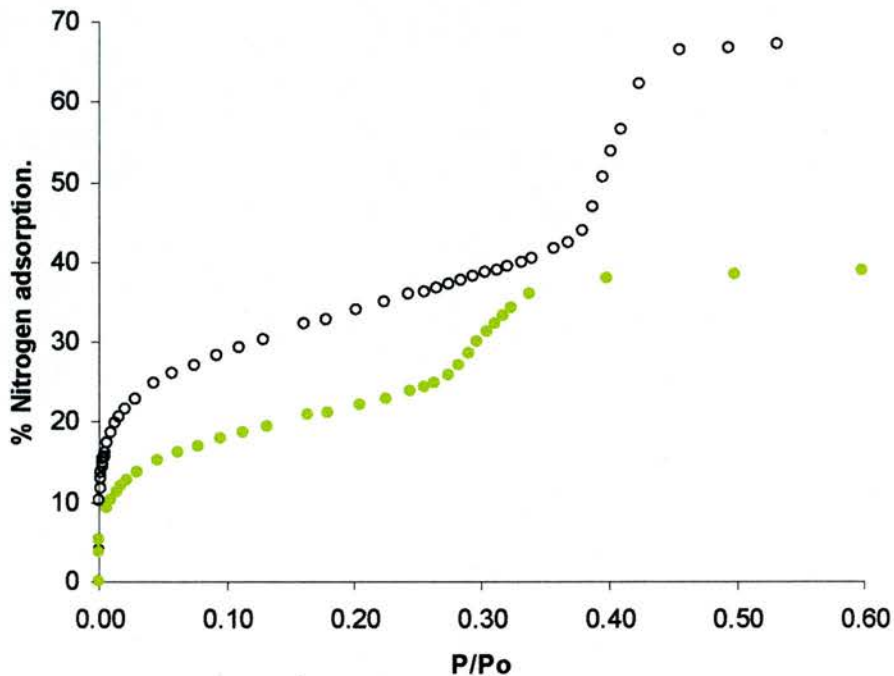


Figure 4.3.3. N_2 adsorption at 77 K of MCM-41 type solids. Black open symbols corresponds to the starting extracted MCM-41 solid. Green symbols correspond to aminopropyl functionalised MCM-41.

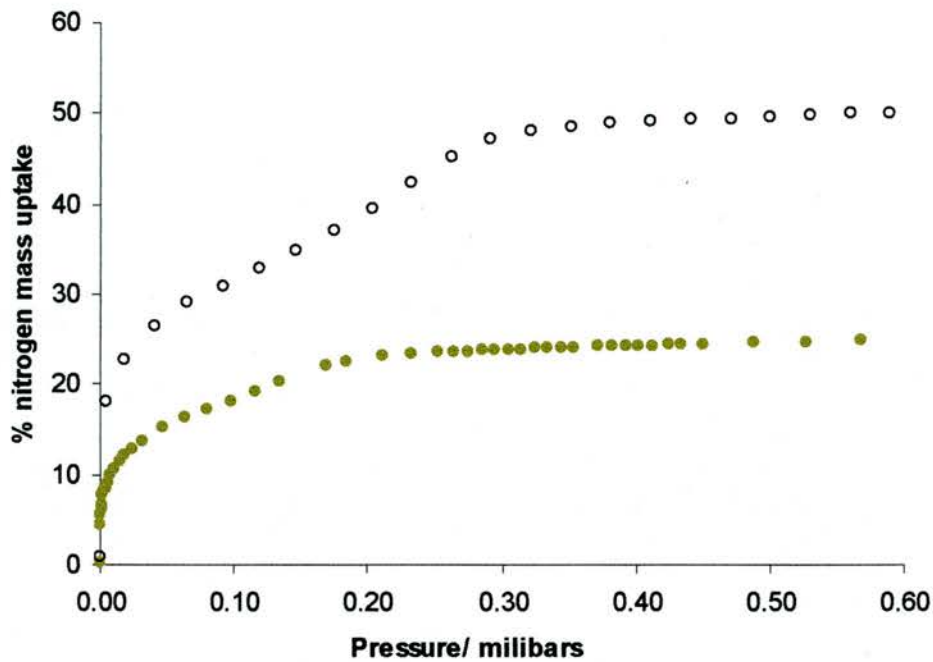


Figure 4.3.4. N₂ adsorption experiments at 77 K in SBA-1 (black open symbols and aminopropyl-SBA-1 (green symbols).

High pressure CO₂ and ethane adsorption experiments

High pressure adsorption CO₂ isotherms were measured using uncompact samples in both the high pressure adsorption apparatus at Edinburgh University (at 263 K) and the low pressure adsorption IGA system (at 268 K) at St. Andrews University. Experiments performed in the IGA system were reversible after outgasing the solid and therefore no signs of chemisorption were appreciated during the conduction of these experiments. It is also important to remember the methodology used to perform the high pressure adsorption experiments presented in this PhD thesis: all the isotherms are actually two experiments measured at even and odd pressures. If chemisorption would take place during the first experiment, the second isotherm would never overlap with the first one. The low pressure region of the high pressure adsorption experiments and the low pressure adsorption experiments performed in the IGA for some materials are compared in Figures 4.3.5 and 4.3.6 . The agreement between the two set of experiments is good.

The increase of CO₂ adsorption at low pressures is larger for the aminopropyl-MCM-41 solids than for the calcined MCM-41. This is more clearly seen through the Henry constant calculated for the different solids, see table 4.3. 2.

	Aminopropyl-MCM-41	Aminopropyl-SBA-1	Calcined MCM-41	Phenyl-MCM-41 (post-synthesis)
Henry constant (mol kg ⁻¹ mbar ⁻¹) *10 ³	17.3	22.4	1.92	2.75

Table 4.3.2. Henry constant for CO₂ at 263 K for different type of solids.

The strength of the interaction of CO₂ with the aminopropyl-SBA-1 solid is larger than for the MCM-41 solids. It is difficult to tell if this is due to the larger amount of aminopropyl groups grafted on this solid, 2.4 mmol/g, or due to the smaller size of the cavities.

Aminopropyl-functionalised solids were also studied by means of high pressure ethane adsorption. The experiments were also conducted using non-compacted solids (Figure 4.3.7). Analysing the isotherms it seems that, apart from the expected shift to lower pressures of the pore filling step, due to the smaller pore size after coating the pores with organic groups, the amine functionalisation does not exert any significant influence on the adsorption of ethane. It is clear that, at low pressures, the adsorption of ethane by the aminopropyl MCM-41 and SBA-1 solids is lower than the calcined of phenyl-functionalised MCM-41.

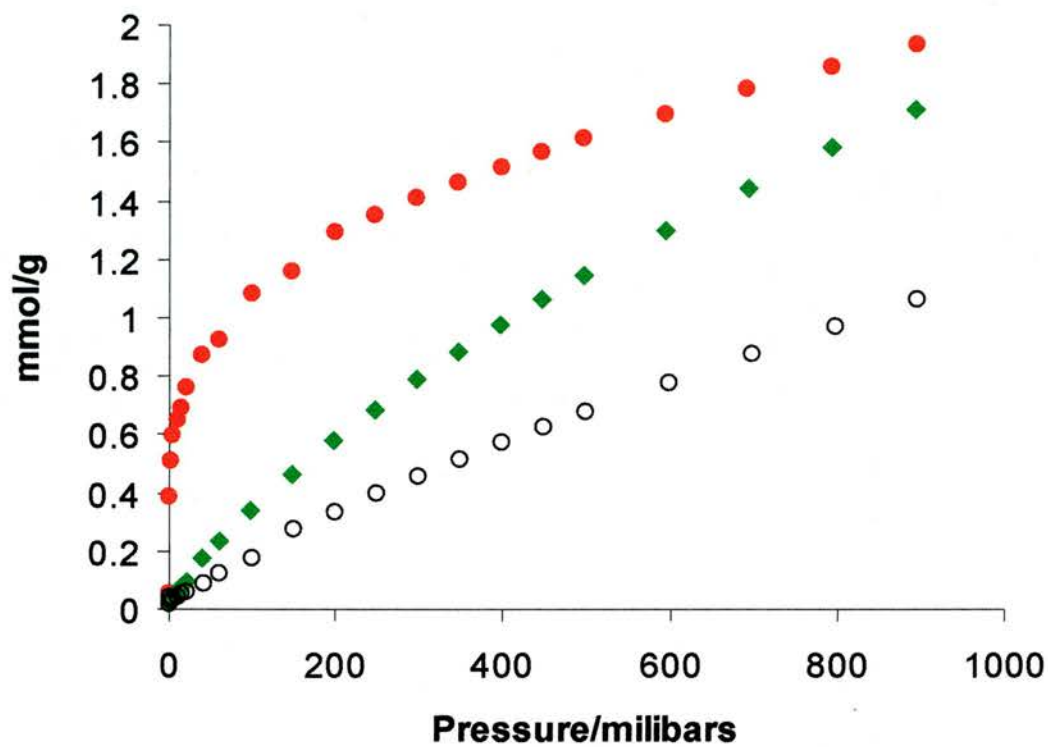


Figure 4.3.5. Low pressure CO₂ adsorption experiments at 268 K performed in the IGA system (St. Andrews University) on MCM-41 solids. Black open symbols, diamond symbols and red symbols correspond to a calcined MCM-41 solid, extracted MCM-41 and aminopropyl-functionalised MCM-41.

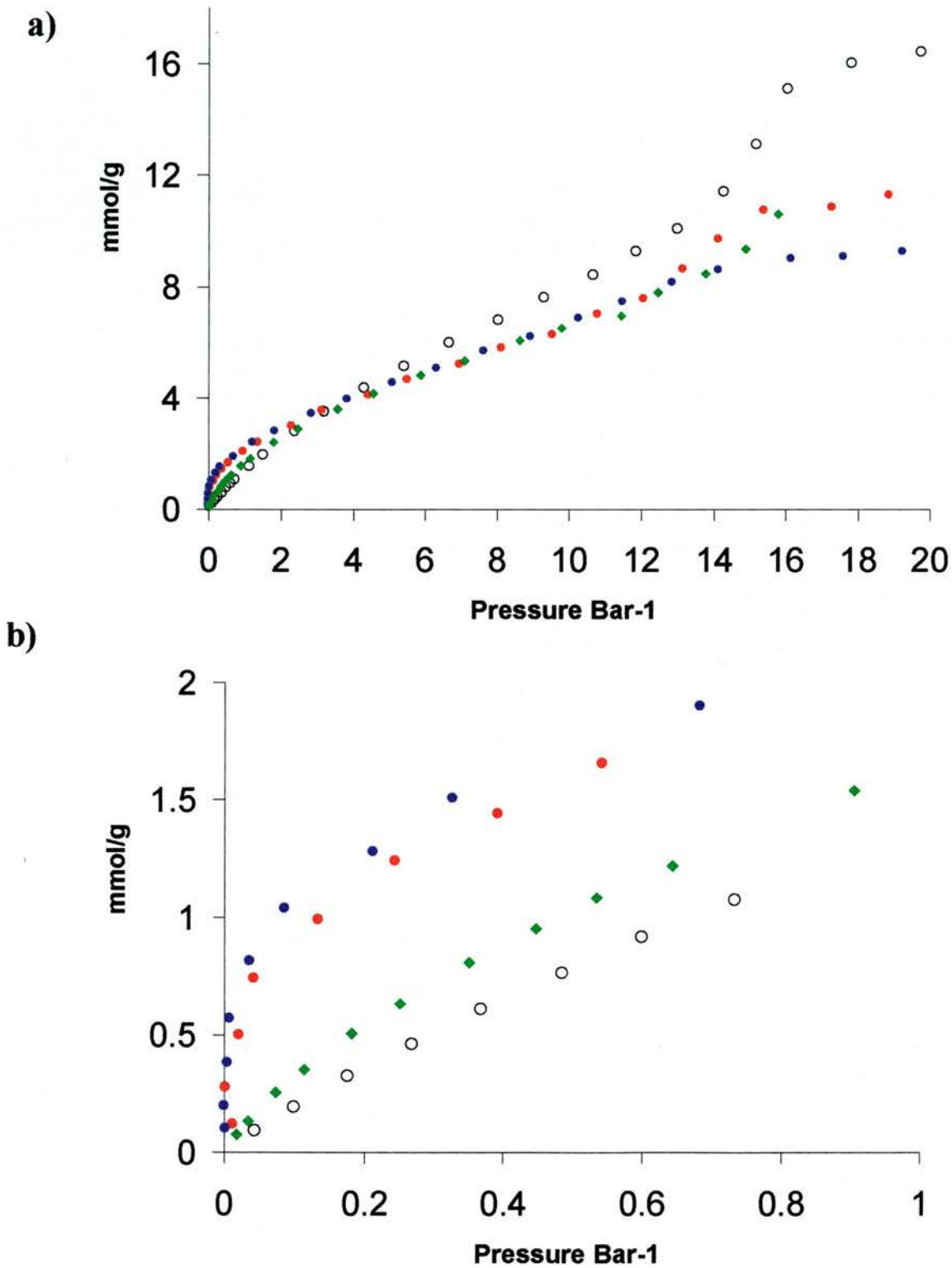


Figure 4.3.6. CO₂ isotherms performed on the high pressure rig at Edinburgh University on MCM-41 and SBA-1 at 263 K. Black open symbols and diamond symbols correspond to calcined MCM-41 and extracted MCM-41. Red and blue symbols correspond to aminopropyl-functionalised MCM-41 and SBA-1

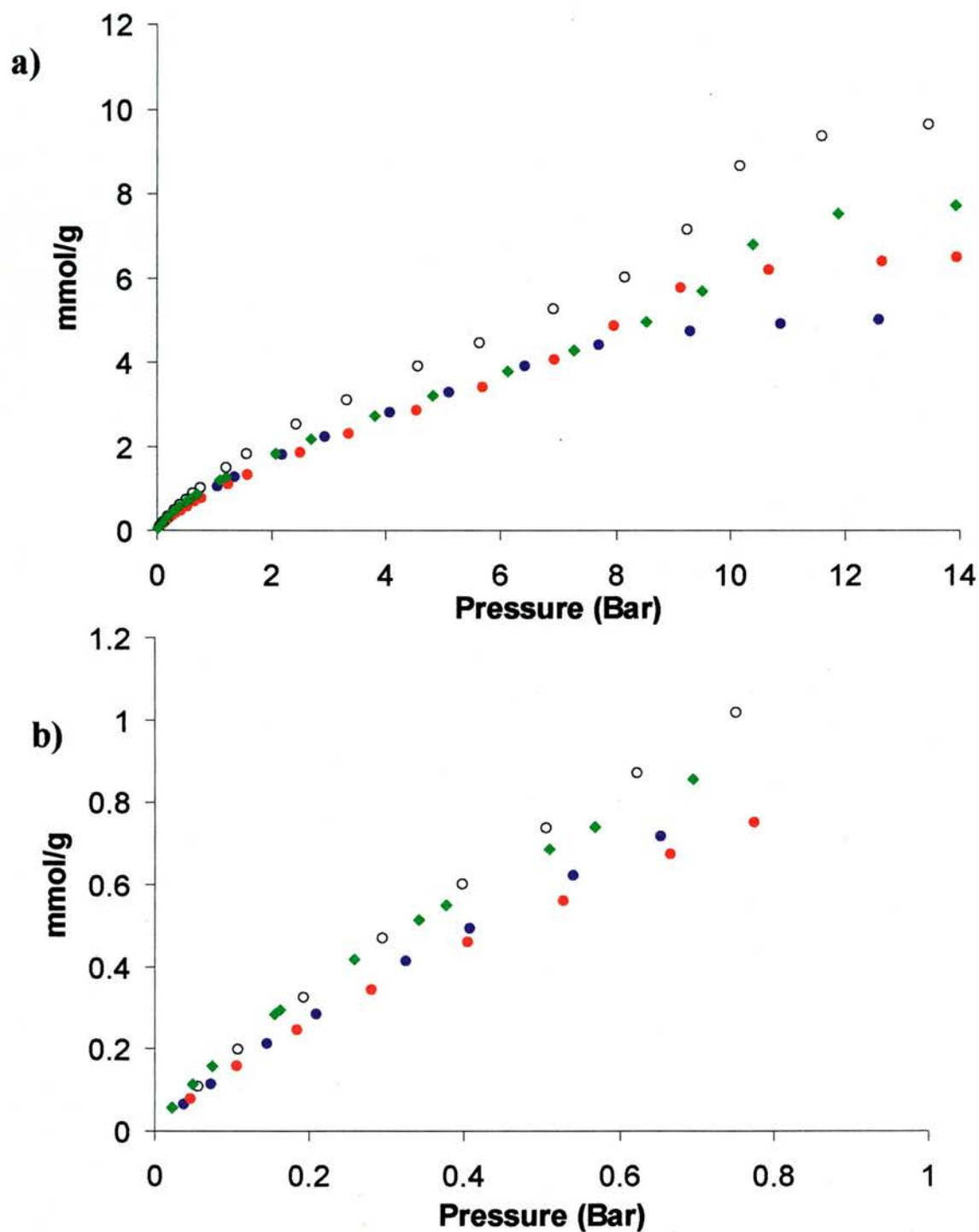


Figure 4.3.7. High pressure ethane isotherms performed on the high pressure adsorption rig (Edinburgh University) at 263 K. Black open symbols and diamond symbols correspond to calcined MCM-41 and extracted MCM-41. Red and blue symbols correspond to aminopropyl-functionalised MCM-41 and SBA-1

Conclusions

Aminopropyl groups have been successfully grafted on SBA-1 and MCM-41 silicate frameworks without affecting the structure of these solids. These organic groups enhance the adsorption of CO₂ without affecting the adsorption of ethane. This result suggests that aminopropyl modification of the pore surface would enhance the selectivity for CO₂ adsorption in CO₂/ ethane mixtures.

4.4. General Conclusions:

Phenyl-functionalised MCM-41, SBA-1 and SBA-2 and aminopropyl functionalised MCM-41 and SBA-1 have been successfully synthesised and characterised by XRD, ²⁹Si and ¹³C NMR, elemental analysis and nitrogen adsorption. The adsorption properties of these organic modified solids are different than the pure inorganic silicates:

- 1) Phenyl-functionalisation exerts a significant influence upon the pore volume of the solids and surface heterogeneity of the solids. It also enhances the affinity of the solids for ethane, but this effect is subtle.
- 2) Aminopropyl-functionalisation also affects the pore volume of the solids. It does not seem to have any strong influence upon the adsorption of ethane but it strongly enhances the physisorption of CO₂ on the solids at low pressures. This makes aminopropyl-functionalised solids candidates as adsorbents for CO₂ and ethane separations in pressure swing process.

4.5. Future work

Adsorptions of CO₂/ ethane mixtures are necessary in order to evaluate the possible selectivity for CO₂ of the aminopropyl-functionalised solid. If the selectivity is actually enhanced by this organic group, solids like MCM-48 could also be of interest due to their small pore size.

References for chapter 4.

- [1] Q. Huo, D. I. Margolese, U. Ciesla, D. G. Demuth, P. Feng, T. E. Gier, P. Sieger, A. Firouzi, B. F. Chmelka, F. Schüth, G. D. Stucky, *Chem. Mater.*, **1994**, 6, 1176.
- [2] Q. Huo, R. Leon, P.M. Petroff, G.D. Stucky, *Science*, **1995**, 268, 1324.
- [3] C.T. Kresge, M.E. Leonowicz, W.J. Roth, J.C. Vartuli, J.S. Beck, *Nature*, **1992**, 359, 710
- [4] A. Stein, B. J. Melde, R. C. Schrodin, *Adv. Mater.*, **2000**, 12, 1403.
- [5] T. Yokoi, H. Yoshitake, T. Tatsumi, *J. Mater. Chem.*, **2004**, 14, 951.
- [6] A. C. C. Chang, S. C. C. Chuang, M. Grey, Y. Soong, *Energ. Fuels*, **2003**, 17, 468.
- [7] C. Schumacher, J. Gonzalez, M. Perez-Mendoza, P. A. Wright, N. A. Seaton, *Stud. Surf. Sci. Catal.*, **2004**, 154, 386
- [8] Q. Cai, W-Y. Lin, F-S. Xiao, W-Q. Pang, X-H. Chen, B-S- Zou, *Microporous Mesoporous Mater.*, **1999**, 32, 1.
- [9] S. Che, Y. Sakamoto, O. Terasaki, T. Tatsumi, *Chem. Mater.*, **2001**, 13, 2237.
- [10] M. J. Kim, R. Ryoo, *Chem. Mater.*, **1999**, 11, 487.
- [11] H. M. A. Hunter, A. E. Garcia-Bennett, I. J. Shannon, W. Zhou, P. A. Wright, *J. Mater. Chem.*, **2002**, 12, 20.
- [12] F. Babonneau, L. Leite, S. Fontlupt, *J. Mater. Chem.*, **1999**, 9, 175
- [13] S. Inagaki, S. Guan, T. Ohsuna, O. Terasaki, *Nature*, **2002**, 416, 304.

Part II

One of the targets of this Project has been to investigate the adsorption properties of microporous organic-inorganic hybrids and to compare it with that of conventional microporous inorganic solids, such as zeolites and aluminophosphates. In this thesis, the aluminium methylphosphonates $\text{Al}_2(\text{CH}_3\text{PO}_3)_3$ - α and - β and the metal organic framework MOF-5, $\text{Zn}_4\text{O}(\text{O}_2\text{CC}_6\text{H}_4\text{CO}_2)_3$ have been investigated as representative of the hybrids solids.

The synthesis, characterisation and adsorption of small molecules of the AlMePO polymorphs are described in chapter 6, along with ^2H NMR studies that address the role of 1, 4-dioxane in the synthesis of AlMePO- β and the mobility of light hydrocarbons and methanol in the AlMePOs and the microporous AlPO_4 -5. Taken together, these studies also characterise the hybrid frameworks used in chapter 7, where highly detailed ^2H NMR studies of the reorientation of monoaromatics within the pores are described. Finally, in chapter 8, attention is turned to the zinc terephthalate MOF-5, where ^2H NMR studies are used to determine the motion of organic linking groups in the framework and benzene adsorbed within the pores.

In each of these studies note is taken of computational studies performed by other groups in parallel on the same systems to complement and help analyse the experimental studies. These studies are: for chapter 6, simulation of the role of dioxane in the synthesis of AlMePO- β and the simulation of the adsorption isotherms of N_2 and CO_2 ; for chapter 7, molecular dynamics simulations of the motion of monoaromatics in AlMePO- α and - β and in chapter 8, simulation of the minimal energy position of benzene in MOF-5. Full acknowledgement is given in the appropriate place in the text.

Chapter 5.

Synthesis, characterisation and adsorption of small molecules in aluminium methylphosphonates α and β

5.1 Introduction:

As described in chapter 1, the microporous hybrid AlMePO polymorphs α and β exhibit novel adsorption properties. These solids are highly hydrophobic and exhibit affinity for small hydrocarbons [1]. The N_2 adsorption isotherm of AlMePO- α is type I, typical of microporous solids, but presents an unusual second step at low pressures. This is due to a packing effect of the nitrogen imposed by the acutely triangular shape of the hybrid walls of the solid [2]. In addition, preliminary work by Pérez-Mendoza on a sample of AlMePO- β [unpublished results], shows appreciable selectivity for the adsorption of ethane from 1:1 methane : ethane mixtures.

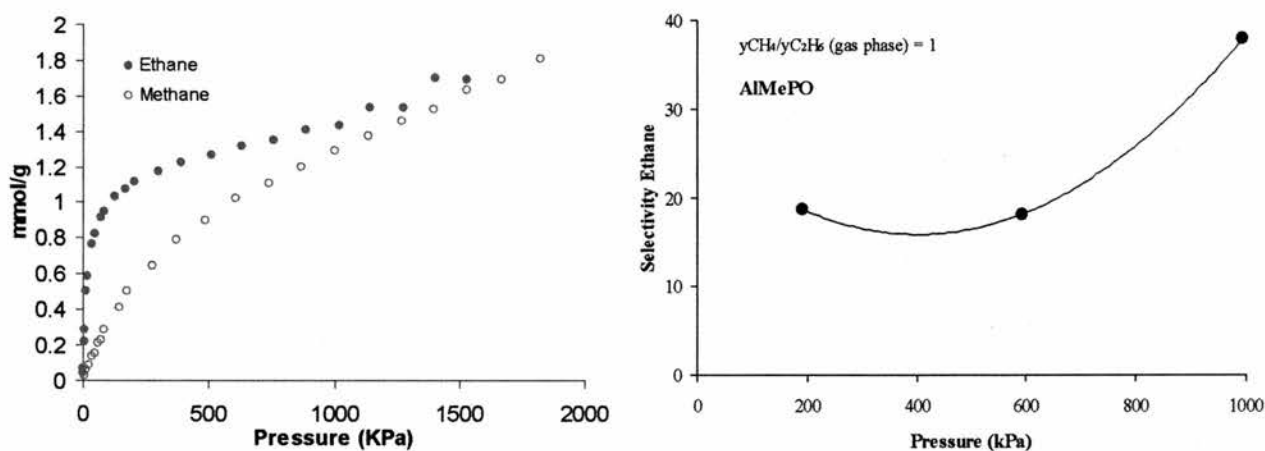


Figure 5.1. Left, high pressure adsorption isotherms of ethane and methane in AlMePO- β at 263.15 K. Right, Selectivity experiments in AlMePO- β using a gas flow of 50% ethane/methane composition.

The selectivity is expressed for ethane and is defined as $\text{selectivity} = \frac{y_2}{y_1} \bigg/ \frac{x_2}{x_1}$, where y is the

composition of the adsorbate phase, x the composition of the gas phase, 1 is methane and 2 is ethane [Pérez-Mendoza, unpublished result].

These data indicate that the AlMePOs represent an interesting class of materials to study, despite their relatively low adsorption capacity (especially compared with zeolites or some of the recent organic-inorganic microporous hybrids [3]). In particular the nature of their internal surface, which is covered by rapidly rotating methyl groups [4], is likely to give them characteristic properties.

The motion of an adsorbed molecule within a porous solid is intimately related to the strength of the interaction between the guest molecule and the framework. This interaction, ΔH , and the loss of rotational freedom after adsorption as a consequence of being in a constrained environment, ΔS , are opposing forces in adsorption [5]. (Remember that the loss of entropy is unfavourable for a process: $\Delta G = \Delta H - T\Delta S$, $\Delta G < 0$ for reaction). For this reason, measuring the dynamics of adsorbed molecules in porous solids is important (and almost unstudied in hybrid solids) in order to understand their adsorption properties. The well known structure and unique adsorption properties of the AlMePOs make these solids of special interest for these sort of studies, which have been the object of this thesis. In this chapter a study of the dynamics of selected molecules of interest (1, 4-dioxane, methanol, isobutane and ethane) is presented. The main technique chosen for the analysis, quadrupolar ^2H NMR, has proved useful to monitor motional processes in different systems [6-12].

Section 5.2 describes the synthesis and characterisation of porous AlMePO- β , AlMePO- α and AlPO₄₋₅, solids that will be used as host frameworks for the ^2H NMR studies. AlPO₄₋₅ has been included in this study in order to compare the results obtained in the hybrids with an inorganic framework of similar structure. Section 5.3 documents the studies of motion of 1, 4-dioxane, the structure direct agent for the synthesis of AlMePO- β . Section 5.4 presents a comparative study, also through ^2H NMR, of the dynamics of methanol, isobutane and ethane in AlMePO- β , AlMePO- α and AlPO₄₋₅.

5.2. Synthesis and characterisation of microporous organic-inorganic hybrid aluminium methylphosphonates α and β and microporous aluminophosphate $AlPO_4-5$

Introduction

This section details the preparation and characterisation of the AlMePO solids and the inorganic $AlPO_4-5$ used as sorbents in this chapter and the next.

Experimental

Several batches of AlMePO- β were reproducibly prepared according to published procedures [13]. Typically $CH_3PO(OH)_2$ (Aldrich 98%), $Al(OH)_3$ (Aldrich 98%)¹, 1, 4-dioxane (Avocado 98%) and H_2O were mixed in the molar ratio 1.5:1:0.5:40 using a magnetic stirrer at room temperature until the gel was homogeneous. The gel was placed in a PTFE-lined stainless steel autoclave for 48 h at 160°C. The product was filtered and dried in air at 60°C overnight. In order to remove the template from the channels the sample was heated under dry nitrogen at 450°C for 12h.

AlMePO- α was synthesised by heating an as-synthesised sample of ground AlMePO- β under a high flow of nitrogen saturated with water vapour. The solid was raised at 10°C/min to 500°C, and kept at this temperature for 8 h. These synthesis conditions were adapted from a published procedure from our group [13] because using as-prepared AlMePO- β as a starting material (rather than a solid with the 1, 4-dioxane already removed) gave a solid with higher adsorption capacity.

$AlPO_4-5$ was synthesised according to the method of Chen *et al* [14] from a gel with composition $Al_2O_3:P_2O_5:1.5Et_3N:100H_2O$. In a typical synthesis, pseudoboehmite, 73.95% Al_2O_3 ¹, was combined with distilled water and the slurry was mechanically stirred for 2 days. Phosphoric acid was added to the mixture and the mixture was stirred overnight. After the addition of Et_3N the mixture was stirred for another 2h. The reaction mixture was autoclaved for 48 h. After filtration, the solid was dried in air overnight and calcined at 550°C under O_2 for 24 h.

¹ The water content of this chemical was determined by a TGA analysis.

Characterisation of AlMePOs - β and α and aluminophosphate AlPO₄-5

The XRD pattern of the AlMePO- β sample (Figure 5.2.1) was indexed according to the space group R3c ($a = 24.650$ Å and $c = 25.299$ Å) in agreement with the unit cell reported for this material. The ³¹P NMR spectrum of the sample (Figure 5.2.2), which shows five signals at 14.9, 13.6, 10.4, 7.2 and 1.7 ppm with relative intensities 1:1:1:1:2 respectively also agrees with previous structural studies. According to these results, the sample was pure AlMePO- β .

The sample of AlMePO- α was also characterised by means of XRD and NMR. The XRD pattern of this sample (Figure 5.2.1) could be indexed on basis of the trigonal space group P31c with unit cell parameters $a = 13.995$ Å and $c = 8.531$ Å, in accord with the literature, but it also shows traces of unreacted AlMePO- β as an impurity. For example, there is a smaller peak next to the (102) reflection of AlMePO- α , that corresponds to the (404) or (413) reflection of AlMePO- β . These traces of unreacted AlMePO- β were also identified by MAS ³¹P and MAS ²⁷Al NMR. It can be seen in Figure 5.2.2 that, at the lower field of the two peaks associated to the ³¹P of the α polymorph, at 1.1 and 6.1 ppm, there are signals at 14.9, 13.6 and 7.2 ppm, that corresponds to β impurities. By appropriate integration of the signals (also the spinning side bands) it was estimated that there was 6% of β in the sample. MAS ²⁷Al NMR also shows the presence of unreacted AlMePO- β (Figure 5.2.3).

In order to characterise the porosity of these samples, and the possible accessibility of guest molecules of interest for ²H NMR experiments, adsorption of N₂ (77 K), CO₂ (196 K) and toluene (298 K) were studied in these solids, see Figure 5.2.4. The N₂ adsorption isotherms of both solids were found to be of type I (IUPAC classification) (Figure 5.2.4). According to the N₂ experiments the pore volume found for AlMePO- β sample was 0.10 cm³/g (8 % wt N₂ uptake at 0.28 P/P₀, 319.3 mbar), slightly smaller than the initially reported by Maeda *et al* [1] 0.13 cc/g. On the other hand, the synthesised sample of AlMePO- α seems to have a larger N₂ adsorption capacity, with a pore volume of 0.14 cm³/g. The pore volume exhibited by this solid is larger than the pore volume observed for previous AlMePO- α synthesised from AlMePO- β using steam at high temperature.

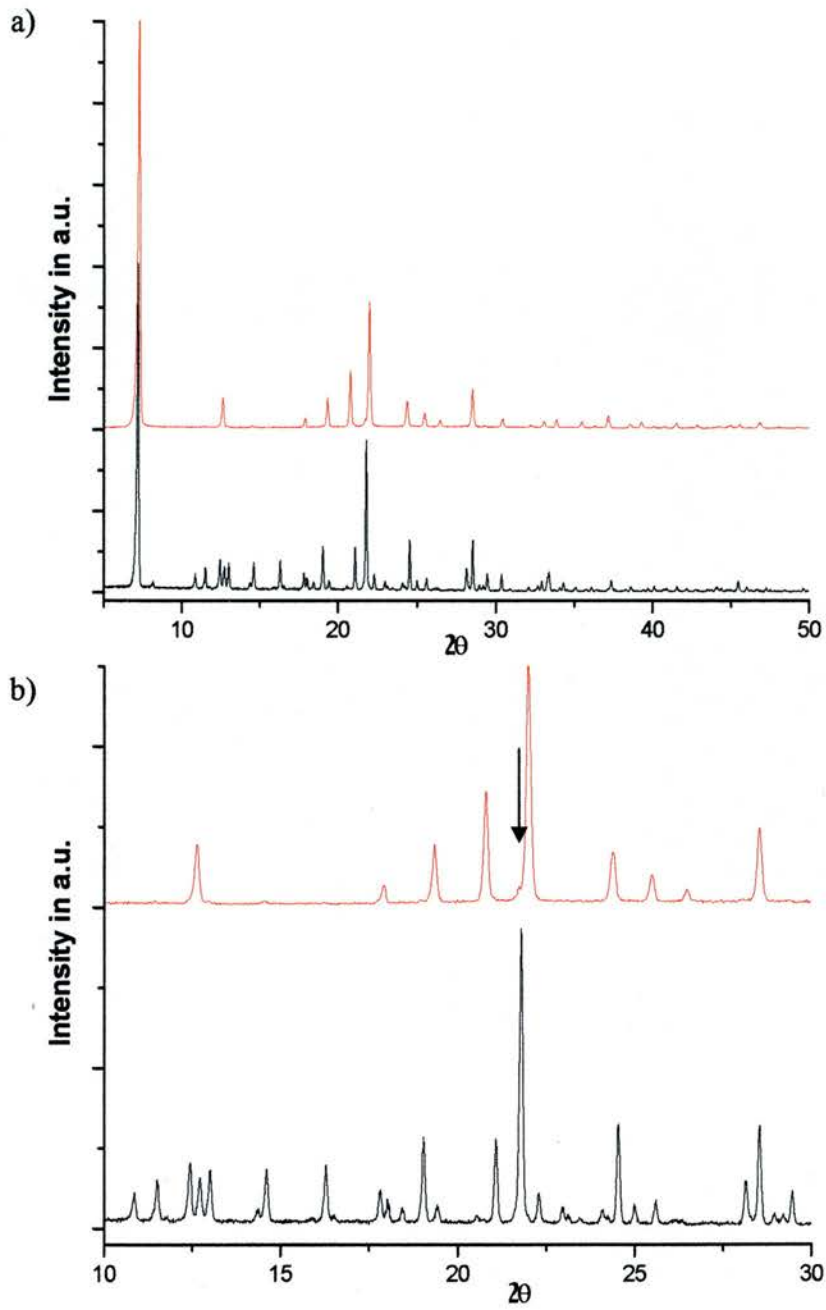


Figure 5.2.1. XRD patterns of AlMePO- β and AlMePO- α (black and red respectively). a) and b) correspond to different scales.

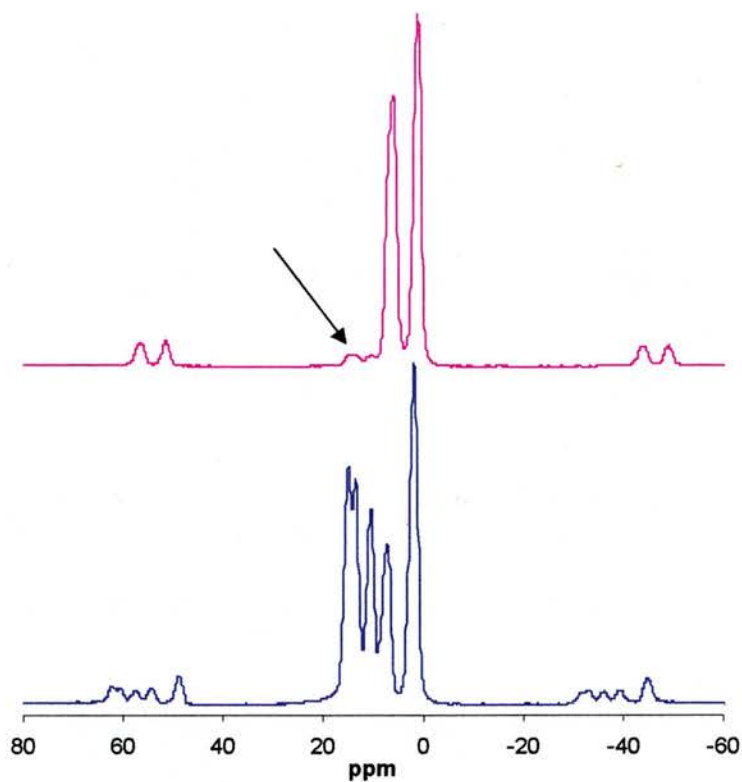


Figure 5.2.2. MAS ^{31}P NMR of $\text{AlMePO-}\beta$ and $\text{AlMePO-}\alpha$, blue and pink respectively. The black arrow indicates the traces of $\text{AlMePO-}\beta$.

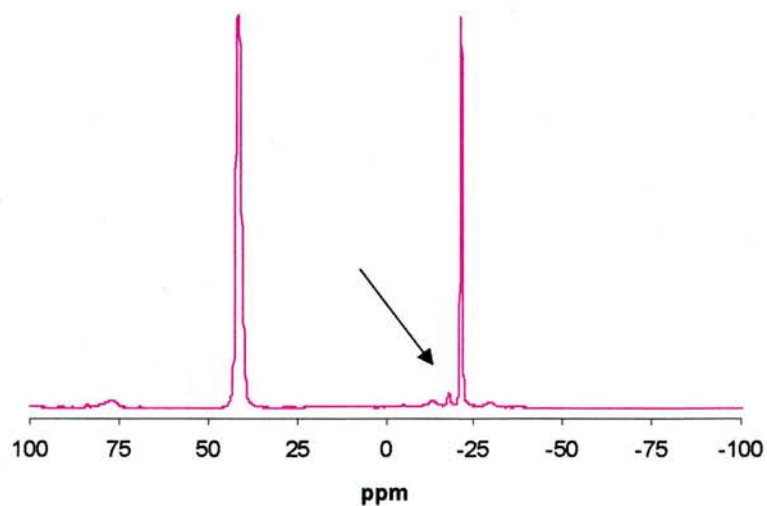


Figure 5.2.3. MAS ^{27}Al NMR of $\text{AlMePO-}\alpha$. The low intensity resonance signal at -17.5 ppm, highlighted with a black arrow, is due to unreacted $\text{AlMePO-}\beta$

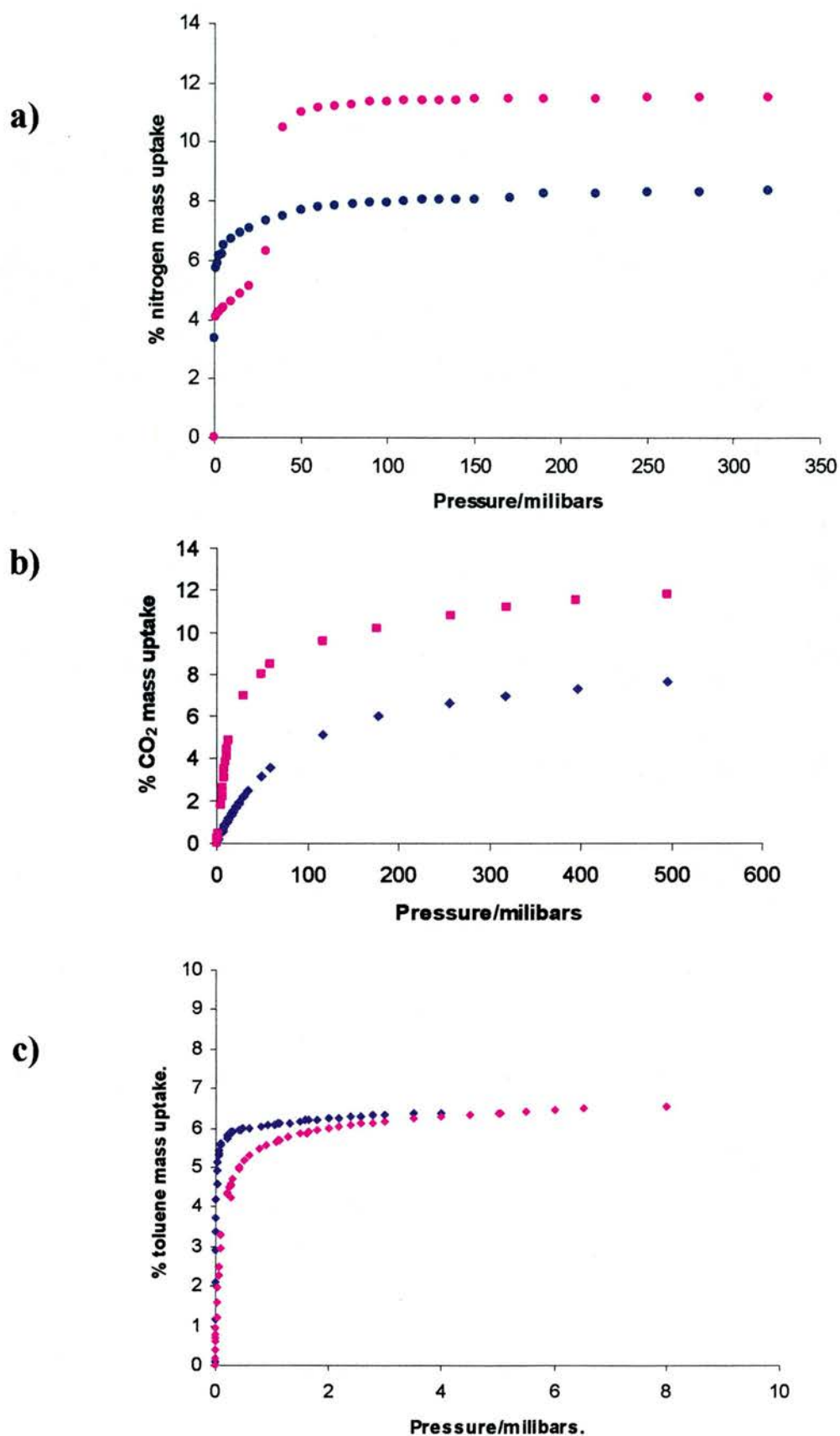


Figure 5.2.4. Adsorption for AlMePO- β (blue) and AlMePO- α (pink). a) N_2 at 77K, b) CO_2 at 196 K and c) toluene at 298 K.

The N_2 adsorption isotherm of AlMePO- α displays a plateau at one third of its maximum loading capacity. This unusual behaviour, first reported by Maeda *et al* [1], is attributed to a change in the packing of the nitrogen molecules within the pores of AlMePO- α with the increase in pressure.

CO_2 adsorption isotherms performed on the two solids are also shown in Figure 5.2.4. Both isotherms have similar shape, type I (IUPAC classification), however, for CO_2 the adsorption of AlMePO- β , 11.8 % *wt* (at 0.26 P/Po), is larger than the adsorption capacity of AlMePO- α 7.6 % *wt* (at 0.26 P/Po).

In parallel with these experimental studies, Schumacher [2] has analysed in detail the adsorption of CO_2 and N_2 by the AlMePOs by means of Monte Carlo simulations. His results suggest that the second step in the nitrogen isotherm is due to a change in packing by which nitrogen changes from two molecules per unit cell, to regular layer-like arrangement of 6 molecules per unit cell (Figure 5.2.5). His work also provides theoretical CO_2 and N_2 adsorption capacities for the AlMePOs, which are compared with experimental results in table 5.2.1.

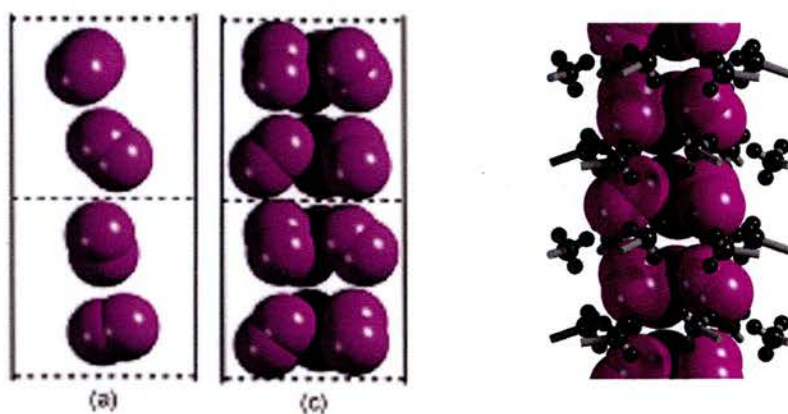


Figure 5.2.5. Left, representation of nitrogen in AlMePO- α at low pressure (a) and at its maximum loading level on a layered array. Right, representation of nitrogen at its maximum loading level in AlMePO- α . Figures adapted from [2].

	Experimental wt % uptake.	Schumacher predicted wt % uptake. [2]	Reported wt % uptake. [1]
N ₂ in β	8.4	11.6	10.5
N ₂ in α	11.4	12.0	7.7
CO ₂ in β	11.5	13.5	-
CO ₂ in α	7.0	6.0	-

Table 5.2.1. Comparison of the experimental adsorption values observed for N₂ and CO₂ in the AlMePOs with predicted adsorption capacities [2] and previous reported values [1].

The comparison of the experimental and predicted nitrogen adsorption capacity of AlMePO- β suggests that some of the channels are not accessible to nitrogen, probably due to crystallisation defects. On the other hand, the porosity of AlMePO- α agrees with the predicted values of Schumacher. CO₂ adsorption capacities of both samples also agree with the predicted values. It seems likely that CO₂ can diffuse through the crystal defects that block nitrogen, due to its smaller kinetic diameter.

The XRD, NMR and adsorption analysis discussed in this section correspond to the samples used for the ²H NMR experiments presented later on in this chapter and in the next. The relatively high toluene adsorption capacity that these solids present makes possible the incorporation of other guest molecules like benzene and para-xylene. For the sake of simplicity of the ²H NMR interpretation it would be more convenient to use pure AlMePO- α , but attempts to synthesis a pure phase with good porosity were not successful. Therefore, although our sample had traces of AlMePO- β , the solid was thoroughly characterised and it was investigated as a host for several compounds for NMR study.

The XRD pattern of the $\text{AlPO}_4\text{-5}$ sample calcined at 550°C (Figure 5.2.6) could be indexed according to a hexagonal unit cell with $a = 13.69 \text{ \AA}$ and $c = 8.4 \text{ \AA}$. These unit cell parameters agree with reported values for $\text{AlPO}_4\text{-5}$.

Nitrogen adsorption experiment reveals a pore volume equal to 0.1 cc/g . This value, slightly smaller than other previously reported for this material (0.146 cc/g), indicates that some of the pores were blocked to N_2 molecules.

The accessibility of aromatic molecules to the channels, necessary in order to perform the mentioned NMR studies, was checked by means of a toluene adsorption experiment. The isotherm (Figure 5.2.7) exhibits rapid increase of uptake of $\sim 6\%$ at very low pressures due to the adsorption of toluene within the micropores. As the pressure is increased, the solid continues to adsorb, possibly on the external surface (Note the small size of the crystals compared to those of $\text{AlMePO}_4\text{-}\beta$ in the SEM micrographs (Figure 5.2.8)).

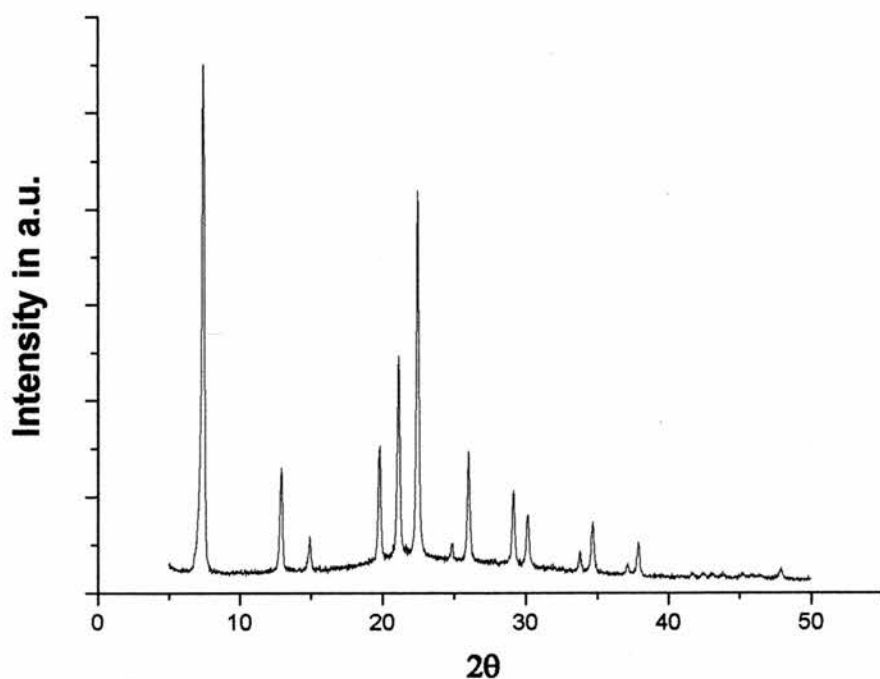


Figure 5.2.6. a) XRD diffraction pattern of $\text{AlPO}_4\text{-5}$ calcined at 550°C .

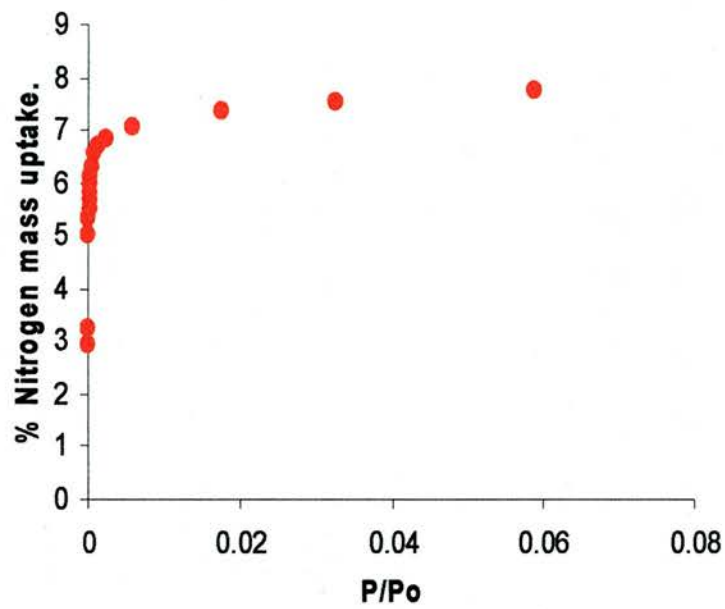
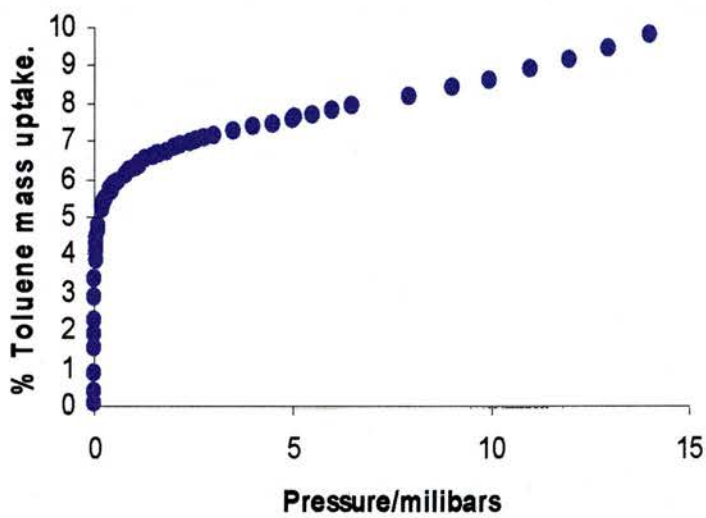
a**b**

Figure 5.2.7. a) Nitrogen adsorption at 77 K and b) toluene adsorption at 293 K of AlPO₄-5.

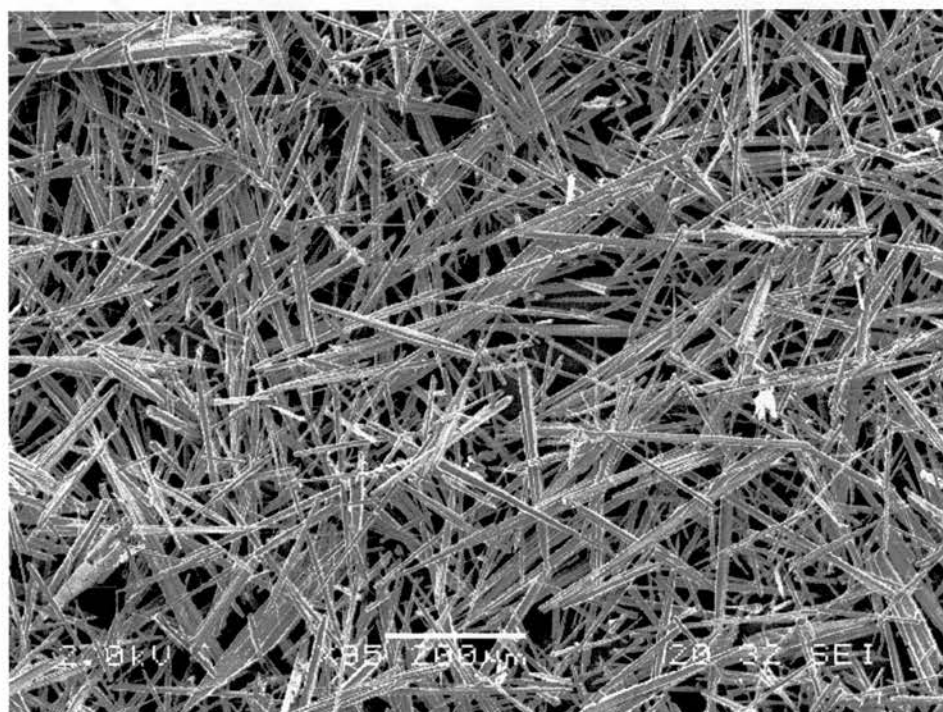
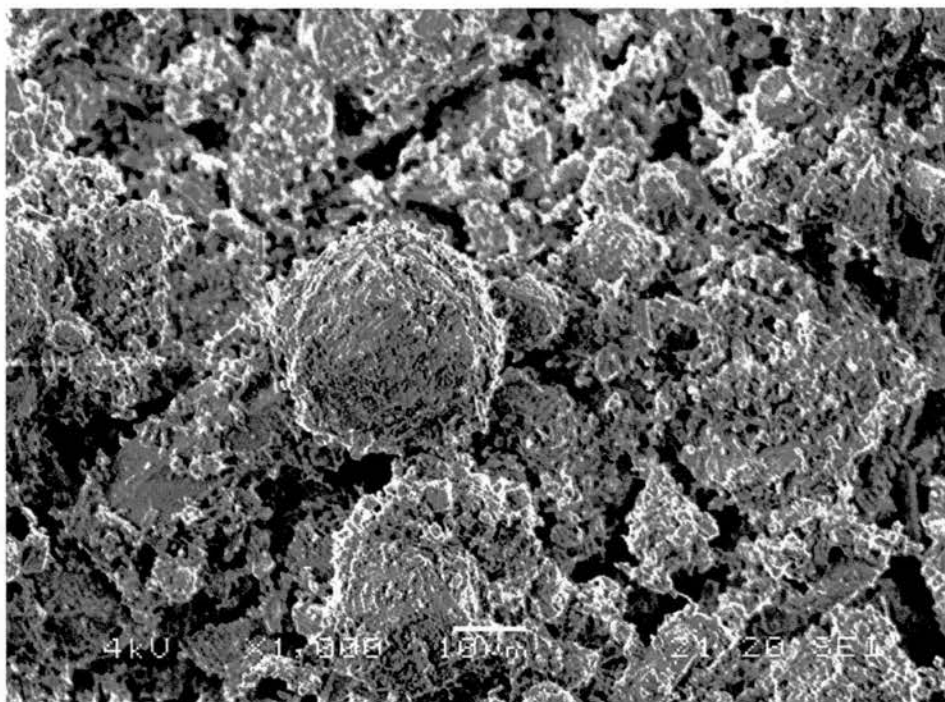


Figure 5.2.8. SEM micrograph of calcined AlPO₄-5 (top) and as-synthesised AlMePO-β sample (bottom).

5.3. Dynamics of 1, 4-dioxane in aluminium methylphosphonates α and β

5.3.1 Introduction

1, 4-dioxane acts as a structure directing agent in the synthesis of AlMePO- β . Notably, the presence of 1, 4-dioxane favours the β over the α polymorph, despite the α polymorph possessing the more thermodynamically stable framework. (Hence β converts to α upon heating in a H₂O-catalysed topotactic transformation [13]).

The role of 1, 4-dioxane as a structure directing agent of AlMePO- β has been investigated through computational methods by Grewal and Cox at Portsmouth University [15]. These calculations suggest that the possible origin of the selective stabilisation effect that 1,4-dioxane exerts upon AlMePO- β , with respect to its polymorph α , during synthesis resides on the higher binding energy of 1, 4-dioxane exhibits with the β framework, rather than a clear geometrical match between the 'template' and the framework.

In order to investigate this further, two different approaches were taken. In the first, deuterated AlMePO- β (Al₂(CD₃PO₃)₃) was prepared using d₈-1, 4-dioxane and investigated by low temperature neutron diffraction (HRPD) in an attempt to locate the minimum energy of 1, 4-dioxane within the channels. Analysis of this diffraction data was not able to locate unambiguously the position of the 1, 4-dioxane molecules within the channels. In the second approach, AlMePO- β (Al₂(CH₃PO₃)₃) was prepared using d₈-1, 4-dioxane. The mobility of the dioxane, measured by ²H quadrupole echo NMR, was compared with that of the same molecule loaded in AlMePO- α prepared from AlMePO- β as described in section 5.2.

In this section a comparative analysis of the dynamics of 1, 4-dioxane within AlMePO- β and AlMePO- α frameworks by means of ²H NMR is reported.

5.3.2 Synthesis and characterisation of AlMePO- β synthesised from d_8 -1, 4-dioxane

Deuterated AlMePO- β was synthesised as described in the previous section (5.2) but using as a template perdeuterated d_8 -1, 4-dioxane (1, 4-dioxane- d_8 99.5 at. % D, GOSS Scientific Instrumental). The XRD pattern of the sample (Figure 5.3.2.1), agrees with published results [1], and showed that the product was a pure phase. ^{13}C NMR spectra of the sample (Figure 5.3.2.2) presented two resonance signals (δ 12.7, 67.7), also in agreement with previous works [13]. The first, broad signal, corresponds to the methyl groups. The second, narrow signal, is due to the 1, 4- d_8 -dioxane in the solid. Through TGA analysis (Figure 5.3.2.3) a weight loss of ~ 6.12 % *wt* was detected between 100 and 600° C. According to V. C. Carter *et al* [13], this weight loss is due to the removal of the 1, 4- d_8 -dioxane molecules from the micropores: 6.12 % *wt* corresponds to nine d_8 -1, 4-dioxane molecules per unit cell.

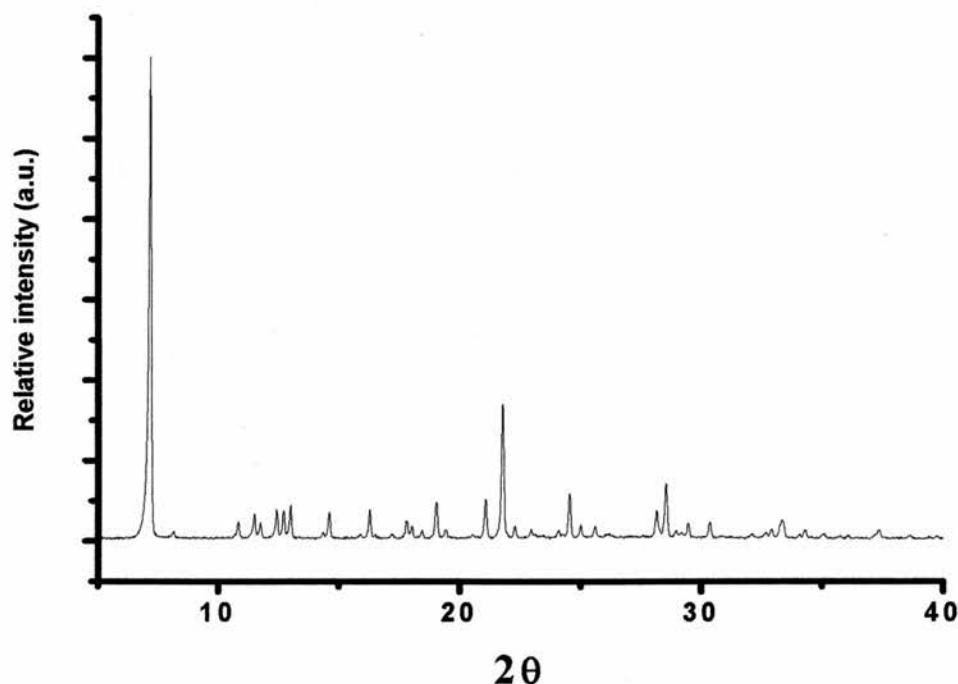


Figure 5.3.2.1. XRD pattern of AlMePO- β synthesised from d_8 -1, 4-dioxane.

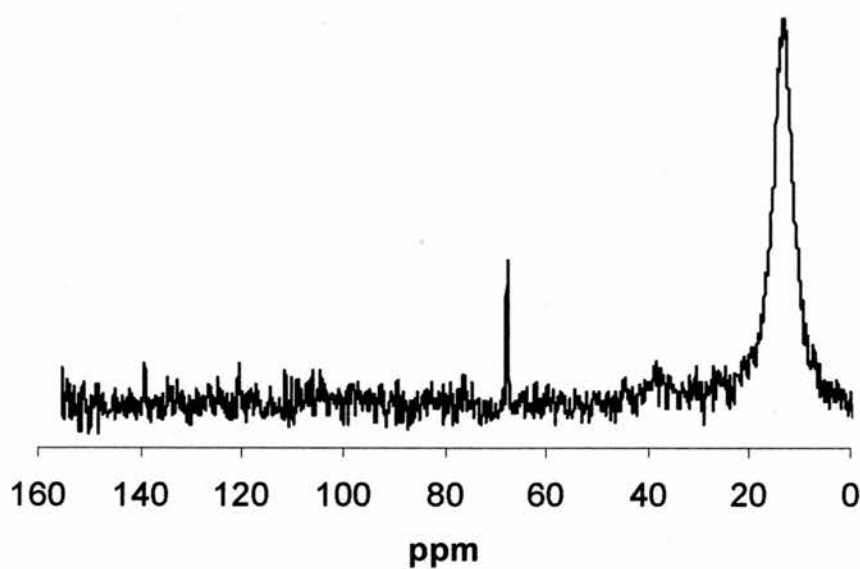


Figure 5.3.2.2. ^{13}C NMR spectra of an as-synthesised sample of AlMePO- β synthesised from 1, 4- d_8 -dioxane.

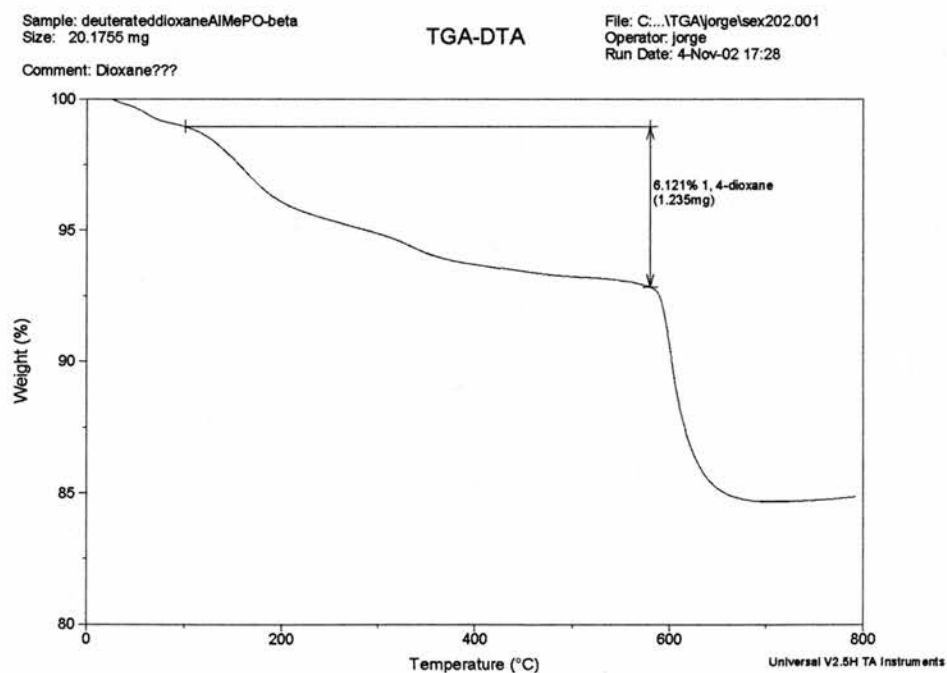
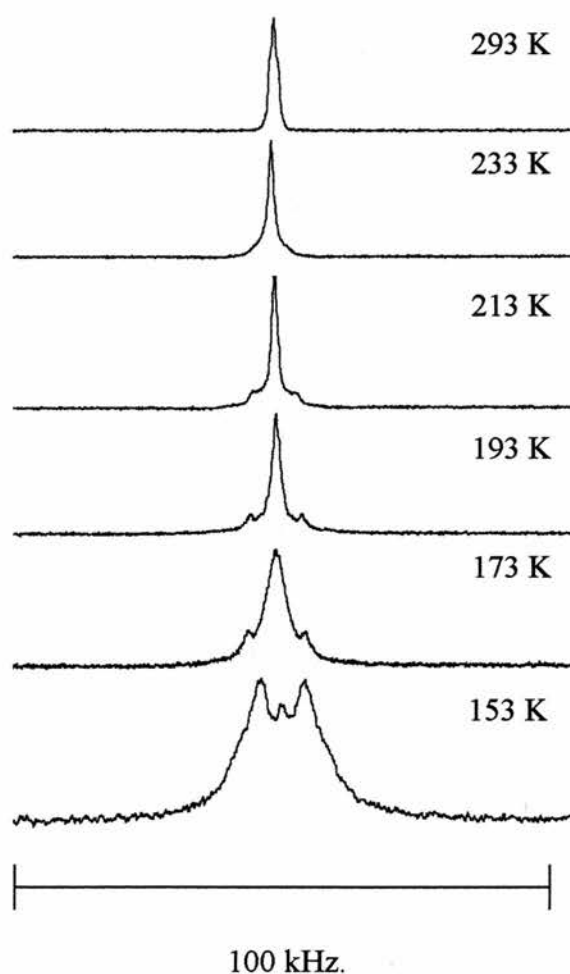


Figure 5.3.2.3. TGA analysis performed under flowing nitrogen on AlMePO- β containing d_8 -1, 4-dioxane. The amount of template found in this sample was 6% in weight.

5.3.3. Variable temperature quadrupole ^2H NMR spectra and T_1 longitudinal relaxation time constant measurements of d_8 -1, 4-dioxane in AlMePO- β

Figure 5.3.3.1 presents ^2H NMR spectra of d_8 -1, 4-dioxane in AlMePO- β at different temperatures. At all temperatures the observed signals are narrow indicating a large averaging of the quadrupole interaction due a rapid motion of the C-D bonds of the template. At 293 K, the signal is very narrow, 2.3 kHz wide. Decreasing temperature the signal width decreases. Table 5.3.3.1 summarises the widths of all the signals (measured at half peak maximum). Note also that with the decrease in temperature two singularities, 10 kHz apart, appear at the base of the spectrum.



Temperature (K)	Signal width (kHz)
293	2.3
233	1.4
213	1.3
193	2.3
173	10.1
153	16.0

Table 5.3.3.1 Summary of the signal width in kHz, measured at half peak maximum, as a function of the temperature.

Figure 5.3.3.1. Quadrupole ^2H NMR spectra of d_8 -1, 4-dioxane in AlMePO- β at different temperatures.

Temperature (K)	T_1 ms ⁻¹
293	652
233	190
213	124
193	70
173	44
153	14

Table 5.3.3.2. Summary of the T_1 relaxation time constant values calculated for 1, 4- d_8 -dioxane in AlMePO- β at different temperatures.

T_1 relaxation time constant of d_8 -1, 4-dioxane were measured as a function of the temperature. Results are summarised in table 5.3.3.2 and Figure 5.3.3.2. These experiments were carried out using the saturation recovery pulse sequence described in the characterisation techniques chapter.

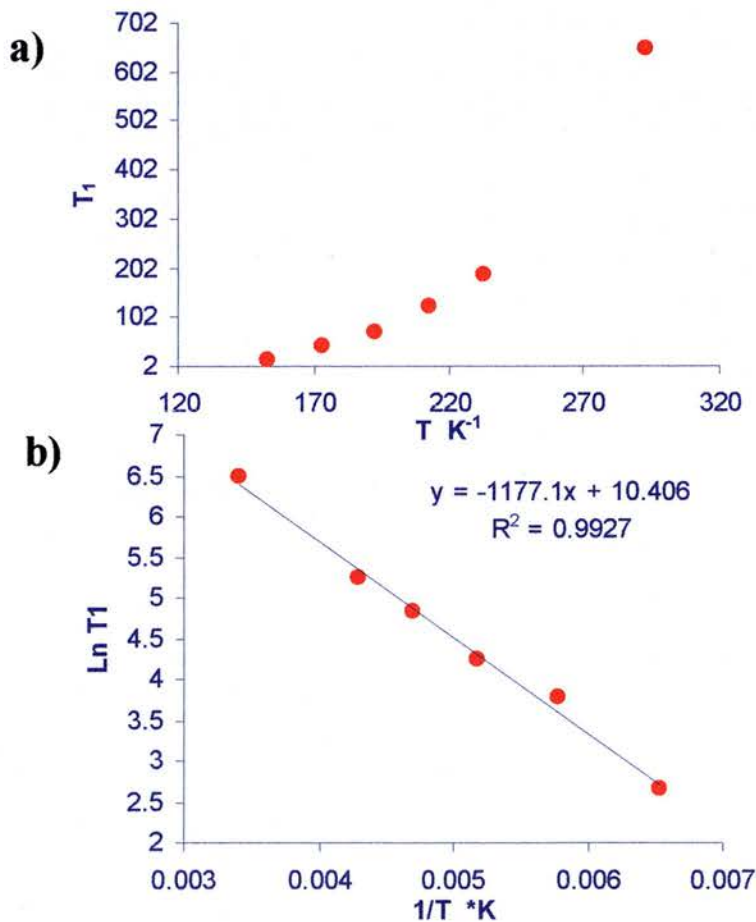
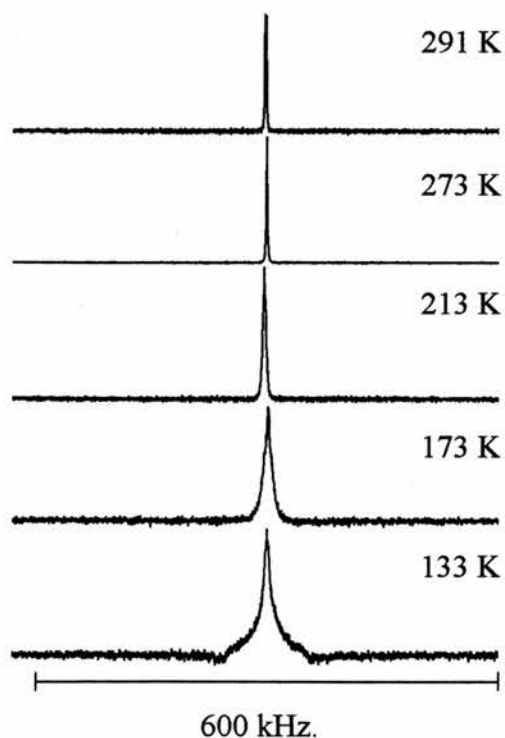


Figure 5.3.3.2. a) Temperature dependence of the T_1 longitudinal relaxation time constant and b) Arrhenius plot for $\ln T_1$ vs. $1/T$ for 1,4- d_8 -dioxane in AlMePO- β .

T_1 relaxation time constants decrease exponentially with temperature as the rotation of the molecules approach the Larmor frequency of deuterium in our magnetic field (76.78 MHz). The theoretical minimum of the curve seems to be below the temperature range studied in this work and therefore, it can be concluded that the rotation of C-D bonds should be faster than the Larmor frequency for all the experimental temperature range. It is possible to estimate an apparent activation energy for the rotations of the 1,4-dioxane from the slope of the Arrhenius plot present in Figure 6.3.5. The calculated activation energy was 9.8 (± 0.4) kJ/mol.

5.3.4. Variable temperature quadrupole ^2H NMR spectra and T_1 longitudinal relaxation time constant measurements of d_8 -1, 4-dioxane loaded in AlMePO- α

AlMePO- α was synthesised from AlMePO- β as described in the previous chapter and was loaded with 6% wt of 1, 4- d_8 -dioxane (1, 4-dioxane- d_8 99.5 at. % D, GOSS Scientific Instrumental) following the methodology described in chapter 2. Figure 5.3.4.1 and table 5.3.4.1 summarise the results of the quadrupole ^2H NMR measurements at different temperatures.



Temperature (K)	Signal width in AlMePO- α (kHz)
291	3.0
273	1.9
213	6.0
173	12
133	11

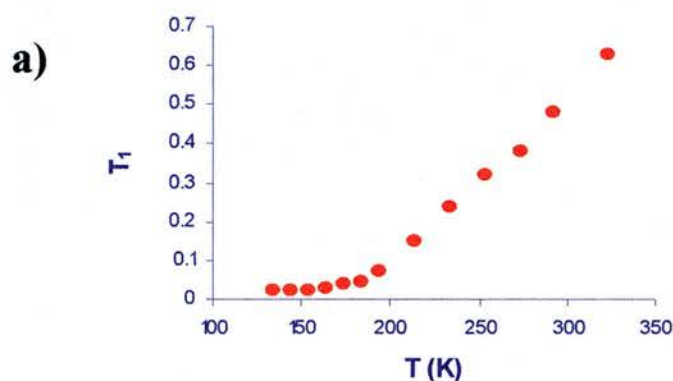
Table 5.3.4.1. Summary of the signal width (in kHz), measured at half peak intensity, as a function of the temperature found for 1, 4- d_8 -dioxane loaded in AlMePO- α

Figure 5.3.4.1. Quadrupole ^2H NMR spectra of d_8 -1, 4-dioxane in AlMePO- α at several temperatures.

At high temperatures the spectra of Figure 5.3.4.1, similar to the spectra recorded in AlMePO- β , are narrow signals that slightly increase their widths with the reduction of the experimental temperature (see table 5.3.4.1). The widths of the signals at 298 and 213 K, measured at half peak intensity, are 3 and 6 kHz respectively. At 153 and 133 K the spectra conserves its shape but the width observed are 13 and 21 kHz, at half peak intensity.

T_1 relaxation time constant measurements were also performed on this solid. Results are summarised in table 5.3.4.2 and Figure 5.3.4.2. The dependence of the T_1 values of dioxane α also seems to reach a minimum at ~ 140 K although it is not as well defined as in β .

As in AlMePO- β , it is also possible to estimate an apparent activation energy for the rotation of 1, 4-dioxane in AlMePO- α from the slope of the Arrhenius plot presented in Figure 7b. The activation energy was $7.5 (\pm 0.4)$ kJ/mol.



Temperature K ⁻¹	T_1 ms ⁻¹
323	630
291	481
273	380
253	318
233	237
213	150
193	70
183	45
173	36
163	27
153	23
143	22
133	24

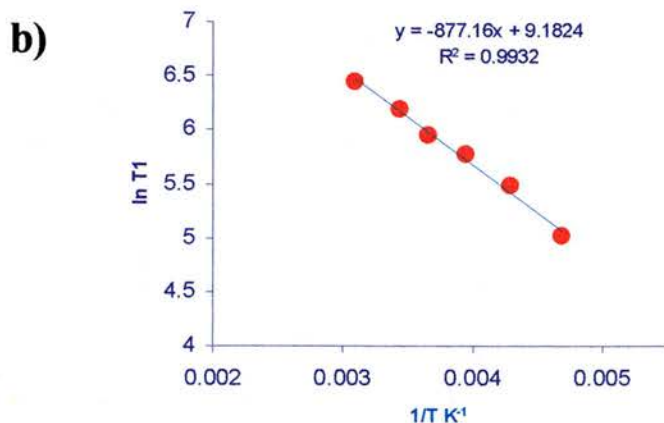


Table 5.3.4.2. Summary of the T_1 relaxation time constant values calculated for d_8 -1, 4-dioxane in AlMePO- α at different temperatures.

Figure 5.3.4.2. a) Temperature dependence of the T_1 longitudinal relaxation time constant and b) Arrhenius plot for $\ln T_1$ vs. $1/T$ for 1, 4- d_8 -dioxane in AlMePO- α .

P. Grewal *et al* [15], who investigated the role of 1, 4-dioxane in stabilising the AlMePO- β polymorph relative to the AlMePO- α and found that there is not a good match between the geometry of 1, 4-dioxane and of the polymorphs and therefore dioxane exhibits disordered packing in both structures. In this work is also found that the binding energy between 1, 4-dioxane and AlMePO- β is higher than those for AlMePO- α . In this thesis, it has been found that the activation energy for the motion of 1, 4-dioxane in AlMePO- β is slightly higher than in AlMePO- α , which is compatible with the previous computational studies.

The nature of the rotational modes that cause the averaging of the quadrupole interaction are almost impossible to elucidate by a line shape analysis of the ^2H spectra due to the narrowness of the signals and due to the flexibility of the 1,4-dioxane molecule. (The ^2H NMR spectra of frozen *d*₈-1, 4-dioxane is already a narrow line 300 Hz broad at half peak intensity).

5.4. Dynamics of methanol, isobutane and ethane in AlMePO- α , AlMePO- β and AlPO₄-5

5.4.1 Introduction

This section presents a comparative study of the dynamics of methanol, isobutane and ethane in AlMePO- α , AlMePO- β and AlPO₄-5. These solids were synthesised according to the procedures described in section 5.2. While methanol is an example of a polar adsorbate, which should emphasise differences between the hybrids AlMePOs and the inorganic AlPO₄-5, isobutane and ethane are examples of light hydrocarbons that should be removed in the purification of hydrogen, one of the original aims of the EPSRC project.

5.4.2. Sample preparation for NMR experiments

The solids were loaded with the guest molecules using the method described in the characterisation technique chapter.

The amounts of deuterated guest molecules adsorbed in the solids were:

-1.5 wt % for ethane (Ethane-d₆ > 99 atom % D, CDN isotopes).

-1.5 wt % isobutane (2-methylpropane-2-d₁ (gas) 98% atom D, CDN isotopes). d₁-isobutane was chosen, rather than fully deuterated isobutane, in order to obtain clear information about the reorientations of the mass centre of molecule respect to the framework.

-2 wt % for methanol (D₃COH 99.5 % D, Cambridge isotopes laboratories, inc).

5.4.3 ^2H NMR studies of d_3 -methanol, d_1 -isobutane and d_6 -ethane in AlMePO- α , AlMePO- β and AlPO $_4$ -5

The acquisition of the ^2H NMR signal from these molecules is difficult for several reasons. The amounts adsorbed for these gas molecules is low, and so long acquisition times were required. However, liquid nitrogen evaporation restricted the length of time the probe could be kept at the necessary low temperatures. In the case of d_1 -isobutane, the acquisition of signal intensity was particularly acute because of the low abundance of ^2H in the molecule. In particular, the signal to noise ratio of the spectra from d_1 -isobutane in AlMePO- α is far from ideal. For ethane, the molecules are not strongly adsorbed in any of the solids at high temperature. Loading the samples with higher amounts at low temperature would lead to a dangerous build up of pressure in the sample tube as the temperature is increased. The small size of these three molecules results in a high degree of freedom and mobility, so that narrow lineshapes were often obtained that could not readily be analysed unambiguously. Nevertheless, a comparison of the lineshapes observed for these deuterated species in the three frameworks is informative and is discussed below.

Figure 5.4.3.1, 5.4.3.2 and 5.4.3.3 present ^2H NMR spectra of d_3 -methanol, d_1 -isobutane and d_6 -ethane respectively. In all figures, spectra at the left, centre and right corresponds to those from deuterated molecules observed in AlPO $_4$ -5, AlMePO- β and AlMePO- α respectively.

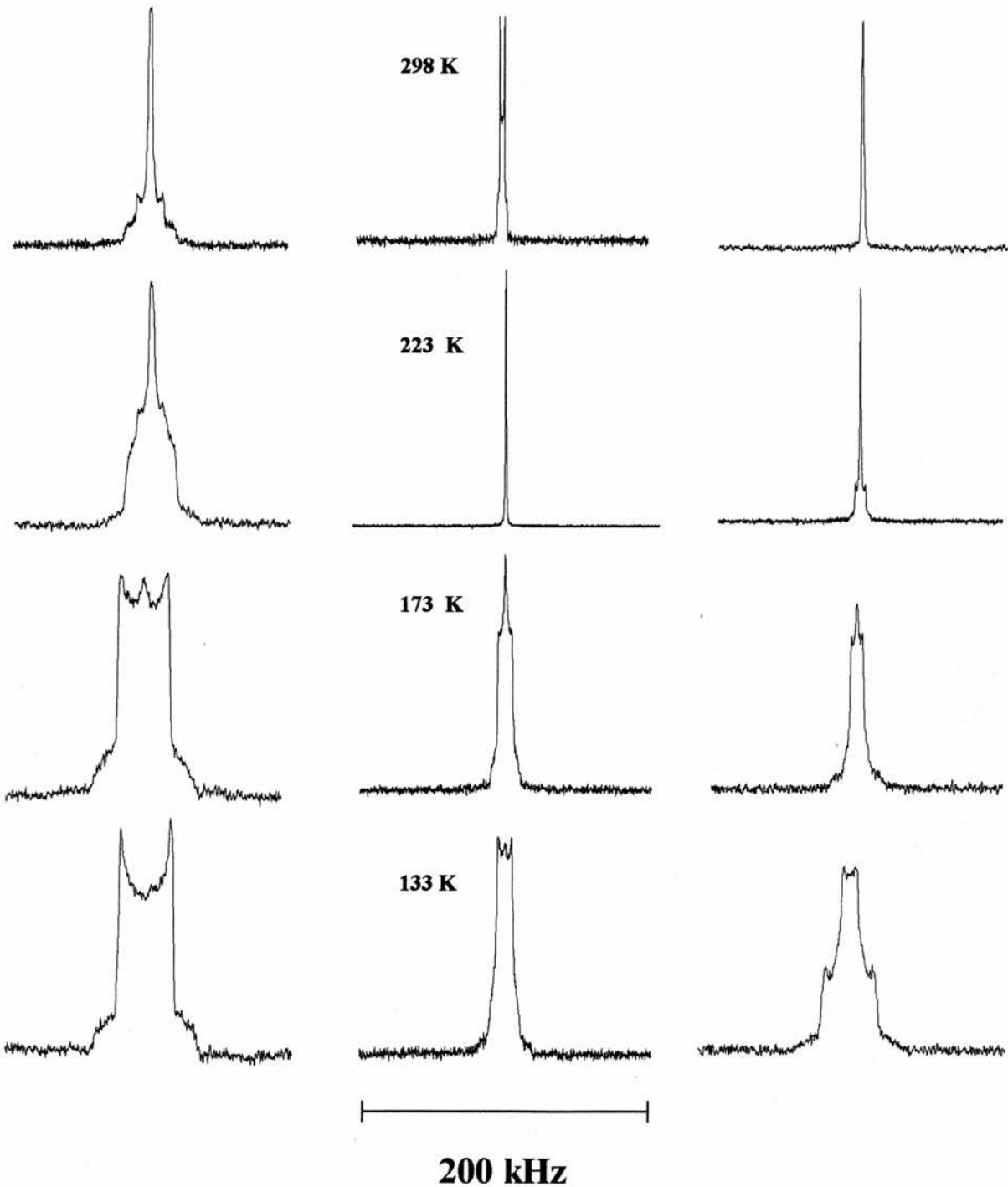


Figure 5.4.3.1. Solid echo ^2H NMR spectra of d_3 -methanol adsorbed in $\text{AlPO}_4\text{-5}$ (left), $\text{AlMePO-}\beta$ (centre) and $\text{AlMePO-}\alpha$ (right) at different temperatures. All experiments were performed using $45\ \mu\text{s}$ between the 90° pulses of the quadrupole echo sequence.

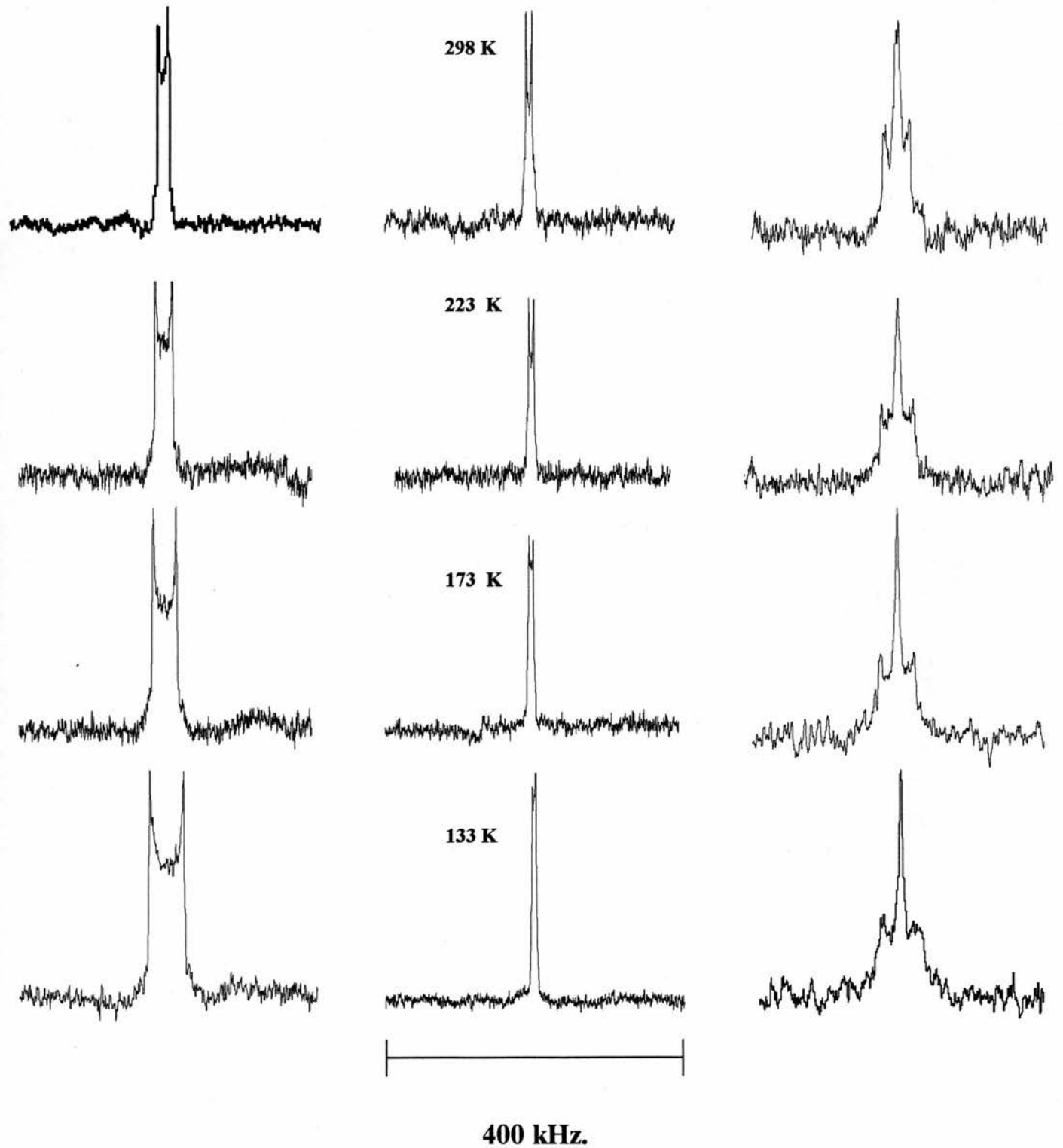


Figure 5.4.3.2. Solid echo ^2H NMR spectra of d_1 -isobutane adsorbed in $\text{AlPO}_4\text{-5}$ (left), $\text{AlMePO-}\beta$ (centre) and $\text{AlMePO-}\alpha$ (right) at different temperatures. All experiments were performed using $45\ \mu\text{s}$ between the 90° pulses of the quadrupole echo sequence.

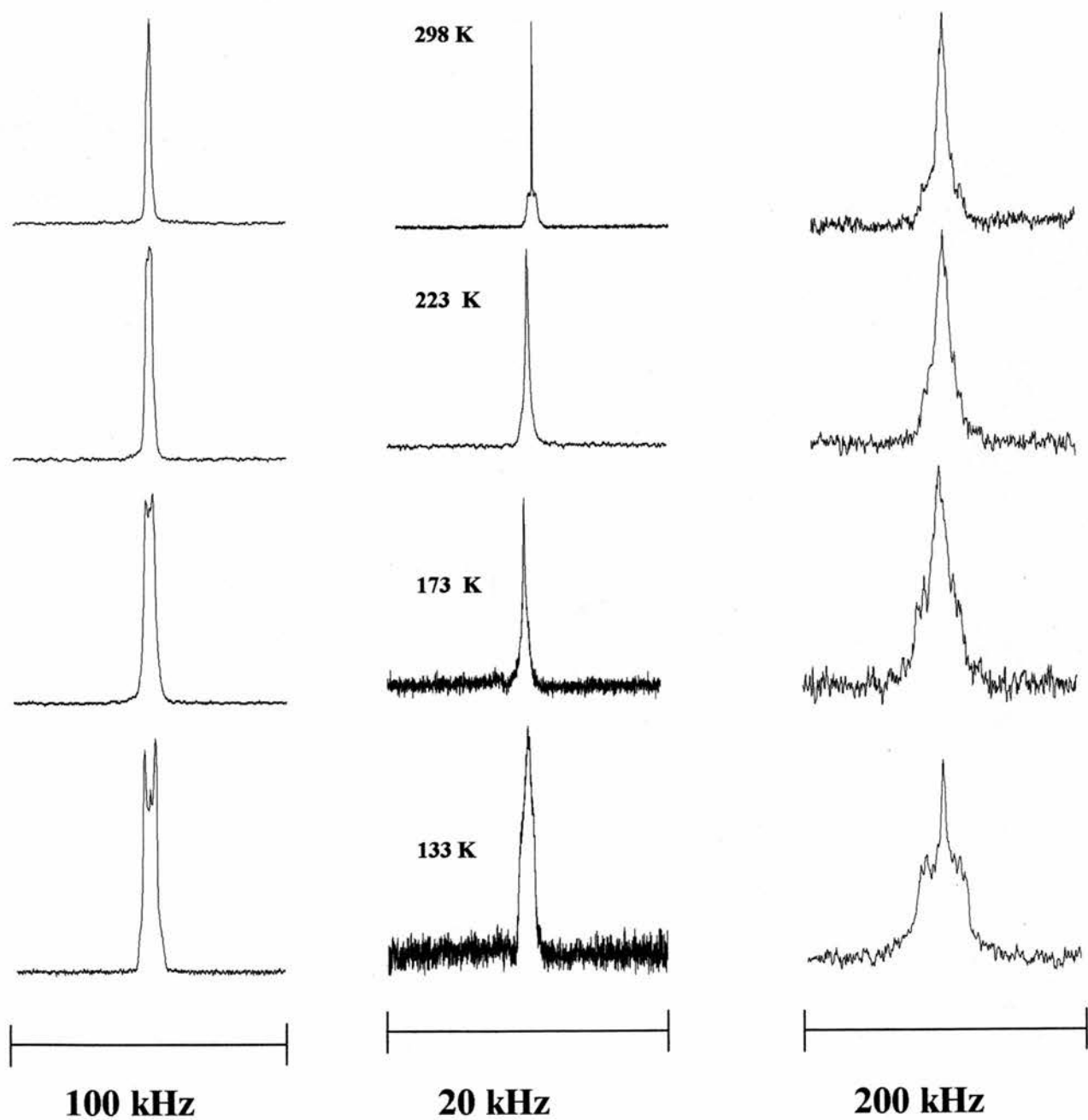


Figure 5.4.3.3. Solid echo ^2H NMR spectra of d_6 -ethane adsorbed in AlPO₄-5 (left), AlMePO- β (centre) and AlMePO- α (right) at different temperatures. All experiments were performed using 45 μs between the 90° pulses of the quadrupole echo sequence.

d₃-methanol

Starting with the experiments performed with *d₃*-methanol in AlMePO- β , the spectra recorded at 133 K shows a uniaxial powder pattern 8 kHz broad. Increasing the temperature to 223 K transforms the signal into a narrow line resulting from molecules undergoing fast isotropic rotations. At 298 K, the signal is a narrow uniaxial powder pattern, 3 kHz broad.

The ^2H NMR spectra acquired for *d₃*-methanol in AlMePO- α appears as a superposition of signals. Interpretation is complicated by the presence of some AlMePO- β impurity. Although this is at low level, it appears from the ^2H NMR (this chapter and chapter 6) that adsorbed molecules are not distributed statistically within the two solids. At 133 K, the signal corresponding to methanol molecules in AlMePO- α is a uniaxial powder pattern 33 kHz broad. (The narrower component of the spectra, 8 kHz broad, has the same width that the one observed for β at the same temperature). At 173 K the spectrum is similar to that recorded in β although an additional broad signal is present. At 223 K, a uniaxial powder pattern 7 kHz broad, is observed, which must correspond to methanol molecules in α , and at 298 K the signal is isotropic. The uniaxial powder patterns of 36 and 7 kHz width, at 133 and 223 K, which are not observed in AlMePO- β , indicate more constrained dynamics in AlMePO- α at these temperatures. Nevertheless, at 298 K the signal is completely isotropic.

Due to the nature of deuterium ($I=1$) and the technique used for the acquisition of the signals (solid echo), the relative area of the signals in each spectrum is not strictly proportional to the number of deuterons associated to the individual signals. Nevertheless, the area of the powder pattern of 8 kHz observed at 133 K is too intense to be produced exclusively by *d₃*-methanol within the AlMePO- β impurity (*ca.* 6 % of the solid) and there must be overlap with a component from methanol molecules in AlMePO- α .

d₃-methanol in AlPO₄-5 at 133 K (Figure 5.4.3.1, left), gives a powder pattern 40 kHz broad. This corresponds to methanol molecules that are almost static about their long axis. With the increase of temperature up to 223 K, a narrow signal is detected at zero frequencies. This corresponds to molecules undergoing big jumps within the channels. Further increase of the temperature produces a spectrum dominated by the narrow

component, indicating that the population of molecules undergoing big jumps has increased. At room temperature, the width of the uniaxial powder pattern observed at the base of the spectra is 20 kHz.

S. Hayashi [12] described the dynamics of d_3 -acetonitrile in $\text{AlPO}_4\text{-5}$ using two types of molecules: molecules freely rotating in at the centre of the channels and molecules with static long axis (see Figure below). The model used in that work allowed the simulation of the experimental spectra decreasing the population of the isotropic molecules with the decrease in temperature.

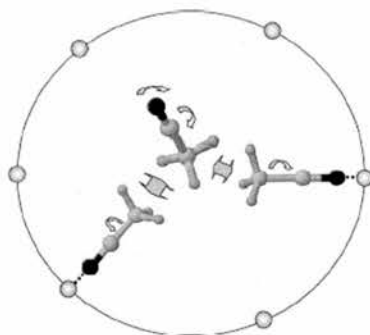


Figure 5.4.3.4. Representation of a free methanol molecule exchanging with molecules adsorbed on the walls. Image adapted from [12].

The ^2H line shapes observed in the present work for d_3 -methanol in $\text{AlPO}_4\text{-5}$ could be approximated by a similar dynamic model. At low temperatures, the methanol molecules are almost static about their long axis, probably due to a strong interaction of their alcohol group with the partial charges of the framework. Increasing the temperature results in highly mobile molecules, probably at the centre of the channels. The uniaxial powder pattern of 20 kHz width detected at 298 K could be associated with static and isotropic species whose exchange rate is coupled within the NMR time scale (Note that 20 kHz is similar to $42/2$ kHz. $42/2$ kHz would be the effective QCC experience by a deuteron atom in a methyl group that, in addition to the three fold axis rotation, is exchanging with another deuteron site with QCC equal to 0 kHz, assuming equal probability for the deuteron atom at the two sites).

As previously explained, unambiguous analysis in terms of a rotational model associated with these signals is not possible, but it is notable that the effective QCC observed for the deuterons at 133 K in AlMePO- β is four times smaller than that observed at the same temperature in AlPO₄-5. According to this, it seems that the mobility of methanol is higher in AlMePO- β than in AlPO₄-5, despite the smaller diameter of its channels.

*d*₁-isobutane

Figure 5.4.3.2 presents the spectra corresponding to *d*₁-isobutane. Uniaxial powder patterns are observed at all temperatures for AlPO₄-5, AlMePO- β and AlMePO- α . The widths of all the signals are summarised in table 5.4.3.1. The narrow component observed in AlMePO- α is thought to be associated with species adsorbed in the impurities and is ignored in the following discussion.

Width of the signal in kHz.			
T/K	AlPO ₄ -5	AlMePO- β	AlMePO- α
298	17	9	37
223	26	8	42
173	35	6	43
123	49	5	48

Table 5.4.3.1. Summary of the signal widths corresponding to the spectra presented in Figure 5.4.3.2.

The signal is produced by the single deuteron atom in the isobutane molecule and not by the deuterons in the methyl group and therefore rotations of the molecule about the C-D bonds would not induce any average of the quadrupole interaction. A static C-D bond would produce a powder pattern signal 126 kHz broad, corresponding to a QCC equal to 168 kHz. The narrow signals observed in all the materials indicate that the mobility

of isobutane is very high. Figure 5.4.3.5 presents a plot of the effective QCC as a function of the temperature for each of the signals in Figure 5.4.3.2. At 133 K, the effective QCC experienced by the deuterons AlMePO- α and AlPO₄-5 is similar. In AlMePO- β this is smaller, suggesting a higher degree of mobility for the guest molecule in its framework.

The increase in temperature produces a considerable decrease of the QCC in AlPO₄-5. On the other hand, the change of the effective QCC in the hybrid frameworks is smaller. In AlMePO- β , the quadrupole interaction increases slightly with the increase of temperature.

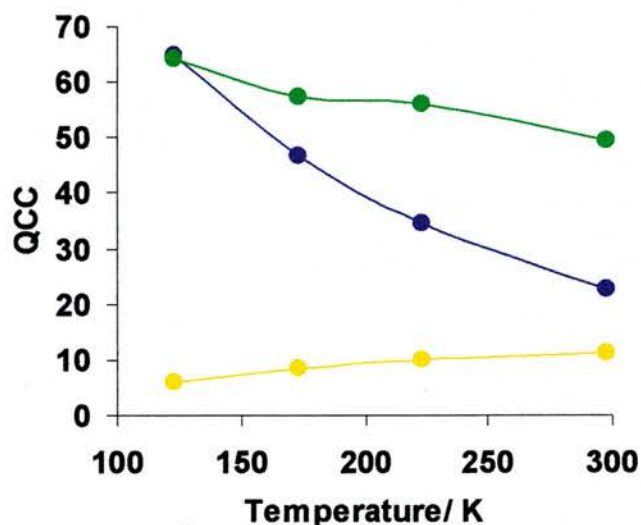


Figure 5.4.3.5 .Summary of the effective QCC (in kHz) as a function of the temperature observed for d₁-isobutane in AlMePO- α (green), AlMePO- β (yellow) and AlPO₄-5 (blue).

In AlMePO- β , the narrow lines observed denote a high degree of rotational freedom for isobutane. On other hand, in AlPO₄-5, despite its larger pore diameter, the mobility of isobutane seems more restricted. This is probably due to the more polar framework of the inorganic material.

Note also that isobutane is much more constrained in AlMePO- α than in AlMePO- β . It is clear that isobutane exhibits a larger rotational freedom in the cylindrical channels of AlMePO- β than in the triangular shape pores of AlMePO- α . Adsorption isotherms of isobutane at 273 K in both AlMePO- α and - β were reported by Maeda [1] (see Figure 5.4.3.6.). It is interesting that, despite the higher interaction that isobutane exhibits in AlMePO- α , the gas uptake of isobutane by AlMePO- β at low pressures is much higher. ^2H NMR suggests that the smaller loss of adsorption entropy of isobutane upon adsorption in AlMePO- β could be the reason for this higher isobutane uptake.

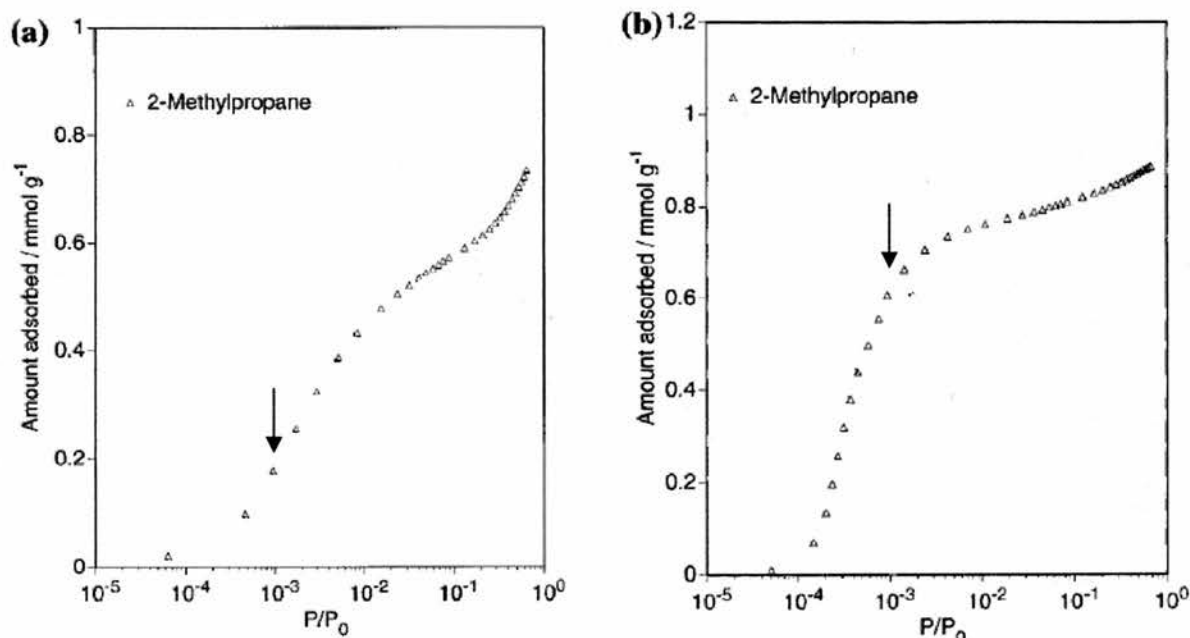


Figure 5.4.3.6. Adsorption isotherms of isobutane in (a) AlMePO- α and (b) AlMePO- β at 273 K reported by Maeda et al. Figures adapted from ref [1].

d₆-ethane.

Quadrupole ^2H NMR spectra of ethane adsorbed in the three frameworks are presented in figure 5.4.3.3. In the three hosts, the narrow line shapes indicate major decrease of the quadrupole interaction due to the motion of the guest species. Due to the small width of the signals detected in AlMePO- β , the acquisition time used to record the free induction decays in this sample (0.04 s) were twenty times larger than those used for the other two frameworks.

In $\text{AlPO}_4\text{-5}$, d_6 -ethane produces a powder pattern spectrum 5 kHz broad at 133 K. At 298 K the signals becomes a narrow isotropic line 1.6 kHz broad at half peak intensity.

The signals detected in $\text{AlMePO-}\beta$ are isotropic and extremely narrow at all temperatures. At 298 K, it can be seen at the base of the spectra a signal, 0.8 kHz broad at half peak intensity, with a spike on top of it. This spike, 0.05 kHz broad at half peak intensity is not due to transmitter of the spectrometer, must be associated with gas molecules outside $\text{AlMePO-}\beta$. (In $\text{AlPO}_4\text{-5}$ and $\text{AlMePO-}\alpha$, these gas molecules, likely to be present during the experiment, were not detected due to the lower acquisition time use for the FIDs that lead to a lower resolution of the spectra). At 133 K the width of the signal at half peak intensity is 1.2 kHz.

The ^2H NMR spectra of d_6 -ethane adsorbed in $\text{AlMePO-}\alpha$ are interesting although, as for previous experiments performed with methanol and isobutane, they are complex. Over the entire temperature range the spectra looks like the superposition of different signals corresponding to ethane molecules in different dynamic states (Note the presence of shoulders on the triangular shape signal at periodic frequencies at different temperatures). At 133K the broad component of the spectra has a width of 38 kHz, quite similar to the 42 kHz of a rotating methyl group. A narrow component is observed that could be associated with ethane molecules in the impurity β . Increase in temperature reduced the overall width of the spectra but not the shape of the signal.

5.4. Conclusions.

Although the high mobility of these molecules makes interpretation via MXQET very difficult, some interesting observations can be made. For each molecule, the mobility is highest in AlMePO- β , which possesses a channel that is close to cylindrical with an homogeneous distribution of rapid rotating methyl groups over the internal surface. This leads to remarkably narrow lineshapes, even for the polar methanol. By contrast, AlPO₄-5, which is fully inorganic, constrains the motion of methanol much more strongly, even though the free diameter of its cylindrical pores is larger. This must be attributable to stronger interactions from the more polar framework. The situation with AlMePO- α appears intermediate between the AlMePO- β and AlPO₄-5 systems, although the influence of unconverted AlMePO- β impurities complicates the interpretation. The more acutely triangular shape of AlMePO- α constrains the motion.

References for chapter 5.

- [1] K. Maeda, Y. Kiyozumi, F. Mizukami, *J. Phys. Chem. B.*, **1997**, 101, 4402.
- [2] C. Schumacher, J. Gonzalez, P. A. Wright, N. A. Seaton, *Phys. Chem. Chem. Phys.*, **2005**, 7, 2351.
- [3] J. L. C. Rowsell, O. M. Yaghi, *Microporous Mesoporous Mater.*, **2004**, 73, 3.
- [4] V. J. Carter, J. P. Kujanpää, F. G. Riddell, P. A. Wright, J. F. C. Turner, C. R. A. Catlow, K. S. Knight, *Chem. Phys. Lett.*, **1999**, 313, 505.
- [5] J. F. M. Denayer, R. A. Ocakoglu, I. C. Arik, C. E. A. Kirschhock, J. A. Martens, G. V. Baron, *Angew. Chem. Int. Ed.*, **2005**, 44, 400.
- [6] H.W.Spiess. *Advances in polymer science*, **1985**. 66. 24; H.W.Spiess. *Colloid and polymer science*, **1983**. 261. 193; H.W.Spiess, *Chem. Rev.*, **1991**, 91, 1321; K. Schmidt-Rohr, W. Spiess, *Academic Press*, **1994**.
- [7] C. I. Ratcliffe, D. V. Soldatov, J. A. Ripmeester, *Microporous Mesoporous Mater.*, **2004**, 73, 71.
- [8] R. N. Devi, M. Edgar, J. Gonzalez, A. M. Z. Slawin, D. P. Tunstall, P. Grewal, P. A. Cox, P. A. Wright, *J. Phys. Chem. B.*, **2004**, 108, 535.
- [9] S. R. Miller, E. Lear, J. Gonzalez, A. M. Z. Slawin, P. A. Wright, N. Guillou, G. Ferey, *Dalton T.*, **2005**, in press.
- [10] Shin-Ichi Nishikiori, *Journal of inclusion phenomena and macrocyclic chemistry*, **1999**, 34, 331.
- [11] I. Kustanovich, H. M. Vieth, Z. Luz, S. Vega, *J. Phys. Chem.*, **1989**, 93, 7427; I. Kustanovich, D. Fraenkel, Z. Luz, S. Vega, H. Zimmerman, *J. Phys. Chem.*, **1988**, 92, 4134.
- [12] S. Hayashi, *Microporous Mesoporous Mater.*, **2003**, 66, 253.
- [13] V. J. Carter, P. A. Wright, J.D. Gale, R.E. Morris, E. Sastre, J. Perez-Pariente, *J. Mater. Chem.*, **1997**, 7, 2287.
- [14] Chia-Ming Chen, Jih-Mirh Jehng, *Catal. Lett.*, **2003**, 85, 73.
- [15] P. Grewal, N. Radhamonyamma, J. Gonzalez, P. A. Wright, P. A. Cox, *Stud. Surf. Sci. Cat.*, 154: 1777-1783 Part A-C 2004.

Chapter 6.

***Dynamics of aromatic
molecules in AlMePO- β ,
AlMePO- α and AlPO₄-5***

6.1 Introduction

Quadrupole ^2H NMR is a powerful method to examine the dynamics of C-D bonds [1]. With the help of appropriate computer programs, ^2H NMR spectra of monoaromatic molecules (like benzene, toluene or para-xylene) are relatively easy to simulate due to the rigid nature of these molecules. Therefore, through ^2H NMR wideline analysis it is possible to obtain very accurate information about the dynamical model of these molecules.

The motion of benzene, toluene and para-xylene have been investigated by ^2H NMR in several systems. A good example of this sort of study was published by Nishikiori [2] who performed an extremely detailed analysis of the out-of-plane motion of benzene in an inclusion compound making use of single crystal structure data and ^2H NMR. The work performed by Ratcliffe *et al.* [3] concerning the dynamics of benzene in a very flexible metal-organic framework inclusion compound is also relevant here due to the hybrid nature of the host. ^2H NMR was used to study the relation between the dynamics of the guest molecules and the dimensions of the flexible framework. From our own group's studies [4] ^2H NMR was of use to understand crystallisation of a Zn 2, 6-naphthalene dicarboxylate host framework in the presence of the aromatic hydrocarbons benzene, toluene and p-xylene (see Figure 6.1.1). The structure includes para-xylene with high selectivity from mixtures of xylene isotherms. In this work, ^2H NMR experiments provided information about the relation between the shape of the channels and the origin of the selectivity for the uptake of para-xylene and other aromatics from solution.

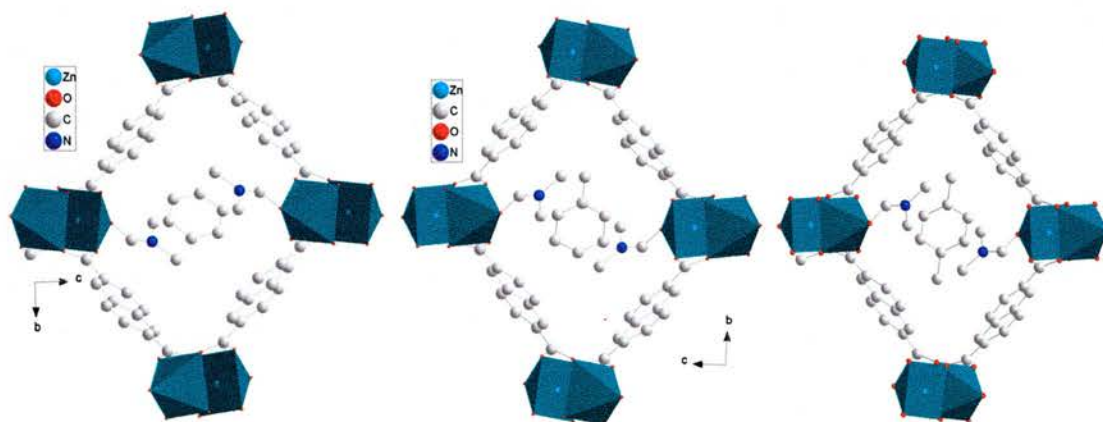


Figure 6.1.1. Representation of zinc 2, 6-naphthalene dicarboxylate frameworks crystallized in the presence of benzene (left), toluene (centre) and para-xylene (right). It was found by ^2H NMR that benzene was clicking fast about its C_6 axis but, on the other hand, toluene and para-xylene were static about their long axis [4].

In all these studies, ^2H NMR was used to link the time averaged structural information obtained by diffraction techniques like single crystal XRD, with the local dynamic behavior of the guest species. Interpretation of the ^2H NMR spectra of solids in which the deuterons are either chemically-bonded to the host framework, or in a molecule located by diffraction techniques, are relatively straightforward. The situation is more complex when the guest molecules are free within the pores of their host framework and there is no crystallographic information about their position. Sometimes, under these circumstances, the ^2H NMR spectra can be ambiguous because several dynamic states could result in the same spectrum. In this case, it is necessary to record a collection of spectra under different conditions (i.e. temperature, guest molecules loading level, time between the quadrupole sequence...) in order to find a dynamic model compatible with all the spectra.

This is the context of most of the work presented in this chapter and also of numerous publications about the dynamics of molecules with the channels and cavities of inorganic zeolites. Closely related examples to the studies of this thesis included those of Vega and co-workers [5] concerning the dynamics of para-xylene, toluene and benzene in Na-ZSM-5 and ZSM-5.

Characterisation of the dynamics of adsorbate molecules in porous solids is important an issue in order to understand the adsorption properties of porous materials. This has been highlighted recently by Denayer *et al.* who recently shown that the rotational mobility of molecules in medium pore zeolites plays an important part in the effects of selectivity for the adsorption of alkanes [6].

The organic-inorganic microporous hybrids AlMePO- α and - β are two closely related polymorphs that exhibit very different adsorption properties from those of pure inorganic zeolitic solids [7-9]. Furthermore, the characteristic triangular shape of the pore in the α -polymorph results in a stepped isotherm for nitrogen [10]. The pore sizes of these AlMePOs, $\sim 6 \text{ \AA}$ in diameter, are similar to those of ZSM-5 type zeolites that are known to show strong shape selective effects in the adsorption and separation of xylene isomers. The origin of this selectivity has been elucidated in part by wide-line ^2H NMR spectroscopy and subsequent lineshape analysis [5].

This chapter describes a study of the mobility of monoaromatic hydrocarbons benzene, toluene and para-xylene within the two AlMePOs polymorphs through quadrupole ^2H NMR wideline analysis. It is the aim of this study to determine the effective free space for the molecules and the constraints on molecular motion that the pores exert. As in chapter 5, $\text{AlPO}_4\text{-5}$ has been included as a host in this study to compare the dynamics of guest species in an inorganic molecular sieve.

It has to borne in mind that in the absence of crystallographic information about the position of the adsorbed molecules, the results yielded by ^2H NMR are models compatible with the real dynamics of the molecule but not proof of it. In this thesis, some of the models proposed on basis of the NMR experiments are compared with results found in parallel by Cox (Portsmouth University) via molecular dynamics simulations (MD).

6.2 Experimental

Table 6.2.1, below, summarises the experiments described in this chapter.

Framework	Adsorbed molecule	Isotope and loading level	Temperatures studied (K)
AlMePO- β	Para-xylene	d_3 , d_3 -para-xylene at 1.5 wt %	373, 298, 133
	Toluene	d_3 - and d_9 -toluene at 4.5 wt %	298, 223, 173, 133
	Benzene	d_6 -benzene at 1.5 wt %	315, 303, 287, 273, 253, 223, 203, 183, 151, 133
		d_6 -benzene at 4.5 wt %	310, 193, 173, 153, 123
AlMePO- α	Para-xylene	d_3 , d_3 -para-xylene at wt 1.5 %	323, 298, 223, 133
	Toluene	d_3 -toluene at 4.5 wt %	298, 223, 173, 133
		d_9 -toluene at 4.5 wt %	298, 223, 173, 153, 143, 133, 123
		d_9 -toluene at 4.5 wt %	298,223,173,133
	Benzene	d_6 -benzene at 1.5 wt %	291, 223, 200, 173, 153, 133
		d_6 -benzene at 4.5 wt %	353, 291, 273, 223, 183, 153, 133, 123
AlPO $_4$ -5	Para-xylene	d_3 , d_3 -para-xylene at 1.5 wt %	298,223,173,133
	Benzene	d_6 -benzene at 4.5 wt %	298, 223, 173, 133

The wide-line ^2H NMR spectra and interpreted dynamics of para-xylene in AlMePO- β , AlMePO- α and AlPO $_4$ -5 will be discussed first because the modes of reorientation of this molecule are strongly constrained in the unidimensional channels of these host frameworks and consequently the spectra are straightforward to analyse. Only the d_3 -, d_3 -isotopomer was examined, since the main aim of this series of experiments was to determine the effective free diameter of the channels as experienced by para-xylene.

Toluene was chosen as a smaller aromatic molecule than para-xylene, but one that would still be unable to tumble freely within the pores. As well as investigating the reorientations of the molecule by analysing the NMR signal from the methyl group (as $-\text{CD}_3$ in d_3 -toluene) the motion of the aromatic ring was studied by using d_8 -toluene (fully deuterated) and d_5 -toluene (in which only the aromatic ring is deuterated).

d_6 -benzene was chosen as a molecular probe because of its simplicity and its closeness in kinetic diameter to the channel dimensions of the AlMePOs.

Experimental. Sample preparation

AlMePO- β , AlMePO- α and AlPO $_4$ -5 were synthesised according to the procedures explained in chapter 5. The solids were loaded with the aromatic hydrocarbons on a calibrated vacuum line using the method explained in the characterisation techniques chapter. According to the toluene adsorption capacity, at the loading levels chosen for the ^2H NMR experiments, the pores should not be full with guest molecules.

The guest molecules loading levels used in the different solids were:

-1.5 wt % for d_3 , d_3 -para-xylene.

-4.5 wt % for d_3 -toluene, d_5 -toluene and d_8 -toluene.

-1.5 and 4.5 wt % for d_6 -benzene.

Spectra simulation

The wide-line analysis of the spectra presented in this chapter was performed by means of computer simulation via MXQET and MXQET1 [11,12] compute code programs. Examples of the input files used for the simulations can be found in the appendix. For the simulations, the QCC of aromatic and aliphatic deuterons were 193 and 168 kHz, according to [13] and [14, 15] respectively.

6.3. d_3 , d_3 -para-xylene as a guest in AlMePO- β

^2H spectra for the labelled para-xylene are typical so-called Pake doublets, uniaxial powder patterns with sharp edges, over the entire temperature range studied (Figure 6.3.1). Analogous results were obtained using 35 and 150 μs between the refocusing pulses of the solid echo pulse sequence. Only the spectra obtained with 35 μs are shown. The distance between the 'horns' increases from 26 kHz to 29 kHz as the temperature is decreased from 373 K to 133 K. As a methyl ($-\text{CD}_3$) group clicking only about its C_3 axis (at the fast limit of motion) would produce a spectrum where these features were separated by 42 kHz, the molecule must be undergoing additional motion in relation to the aluminophosphonate framework. The most likely type of motion, given the geometry of the molecule-channel complex and the lineshape of the signal, is that the para-xylene is moving so that its long axis is moving between different sites on a cone. MXQET simulations, in which the half-angles of the cone of motion were varied to match the observed spectra, predict that the cone's half-angle decreases from 30° to 27° over the temperature range examined. These simulations are independent of the number of sites used to describe the motion of the molecule's long axis around the cone.

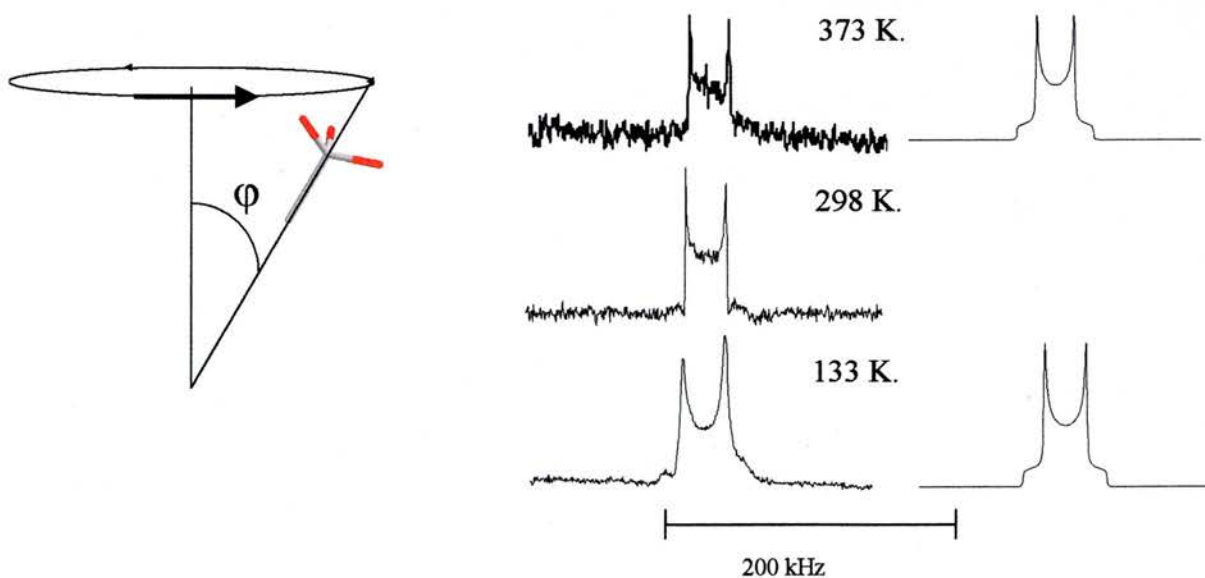


Figure 6.3.1. The quadrupole ^2H NMR spectra of d_3 , d_3 -para-xylene in AlMePO- β can be simulated assuming fast motion of the para-axis around three sites on a cone and associated rapid clicking of the CD_3 group around its axis (left) to give a good match (right) for a cone half angle of 30° at 373 K and 27° at 133 K.

6.4. d_3, d_3 -para-xylene as a guest in AlMePO- α

Quadrupole ^2H NMR spectra of d_3, d_3 -para-xylene adsorbed on the AlMePO- α sample are shown in Figure 7.4.1. At each temperature, two set of spectra were recorded using 35 and 150 μs between the 90° pulses of the quadrupole echo sequence. No differences in line shape were observed between both sets of spectra and only those obtained with 35 μs between the refocusing pulses are presented. Over most of the temperature range studied, the spectra appear as a superposition of two Pake doublets with different width. Noticeably, one set of signals has the same peak-to-peak separation as that observed for AlMePO- β , so this was attributed to signal from para-xylene adsorbed in the small amount of unconverted AlMePO- β .

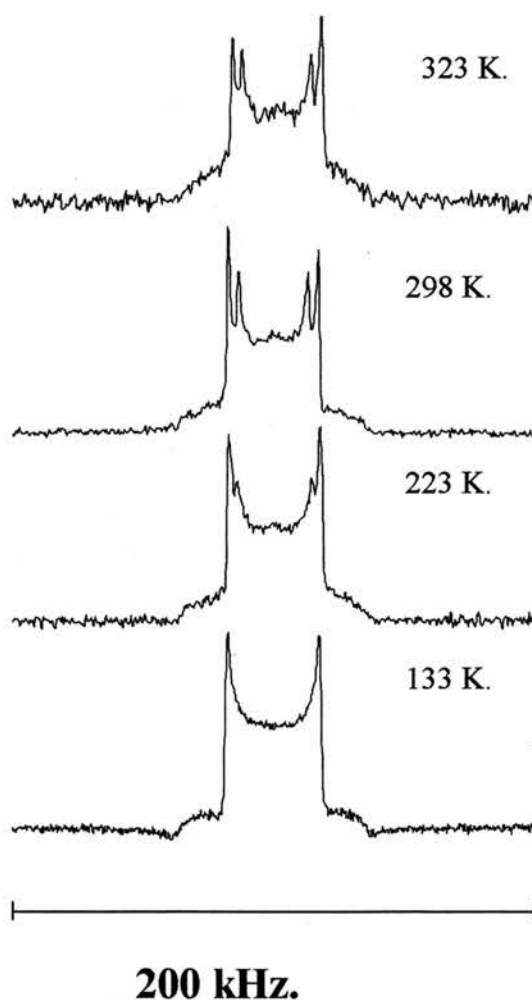


Figure 6.4.1. Quadrupole echo ^2H NMR of d_3, d_3 -para-xylene adsorbed in AlMePO- α

Although it was not possible to quantify accurately the relative intensities of the two signals, it appears that the para-xylene adsorbs preferentially onto the larger pore AlMePO- β at the higher temperatures, because the relevant ^2H signal is larger than expected on the basis of ^{31}P NMR of the amount of the unreacted AlMePO- β . The signal attributed to para-xylene in AlMePO- α is broader, with peak-to-peak separations increasing from 34.5 kHz (at 298 K) to 35.5 kHz (at 133 K). These lineshapes can be simulated by allowing the long axis of the xylene to move around cones with half-angles 19° and 18° , respectively.

It is interesting to note the small effect of temperature on the reorientation of the long axis of paraxylene molecule in AlMePO- α , compared to its change in AlMePO- β .

6.5. d_3 , d_3 -paraxylene as guest in $\text{AlPO}_4\text{-5}$

The spectra of d_3 , d_3 -para-xylene adsorbed in $\text{AlPO}_4\text{-5}$, shown in Figure 6.5.1, were recorded using 35 μs between the 90° pulses of the solid echo pulse sequence.

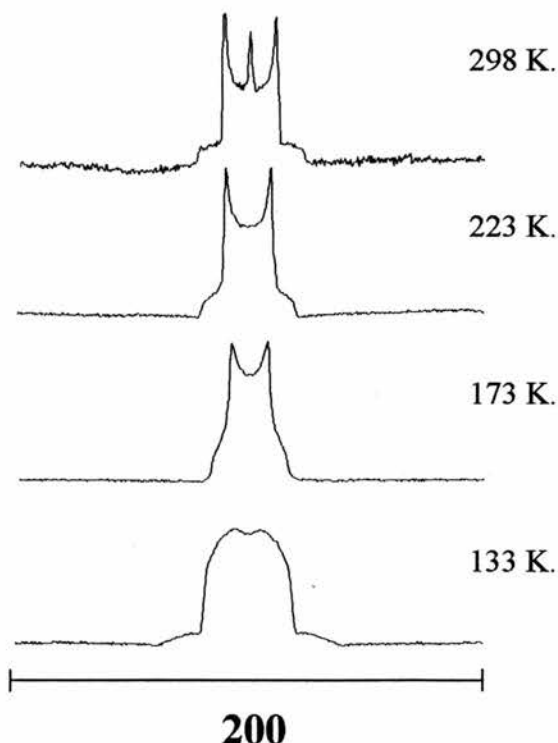


Figure 6.5.1. Quadrupole ^2H NMR spectra of d_3 , d_3 -paraxylene in $\text{AlPO}_4\text{-5}$ at different temperatures. These experiments were acquired with 35 μs between the 90° pulses of the solid echo pulse sequence.

For the AlMePOs, no changes in lineshape were observed using 150 μ s instead of 35 μ s. At 298, 223 and 173 K the signals are uniaxial powder patterns with 24, 22 and 15 kHz between the singularities, respectively. At 133 K the signals broadens and adopts a different shape. The width at half signal intensity is 36 kHz.

It is unlikely that para-xylene could rotate isotropically within the channels of $\text{AlPO}_4\text{-5}$, therefore, the spike at zero frequency detected at 298 K should be associated with molecules adsorbed on the external surface of the crystals. Note that the particle size of the sample is very small and that the toluene isotherm reveals surface adsorption of the vapour.

The powder patterns observed above 173 K are well defined and can be simulated using a cone type of motion of the methyl group. It is an interesting result that the width of the signal decreases with the increase of temperature. The values obtained for the cone angles at the different temperatures are 32, 34 and 40° at 298, 223 and 173 K. The cone angle increases with the decrease of temperature.

Numerous attempts to simulate the spectra at 133 K by a single dynamic state were unsuccessful. After many trials of calculations, it seems that the spectrum cannot be reproduced using a fast cone-type motion model for the long axis of the paraxylene molecule. This spectrum seems also unlikely to be associated with molecules reorientating in an intermediate exchange rate ($\sim 10^5$ Hz) because experiments performed with 35 and 150 μ s between the refocusing pulses of the solid echo pulse sequence gave the similar spectra. The line shape observed at 133 K could be associated with several para-xylene molecules undergoing reorientations with different cone angles. This is only speculative and more NMR experiments (for example, using different loading levels) or molecular dynamics analyses are required to understand the nature of this signal.

6.6. Summary and conclusions of the motion of paraxylene in *AlMePO-β, -α and AlPO₄-5*

The results show that ²H NMR of the d₃-, d₃-para-xylene molecule is a sensitive probe of the channel dimensions in AlMePO-β, -α, AlPO₄-5. The spectra are readily simulated by a model for the motion where the long axis moves around a cone. These experiments provide information about the accessible diameter of the microchannels, **L** according to Figure 6.6.1. If φ is the cone angle describing the cone type of motion for the molecule in the pore, then **I** is readily calculated taking into account the length of the paraxylene molecule from sp³-C to sp³-C, 5.78 Å¹, by the mathematical relation

$$I = 5.78 \sin \varphi \text{ \AA}$$

Then, **L** can be calculated taking into account the C-D distance (1.1 Å), the van der Waals radius for D (1.2 Å) and the angle θ, which is the angle between the C-D bond and a line perpendicular to the channel wall. It can be seen that θ = φ - 19.5°.

All these together make the accessible diameter **L**,

$$L = I + 2*(1.1*\cos\theta) + 2*1.2 \text{ \AA}.$$

The maximum cone angle found for the long axis of paraxylene in AlMePO-β, AlMePO-α and AlPO₄-5 are 30, 19 and 40° respectively. According to the mathematical relation presented before, the accessible pore diameters for para-xylene in AlMePO-β, AlMePO-α and AlPO₄-5 are 7.45, 6.47 and 8.2 Å (compared to crystallographic estimates of 6.0, 5.3 and 8.6 Å respectively).

¹ The bond lengths used for this estimation were 1.38 and 1.51 Å for C(aromatic)-C(aromatic) and C(aromatic)-Csp³ respectively.

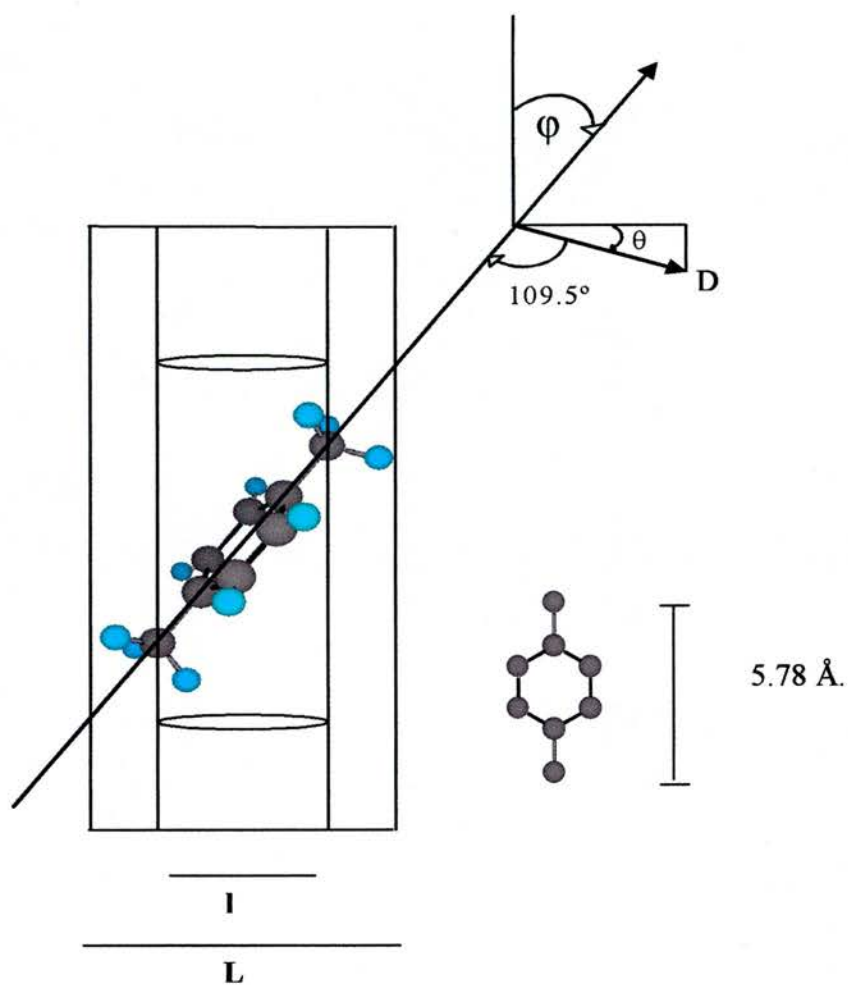


Figure 6.6.1. Geometrical model use to calculate the accessible pore diameter for para-xylene in AlMePO- α , - β and AlPO $_4$ -5 according to the ^2H NMR results. The accessible pore diameter for the molecule is L .

Toluene

6.7. Toluene as a guest in AlMePO- β

Quadrupolar ^2H NMR spectra of d_3 - and d_8 -toluene adsorbed at 4.5 wt % in AlMePO- β at temperatures from 133 K to 298 K are shown in Figure 6.7.1. As for para-xylene, the spectra were collected using 35 and 150 μs between refocusing pulses at each temperature. Figure 6.7.1 presents spectra acquired with 35 μs delay. No differences in line shape were observed between the two sets of experiments at 298 and 223 K. At lower temperatures, the spectra of d_8 -toluene recorded with 150 μs exhibit the same shape than those presented in figure 6.7.1, but the intensity of the signal at zero frequency is slightly reduced.

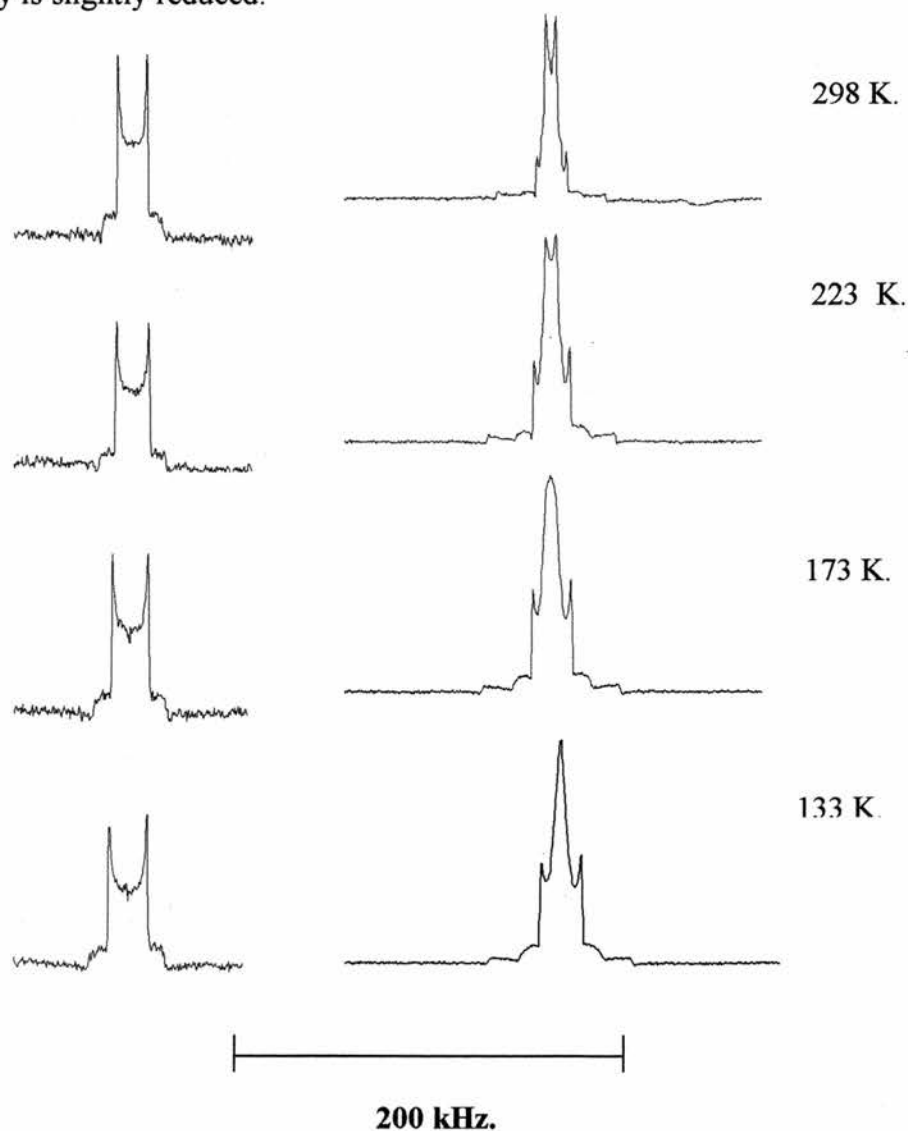


Figure 6.7.1. ^2H solid echo spectra of d_8 -toluene (right) and d_3 -toluene (left) adsorbed in AlMePO- β at different temperatures.

The spectra of d_3 -toluene contain direct information about the motion of toluene about its para-axis. Uniaxial powder patterns with sharp edges are observed at all temperatures, indicating that there is only one dynamic state. The width of these signals are 18, 20, 23 and 24 kHz, which gives an average QCC of 24, 27, 31, and 32 kHz at 298, 223, 173 and 133 K respectively.

The lineshapes can be simulated using a similar motion around a cone that was employed for para-xylene, again taking the motion of $-CD_3$ groups around their C_3 axis to be in the fast limit ($> 1 \times 10^9$ Hz) and reorienting the para-axis of the toluene at three sites on a cone. The cone half-angle that successfully matches the data are 38° at 298 K, 35° at 223 K, 33° at 173 K and 32° at 133 K, (see Figure 6.7.2).

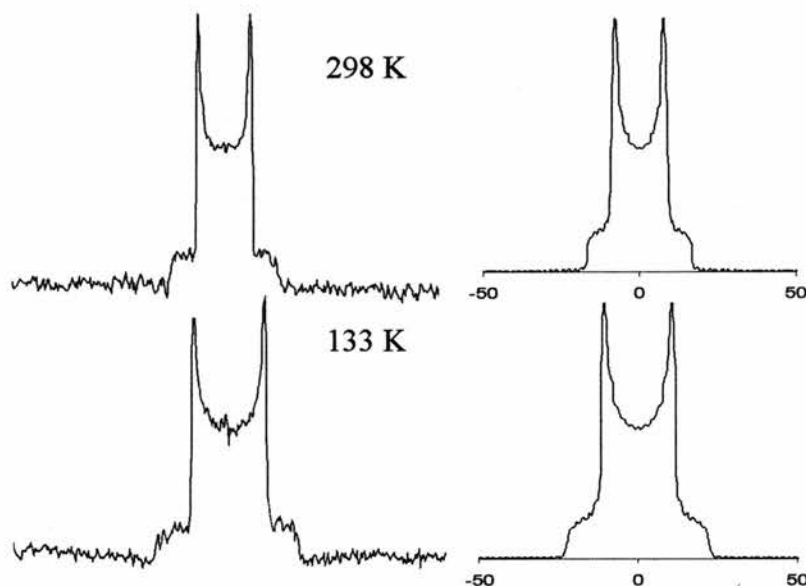


Figure 6.7.2. 2H NMR quadrupole echo for d_3 -toluene adsorbed in AlMePO- β at 298 and 133 K. Experimental (left) and simulated (right).

The spectra recorded on d_8 -toluene adsorbed in AlMePO- β result from the superposition of signals from the methyl group (already analysed using d_3 -toluene), the aromatic deuterons in ortho- and meta-positions (strong signal) and the aromatic deuteron para to the methyl group (a weak, broad signal).

The signal widths from the aromatic deuteron in the para-position are 65, 74, 79 and 82 kHz at 298, 223, 173 and 133 K respectively, are consistent with that from a single deuteron exchanging between three sites on cones with the same angle as those determined from the analysis of the d_3 -toluene spectra. The remaining signal from the d_8 -toluene arises from the aromatic deuterons in ortho- and meta-positions. At 298 K this takes the form of a narrow double peak 7 kHz wide. The shape of the narrow signal changes with decreasing temperature. At 223 K the signal has still a double peak shape, 20 kHz wide, and the deepness of it is smaller than the one obtained at 298 K. The shape of the signals at 173 K and 133 K is triangular with a width at half peak intensity of 11 and 8 kHz respectively. To simulate this signal, the aromatic ring was permitted to exchange between three positions, related by rotations of 120° ($2\pi/3$), to reflect the three fold rotation symmetry of the AlMePO- β channels (the structure has space group symmetry R-3c). This motion is executed by molecules undergoing fast exchange between three sites on a cone, as described previously for para-xylene (see Figure 6.7.3). The exchange rate used to describe the rotation of the aromatic ring about its para axis between the three sites was 7.0×10^6 , 3.0×10^6 , 1.4×10^6 and 5.0×10^5 Hz at 298, 223, 173 and 133 K respectively.

The calculations corresponding to the spectra recorded at 298 and 233 K yielded peak doublet signals, 7 and 8 kHz wide, analogous to those observed experimentally. The line result of the simulation at 173 K is almost triangular, 11 kHz wide at half peak intensity. At 133 K, the calculated spectra is triangular, 8 kHz wide at half peak intensity. The sum of the simulations for deuteron atoms in ortho- and meta-position are presented in Figure 6.7.5.

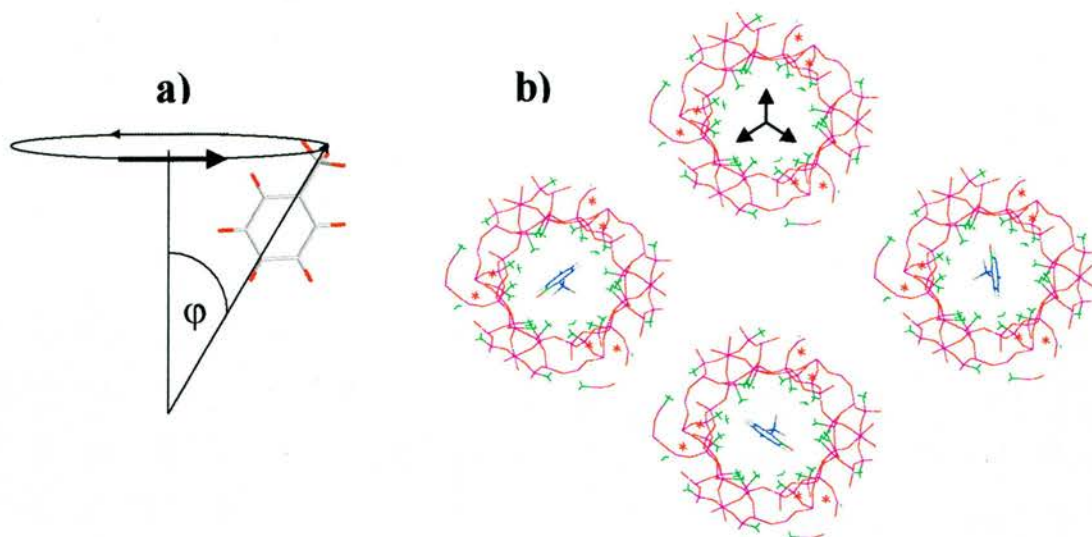


Figure 6.7.3. Representation of the motional model used to describe the ^2H NMR experiments on toluene in AlMePO- β . a) Toluene molecule reorientating its para axis in a cone type of motion. b) AlMePO- β view down the channels. The black arrows indicate the three directions used to describe the 120° jumps of the aromatic ring of toluene. See as well a representation of three toluene molecules with different orientations of the aromatic ring respect to the host framework. One deuteron atom has been highlighted in red.

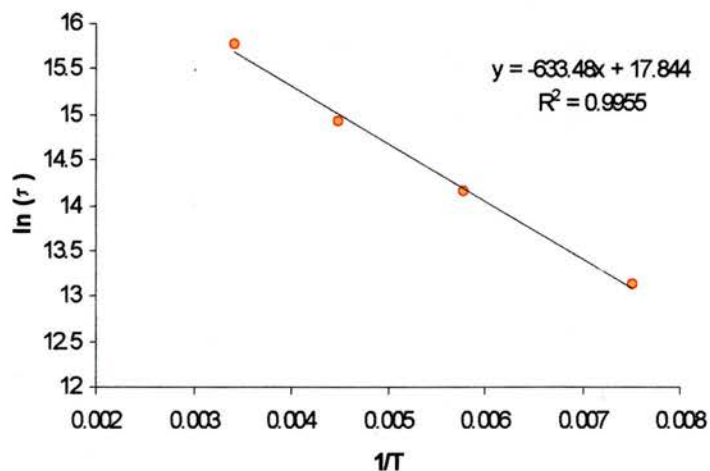


Figure 6.7.4. Arrhenius plot of \ln (exchange rate) of the aromatic ring about its para axis of toluene in AlMePO- β vs $1/T$. The estimated activation energy for this motion is $5.3(8)$ kJ/mol.

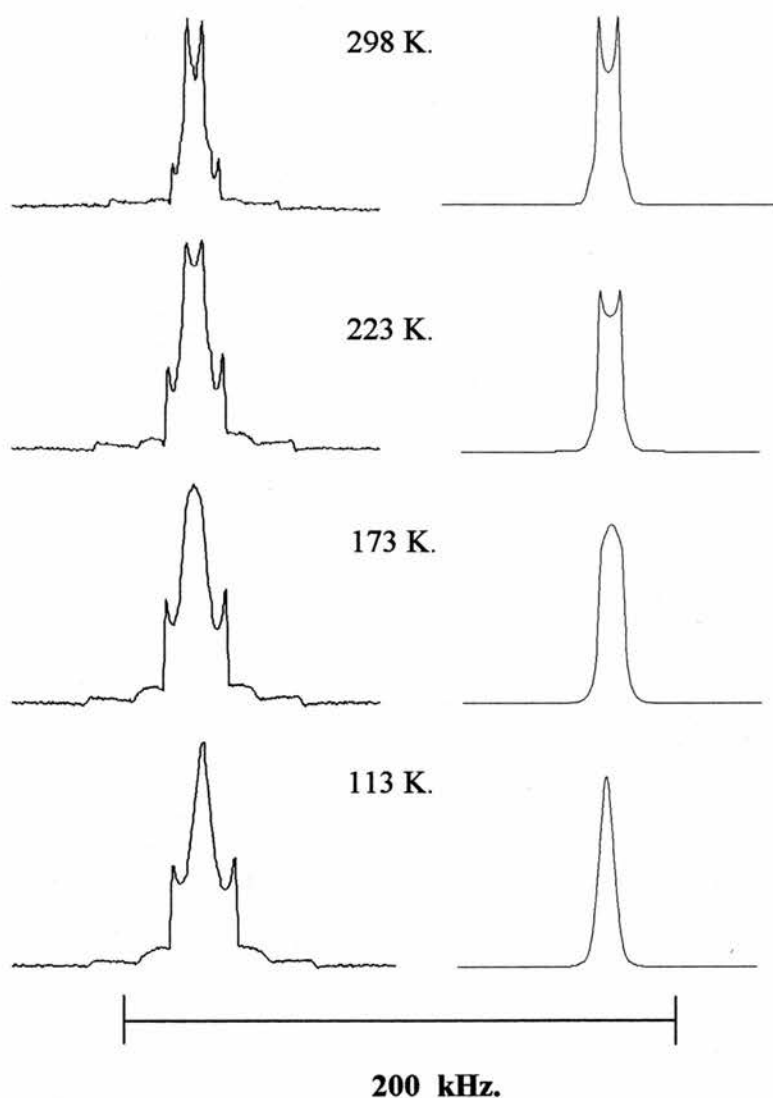


Figure 6.7.5. Experimental ^2H quadrupole NMR of d_8 -toluene adsorbed on AlMePO- β (left) and simulated spectra corresponding to the aromatic deuterons in ortho- and meta-position (right).

Combining all the simulated spectra gives the simulated d_8 -toluene spectra (Figure 6.7.6 and 6.7.7.) Using an Arrhenius plot ($\ln(\text{frequency})$ vs $1/T$) to analyse the frequencies of exchange required to simulate this part of the d_8 -toluene signal gives an activation energy of 5.3(8) kJ/mol for the aromatic group rotation (Figure 6.7.4).

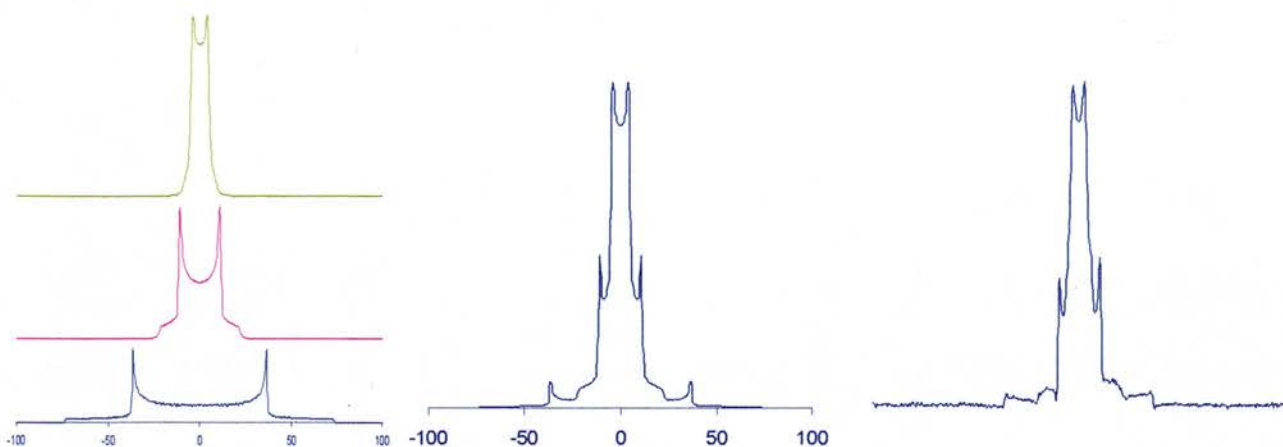


Figure 6.7.6. Experimental spectra of d_8 -toluene in AlMePO- β at RT, bottom left, and simulated spectra, bottom right, for the corresponding temperatures built as a superposition of the signals simulated independently. Aromatic signal produced by deuterons in ortho and meta (blue), methyl signal (pink), signal from deuteron in para (green).

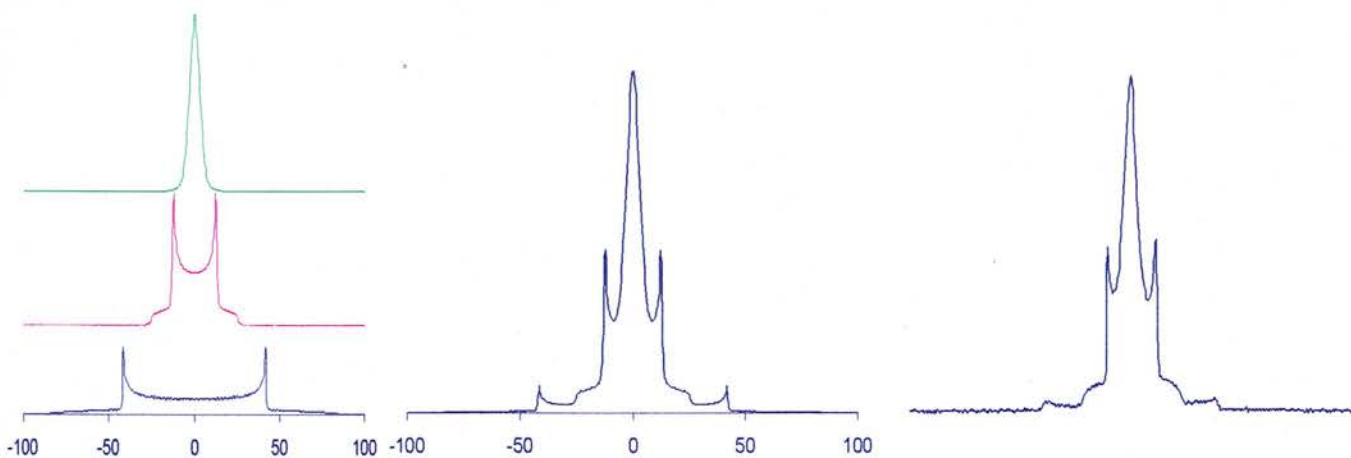


Figure 6.7.7. Experimental spectra of d_8 -toluene in AlMePO- β at 133 K, bottom left, and simulated spectra, bottom right, for the corresponding temperatures built as a superposition of the signals simulated independently. Aromatic signal produced by deuterons in ortho and meta (blue), methyl signal (pink), signal from deuteron in para (green).

According to the experimental ^2H NMR experiments, the dynamics of toluene in AlMePO- β agree with the following model: The para axis of the molecule undergoes fast reorientations in a cone type of motion of 38° at 298 K. Decreasing the temperature to 133 K reduces the cone angle to 32° but the motion is still fast. The aromatic ring spins about the para axis in a three fold axis. The exchange rate of the aromatic ring, fast at 298 K, reduces drastically with the decrease in temperature. The activation energy for the motion of the aromatic ring about its para axis has been estimated from an Arrhenius plot, 5.3 (8) kJ/mol.

The next figure summarises the QCC observed for the signal associated with the methyl group of the toluene molecule as a function of the temperature. The QCC observed for the methyl group of para-xylene is also included for comparison. It is observed that the dynamics of toluene are more affected than those of para-xylene by the change in temperature.

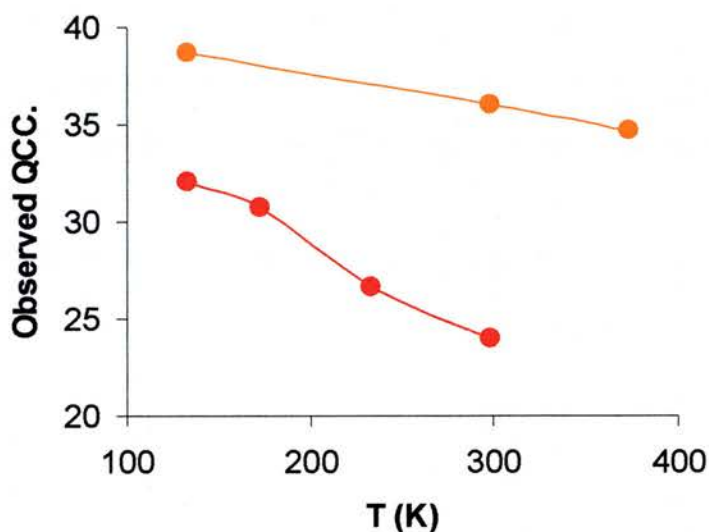


Figure 6.7.8. Observed QCC for the methyl groups in toluene (red) and para-xylene (orange) molecules as a function of the temperature .

6.8 Toluene as guest in AlMePO- α

Figure 6.8.1 presents spectra of d_3 -, d_5 - and d_8 -toluene at 4.5 wt % in AlMePO- α at different temperatures using 35 μ s between the refocusing pulses of the solid echo pulse sequence. At certain temperatures, spectra were recorded with other echo delays.

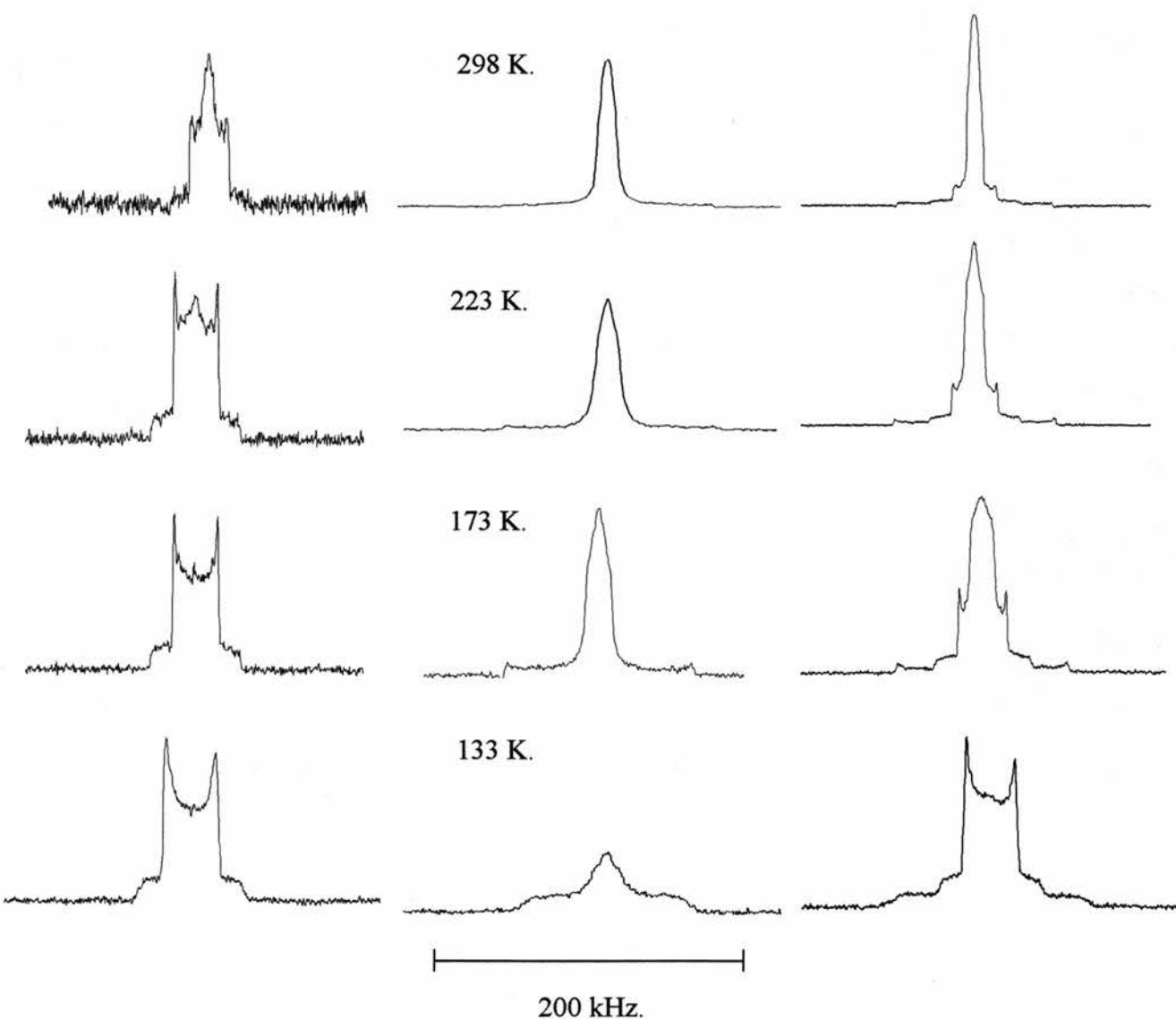


Figure 6.8.1. ^2H NMR quadrupole echo spectra of α,α,α - d_3 toluene (left), d_5 -toluene (centre) and d_8 -toluene (right) in AlMePO- α at different temperatures. These experiments were acquired using 35 μ s between the 90 $^\circ$ pulses of the quadrupole echo sequence.

*d*₃-toluene in AlMePO- α

For *d*₃-toluene, the low temperature data (133 K) display a uniaxial powder pattern with 32 kHz separation between the horns. No differences were observed using 150 μ s between the 90° pulses of the solid echo pulse sequence. The reduction of the width with respect to 42 kHz, which corresponds to a methyl group only clicking about its C₃ axis, indicates that additional motional anisotropic averaging process take place at this temperature. The width of the signal observed at 173 K is still 32 kHz but the edges of the horns are sharper than those observed at 133 K. At 223 and 298 K, the widths of the uniaxial powder pattern are 31 and 27 kHz, respectively.

These signals can be simulated by the toluene moving so that its long axis exchanges between different sites on a cone, as was the case for AlMePO- β (Figure 6.8.2). The shape of the channels in AlMePO- α is markedly triangular, so the lineshape was simulated by the toluene molecule moving over three sites on the cone, with a half angle that changes from 22° at 123 K to 29° at 298 K. Additional evidence for this mode of motion is provided by molecular dynamic simulations, snapshots of which are shown in Figure 6.8.3.

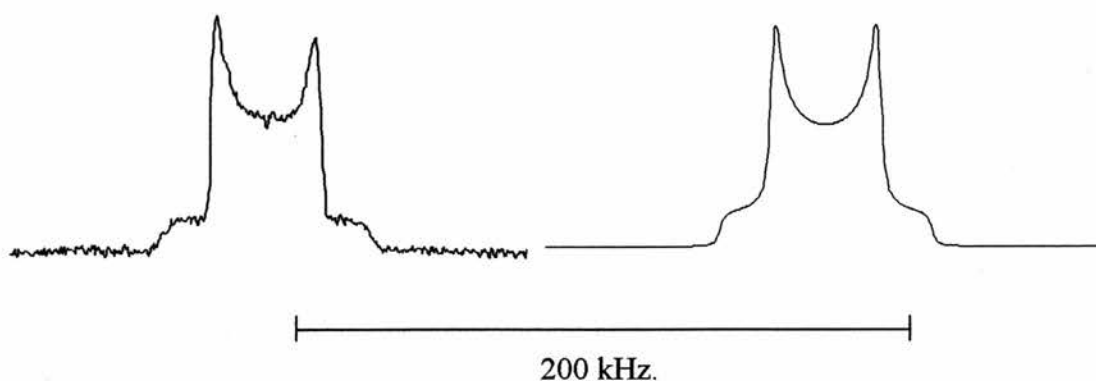


Figure 6.8.2. Experimental ²H spectrum for *d*₃-toluene in AlMePO- α at 133 K (left) and simulated ²H NMR spectra for a methyl group clicking fast about its C₃ axis and jumping fast in a cone of three sites cone angle 22°.

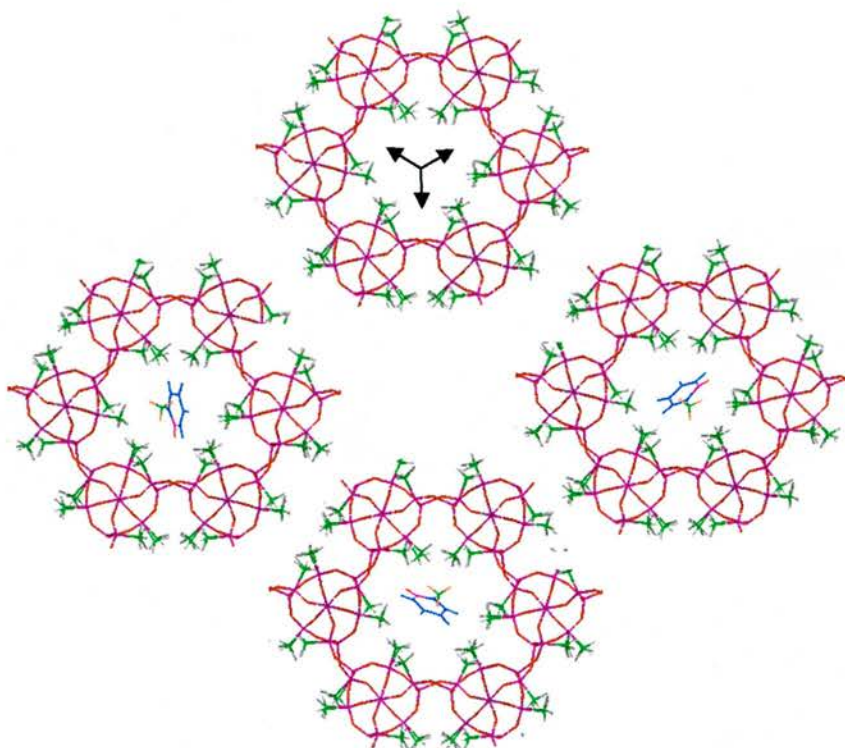


Figure 6.8.3. Molecular dynamics snapshots of toluene in AlMePO- α . The black arrows indicate the three directions used to describe the 120° jumps of the aromatic ring of toluene in the ^2H NMR model

In addition to the uniaxial powder pattern observed at all temperatures, at 223 K there is clear signal at zero frequency that grows in strength as the temperature is increased.

This signal takes the form of a triangular shape with 8 kHz halfwidth.

To obtain information on the origin of the additional signal, spectra were collected with different delays between the refocusing pulses. Here use is made of the fact that different species can have different relaxation times due to their molecular motion or to interactions with the guest molecules and their host. In figure 6.8.4 spectra obtained using 35 and 150 μs between the 90° pulses of the quadrupole echo sequence are compared. It can be clearly seen that, with the time increase between the 90° pulses of the quadrupole echo sequence, the intensity of the narrow signal at zero frequencies

decreases substantially compare with the uniaxial powder pattern at rt and 223 K. This is due to different T_2 relaxation times of different species associated with the signals. The shape of the spectrum associated with a single dynamic process in an intermediate exchange rate depends on the time between the 90° of the solid echo pulse sequence. But it is unlikely that this triangular signal is associated with molecules undergoing reorientations in an intermediate exchange rate because it arises upon increasing temperature. Therefore, it must be produced by species undergoing fast motion.

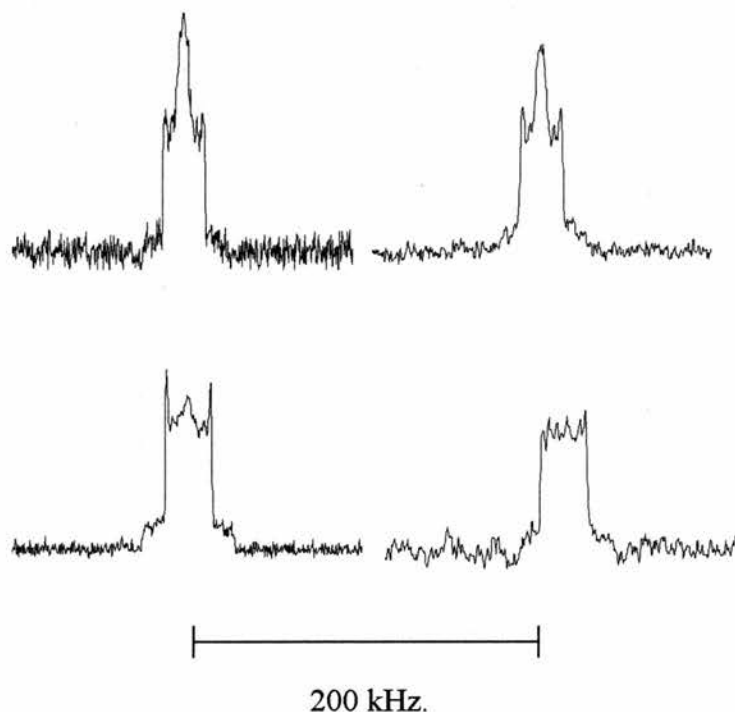


Figure 6.8.4. ^2H NMR spectra of toluene adsorbed in AlMePO- α at 298 K (top) and 223 K (bottom). Left and right correspond with 35 and 150 μs between the 90° of the quadrupole sequence.

The nature of the motional mode that generates this triangular shape signal is therefore not readily modelled. The simulated spectrum presented in Figure 2.4.11 (Characterisation techniques chapter, corresponding to a methyl groups jumping between two discrete sites 109.5° apart) has a width of 42 kHz at the bottom of the signal. This motional mode can not associate with the narrow signal observed at 223 and 298 K because the width of the experimental signals at the base of the spectra is 31 kHz.

After many trial calculations, a single dynamic state for toluene able to reproduce this signal using a fast exchange rate for the cone type of motion of the para axis has not been found. It could be that this signal is produced by a collection of molecules undergoing cone type of motion with slightly different cone angles. This distribution of molecules, with different energies, seems to be compatible with the fact that the width of this signal at half peak intensity slightly decreases with the increase in temperature due to an increase of population of molecules with higher energy. In Figure 6.8.5 some MXQET simulations for the methyl group of toluene undergoing jumps with large cone angles are given. (With the line width ($1/T_2 = 1$ kHz) used for the simulation for the largest cone angle the characteristic powder pattern is not observed and the spectrum appears as a broad signal at zero frequency).

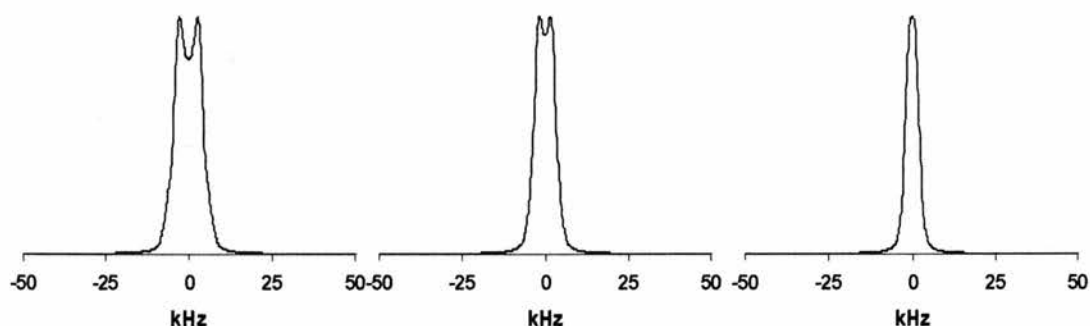


Figure 6.8.5. Simulated ^2H NMR spectra for a methyl group clicking fast about its C_3 axis and jumping fast in a cone of three sites and cone angles of 48° , 50° and 52° (left, centre and right respectively).

At temperatures above 133 K, a weak second signal, symmetric with respect to zero frequency (Figure 6.8.6) is observed. The width of this second signal is 18, 22 and 24 kHz at 298, 223 and 173 K. This is due to toluene adsorbed on AlMePO- β impurity. The d_3 -toluene spectra recorded at 133 K is slightly broader due to the overlapping of the signal associated with the impurity and AlMePO- α .



Figure 6.8.6. Quadrupole ^2H NMR spectra of d_3 -toluene adsorbed in AlMePO- α at 173 K. The signals marked with black arrows are associated with toluene adsorbed in the AlMePO- β impurities of the sample.

-d₈- and d₅-toluene adsorbed in AlMePO- α

The spectra obtained for d₈-toluene appear as superposition of three signals corresponding to three dynamically non-equivalent deuterons within the toluene molecule (see Figure 6.8.7). The widths of all the signals identified for d₈-toluene are summarised in table 6.8.1.

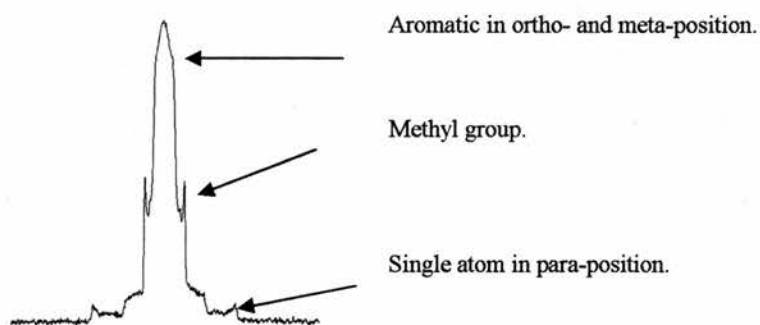


Figure 6.8.7. ²H NMR quadrupole echo spectra of d₈-toluene at 173 K in AlMePO- α . It can be seen that the signal observed is the superposition of three different components produced by deuterons undergoing different type of motion.

The d₈- spectrum at 173 K, Figure 6.8.1, shows a signal of 31 kHz width produced by the methyl group, one broad signal at the base of the spectra, 114 kHz width, produced by the single atom in para-position and other signal at zero frequencies, 18 kHz width half peak intensity, observed between the methyl signal produced by the aromatic atoms in ortho- and meta-positions. At 223 K the signals produced by the methyl groups and the deuteron para to the methyl group have a width of 31 and 111 kHz respectively and the signal associated with the atoms in ortho and meta, more intense than at 173 K, is 14 kHz at half peak intensity. The increase of intensity of the signal at zero frequency is due to molecules performing large jumps inside the channels, associated also with the triangular signal observed with d₃-toluene. At 298 K the three signals are narrower due to increased mobility of the molecules. The methyl signal has 28 kHz width, the para atom produced a 108 kHz signal and the aromatic meta and ortho atoms produced a signal of 10 kHz width. At 123 K the signals observed is basically the same as the signal produced by d₃-toluene, the only difference observed is set of broad shoulders at

the base of the spectra of 136 kHz width. Apparently the signal of the aromatic deuterons in ortho and meta positions seems to be “buried” under the methyl signal.

The results obtained using d_5 -toluene (Figure 6.8.1) only present the signals associated with the aromatic ring. The widths of the signals in these experiments are the same as those found using d_8 -toluene.

Signal width/ kHz	298 K	223 K	173 K	123 K
Methyl	28.2	31	31.5	32
Aromatic in ortho- and meta-position.	10	14.3	18	?
Aromatic in para-position	110	111	114	136

Table 6.8.1. Summary of ^2H spectral details found for d_5 -toluene in AlMePO- α at different temperatures. The widths of signals from ortho and meta-aromatic deuterons were measured as the width at half maximum signal intensity.

Signal attenuation of the aromatic ring due to slow motion

Figure 6.8.8. presents some experiments corresponding to d_5 -toluene in AlMePO- α at low temperatures. It can be seen that the intensity of the signal associated with the aromatic deuterons in ortho and meta position drastically decreases with the decrease in temperature. This is because, during the solid echo, some magnetisation is not refocused by the second 90° pulse of the pulse sequence. According to the literature [12], this signal attenuation suggests a motion at the intermediate exchange rate for the aromatic ring about its para axis.

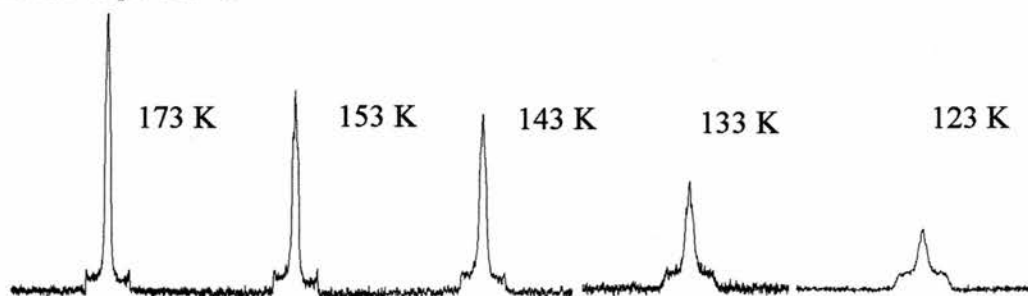


Figure 6.8.8. ^2H NMR spectra of d_5 -toluene adsorbed in AlMePO- α at different temperatures. The intensity of the signals has been normalised using the broad signal associated with the single atom in para position.

The mobility of guest molecules within the hybrid materials studied in this work, as in many microporous solids already studied [5], should be affected by the interaction between adsorbed molecules. The reproducibility of the method used for the sample preparation during this work is confirmed by the similarity of the spectra obtained using different isomers at all the temperatures studied.

Simulations of the signal from the aromatic deuterons for either d_8 -toluene or d_5 -toluene provide information about the dynamics of the aromatic ring around its para axis. The signal associated with the single atom in para position provides information about the motion of the para axis with respect to the host framework, like the methyl signal, and it can be simulated using one single site interchanging between three positions in a cone type of motion with the same cone angles used for the simulations of the methyl signal.

The signal produced by the aromatic deuterons in ortho and meta position was simulated using a similar model for toluene in AlMePO- β : reorientations of the aromatic ring within three planes separated by an angle of 120° while the para axis of the molecule describes the cone type of motion found in the experiments performed with d_3 -toluene (see Figure 6.8.3.).

The spectrum observed at 173 K is analysed in the first place for simplicity. The signal at the bottom of the spectra associated with the single atom in para position, 115 kHz width was simulated by one single deuteron jumping between three orientations in a cone of 22° . This produces powder pattern of 114 kHz, very similar value to the width observed experimentally. The signal attributed to the deuteron atoms in meta and ortho aromatic positions has been reproduced using the same motional model for the para axis of the molecule described previously, a fast three-sites motion in a cone of half angle 22° while the aromatic deuterons were performing 120° jumps about the para axis at an intermediate exchange rate of 7.0×10^5 Hz. The simulated spectra are presented in Figure 6.8.9. The line width of this spectrum at half intensity, 16 kHz, is similar to the experimental width, which is 17 kHz. The experimental spectra obtained 173 K can be reproduced by addition of the individual spectra for the different parts of the molecule (see Figure 6.8.10).

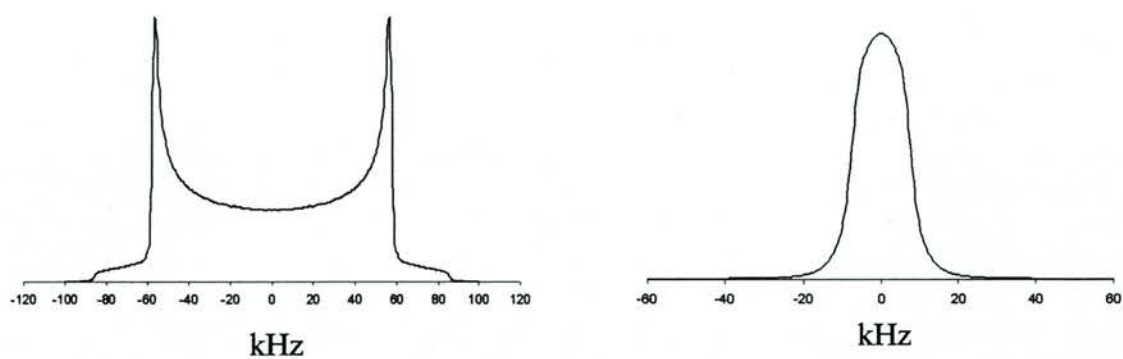


Figure 6.8.9. Simulated spectra for the aromatic deuterons in a toluene molecule whose para axis is jumping between three positions in a cone type of motion with cone angle of 22° . Left, simulation for single atom in para position. Right, simulation for atoms in meta and ortho position performing 120° flips around its para axis with an exchange rate of $7.0 \cdot 10^5$ Hz.

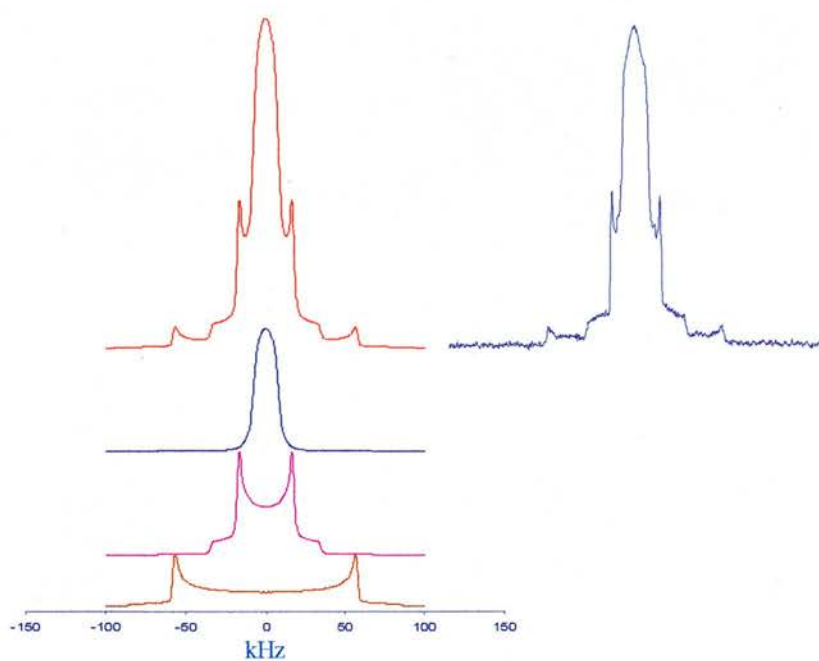


Figure 6.8.10. Right experimental spectra for d_8 -toluene at 133 K adsorbed in AlMePO- α . Left, simulated spectra built as a superposition of components.

At higher temperatures the spectra for d_8 -toluene present the same trend as those for d_3 -toluene. The signal assigned to the single atom in the aromatic ring in para position has almost the same width from 173 K until 253 K, which suggests that the reorientation of the toluene molecule with respect to its para axis is basically the same at these temperatures. This is consistent with the conclusions found previously with d_3 -toluene. At 298 K the width of the signal for the single atom in para position narrows to 108 kHz. This could be simulated using the same model described before, three discrete sites in a cone type of motion with 29° cone angle, the same cone angle used for the simulation of the methyl signal. This produces a spectrum with 104 kHz separation between the horns of the powder pattern, similar to the experimental value, 108 kHz.

The width of the signal associated with the atoms in meta and para position at 223 K is 14 kHz. This slight decrease in width with respect to the signal observed at 173 K has to be produced by a change of the exchange rate of the aromatic ring around its para axis, as the cone angle of the para axis respect to the host framework remains the same in this temperature range. However, the shape of the signal remains unchanged. This indicates that the aromatic ring is still clicking about its para axis in an intermediate exchange rate. Fast clicking about its para axis would produce a signal with a uniaxial powder pattern (Figure 6.8.11).

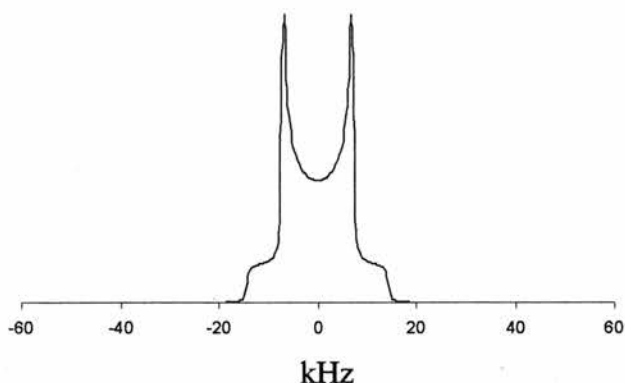


Figure 6.8.11. Simulation for a deuteron in ortho of a toluene molecule which para axis is jumping fast in a cone of 3 sites and cone angle of 22° . The aromatic ring is rotating fast about its para axis. This rotational mode has not been observed for toluene in AlMePO- α .

Summary of the motion of toluene in AlMePO- α

Two dynamic states are observed for toluene in AlMePO- α and they are temperature dependent. At low temperatures the toluene molecule seems to be precessing in a cone with half cone angle approximately 22° . With the increase of temperature another dynamic state appears in which the toluene seems to be precessing with a much higher cone angle, approximately 52° . The aromatic ring is rotating about the para axis of the molecule at all temperatures studied. The rotation can be described as 120° flips in an intermediate exchange rate for most of the experimental temperature range.

6.9 Summary and conclusions of the motion of toluene in the AlMePOs

^2H quad echo NMR of toluene in the AlMePOs indicates that the observed spectra can in large part be simulated by considering the para-axis of the toluene to exchange between at least three sites on a cone within the channels, while the aromatic ring undergoes an independent $2\pi/3$ flip around the long axis of the molecule. This is broadly in agreement with the motion that is predicted by molecular dynamics simulations. The details of the fit parameters used in the MXQET program to successfully match the observed spectra are summarised in table 6.9.1. An additional high temperature dynamic state of toluene in AlMePO- α has also been observed, and is attributed to toluene molecules, the para-axes of which are undergoing larger jumps (*ca.* 50° half angles). Using similar geometrical arguments to those employed for para-xylene, accessible diameters for toluene in AlMePO- β and AlMePO- α are calculated as 6.24 and 5.46 Å respectively, according to the cone angles found for the long axis of the molecule at 298 K (38° and 29° for AlMePO- β and AlMePO- α respectively).

	Temperature/ K.	Half cone angle described by the para axis of toluene	Exchange rate of the aromatic deuterons about the para axis (Hz^{-1})
AlMePO-α	298	29°	Not calculated. ^a
	223	25°	Not calculated. ^a
	173	24°	$7.0 \cdot 10^5$
	123	22°	Not calculated. ^b
AlMePO-β	298	38°	$7.0 \cdot 10^6$
	223	35°	$3.0 \cdot 10^6$
	173	33°	$1.4 \cdot 10^6$
	123	32°	$5.0 \cdot 10^5$

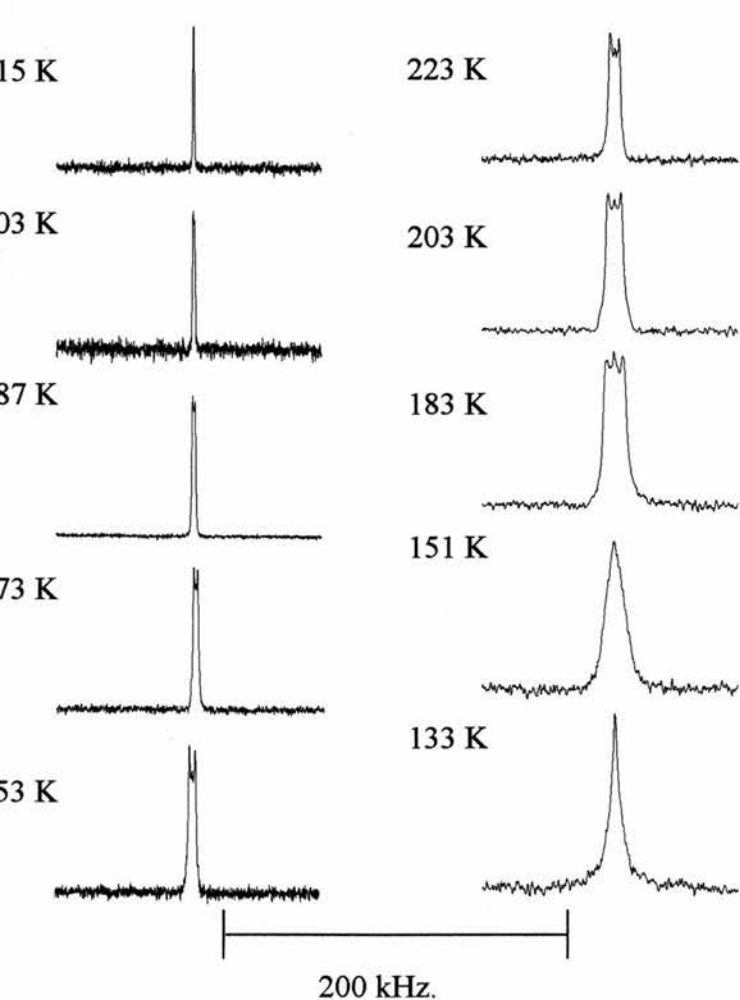
Table 6.9.1. Summary of the MXQET parameters used for the simulation of the toluene spectra in AlMePO- α and β . ^a Two dynamic states present. ^b Strongly attenuated echo signal not matched by MXQET.

Toluene also provides evidence of the different geometric constrain that molecules can experience within the two microporous materials. Note that at the same temperature 173 K, the exchange rate used for the rotation the aromatic ring about the para axis, to simulate the spectra of the deuterons in meta and ortho, was $1.4\text{E}6$ and $7.0\text{E}5$ Hz in AlMePO- β and AlMePO- α respectively. According to this, at 173 K the aromatic ring of toluene rotates two times faster in AlMePO- β . Signal from the aromatic ortho- and meta- deuterons of toluene in AlMePO- α is found to decrease in intensity as the temperature is decrease, suggesting that the rotational exchange occurs at an intermediate exchange rate at this temperature and adding further detail to the model.

Benzene

6.10. *d*₆-benzene as a guest in AlMePO-β

Two different loadings of benzene in AlMePO-β were studied by ²H NMR, 1.5 wt % and 4.5 wt %, corresponding to one molecule every 33 and 11 Å respectively along the channels. ²H quadrupole NMR spectra of AlMePO-β loaded with 1.5 wt % of *d*₆-benzene are shown in Figure 6.10.1. The line shapes observed above 287 K are isotropic. The decrease in temperature changes the signals to a peak doublet that increases its width with the reduction of temperature. At 151 and 133 K the shape of the signals is triangular. Their widths, measured at half maximum peak intensity, are 15.0 and 7.0 kHz respectively. Table 6.10.1 describes the width of signals observed at all temperatures.

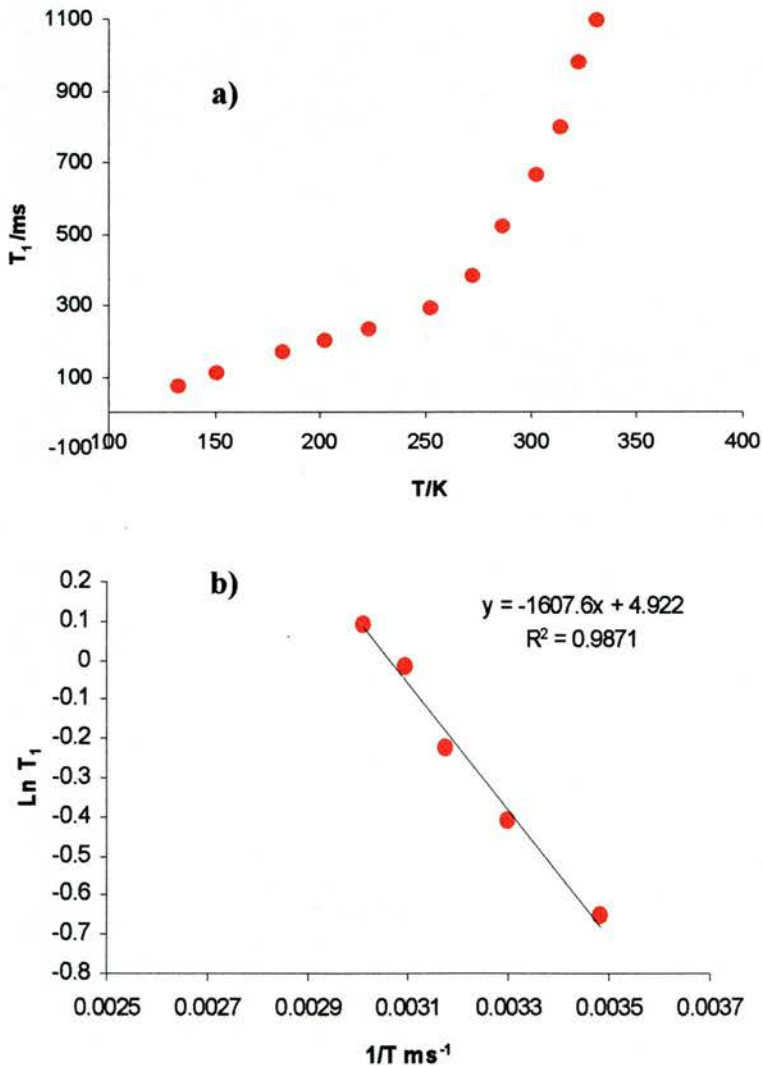


Temp / K	Spectrum width kHz ⁻¹
315	isotropic
287	1.8
273	2.3
253	3.1
223	5.1
203	7.0
183	10.0
151	15.0
133	7.0

Table 6.10.1. Experimental width of the signals presented in figure 1. At 151 and 133 K the width of the signal was measured at half peak intensity.

Figure 6.10.1. ²H NMR of AlMePO-β loaded with 1.5 wt % of *d*₆-benzene at several temperatures. At interval of 35 μs was used between the 90° pulses of the quadrupole echo sequence.

The dynamics of benzene was further characterised by measuring the spin lattice relaxation time constant at various temperatures using the saturation-recovery pulse sequence described in the characterisation techniques chapter. Spin-lattice relaxation time constants were calculated from exponential fits to the evolution of total magnetisation as a function of the time τ_0 . Figure 6.10.2 presents the evolution of the T_1 constant with the temperature. It can be seen that the T_1 time constant decreases with the temperature. On the high temperature side, the plot of $\ln T_1$ against $1/T$ is linear and the apparent activation energy for the motion of benzene, $13.1(3) \text{ kJmol}^{-1}$, can be estimated from the slope of the Arrhenius dependence.

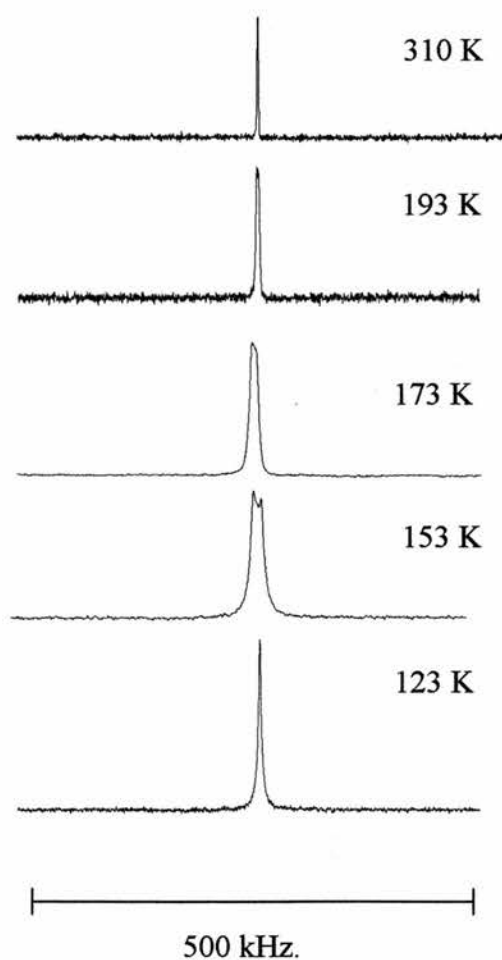


T/K	T_1 /ms
332	1094
323	980
315	799
303	663
287	520
273	380
253	290
223	231
203	196
183	165
151	110

Table 6.10.2. T_1 relaxation time constants for benzene in AlMePO- β at 1.5 wt % loading at different temperatures.

Figure 6.10.2. a) T_1 relaxation time constants for benzene in AlMePO- β 1.5 wt % loading level as a function of temperature. b) Arrhenius plot for $\ln T_1$ vs $1/T$ for benzene in AlMePO- β at 1.5 wt % loading level.

Vega *et al.* [5] observed that the concentration of guest molecules strongly influences the dynamics of aromatic molecules in zeolites. It is expected that the interaction between guest species will also play a role in the dynamics of adsorbed molecules in AlMePO- α and β , due to the small diameter of their cylindrical channels. In order to investigate this possible change in dynamics, quadrupole ^2H NMR experiments were recorded at different temperatures on a sample loaded with a 4.5 wt % of benzene, which corresponds to seven benzene molecules per unit cell. Representative spectra are shown in Figure 6.10.3. Table 6.10.3 summarises the width of the signals measured at half peak intensity. It can be observed that at this loading the isotropic component is present in a wider range of temperatures. At 173 K the signal broadens and at 153 K the shape is a peak doublet of 6.1 kHz. Further reduction of the temperature leads to isotropic line again. The observed spectra suggests that the mobility of benzene is higher at 4.5 wt % loading



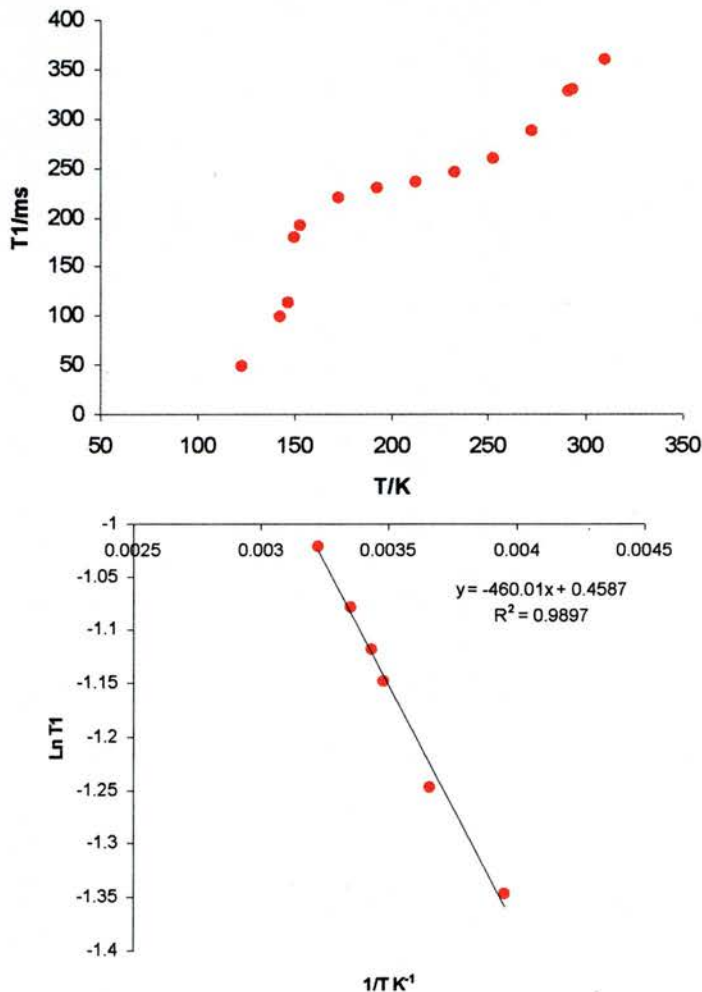
Temp / K	Spectrum width kHz ⁻¹
310	1.3
193	2.9
173	4.6
153	6.1
123	6.2

Table 6.10.3. Experimental line width (measure at half maximum peak intensity) of the signals shown in figure 6.10.3.

Figure 6.10.3. Variable temperature quadrupole ^2H NMR spectra of benzene at 4.5 wt % adsorbed in AlMePO- β .

T_1 longitudinal relaxation time constants for benzene in AlMePO- β at 4.5 wt % loading level were also calculated. Figure 6.10.4 and table 6.10.4 summarise the results. The T_1 relaxation time constants found at this loading level are different from those described previously (6.10.2). At high temperatures, T_1 values are drastically smaller and, the evolution of the T_1 values with the temperature follows a 'double dip' exponential decay. This 'double dip' is probably associated with two relaxation mechanisms due to different rotational modes of the benzene within the microchannels of AlMePO- β .

The activation energy for the motion of benzene, 3.8 (1) kJmol⁻¹, was also calculated from the slope of the Arrhenius dependence (Figure 6.10.4). This energy is considerably smaller than the one observed at the lower loading of benzene, 13.1 (2) kJmol⁻¹.



T (K)	T_1 (s)
310	0.36
294	0.33
291	0.327
273	0.287
253	0.26
233	0.245
213	0.236
193	0.229
173	0.22
153	0.19
150	0.178
147	0.11189
143	0.098
123	0.04772

Table 6.10.3. Summary of T_1 relaxation time constants for benzene adsorbed in wt 4.5 % in AlMePO- β at different temperatures.

Figure 6.10.4. a) T_1 relaxation time constants for 4.5 wt % benzene in AlMePO- β loading level as a function of temperature. b) Arrhenius plot for $\ln T_1$ vs $1/T$ for benzene in AlMePO- β at 4.5 wt % loading level.

The signals observed in these two samples suggested that the mobility of benzene within the channels of AlMePO- β is very high although at low temperatures an anisotropic component in its dynamics is observed, and is modelled as described below. For the simulation of these narrow signals, it is more appropriated to use the computer code MXQET1, rather than MXQET, because it allows having independent QCC for different sites. Two different sites for the benzene molecule within the channels of AlMePO- β have been defined. The first, with a QCC equal to 0 kHz, corresponds to molecules at the centre of the channels tumbling freely. The second, used to describe molecules with more constrained dynamics, has a QCC of 96.5 kHz (half the rigid state) and is associated with benzene molecules close to the walls spinning fast around their hexagonal axis. Representation of both sites used for the simulations can be seen in Figure 6.10.5. Assuming a fast exchange rate for the C-D bonds, the effective QCC experience at the nucleus is the average of the QCC scaled by the population of each site. According to this,

$$QCC_{\text{effective}} = 96.5 * N_{\text{wall}} \text{ (kHz)} \quad \text{Equation 1}$$

where N_{wall} is the population of molecules undergoing anisotropic motion. Taking into account that the width of the experimental signals is $\frac{3}{4}QCC_{\text{effective}}$, the populations of molecules in each site can be calculated.

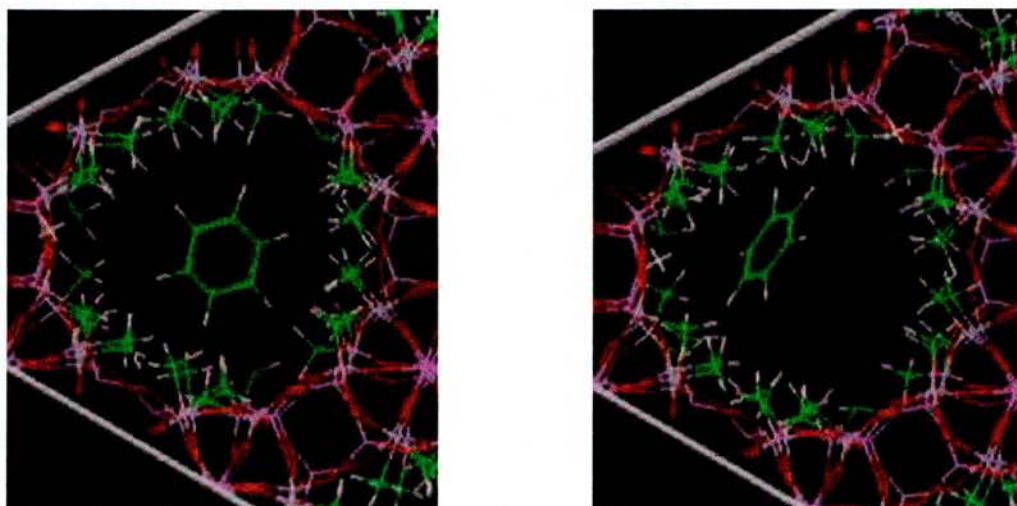


Figure 6.10.5. Representation of benzene at the two sites used for the ^2H NMR simulation. Left, at the centre of the channel. Right, closer to the wall.

The estimated population of benzene molecules used for the simulations at the two sites at different temperatures are summarised in Table 6.10.5. Representative calculated spectra are presented in Figure 6.10.6. Between 287 and 183 K, the exchange rate between the two types of molecules was fast, $1.0 \text{ E}7 \text{ s}^{-1}$. The populations of each type of molecule at the different temperatures were calculated according to Equation 1. If $N_{\text{iso}}/N_{\text{wall}}$ is defined as the ratio of the number of molecules isotropically rotating at the central space of the channels to the number closer to the wall, then the activation energy for the jump between the two sites can be estimated from the slope of the plot of $\ln(N_{\text{iso}}/N_{\text{wall}})$ vs. $1/T$ (Figure 6.10.7). According to this, the calculated activation energy for this jump is 6.5 kJ/mol.

At 151 and 133 K the signal has a triangular shape. It is unlikely that the decrease of temperature would produce an increase of mobility of the molecules, so this change in line shape must be due to a dynamic process in an intermediate exchange rate. The population ratio, $N_{\text{iso}}/N_{\text{wall}}$, used for the simulation of the spectra at 151 and 133 K were calculated from the extrapolation of the temperature dependence presented in figure 6.10.7 to these temperatures. In order to obtain the experimental shapes the exchange between the two types of molecules were $4.5 \text{ E}5$ and $5.0 \text{ E}4 \text{ s}^{-1}$ at 151 and 133 K respectively.

According to this model, the dynamics of the two types of benzene molecules (isotropic rotation and rotations about the six fold axis) is still fast at the lowest temperature. The interchange between the two types of molecules is in the intermediate exchange rate.

In the intermediate exchange rate domain, the ^2H NMR line shapes are sensitive to the separation time between the 90° pulses of the quadrupole sequence. Figure 6.10.7 shows an array of spectra obtained at 151 K using different times for this quadrupole echo delay. It is observed that, apart from overall intensity reduction, the increase of the echo delay changes the shape and reduces the width of the signals (measured at half peak intensity). In order to test the proposed model for the motion of benzene, an array of simulations was performed, adjusting the simulated echo delay to the experimental value. The results of these calculations are presented in Figure 6.10.8. The MXQET1 computer code, by default, normalises the spectral intensities. The simulated results presented in Figure 6.10.8 have been scaled according to the experimental spectra. It can be seen that the model is consistent with the experimental results.

N_{iso}	N_{wall}	$\ln(N_{\text{iso}}/N_{\text{wall}})$	Temp / K	$1/T$ *K
0.97	0.03	3.416657	273	0.003663
0.96	0.04	3.106682	253	0.003953
0.93	0.07	2.579548	223	0.004484
0.90	0.10	2.23423	203	0.004926
0.86	0.14	1.830579	183	0.005464
0.72	0.28	0.962697	151	0.006623
0.58	0.41	0.345361	133	0.007519

Table 6.10.5. Populations of benzene at the two sites used for the ^{2}N NMR simulations at different temperatures. N_{iso} and N_{wall} corresponds with molecules at the centre of the channel (0 kHz QCC) and molecules close to the wall (96.5 kHz QCC) respectively.

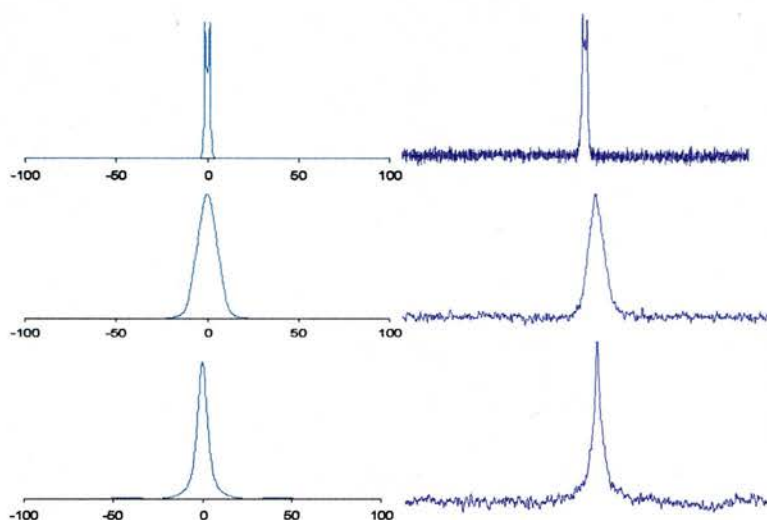


Figure 6.10.6. Simulated (left) and experimental (right) spectra at different temperatures. Top, middle and bottom corresponds to 253, 151 and 133 K respectively. Details of the parameters use for these simulations are explained in the text.

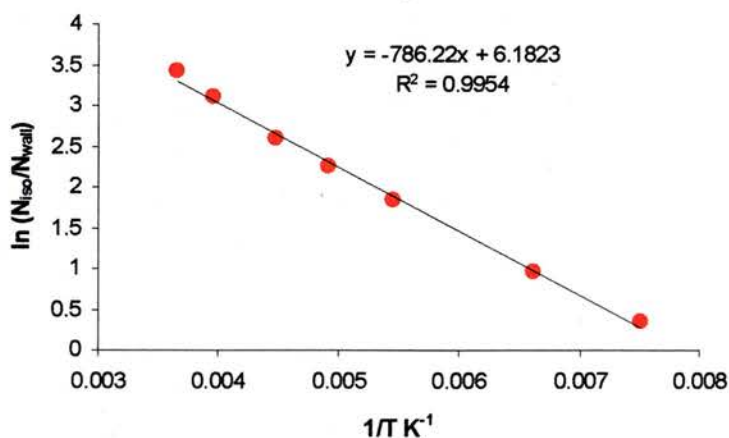


Figure 6.10.7. Arrhenius plot of $\ln N_{\text{iso}}/N_{\text{wall}}$ vs $1/T$ for C_6D_6 in AlMePO- β at 1.5 wt % loading level.

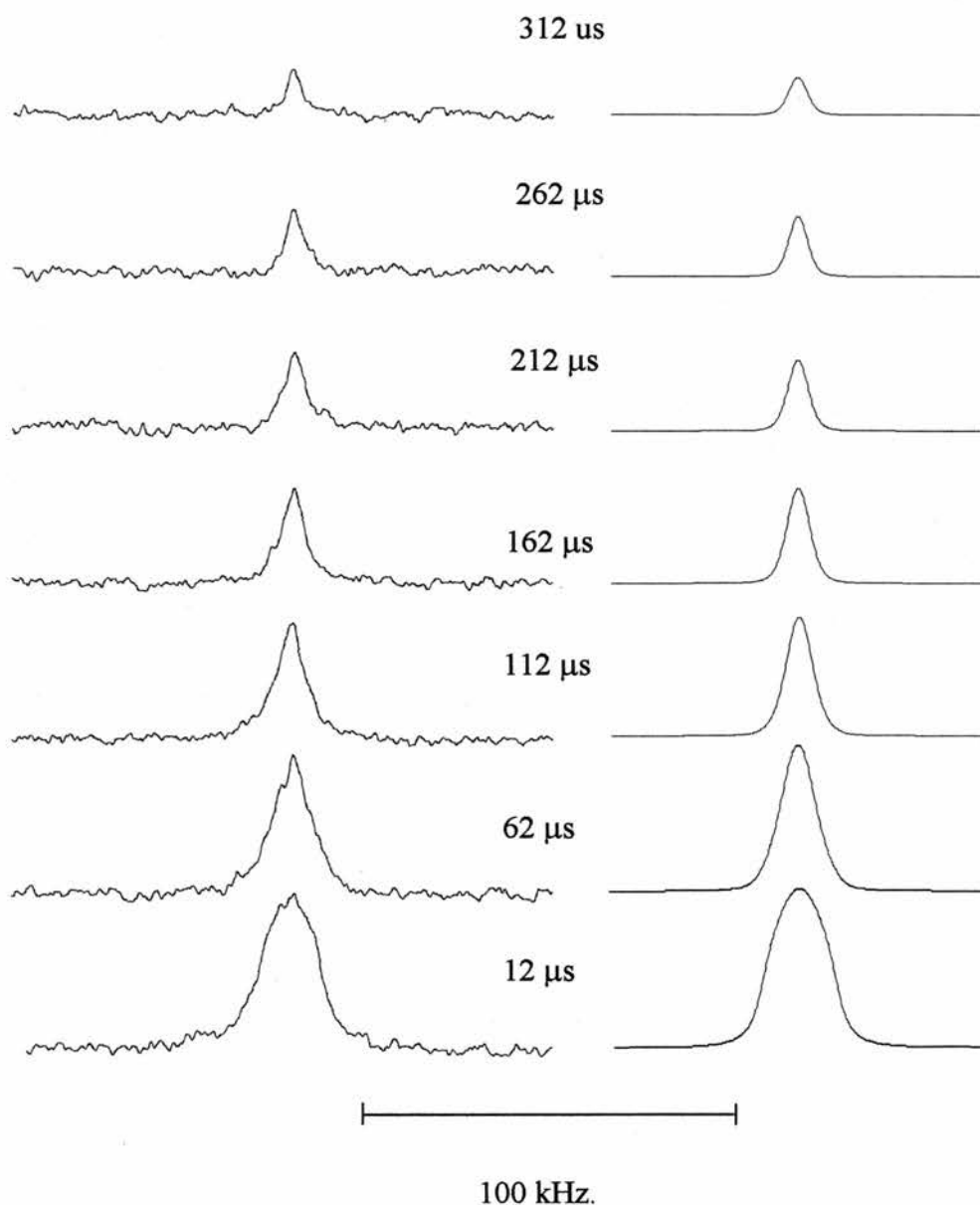


Figure 6.10.8. (Left) ^2H NMR spectra from experiments performed on a sample of AlMePO- β loaded with C_6D_6 at 151 K using different times between the 90° pulses of the quadrupole echo pulse sequence. (Right) MXQET1 simulated spectra.

The plots of the T_1 vs temperature suggest that the curves have a minimum below the lowest temperature accessible in this work. This minimum is associated with molecules undergoing rotational modes on resonance with the ^2H Larmor frequency in our magnet (76.78 MHz, fast exchange rate). This is also compatible with the model because it assumes molecules undergoing fast rotations at all temperatures.

Molecular dynamic calculations performed by Cox are also compatible with the model proposed from the ^2H NMR analysis. Note in Figure 6.10.9, the isotropic trajectory followed by benzene within AlMePO- β .

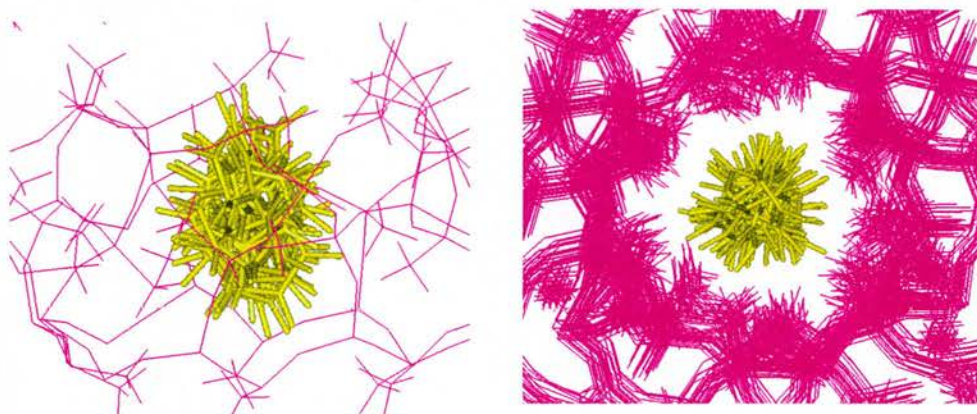


Figure 6.10.9. Trajectory found for benzene in AlMePO- β at 298 K through Molecular Dynamic calculations [17]. The simulation describes 10^{-10} s of real time motion.

Summary

The motion of C_6D_6 in AlMePO- β has been analysed by means of ^2H NMR. Two loading levels of benzene have been studied: 1.5 and 4.5 % *wt*, which correspond to 2.3 and 7 molecules per unit cell respectively. The spectra of these samples, which are very similar, indicate that the dynamics of benzene at both loading levels is almost isotropic, although some anisotropic component is present at low temperatures.

Spin lattice T_1 relaxation constant measurements performed at different temperatures allow the calculation of the activation energies for the isotropic motion of benzene at the two loading levels. These energies are 13.1 and 3.8 kJ/mol for solids loaded with 1.5 and 4.5 % *wt*.

A model has been proposed to describe the motion of C_6D_6 via the MXQET1 computer code. It makes use of two types of molecules: Molecules rotating isotropically and molecules rotating about their hexagonal axis. According to this model, the effect of the temperature is merely a shift of the population of the guest molecules between two sites with different energies. The model allows the simulation the experimental spectra and seems compatible with molecular dynamic calculations.

6.11. d_6 -benzene as a guest in AlMePO- α

The dynamics of benzene in AlMePO- α have been studied performing analogous experiments similar to those described for its polymorph AlMePO- β . AlMePO- α was loaded with 1.5 and 4.5 wt % in of benzene, which correspond to one molecule every 33 and 11 Å along the channels. ^2H NMR signals were collected at several temperatures using the solid echo pulse sequence. Longitudinal T_1 relaxation time constants were measured using a saturation-recovery solid echo pulse sequence.

Figure 6.11.1 shows representative quadrupole ^2H NMR of C_6D_6 loaded in AlMePO- α at 1.5 wt %.

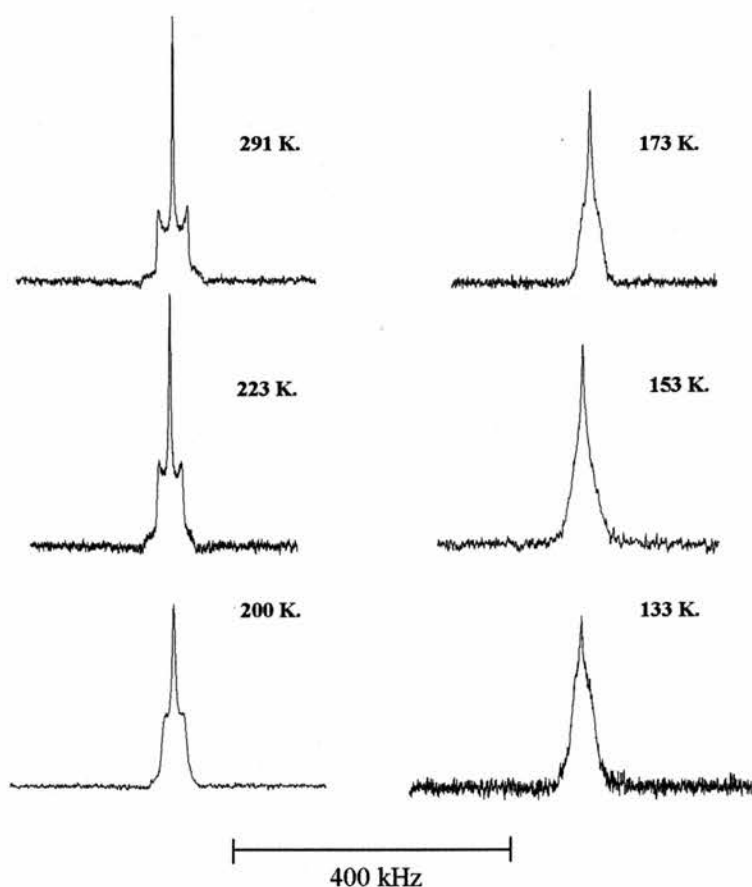


Figure 6.11.1. Representative ^2H NMR spectra of AlMePO- α loaded with C_6D_6 at 1.5 wt % loading at various temperatures.

Between 291 K and 200 K it can be appreciated an isotropic signal at zero frequency, 1 kHz broad at half peak intensity, superposed on a uniaxial powder pattern. The widths of these uniaxial powder patterns are 24, 23.5, 22.7, 21.5 and 20.0 kHz at 291, 273, 250, 233 and 200 K respectively. At lower temperatures the signal adopts a triangular shape.

^2H NMR spectra of AlMePO- α loaded with 4.5 wt % of benzene are shown in 6.11.2. The observed signals are similar to those found using 1,5 wt % loading. Over most of the range of temperature studied the spectra present a superposition of two components, corresponding to benzene molecules in different dynamic states.

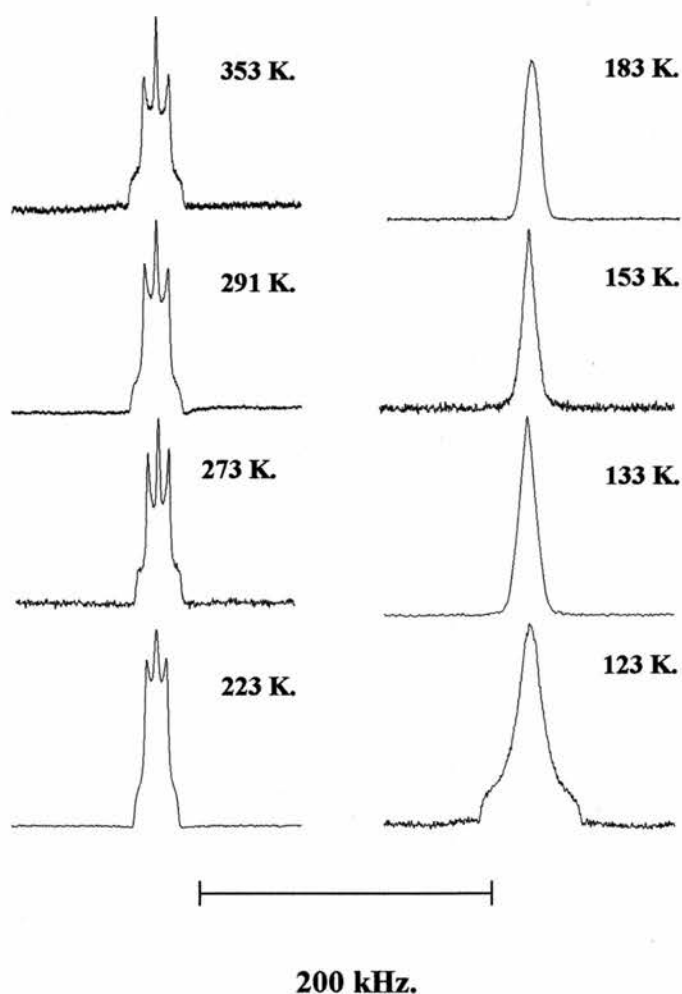


Figure 6.11.2. ^2H NMR spectra of AlMePO- α loaded with 4.5 % in weight of C_6D_6 at several temperatures. The time spacing between the 90° pulses of the quadrupole echo sequence was $35\mu\text{s}$.

At 353 K there are two different signals. One is a uniaxial horn shape powder pattern of 17.4 kHz width, which corresponds to an effective QCC of 24 kHz, very small compared with the QCC observed for rigid C-D bonds, 193 kHz. This indicates benzene molecules undergoing anisotropic motion at this temperature. The other signal observed is a very narrow line, 1.4 kHz, superposed on top of the first one. This corresponds with benzene molecules spinning isotropically. The decrease of temperature produces a gradual narrowing of the uniaxial powder pattern and a decrease of intensity of the isotropic component. The line shape observed between 183 K and 123 K are different from those observed at higher temperature pointing to a change in the dynamic state of the benzene molecules. At 153 K a triangular shape signal of 34 kHz width at the base and 13 kHz width measured at half of the peak intensity is observed. The signal observed at 123 K is 70 kHz broad at the base and 20.8 kHz width measured at half peak intensity.

The narrow isotropic line overlapping with the uniaxial powder pattern indicates that in our solid there are two types of benzene molecules the motions of which are not coupled on the NMR time scale. It is likely that the narrow component is associated with benzene molecules adsorbed on the AlMePO- β impurity.

Spin lattice T_1 relaxation time constants were measured in both samples using a saturation-recovery pulse sequence. Figure 6.11.3 and Table 6.11.1 summarise the results of these experiments. At low temperatures, the T_1 values were calculated from exponential fits of the evolution of the area of the signal as a function of the time τ_0 . At high temperatures the spectra give horn shape powder patterns enabling the increase of intensity of the singularities of signals to be used for the exponential fits, minimising the error due to the presence of AlMePO- β impurity. It can be seen in figure 7.9.3 that the plots of T_1 vs. T exhibit a minimum at ~ 140 K, indicating that the frequency of the rotation of the guest molecules approximates the ^2H precession frequency in our magnetic field (76.78 MHz). The activation energies for the motion of benzene were calculated at both loading levels from the Arrhenius dependences presented in Figure 6.11.3. These activation energies were 6.94 and 9.80 kJmol^{-1} for the samples loaded at 1.5 and 4.5 wt % of benzene respectively.

a)	T/K	T_1 /ms	b)	T/K	T_1 /ms
	293	600		289	366
	273	430		273	283
	250	300		253	230
	233	270		223	122
	200	138		203	94
	173	78		183	46
	153	40		163	27
	133	36		143	21
	123	52		133	20

Table 6.11.1. Summary of the spin-lattice T_1 relaxation time constants for benzene in AlMePO- α at a) 1.5 and b) 4.5 wt % loading level.

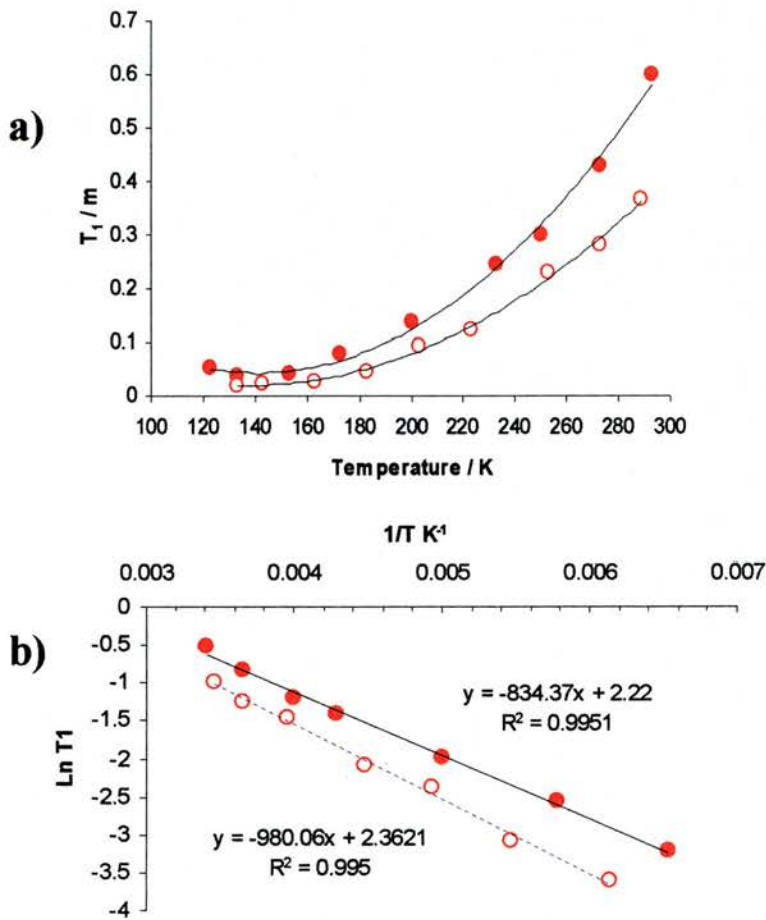


Figure 6.11.3. a) Dependences of the spin-lattice T_1 relaxation time constant with the temperature and, b) Arrhenius plots of $\ln T_1$ vs $1/T$ for benzene in AlMePO- α . Solid and open symbols correspond to samples loaded with 1.5 and 4.5 wt % of benzene respectively.

The nature of the rotational modes that generate the spectra observed at the different temperatures was investigated using the MXQET computer code.

The experimental spectral lines obtained at all temperatures are narrow compared with the powder pattern spectra for a static C-D bond. The in-plane rotation of the benzene about its hexagonal axis is a natural rotational mode for this molecule that has been observed in several host frameworks. Due to the narrow of the spectra, it is likely that this rotational mode is contributing to the reduction of the quadrupole interaction.

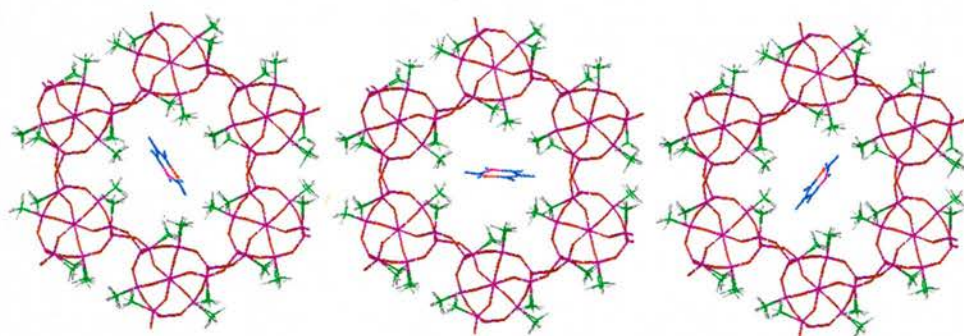


Figure 6.11.4. Representation of benzene in AlMePO- α channel with three different orientations according to the model used for the simulations of the experimental spectra. These images have been adapted from snapshots of Molecular Dynamics calculations performed by Dr. P. A. Cox.

The ^2H -NMR spectra of a fast in-plane rotating benzene molecule can be simulated using MXQET interchanging six sites with six fold symmetry in at an exchange rate of 10^9 s^{-1} . This motion produces an effective QCC equal to 96.5 kHz, half of the value obtained for rigid C-D. The effective QCC observed at all temperatures are even smaller pointing that other motional modes contribute to the averaging of the QCC. The channels of AlMePO- α have a clear triangular shape when viewed down the [001] direction. This suggests that benzene molecules could have three equivalent orientations with the molecular plane parallel to this c axis in a three fold axis symmetry respect to the aluminium methylphosphonate framework. This orientation of the benzene molecule with respect to the channels also agrees with Molecular Dynamics calculations performed by Cox. (Figure 6.11.5) In the MXQET model used for the simulations, the plane of the intermediate frame in which the benzene ring undergoes in-plane rotation is exchanged between three equivalent positions with three fold symmetry.

The simulated MXQET ^2H -NMR spectra for a benzene molecule in a dynamic state that considers both the fast rotation of benzene about its hexagonal axis and the fast jumping

of the molecule in three independent frames at 120° each other, as indicated in the Figure 6.11.4., gives a powder pattern with an effective QCC of 46.65 kHz, which is still large compared with the experimental QCC observed at the highest temperature studied. If fast 30° out of plane motion for the benzene in the intermediate frames are included in the dynamic model the simulation gives a horn shape powder pattern spectra with 17 kHz separation between the two horns, corresponding to an effective QCC of 24 kHz, the same as experimentally observed.

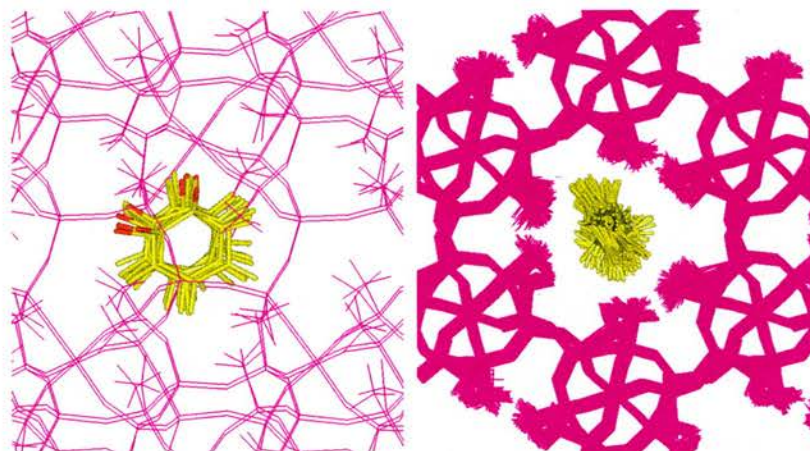


Figure 6.11.5. Trajectories of benzene in AlMePO- α at 298 K found through molecular dynamics [17]. The simulation describes 10^{-10} s of real time motion.

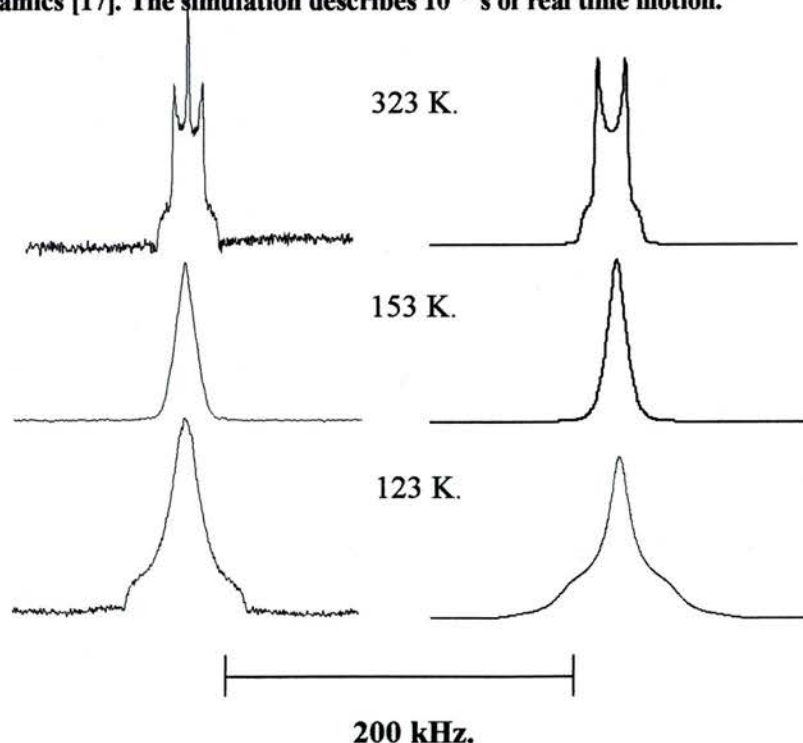


Figure 6.11.6. Experimental (left) and simulated (right) ^2H NMR for benzene adsorbed in AlMePO- α at 323, 153 and 123 K.

The line shape observed at 323 K is maintained down to 223 K indicating that the dynamic state of the benzene molecule in this range of temperatures is the same. At 153 K the spectra presents a triangular shape (Figure 6.11.6.). The triangular signal can be simulated with MXQET using the same sites and angles used before but now using $5.0E5\text{ s}^{-1}$ as a exchange rate for the C_6 clicking of the benzene molecule about its C_6 axis. The exchange rate used to describe the motion of the benzene molecule with respect to the framework was $1.0E7\text{ s}^{-1}$, still at the fast limit of motion. At 123 K the NMR signal broadens to 20.8 kHz at half peak intensity and 70 kHz at the base. This indicates another change in the dynamic state of benzene with the decrease of temperature. After many trials of calculation, it was found that using $2.0E6\text{ s}^{-1}$ for the exchange rate of the intermediate frames defined before and $4.8E4\text{ s}^{-1}$ as exchange rate for the benzene around its C_6 axis, the experimental spectrum could be reasonably reproduced, as can be seen in Figure 6.11.6.

The dependence of the spin-lattice T_1 relaxation time constant with the temperature suggests that the rotation of the benzene is faster than the Larmor frequency of ^2H in our magnetic field at temperatures higher than 140 K. The model proposed for the motion of benzene is compatible with these conclusions. Note that the exchange rate of the intermediate frame at 153 K is fast. On the other hand, according to the T_1 measurements, the rotation frequency of the molecules at 123 K should be below the Larmor frequency and this agree with the exchange rates used in the simulation at that temperature.

It is clear that there are differences between the experimental and simulated spectra at 123 K but one has to consider the limitations at the time to describe the motional model for the molecules with the computer code. In the model presented, the exchange rate between all the sites in the intermediate exchange is unique (see input file in appendix). Other models were attempted to simulate the temperature-dependent ^2H spectra but no other physically reasonable solutions were obtained.

Summary:

The motion of benzene in AlMePO- α has been analysed by means of ^2H NMR. Two loading levels have been studied: 1.5 and 4.5 wt % Due to the similar spectra observed at both loading level it seems that the dynamics of benzene are not greatly affected by the interaction between molecules.

The dependence of the spin-lattice T_1 relaxation times constants with the temperature, similar at both loading levels, shows a minimum at ~ 140 K indicating that rotation frequency of the molecules reaches the Larmor frequency in our magnetic field (76.78 MHz). It was possible to estimate the activation energy for the motion of benzene at both loading levels. The values for the activation energies are 6.94 and 9.80 kJmol^{-1} for 1.5 and 4.5 wt % loading levels.

With the help of the MXQET computer code, a model has been proposed for the motion of benzene in the AlMePO- α . This model is consistent with molecular dynamics simulations and allows the simulation of the experimental spectra It is compatible with the conclusion obtained from the relaxation experiments about the rotation frequencies of the molecules in the experimental temperature range. In the model, the benzene molecule is rotating fast about its six-fold axis. The molecular plane, parallel to the c axis of the framework, rotates by 120° according to the symmetry of the channel. The molecule also undergoes 30° out of plane jumps in each frame. This model allows the simulation of the entire spectral temperature range by changing the speed of rotation about the six-fold axis and the exchange rate of the molecule in the intermediate frames.

6.12. D_6 -benzene as a guest in $AlPO_4-5$

2H quadrupolar NMR of d_6 -benzene in $AlPO_4-5$ adsorbed at 4.5 wt % at different temperatures can be seen in the Figure below. All spectra are uniaxial powder patterns. The widths of the signals are 29, 30, 33 and 33 kHz at 290, 223, 173 and 133 K respectively. A narrow signal of 2 kHz width (measured at half peak intensity) is observed on top of the uniaxial powder pattern at 290 and 223 K.

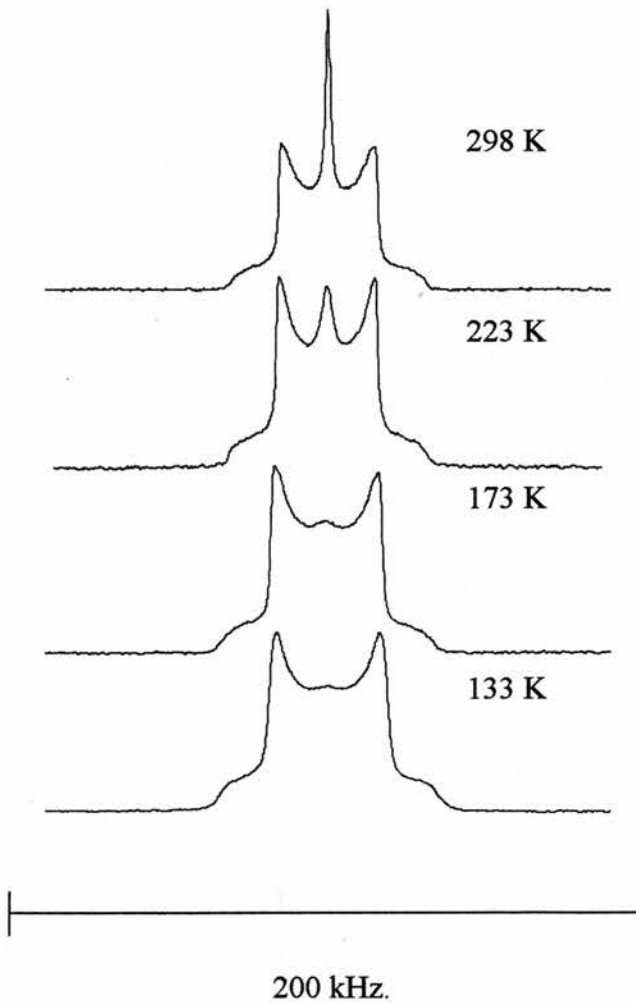


Figure 6.12.1. Experimental 2H quadrupole NMR of d_6 -benzene adsorbed in $AlPO_4-5$.

It is clear that at 298 K there are two different dynamic states for benzene: molecules rotating isotropically and molecules with constrained dynamics, associated with the signal at zero frequency and with the powder pattern horn shape signal respectively.

The spectrum associated with molecules undergoing constrained dynamics at 133 K, 33 kHz width, can be simulated defining a benzene molecule clicking fast about its C_6 axis and moving the benzene into three intermediate frames separated by 120° . This produced a spectrum of 34 kHz width, which is similar to the experimental value. The spectra observed at 298 K, 29 kHz width, can be simulated if 15° out of plane motion is incorporated in the simulation (see Figure 6.12.2).

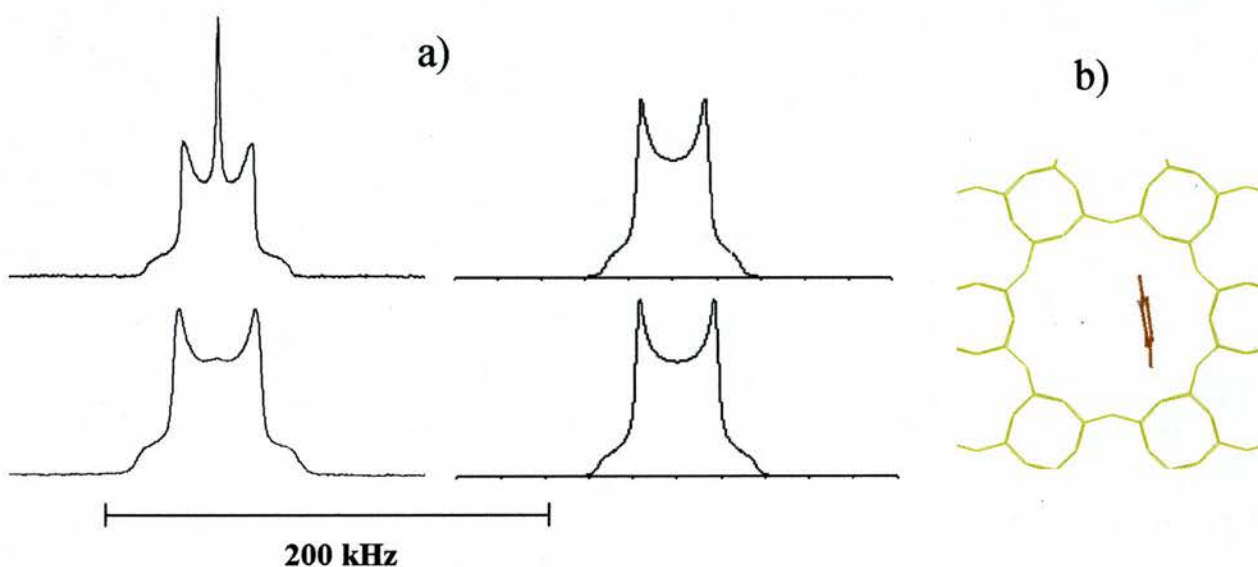


Figure 6.12.2. a) Experimental (left) and simulated (right) ^2H NMR spectra of benzene in $\text{AlPO}_4\text{-5}$. b) Representation of a benzene molecule within a channel of $\text{AlPO}_4\text{-5}$ undergoing in-plane rotation parallel to the channel wall.

It is interesting that, despite its larger pore size, benzene displays more constrained dynamics in $\text{AlPO}_4\text{-5}$ than in the aluminium methylphosphonates. The different dynamics that benzene exhibits must be related to the higher polarity of the microchannels of $\text{AlPO}_4\text{-5}$. It can be concluded that the interaction of benzene with the inorganic framework is strong and, over most of the experimental temperature range, benzene molecules undergo in-plane rotations close to the walls most of the time. At high temperatures there is a small fraction of molecules undergoing free tumbling.

6.13. Summary of the motion of benzene in the AlMePOs

The contrasting dynamic modes and ^2H wideline quadrupole echo spectra for C_6D_6 benzene in the two AlMePO polymorphs illustrate the ability of the technique to differentiate between pore systems of closely similar dimensions and chemical characteristics. In AlMePO- β , the benzene undergoes isotropic motion down to the lowest temperatures measured, as well as spending a relatively small fraction of its time at the walls of the channels. This very high mobility, which is greater than that observed on $\text{AlPO}_4\text{-5}$, cationic zeolites such as Na-X or Na-Y [17], or on the large pore metal organic framework MOF-5 [16, also chapter 7], is likely to be a consequence of the rapidly rotating methyl groups that line the channels and are most closely in contact with the adsorbate. Although the internal surfaces in AlMePO- α are similar, the more restricted channel space, which is strongly triangular in shape, prevents isotropic reorientation, and the benzene molecules exchange between sites in which the plane of the rotating aromatic rings remain approximately parallel to the channel axis. This constraining effect of the pores of AlMePO- α has previously been shown to give interesting effects in the adsorption of N_2 molecules, as a result of constrained modes of packing [6]. The results found through wideline analysis of the ^2H NMR spectra of benzene in the AlMePOs agree with molecular dynamics calculations (P. Grewal and Dr. P. A. Cox). Denayer *et al.* [6] show that, for some zeolites, isopentane is observed to adsorb preferentially over n-pentane, which is reverse of that expected on grounds of the enthalpy of adsorption. This example of 'inverse shape selectivity' is explained in terms of the retention of the rotational mobility of isopentane within the zeolites cages compared to n-pentane, which is not expected to rotate, and therefore has a more negative entropy of adsorption. For benzene in mixtures of AlMePO-s, it would be expected that benzene would adsorb preferentially in the β polymorph, where it retains rotational entropy. This could in part explain the higher ^2H signal of benzene in untransformed - β in the AlMePO- α than be would expected on basis of the NMR and XRD measurements (chapter 5, synthesis of AlMePOs).

6.14. General conclusions

Variable temperature quadrupole echo ^2H NMR has been performed on the d_3 , d_3 -para-xylene, d_3 -, d_5 - and d_8 -toluene and d_6 -benzene within the $\text{Al}_2(\text{CH}_3\text{PO}_3)_3$ polymorphs α and β . Although the pore structure of the two solids is very similar, the slightly different channel shapes (the cross section of $\text{AlMePO-}\alpha$ is remarkably triangular) results in important differences in the spectra. The motion of d_3 , d_3 -para-xylene in both polymorphs, as interpreted from the analysis of the ^2H NMR spectra of the rapid rotating CD_3 groups, is approximately by the molecule moving between different sites on a cone, half cone angle of which depends on the effective diameter of the pores. By this measure, which takes no account of deviations of the pore from perfect cylinders, the pore sizes of β and α estimated at 7.3 and 6.2 Å, respectively, which are slightly larger than the crystallographic estimates.

The ^2H NMR of toluene in these solids can in large part be simulated by again considering the para-axis to exchange between (at least) three sites on a cone with the aromatic ring performing independent $2\pi/3$ flips. This is broadly in agreement with the motion that is predicted by molecular dynamics simulations. Signal from the aromatic ortho- and meta-deuterons of toluene in $\text{AlMePO-}\alpha$ is found to decrease in intensity as the temperature is decreased, suggesting that the rotational exchange occurs at an intermediate exchange rate at this temperature and adding further detail to the model.

Measurements on d_6 -benzene adsorbed in the two polymorphs show the most striking differences. Although the change in structure between the two solids is small, the change in channel shape has a major effect on the motion of benzene. In the slightly more cylindrical channels of $\text{AlMePO-}\beta$, it is able to tumble freely, and does this at all the temperatures studied. As the temperature is lowered it also spends some time at the sites closer to the walls. The situation is very different in $\text{AlMePO-}\alpha$, in the channels of which benzene motion is strongly constrained. By combining ^2H NMR with molecular dynamics simulation, it appears that the strongly triangular shape prevents isotropic motion, restricting the benzene to flipping between the symmetry-related sites in the pores, with the plane of the aromatic ring approximately parallel to the channel axes. The observed lineshape is matched most closely if additional motion due to rotation of the benzene around its C_6 axis and some out of plane motion are also included.

These results show the ability of the two closely similar microporous solids to differentiate strongly between aromatics on the basis of their size and shape. For the example of benzene adsorbed in the AlMePO- β , the high observed mobility can be attributed to the rotating methyl groups lining the pores. Note that in AlPO₄-5, which possesses channels of larger diameter, the dynamics of benzene is much more constrained.

References for chapter 6.

- [1] H.W.Spiess, *Advances in polymer science*, **1985**, 66, 24; H.W.Spiess, *Colloid and polymer science*, **1983**, 261, 193; H.W.Spiess, *Chem. Rev.*, **1991**, 91, 1321. K. Schmidt-Rohr, W. Spiess, *Multidimensional Solid-State NMR and Polymers. (Academic Press)*, **1994**.
- [2] Shin-Ichi Nishikiori, *Journal of inclusion phenomena and macrocyclic chemistry*, **1999**, 34, 331.
- [3] C. I. Ratcliffe, D. V. Soldatov, J. A. Ripmeester. *Micro. Meso. Mater.* **2004**, 73, 71.
- [4] R. N. Devi, M. Edgar, J. Gonzalez, A. M. Z. Slawin, D. P. Tunstall, P. Grewal, P. A. Cox, P. A. Wright, *J. Phys. Chem. B.*, **2004**, 108, 535.
- [5] I. Kustanovich, H. M. Vieth, Z. Luz, S. Vega, *J. Phys. Chem.*, **1989**, 93, 7427; I. Kustanovich, D. Fraenkel, Z. Luz, S. Vega, H. Zimmerman, *J. Phys. Chem.*, **1988**, 92, 4134.
- [6] J. F. M. Denayer, R. A. Ocakoglu, I. C. Arik, C. E. A. Kirschhock, J. A. Martens, G. V. Baron, *Angew. Chem. Int. Ed.*, **2005**, 44, 400.
- [7] K. Maeda, J. Akimoto, Y. Kiyozumi, F. Mizukami, *Angew. Chem. Int. Edit.*, **1995**, 34, 1199.
- [8] K. Maeda, J. Akimoto, Y. Kiyozumi, F. Mizukami, *J. Chem. Soc. Chem. Commun.*, **1995**, 1033.
- [9] K. Maeda, Y. Kiyozumi, F. Mizukami, *J. Phys. Chem. B.*, **1997**, 101, 4402.
- [10] C. Schumacher, J. Gonzalez, P. A. Wright, N. A. Seaton, *Phys. Chem. Chem. Phys.*, **2005**, 7, 2351.

- [11] M.S. Greenfield, A. D. Ronemus, R. L. Vold, R. R. Vold, P. D. Ellis, T. E. Raidy, *J. Mag. Res.*, **1987**, 72, 89.
- [12] J. H. Ok, R. R. Vold, R. L. Vold, M. C. Etter, *J. Phys. Chem.*, **1989**, 93, 7618.
- [13] T. Sato, K. Kunimori, S. Hayashi, *Phys. Chem. Chem. Phys.*, **1999**, 1, 3839.
- [14] V. J. Carter, J. P. Kujanpää, F. G. Riddell, P. A. Wright, J. F. C. Turner, C. R. A. Catlow, K. S. Knight, *Chem. Phys. Let.*, **1999**, 313, 505.
- [15] S. R. Miller, E. Lear, J. Gonzalez, A. M. Z. Slawin, P. A. Wright, N. Guillou, G. Ferey, *Dalton. Trans.*, **2005**, (in press).
- [16] J. Gonzalez, R. N. Devi, D. P. Tunstall, P. A. Cox, P. A. Wright, *Microporous Mesoporous Mater.* (in press).
- [17] S.M. Auerbach, L. M. Bull, N. J. Henson, H. I. Metiu, A. K. Cheetham, *J. Phys. Chem.*, **1996**, 100, 5923.

Chapter 7.

Synthesis and ^2H NMR studies of the metal organic framework MOF-5

7.1. Introduction:

The zinc-benzenedicarboxylate MOF-5[1,2] is a prototypical coordination polymer. The framework structure possesses large cubic cavities, with Zn_4O units at each of the cube's corners, linked by benzene dicarboxylate units. The inorganic 'nodes' can be considered as four ZnO_4 tetrahedra, all sharing a central oxygen, with tetrahedral symmetry and composition Zn_4O_{13} . The solid may be crystallised successfully from dilute solution, for example from the solvents dimethylformamide (DMF) [1] or diethylformamide (DEF) [2], either at room temperature or solvothermally. These routes give crystalline samples, the individual crystals possessing well defined cubic morphologies. The individual crystallites are of sufficient quality, for example, to permit elucidation of the structure by single crystal X-ray diffraction. More recently, a synthetic route has been reported whereby microcrystalline powders of the same composition and similar structure can be prepared rapidly by mixing at room temperature (MOCP-L of Huang *et al.*) [3]. In the as-synthesised forms of these solids the pores are full of solvent molecules (DMF, DEF). Upon heating, however, the solvent molecules can be removed to leave the solid with accessible pore volume of around $1.04 \text{ cm}^3/\text{g}$.

Although a great deal is known about the average structure of metal organic frameworks from X-ray crystallography, their dynamic and other properties are less well studied. In this chapter, the results of studies of the dynamics of the aromatic groups in the framework of MOF-5 and the closely related solid, MOCP-L, and of the adsorbed d_6 -benzene molecules within the pores, are reported. The wideline spectra are analysed using the program MXQET [4] in terms of the type of frequency of motion as a function of temperature, to give a unique insight into the intra-pore environment of these materials. The MOF-5 and related solids are an ideal for studies of this kind. Not only is the solid readily prepared and stable to solvent removal, but the nature of the way the benzene groups in the framework are attached at each end, only permitting oscillation or rotation about a single axis, makes interpretation of the ^2H spectra from the framework groups straightforward. Furthermore, the symmetry and rigidity of the d_6 -benzene adsorbate makes interpretation of its ^2H NMR spectra relatively unambiguous.

7.2. Synthesis of metal organic frameworks

MOF-5 was synthesised according to the method of Yaghi [2]. Typically 0.1 g of $\text{Zn}(\text{NO}_3)_2 \cdot 6\text{H}_2\text{O}$ (Aldrich, 98%) and 0.0401 g of terephthalic acid were dissolved in two closed glass tubes with 15 ml of freshly opened diethylformamide (99% Aldrich) in each with the help of magnetic stirrers and an ultrasonic bath. The two solutions were placed together in a Teflon-lined autoclave with another extra 5-7 ml of diethylformamide used to wash the glass tubes. White crystals were observed after heating the reaction mixture for 12h at 100°C. During the filtration under reduced pressure the crystals were washed several times with fresh solvent. The solid was stored under fresh diethylformamide in a closed 25 ml sample bottle

MOCP-L was prepared according to the method of Huang *et al.* [3] 1.21g $\text{Zn}(\text{NO}_3)_2 \cdot 6\text{H}_2\text{O}$ (Aldrich, 98%) and 0.34 g of terephthalic acid were dissolved in two closed Erlenmeyer flasks at room with 20 ml of dimethylformamide (99% Lancaster) in each with the help of magnetic stirrers and ultrasonic bath. Similar to the synthesis of MOF-5, the solutions were kept isolated to reduce moisture uptake. After the solids were completely dissolved, the $\text{Zn}(\text{NO}_3)_2 \cdot 6\text{H}_2\text{O}$ solution was added to the terephthalic acid solution with another extra 5-7 ml of solvent used to washed the first conical flask. Instantaneous precipitation of the solid was achieved by adding 1.6g of triethylamine to the reaction mixture under fast stirring conditions. After 30 min stirring at room temperature a white precipitate was collected by filtration. The product was washed several times with fresh solvent and stored under fresh dimethylformamide. (In the reported synthetic method by Huang [3] the solid was dried at 90°C, on air, before being stored in a dessiccator. This was avoided, and the solid was kept under fresh solvent before it was further characterised or used as a host framework for ^2H NMR studies).

Two different sources of terephthalic acid were used for these preparations of MOF-5 and MOCP-L. Partially deuterated d_4 -MOF-5 and d_4 -MOCP-L were synthesised from d_4 -terephthalic acid (Aldrich 97 atom % D) and fully protonated MOF-5 was synthesised using protonated terephthalic acid (Aldrich, 98%).

7.3. Characterisation of metal organic frameworks MOF-5 and MOCP-

The X-ray diffraction patterns measured on as-synthesised solids and samples evacuated at 573 K are presented in Figure 7.3.1. The as-synthesised patterns of both sets of solids may be indexed by a cubic unit cell with $a = 25.7(1) \text{ \AA}$, in agreement with those published for MOF-5 in ref 1. SEM studies reveal a regular cubic morphology (*ca.* 100 μm dimension) for the sample synthesised solvothermally and an irregular fine grained morphology for the sample synthesised by the direct mixing approach (Figure 7.3.2).

After heating the samples under vacuum at 573 K both solids remain crystalline, as can be seen in the XRD measurements of the samples that had been studied by NMR (Figure 7.3.1). Note that the XRD patterns of both solids are very similar before and after the removal of the guest molecules and different from the XRD pattern reported MOCP-L (Figure 7.3.3.).

Nitrogen adsorption experiments (Figure 7.3.4) show that both solids are highly porous with similar pore volumes: 0.95 and 0.81 cm^3/g for the samples prepared according to the methods of Eddaoui *et al.* [2] and Huang *et al.*[3] respectively. The nitrogen pore volume found for the sample of MOF-5 agrees with previous values reported for this solid. On the other hand, the adsorption capacity of our MOCP-L sample (531 cc/g STP at 0.4 P/Po) seems two times larger than the reported capacity for this solid by Huang *et al.* [3] (200 cc/g STP at 0.4 P/Po).

The MOCP-L solid prepared here has an XRD pattern and a N_2 adsorption capacity closer to MOF-5 than to the MOCP-L solid reported by Huang *et al.*[3]. The reasons for these differences are not clear but it should be note that these coordination polymers are not stable in air. In this project, care has been taken to minimise the contact of water with the solids (using fresh solvents, isolating the reaction mixtures). In addition, drying our as-synthesised MOCP-L solid at 90 $^\circ\text{C}$, in an oven open to air for few hours, produces an XRD pattern similar to the reported by L. Huang *et al.* (Figure 7.3.5).

It has also been observed that the MOF-5 solid loses an important degree of its porosity if it is not stored in a dry environment. In Figure 7.3.6 the XRD patterns of a MOF-5 sample that was kept in contact with atmospheric moisture for few days and for one month are presented. These XRD patterns are similar to those corresponding to MOCP-

L and MOCP-H materials of Huang (Figure 7.3.3). It is very clear that MOF-5, like MOCP-L, is highly unstable to H₂O and so it must be kept in anhydrous conditions.

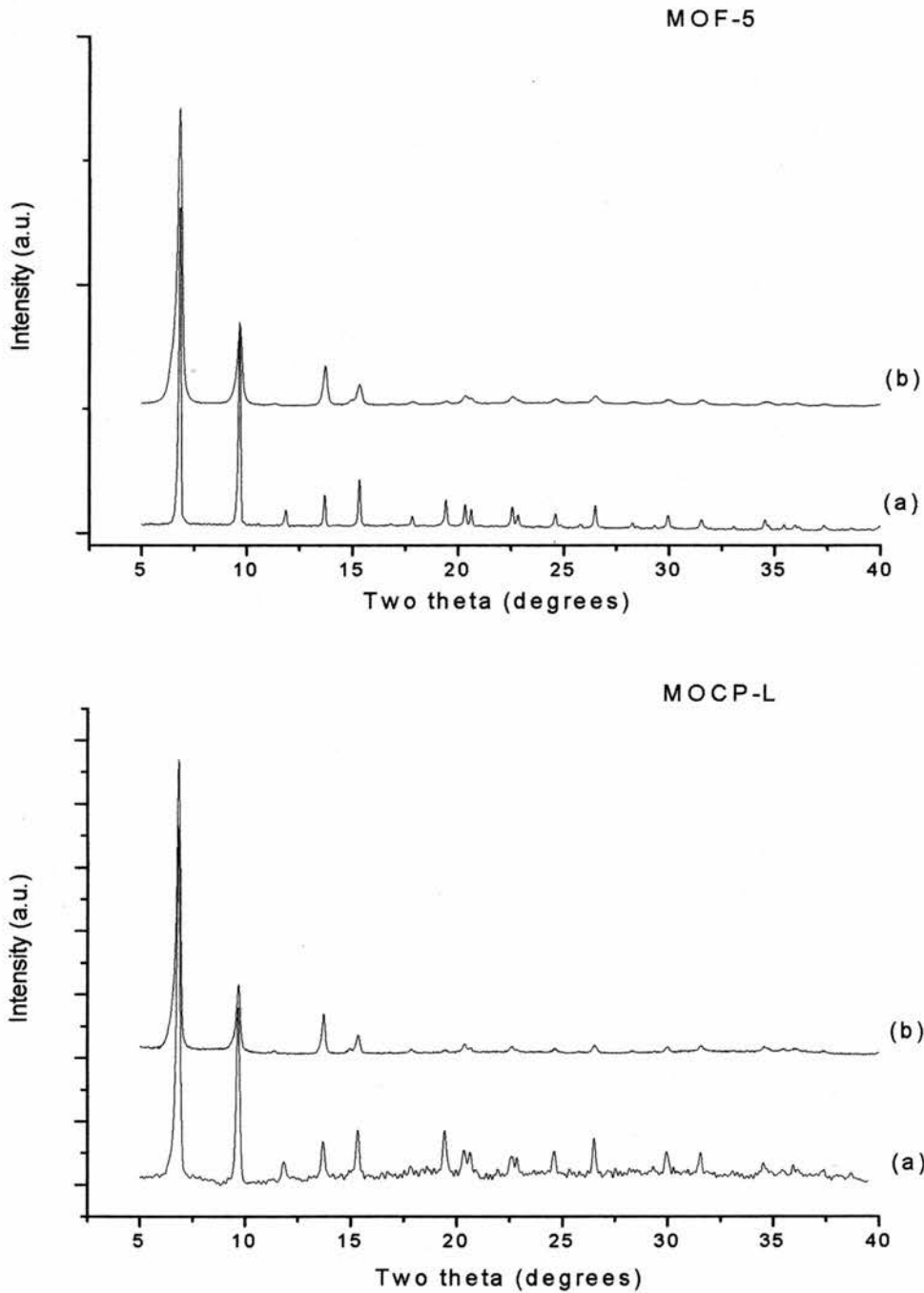


Figure 7.3.1. XRD patterns of (top) d₄-MOF-5 prepared by slow solvothermal crystallisation from diethylformamide and (bottom) MOCP-L, prepared by fast room temperature precipitation from dimethylformamide. For each material the diffraction was recorded (a) as-synthesised and (b) after solvent removal at 573 K. These XRD patterns were recorded on solids after the NMR experiments to check the integrity of the structure.

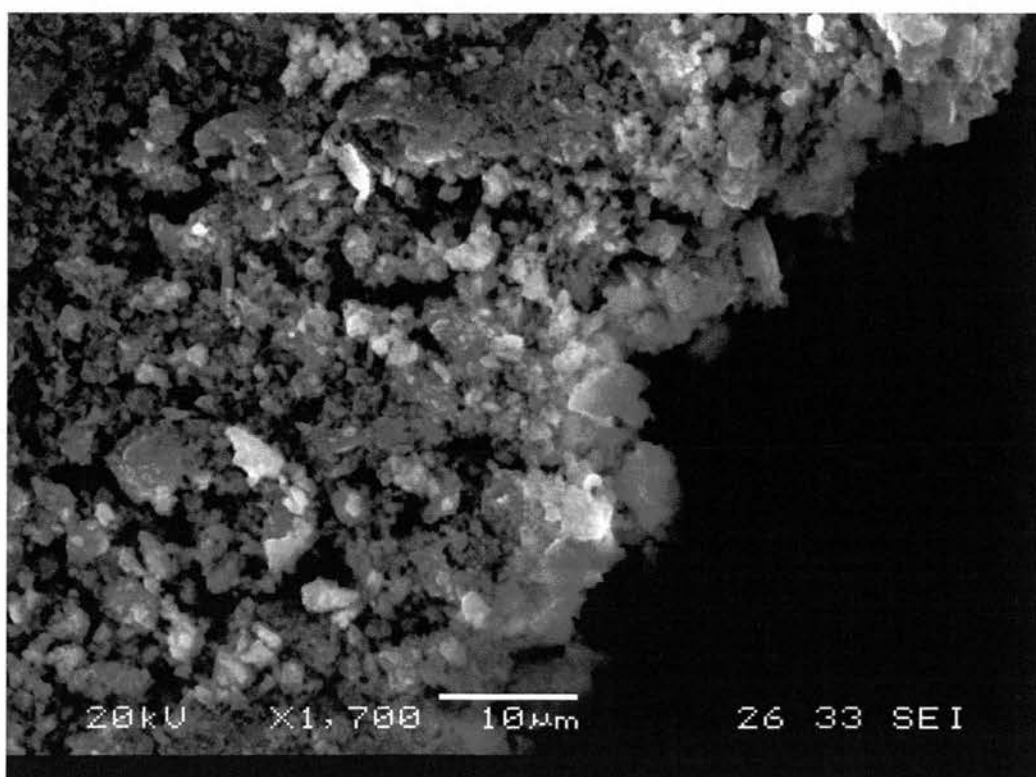
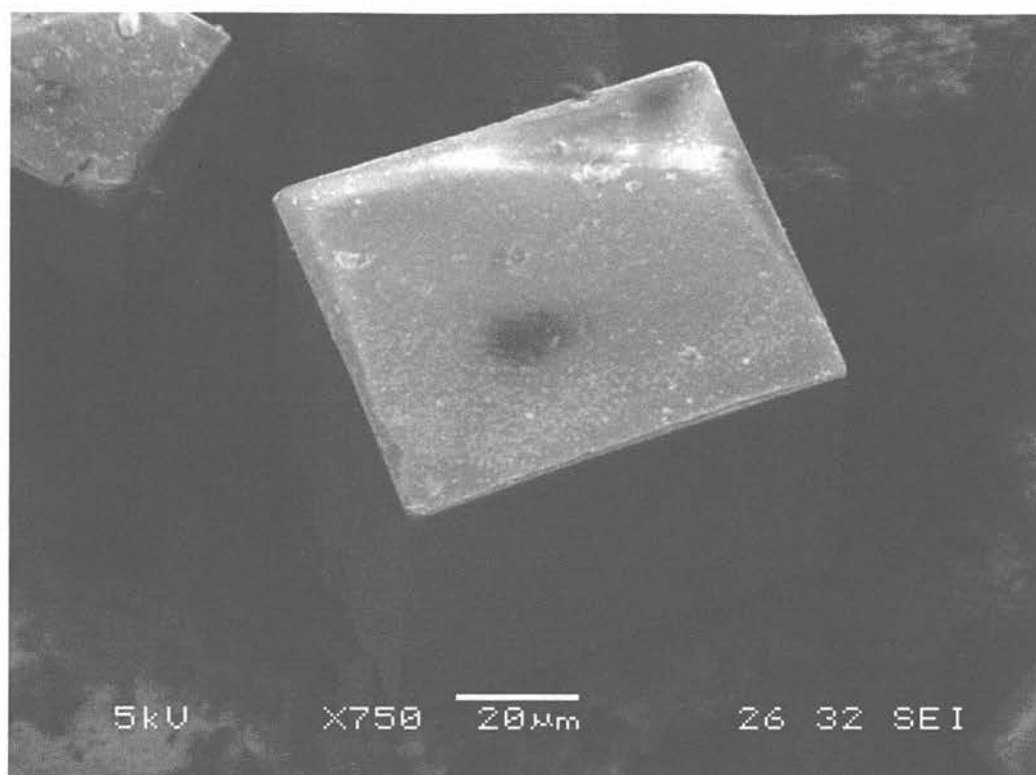


Figure 7.3.2. SEM pictures of MOF-5 synthesised by slow crystallisation (up) and by fast precipitation (down).

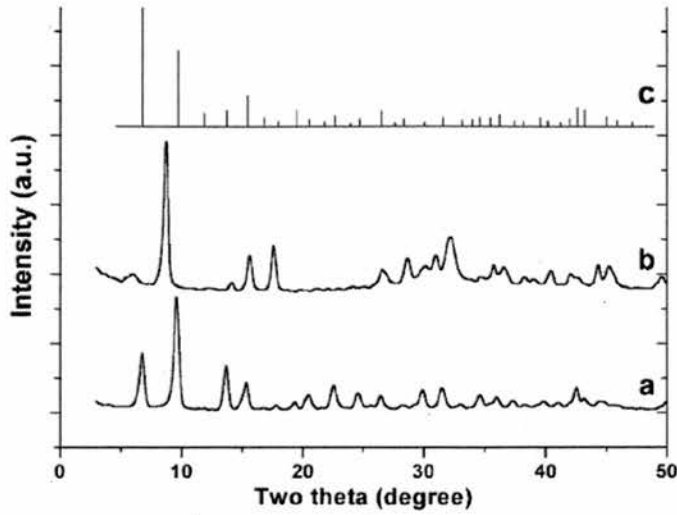


Figure 7.3.3. XRD patterns of MOCP-L, MOCP-H and simulated XRD pattern for MOF-5 published by Huang *et al* [3].

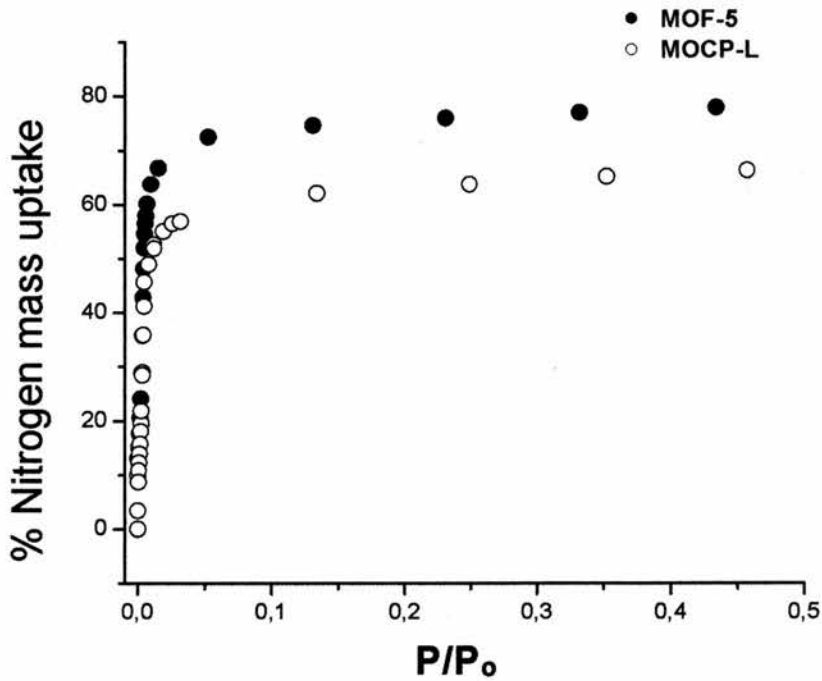


Figure 7.3.4. Nitrogen adsorption isotherms in MOF-5 for the samples synthesised by slow solvothermal crystallisation (solid symbols) and fast precipitation (open symbols) according to ref [2] and [3] respectively.

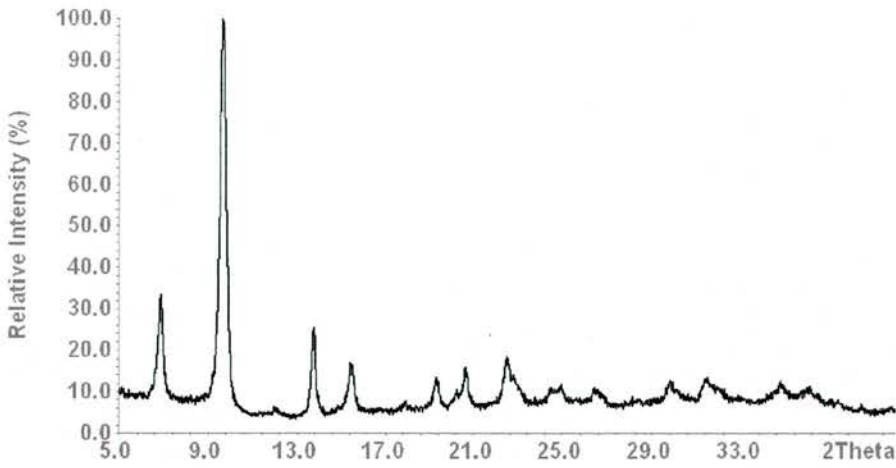


Figure 7.3.5. XRD pattern of MOCP-L dried at 90°C in an oven open to air for a few hours.

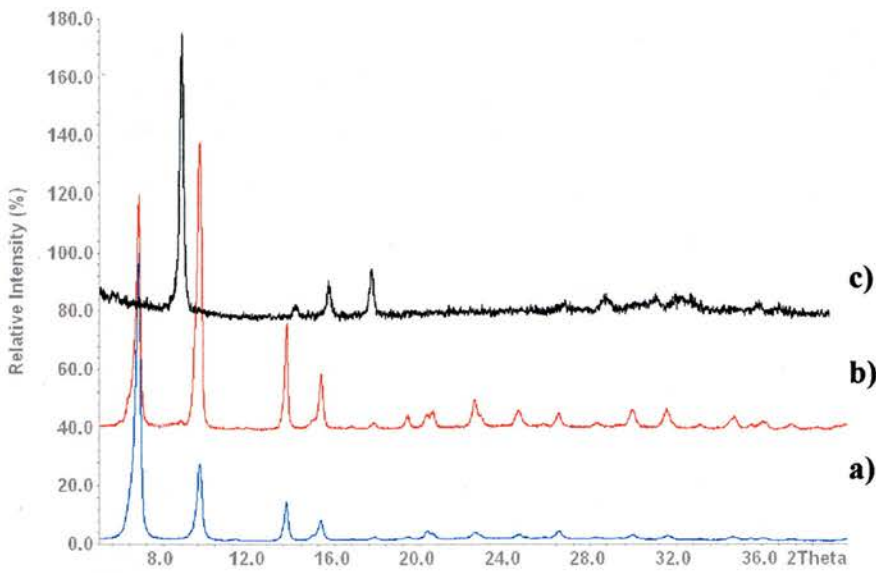


Figure 7.3.6. a) XRD patterns of MOF-5 solid evacuated under vacuum. b) and c) correspond to XRD patterns of as-synthesised samples that have been kept in contact with atmospheric moisture for few days and one month.

7.4. NMR sample preparation

As described in Chapter 2, for the ^2H NMR experiments on desolvated samples, d_4 -MOF-5 and d_4 -MOCP-L were placed into specially adapted glassware consisting of a Pyrex NMR tube (5 mm in diameter) attached to a Schlenk tube. The samples were evacuated on an adsorption line at 573 K, sufficient to remove all solvent molecules without causing the framework structure to lose crystallinity. The sample tubes were partially immersed in liquid nitrogen before sealing the other end of the glass tube with a flame. Protonated samples of MOF-5 were also heated under vacuum at 573 K to remove solvent molecules, and the samples quickly weighed into the glassware described before and further evacuated at 573 K before loading with a known quantity of d_6 -benzene in the gas handling line. The benzene loading level was 20% in weight, one quarter of the maximum benzene adsorption capacity [2], which corresponds to two benzene molecules per tetrahedral Zn_4O_{13} 'nodal unit'. Prior to sealing, the glass tubes were kept at 60°C for one hour to enable equilibration of the sorbent-adsorbate system to be reached.

When loading the samples tubes with the solids, particles remained in the place where the flame was later applied in order to melt the glass and seal the samples (See Figure 7.4.1). For the collection of the NMR spectra, the part of tube with the carbonised solid, was as far as possible left outside the coil in order to minimise the effect of this decomposed material upon the spectra. Nevertheless, sometimes particles of carbonised solid drop on to the sample. This was more apparent with the MOF-5 sample, possibly due to its much larger particle size. In order to check the structural integrity of the solids, after the NMR experiments the sample tubes were opened and rapid XRD analysis performed, see Figure 7.3.1.



Figure 7.4.1. Sealed Pyrex tube with MOCP-L.

7.5. ^2H NMR studies on the framework

^2H wideline NMR spectra of as-prepared MOF-5 and MOCP-L, prepared using d_4 -terephthalic acid and measured up to 373 K (Figure 7.5.1) show changes in line shape resulting from the temperature dependent motion of the phenyl groups.

For MOF-5, an axially symmetric anisotropic powder pattern with sharp edges at ± 67.5 kHz is observed at 298 K, in addition to a sharp but narrow central line. The latter is attributed to a small amount of mobile deuterated hydrocarbon produced as a result of pyrolysis of small amounts of the solid upon sealing. (Even if the benzene ring were freely rotating about its para axis the signal observed would not be an isotropic line [5].)

The ± 67.5 kHz signal is the typical splitting observed for static C-D bonds corresponding to an effective quadrupole coupling constant (QCC) of 180 kHz [6,7]. Upon raising the temperature to 373 K, the signal changes to one with sharp edges at ± 16 kHz and shoulders at ± 63.5 kHz and ± 78.0 kHz. The same lineshape can be simulated for aromatic deuterons undergoing π flips at the fast exchange limit. MXQET simulation indicates the lineshape can be matched by an average quadrupole tensor with features at ± 17 , ± 67 and ± 84 kHz. The experimental values are slightly narrower than that simulated probably due to other sorts of motions (such as librations) at this temperature. The spectra recorded between 298 K and 373 K are the superposition of the two components described above.

^2H NMR spectra of MOCP-L samples show a similar behaviour, except that there appears to be rapid flipping of a portion of the framework benzene rings at temperatures as low as 173K, at which temperature all benzene rings are stationary in MOF-5. At 373 K only signal from molecules performing π flips is observed for MOCP-L, whereas at 223 and 298 K the signal is made up of the superposition of two components, static rings and those undergoing π flips. (It is difficult to quantify the occupancies of this dynamic states because ^2H nucleus is quadrupolar, $I=1$, and also due to the nature of the technique use for the acquisition of the NMR signals, solid echo pulse sequence, which would enhance the signal of the dynamic state with longer transverse magnetization decay, T_2).

In summary, the framework benzene rings of both as-prepared samples are undergoing fast π flips about their para axis at 373 K, whereas at lower temperatures the mobility of the aromatic rings of the samples prepared by the two methods seems to be different. In the MOF-5 sample below 298 K they are essentially static over the NMR time scale while in MOCP-L there is still a fraction of aromatic rings performing fast π flips. It may be that the fast precipitation of the phase achieved by the direct mixing, with large numbers of surface or internal defects, provides lower barriers to the rotation of some of the framework groups.

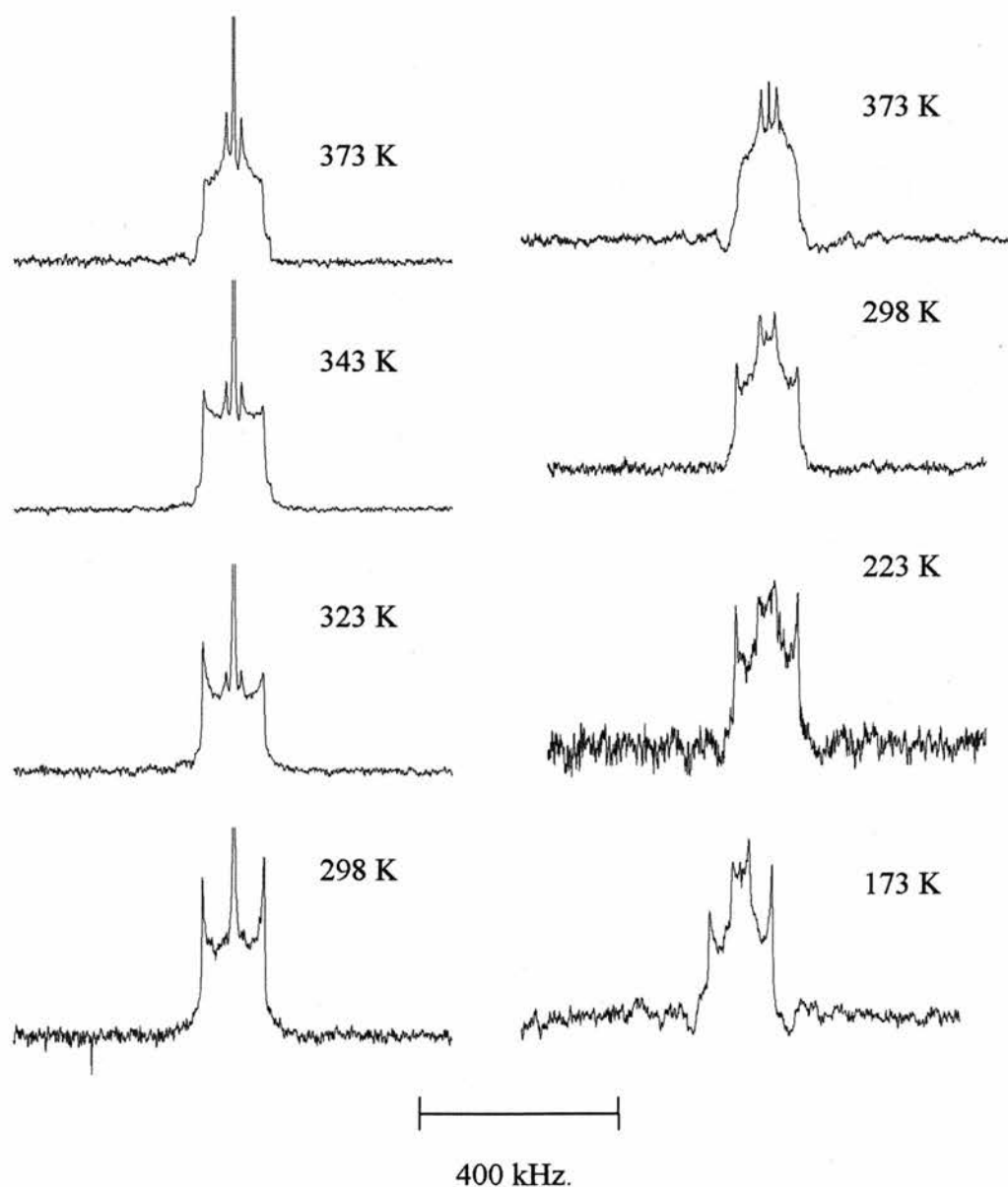


Figure 7.5.1. ^2H NMR spectra of d_4 -MOF-5 (left) and d_4 -MOCP-L (right) synthesised from d_4 -terephthalic acid according to ref [2] and [3] respectively.

7.6. Mobility of adsorbed d_6 -benzene.

The MOF-5 structure type can exchange different guest molecules without losing its structure [1,2]. We have studied this further exploring the difference in mobility that perdeuterated benzene has within the cavities of the solids synthesised by slow crystallisation and fast precipitation.

^2H NMR spectra of deuterated benzene adsorbed in MOF-5 and MOCP-L (Figure 7.6.1) reveal that the benzene is fully mobile in both materials at 200 K and above. This sharp central peak arises from complete averaging of the quadrupole interaction by the isotropic motion of benzene within the cavities. Upon cooling below 200 K an axially symmetric powder pattern, 68 kHz in width, characteristic for the in-plane rotation of the benzene molecule, is observed. However, this in-plane rotation is the only mode of motion at 143 K and below for MOF-5, and at 120 K and below for MOCP-L, indicating that the benzene is slightly more mobile in the fine grained material.

Arrhenius plots of ^2H spin-lattice relaxation time of benzene adsorbed in the two samples are shown in figures 7.6.2. The curves appear to conform to a single activation energy for each set of measurements, taking in to the account only the measurements where the benzene undergoes isotropic rearrangement. The activation energy for the isotropic reorientation of benzene was 6.14 (4) kJ/mol for MOF-5 and 3.70 (2) kJ/mol for MOCP-L. The activation energy for the isotropic motion of benzene within the cavities of other microporous solids has been studied already by several groups. For example, the values that we have found are smaller than those reported by Auerbach *et al.* [6] for benzene in siliceous Faujasite (10.2 kJ/mol) and Na-Y zeolite (23.5 kJ/mol). However, benzene is found to undergo isotropic rearrangement in pure SiO_2 zeolite Y, down to 155 K, at which temperature it begin to spend part of the time executing in plane rotation in the zinc carboxylate materials.

In an experiment to determine whether the motion of the benzene is correlated with the motion of benzene groups in the framework, ^2H NMR spectra were measured for a sample of d_4 -MOF-5 with adsorbed, fully protonated benzene, at a temperature, 298 K,

where adsorbed benzene molecules are known to be reorientating isotropically. At this temperature the framework groups are stationary, so that the motions of host and guest are not correlated under those conditions.

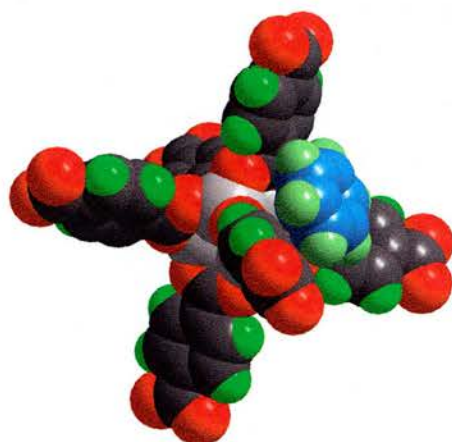
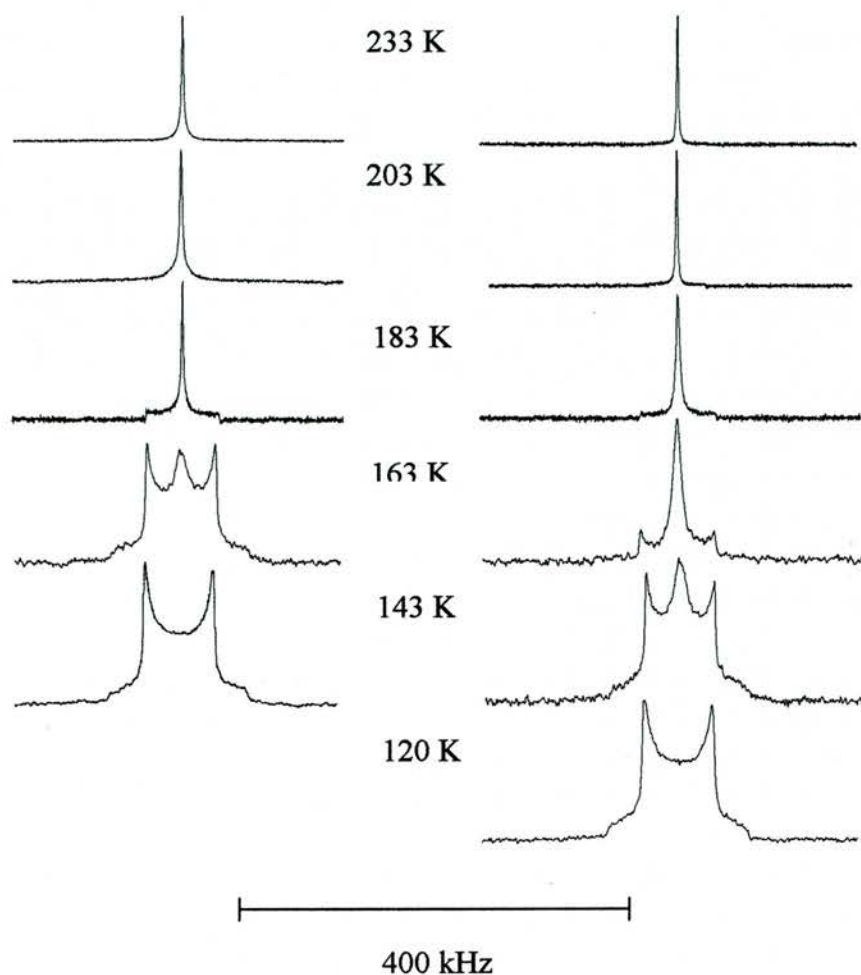


Figure 7.6.1. (Top) ^2H NMR spectra of d_6 -benzene adsorbed in MOF-5 (left) and MOCP-L (right) at different temperatures. Samples were synthesised according to reference 2 and 3 respectively. Note the 68 kHz signal width observed at low temperatures corresponding to a benzene undergoing in-plane rotation. (Bottom) Minimal energy location of benzene in MOF-5 proposed by Cox.

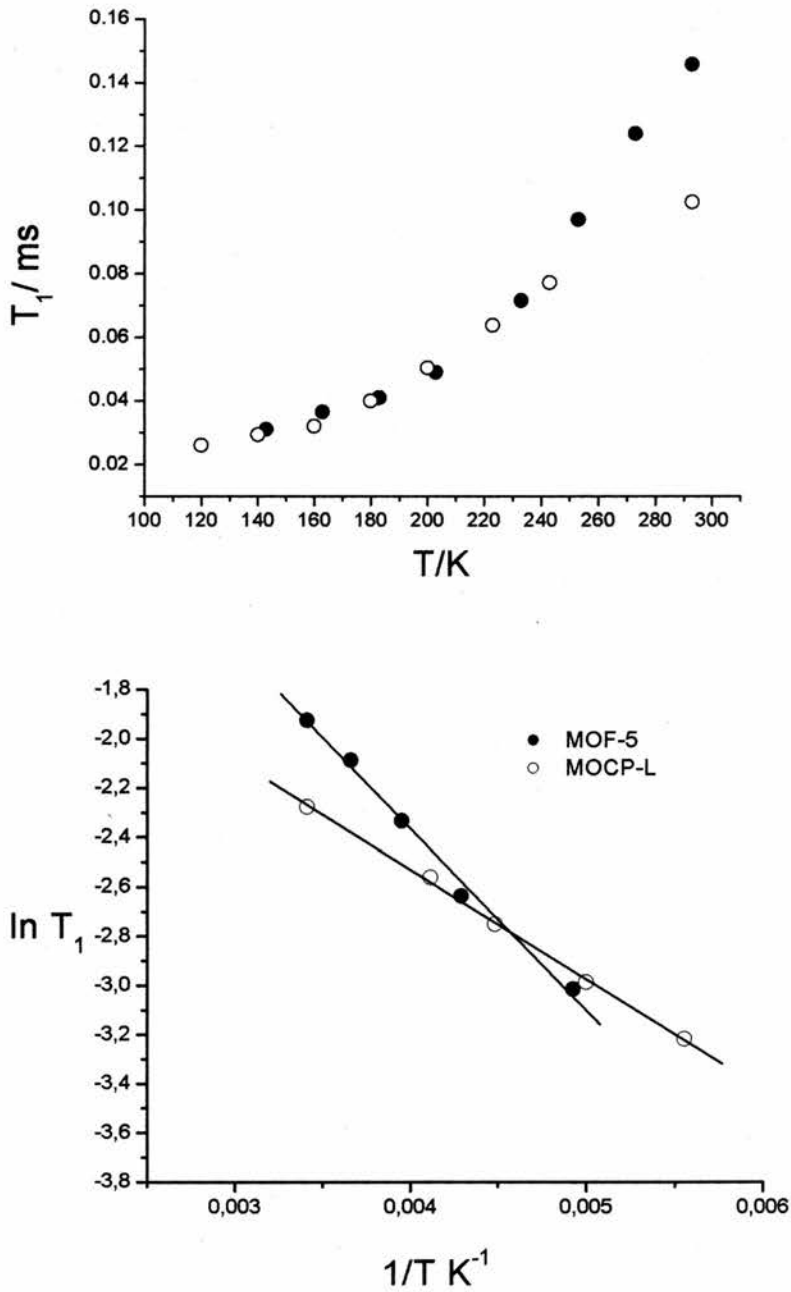


Figure 7.6.2. Temperature dependence of the longitudinal T_1 relaxation time constant (left) and Arrhenius plot for $\ln T_1$ vs. $1/T$ for C_6D_6 adsorbed in MOF-5 (solid symbols) and MOCP-L (open symbols) synthesised according to references 2 and 3 respectively.

7.7. Conclusions

Metal organic framework coordination polymers MOF-5 and MOCP-L solids have been synthesised via the solvothermal and rapid precipitation methods reported in ref [2] and [3]. The mobility of aromatic linking groups in MOF-5 and MOCP-L has been measured by ^2H wideline NMR. The linking groups are shown to become mobile and undergo π flips around their para-axis in MOF-5 at temperatures of 323 K and above 373 K, all the groups are executing this motion.

These solids readily adsorb benzene. At a loading of 20 % by weight, corresponding to two molecules per tetrahedral inorganic nodal unit of the MOF-5 structure, the motion of benzene has been examined. At low temperatures (143 K for MOF-5 and 120 K for MOCP-L) its only motion is rotation about its C_6 axis but at higher temperatures it undergoes isotropic motion. The activation energies of isotropic motion of benzene in MOF-5 and MOCP-L are 6.14(4) kJ/mol and 3.70 (2) kJ/mol , as measured from an Arrhenius plots of T_1 relaxation data. Notably, the benzene ring executes isotropic motion even at temperatures at which the linking aromatic groups are stationary.

Computer simulation of interaction between benzene and MOF-5 performed by Cox suggests that the minimum energy site is on the three-fold site close to the inorganic Zn_4O_{13} cluster.

References for chapter 7.

- [1] H. Li, M. Eddaoudi, M. O'Keeffe, O. M. Yaghi, *Nature*, **1999**, 402, 276
- [2] M. Eddaoui, J. Kim, N. Rosi, D. Vodak, J. Wachter, M. O'Keeffe, O. M. Yaghi, *Science*, **2002**, 295, 469
- [3] L. Huang, H. Wang, J. Chen, Z. Wang, J. Sun, D. Zhao, Y. Yan., *Microporous Mesoporous Mater.*, **2003**, 58, 105
- [4] M.S. Greenfield, A. D. Ronemus, R. L. Vold, R. R. Vold, P. D. Ellis, T. E. Raidy, *J. Mag. Res.*, **1987**, 72, 89
- [5] I. Kustanovich, D. Fraenkel, D. L. S. Vega, H. Zimmermann, *J. Phys. Chem.*, **1988**, 92, 4134
- [6] S.M. Auerbach, L. M. Bull, N. J. Henson, H. I. Metiu, A. K. Cheetham, *J. Phys. Chem.*, **1996**, 100, 5923
- [7]] R. N. Devi, M. Edgar, J. Gonzalez, A. M. Z. Slawin, D. P. Tunstall, P. Grewal, P. A. Cox, P. A. Wright, *J. Phys. Chem. B.*, **2004**, 108, 535

Appendix.

Representative MXQET and MXQET1 input files used during this thesis for calculation of ^2H NMR spectra.

Deconvolution of the MAS ^{29}Si NMR spectra of Figure 3.2.3.7 (chapter 3).

Benzene undergoing in-plane rotation:

```
DO MATRIX TESTS? ->N
# SPECTRA TO BE CALCULATED -> 1
OUTPUT FILE ( NO EXT. ) ->SIMDATA/benzene
# OF AXES ->1
PARAMETERS FOR AXIS 1:
# EXCHANGE SITES -> 6
SITE 1: THETA -> 90.0000 PHI -> 0.0000 RHO -> 0.0000
SITE 2: THETA -> 90.0000 PHI -> 60.0000 RHO -> 0.0000
SITE 3: THETA -> 90.0000 PHI ->120.0000 RHO -> 0.0000
SITE 4: THETA -> 90.0000 PHI ->180.0000 RHO -> 0.0000
SITE 5: THETA -> 90.0000 PHI ->240.0000 RHO -> 0.0000
SITE 6: THETA -> 90.0000 PHI ->300.0000 RHO -> 0.0000
MODEL: ALL SITES EXCHANGE=1, NEAREST NEIGHBOR=2, OTHER=3 ->2
EXCHANGE RATE (1/sec) -> 1.00000E+07
EQUAL A PRIORI PROBABILITIES? ->Y
SITE SYMMETRY (Cn), n-> 6
90 DEGREE PULSE LENGTH (us) -> 3.6000
COMPOSITE PULSE? ->N
PULSE SPACING (us) ->100.0000
SPECTRAL WIDTH (kHz) ->400.0000
# POWDER INCREMENTS ->110
# POINTS OF FID CALCULATED -> 200
# REAL POINTS IN SPECTRUM ->1024
QCC (kHz) ->193.0000
STATIC ASYMMETRY PARAMETER -> 0.0000
LORENTZIAN BROADENING (kHz) -> 1.000
GAUSSIAN BROADENING (kHz) -> 1.000
CALCULATE VIRTUAL FID? ->Y
SPECIAL SCALING FACTOR? ->Y      SCALING FACTOR -> 2000.0000
```

Methyl group rotating around its C3 axis:

```
DO MATRIX TESTS? ->N
# SPECTRA TO BE CALCULATED ->1
OUTPUT FILE ( NO EXT. ) ->SIMDATA/methyl
# OF AXES ->1
EQUAL A PRIORI PROBABILITIES? ->Y
PARAMETERS FOR AXIS 3:
# EXCHANGE SITES -> 3
SITE 1: THETA ->109.5000 PHI -> 30.0000 RHO -> 90.0000
SITE 2: THETA ->109.5000 PHI ->150.0000 RHO -> 90.0000
SITE 3: THETA ->109.5000 PHI ->270.0000 RHO -> 90.0000
MODEL: ALL SITES EXCHANGE=1, NEAREST NEIGHBOR=2, OTHER=3 ->1
EXCHANGE RATE (1/sec) ->1.0E7
EQUAL A PRIORI PROBABILITIES? ->Y
SITE SYMMETRY (Cn), n->3
90 DEGREE PULSE LENGTH (us) ->3.6
COMPOSITE PULSE? ->N
PULSE SPACING (us) ->20.0
SPECTRAL WIDTH (kHz) ->400.0
# POWDER INCREMENTS ->1024
# POINTS OF FID CALCULATED ->1024
# REAL POINTS IN SPECTRUM ->1024
QCC (kHz) ->168.00
STATIC ASYMMETRY PARAMETER ->0.0
LORENTZIAN BROADENING (kHz) ->1.0
GAUSSIAN BROADENING (kHz) ->1.0
CALCULATE VIRTUAL FID? ->N
SPECIAL SCALING FACTOR? ->N      SCALING FACTOR ->2000.0
```

Aromatic π -flip.

```
DO MATRIX TESTS? ->N
# SPECTRA TO BE CALCULATED -> 1
OUTPUT FILE ( NO EXT. ) ->SIMDATA/aromatic 180 flip
# OF AXES ->1
PARAMETERS FOR AXIS 1:
# EXCHANGE SITES -> 2
SITE 1: THETA -> 60.0000 PHI -> 0.0000 RHO -> 0.0000
SITE 2: THETA -> 60.0000 PHI ->180.0000 RHO -> 0.0000
MODEL: ALL SITES EXCHANGE=1, NEAREST NEIGHBOR=2, OTHER=3 ->2
EXCHANGE RATE (1/sec) -> 1.0E7
EQUAL A PRIORI PROBABILITIES? ->Y
SITE SYMMETRY (Cn), n->2
90 DEGREE PULSE LENGTH (us) -> 3.600
COMPOSITE PULSE? ->N
PULSE SPACING (us) ->35.0000
SPECTRAL WIDTH (kHz) ->200.0000
# POWDER INCREMENTS ->400
# POINTS OF FID CALCULATED -> 200
# REAL POINTS IN SPECTRUM ->1024
QCC (kHz) ->193.0000
STATIC ASYMMETRY PARAMETER -> 0.0000
LORENTZIAN BROADENING (kHz) -> 1.0000
GAUSSIAN BROADENING (kHz) -> 1.0000
CALCULATE VIRTUAL FID? ->Y
SPECIAL SCALING FACTOR? ->N      SCALING FACTOR -> 2000.0000
```

Aromatic ring rotating around a para axis by 120° (2π / 3 flips).

```
DO MATRIX TESTS? ->N
# SPECTRA TO BE CALCULATED -> 1
OUTPUT FILE ( NO EXT. ) ->SIMDATA/120flip7.0E5c
# OF AXES ->1
PARAMETERS FOR AXIS 1:
# EXCHANGE SITES -> 3
SITE 1: THETA -> 60.0000 PHI -> 0.0000 RHO -> 0.0000
SITE 2: THETA -> 60.0000 PHI ->120.0000 RHO -> 0.0000
SITE 3: THETA -> 60.0000 PHI ->240.0000 RHO -> 0.0000
MODEL: ALL SITES EXCHANGE=1, NEAREST NEIGHBOR=2, OTHER=3 ->2
EXCHANGE RATE (1/sec) -> 1.0E7
EQUAL A PRIORI PROBABILITIES? ->Y
SITE SYMMETRY (Cn), n->3
90 DEGREE PULSE LENGTH (us) -> 3.500
COMPOSITE PULSE? ->N
PULSE SPACING (us) ->35.0000
SPECTRAL WIDTH (kHz) ->200.0000
# POWDER INCREMENTS ->400
# POINTS OF FID CALCULATED -> 200
# REAL POINTS IN SPECTRUM ->1024
QCC (kHz) ->193.0000
STATIC ASYMMETRY PARAMETER -> 0.0000
LORENTZIAN BROADENING (kHz) -> 1.0000
GAUSSIAN BROADENING (kHz) -> 1.0000
CALCULATE VIRTUAL FID? ->Y
SPECIAL SCALING FACTOR? ->N      SCALING FACTOR -> 2000.0000
```

Methyl group moving in a cone type of motion of 25° half cone angle while undergoes rotations around its C3 axis.

```
# OF AXES ->2
PARAMETERS FOR AXIS 1:
# EXCHANGE SITES -> 3
SITE 1: THETA -> 25.0000 PHI -> 0.0000 RHO -> 0.0000
SITE 2: THETA -> 25.0000 PHI ->120.0000 RHO -> 0.0000
SITE 3: THETA -> 25.0000 PHI ->240.0000 RHO -> 0.0000
MODEL: ALL SITES EXCHANGE=1, NEAREST NEIGHBOR=2, OTHER=3 ->2
USE HARD COLLISION MODEL? ->N
EXCHANGE RATE (1/sec) -> 1.00000E+09
EQUAL A PRIORI PROBABILITIES? ->Y
PARAMETERS FOR AXIS 3:
# EXCHANGE SITES -> 3
SITE 1: THETA ->109.5000 PHI -> 30.0000 RHO -> 0.0000
SITE 2: THETA ->109.5000 PHI ->150.0000 RHO -> 0.0000
SITE 3: THETA ->109.5000 PHI ->270.0000 RHO -> 0.0000
MODEL: ALL SITES EXCHANGE=1, NEAREST NEIGHBOR=2, OTHER=3 ->2
EXCHANGE RATE (1/sec) ->1.0E9
EQUAL A PRIORI PROBABILITIES? ->Y
SITE SYMMETRY (Cn), n->3
90 DEGREE PULSE LENGTH (us) ->3.6
COMPOSITE PULSE? ->N
PULSE SPACING (us) ->20.0
SPECTRAL WIDTH (kHz) ->200.0
# POWDER INCREMENTS ->110
# POINTS OF FID CALCULATED ->256
# REAL POINTS IN SPECTRUM ->1024
QCC (kHz) ->168.00
STATIC ASYMMETRY PARAMETER ->0.0
LORENTZIAN BROADENING (kHz) ->0.1
GAUSSIAN BROADENING (kHz) ->0.1
CALCULATE VIRTUAL FID? ->Y
SPECIAL SCALING FACTOR? ->N      SCALING FACTOR ->2000.0
```

Aromatic ring performing 120° flips around its para axis while the para axis moves in a cone type of motion of 30° half cone angle.

```
OUTPUT FILE ( NO EXT. ) ->SIMDATA/aromatic ring in cone of 30°
# OF AXES ->2
PARAMETERS FOR AXIS 1:
# EXCHANGE SITES -> 2
SITE 1: THETA -> 30.0000 PHI -> 0.0000 RHO -> 0.0000
SITE 2: THETA -> 30.0000 PHI ->120.0000 RHO -> 0.0000
SITE 3: THETA -> 30.0000 PHI ->240.0000 RHO -> 0.0000
MODEL: ALL SITES EXCHANGE=1, NEAREST NEIGHBOR=2, OTHER=3 ->2
USE HARD COLLISION MODEL? ->N
EXCHANGE RATE (1/sec) -> 1.00000E+07
EQUAL A PRIORI PROBABILITIES? ->Y
PARAMETERS FOR AXIS 3:
# EXCHANGE SITES -> 3
SITE 1: THETA -> 60.0000 PHI -> 30.0000 RHO -> 90.0000
SITE 2: THETA -> 60.0000 PHI ->150.0000 RHO -> 90.0000
SITE 3: THETA -> 60.0000 PHI ->270.0000 RHO -> 90.0000
MODEL: ALL SITES EXCHANGE=1, NEAREST NEIGHBOR=2, OTHER=3 ->2
EXCHANGE RATE (1/sec) ->1.0E7
EQUAL A PRIORI PROBABILITIES? ->Y
SITE SYMMETRY (Cn), n->3
90 DEGREE PULSE LENGTH (us) ->3.6
COMPOSITE PULSE? ->N
PULSE SPACING (us) ->20.0
SPECTRAL WIDTH (kHz) ->400.0
# POWDER INCREMENTS ->1024
# POINTS OF FID CALCULATED ->1024
# REAL POINTS IN SPECTRUM ->1024
QCC (kHz) ->193.00
STATIC ASYMMETRY PARAMETER ->0.0
LORENTZIAN BROADENING (kHz) ->1.0
GAUSSIAN BROADENING (kHz) ->1.0
CALCULATE VIRTUAL FID? ->N
SPECIAL SCALING FACTOR? ->N      SCALING FACTOR ->2000.0
```

Benzene ring undergoing in-plane C6 rotations, in three planes orientated at 120° around a common axis.

```
DO MATRIX TESTS? ->N
# SPECTRA TO BE CALCULATED -> 1
OUTPUT FILE ( NO EXT. ) ->SIMDATA/benzene in three planes
# OF AXES ->2
PARAMETERS FOR AXIS 1:
# EXCHANGE SITES -> 3
SITE 1: THETA -> 90.0000 PHI -> 0.0000 RHO -> 0.0000
SITE 2: THETA -> 90.0000 PHI ->120.0000 RHO -> 0.0000
SITE 3: THETA -> 90.0000 PHI ->240.0000 RHO -> 0.0000
MODEL: ALL SITES EXCHANGE=1, NEAREST NEIGHBOR=2, OTHER=3 ->2
USE HARD COLLISION MODEL? ->N
EXCHANGE RATE (1/sec) -> 1.00000E+07
EQUAL A PRIORI PROBABILITIES? ->Y
PARAMETERS FOR AXIS 2:
# EXCHANGE SITES -> 6
SITE 1: THETA -> 90.0000 PHI -> 30.0000 RHO -> 90.0000
SITE 2: THETA -> 90.0000 PHI -> 90.0000 RHO -> 90.0000
SITE 3: THETA -> 90.0000 PHI ->150.0000 RHO -> 90.0000
SITE 4: THETA -> 90.0000 PHI ->210.0000 RHO -> 90.0000
SITE 5: THETA -> 90.0000 PHI ->270.0000 RHO -> 90.0000
SITE 6: THETA -> 90.0000 PHI ->330.0000 RHO -> 90.0000
MODEL: ALL SITES EXCHANGE=1, NEAREST NEIGHBOR=2, OTHER=3 ->2
EXCHANGE RATE (1/sec) -> 1.00000E+07
EQUAL A PRIORI PROBABILITIES? ->Y
SITE SYMMETRY (Cn), n-> 6
90 DEGREE PULSE LENGTH (us) -> 3.2000
COMPOSITE PULSE? ->N
PULSE SPACING (us) -> 20.0000
SPECTRAL WIDTH (kHz) ->200.0000
# POWDER INCREMENTS ->110
# POINTS OF FID CALCULATED -> 100
# REAL POINTS IN SPECTRUM ->1024
QCC (kHz) ->193.0000
STATIC ASYMMETRY PARAMETER -> 0.0000
LORENTZIAN BROADENING (kHz) -> 1.0000
GAUSSIAN BROADENING (kHz) -> 1.0000
CALCULATE VIRTUAL FID? ->Y
SPECIAL SCALING FACTOR? ->N      SCALING FACTOR -> 2000.0000
```

Benzene ring undergoing in-plane C6 rotations, in three planes orientated at 120° around a common axis plus 10° out of plane motion.

```
DO MATRIX TESTS? ->N
# SPECTRA TO BE CALCULATED -> 1
OUTPUT FILE ( NO EXT. ) ->SIMDATA/10°conec
# OF AXES ->2
PARAMETERS FOR AXIS 1:
# EXCHANGE SITES -> 9
SITE 1: THETA -> 80.0000 PHI -> 0.0000 RHO -> 0.0000
SITE 2: THETA -> 80.0000 PHI ->120.0000 RHO -> 0.0000
SITE 3: THETA -> 80.0000 PHI ->240.0000 RHO -> 0.0000
SITE 4: THETA ->100.0000 PHI -> 0.0000 RHO -> 0.0000
SITE 5: THETA ->100.0000 PHI ->120.0000 RHO -> 0.0000
SITE 6: THETA ->100.0000 PHI ->240.0000 RHO -> 0.0000
SITE 7: THETA -> 90.0000 PHI -> 0.0000 RHO -> 0.0000
SITE 8: THETA -> 90.0000 PHI ->120.0000 RHO -> 0.0000
SITE 9: THETA -> 90.0000 PHI ->240.0000 RHO -> 0.0000
MODEL: ALL SITES EXCHANGE=1, NEAREST NEIGHBOR=2, OTHER=3 ->2
USE HARD COLLISION MODEL? ->N
EXCHANGE RATE (1/sec) -> 1.00000E+07
EQUAL A PRIORI PROBABILITIES? ->Y
PARAMETERS FOR AXIS 2:
# EXCHANGE SITES -> 6
SITE 1: THETA -> 90.0000 PHI -> 30.0000 RHO -> 90.0000
SITE 2: THETA -> 90.0000 PHI -> 90.0000 RHO -> 90.0000
SITE 3: THETA -> 90.0000 PHI ->150.0000 RHO -> 90.0000
SITE 4: THETA -> 90.0000 PHI ->210.0000 RHO -> 90.0000
SITE 5: THETA -> 90.0000 PHI ->270.0000 RHO -> 90.0000
SITE 6: THETA -> 90.0000 PHI ->330.0000 RHO -> 90.0000
MODEL: ALL SITES EXCHANGE=1, NEAREST NEIGHBOR=2, OTHER=3 ->2
EXCHANGE RATE (1/sec) -> 1.00000E+07
EQUAL A PRIORI PROBABILITIES? ->Y
SITE SYMMETRY (Cn), n-> 6
90 DEGREE PULSE LENGTH (us) -> 3.2000
COMPOSITE PULSE? ->N
PULSE SPACING (us) -> 20.0000
SPECTRAL WIDTH (kHz) ->200.0000
# POWDER INCREMENTS ->110
# POINTS OF FID CALCULATED -> 100
# REAL POINTS IN SPECTRUM ->1024
QCC (kHz) ->193.0000
STATIC ASYMMETRY PARAMETER -> 0.0000
LORENTZIAN BROADENING (kHz) -> 1.0000
GAUSSIAN BROADENING (kHz) -> 1.0000
CALCULATE VIRTUAL FID? ->Y
SPECIAL SCALING FACTOR? ->N      SCALING FACTOR -> 2000.0000
```

MXQET1 file corresponding to a benzene molecule jumping between two sites. One corresponds to an in-plane rotating benzene molecule and the other to isotropic rotating molecule.

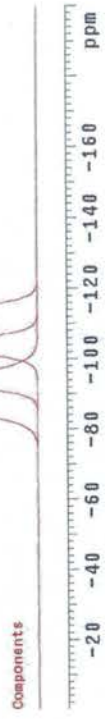
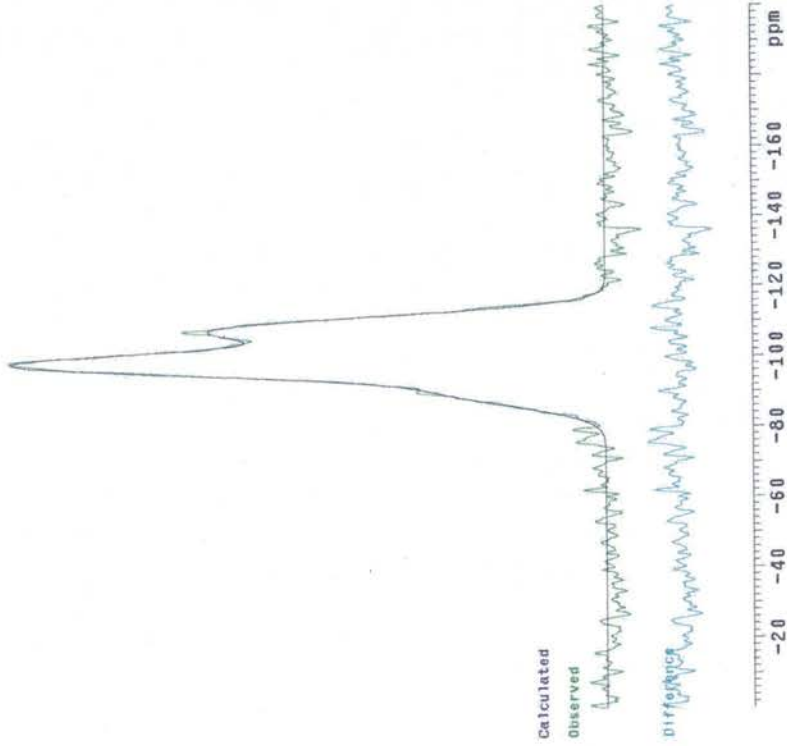
```
do matrix tests? ->n
# spectra to be calculated -> 1
output file ( no ext. ) ->Yaacabo5
# of axes ->1
parameters for axis 1:
# exchange sites -> 2
site 1: theta -> 90.0000 phi -> 0.0000 rho -> 0.0000
site 2: theta -> 0.0000 phi -> 0.0000 rho -> 0.0000
model: all sites exchange=1, nearest neighbor=2, other=3 ->3
-1.0,1.0
1.0,-1.0
exchange rate (1/sec) ->1.0E7
equal a priori probabilities? ->N
0.28,0.72
site symmetry (cn), n-> 1
90 degree pulse length (us) -> 3.6000
composite pulse? ->N
pulse spacing (us) ->62.0000
spectral width (khz) ->200.0000
# powder increments ->200
# points of fid calculated -> 512
# real points in spectrum ->1024
qcc (khz) -> 96.50 0.00
static asymmetry parameter -> 0.000 0.000
lorentzian broadening (khz) -> 1.0000
gaussian broadening (khz) -> 1.0000
calculate virtual fid? ->y
```

Sample 1

data21/paw28Nov0401.f1d

No	ppm	HZ	GF	X
1	-108.4	486.5	1.00*	34.3
2	-96.9	484.8	1.00*	49.4
3	-90.3	605.8	1.00*	16.4

Final chi squared: 2537



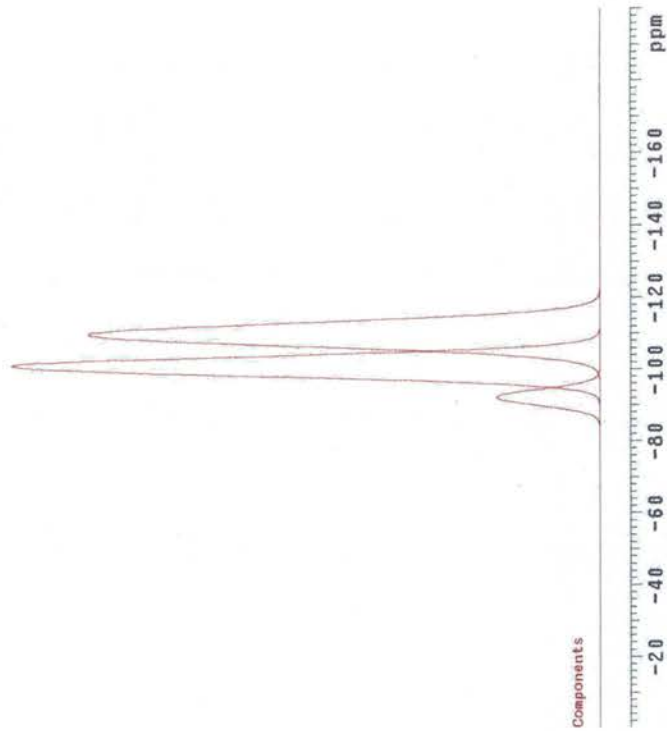
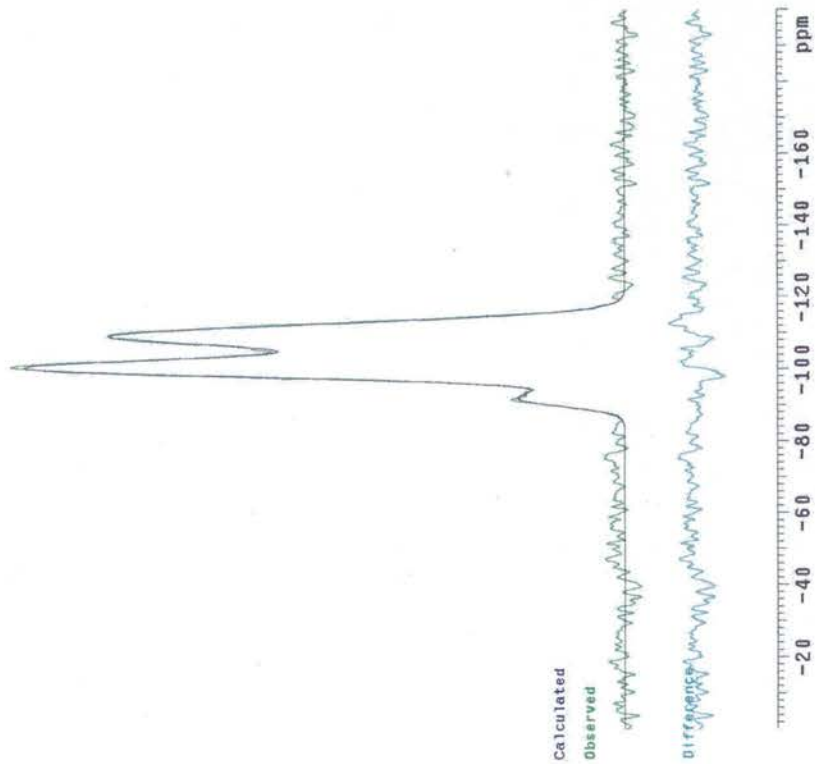
Lineshape is $GF \cdot \text{Gaussian} + (1 - GF) \cdot \text{Lorentzian}$
* indicates parameter fixed during fitting

Sample 2

data21/paw27Nov0401.fid

No	ppm	HZ	GF	X
1	-109.7	447.2	1.00*	47.4
2	-100.9	376.7	1.00*	45.9
3	-92.1	311.9	1.00*	6.7

Final chi squared: 1874



Lineshape is $GF * \text{Gaussian} + (1 - GF) * \text{Lorentzian}$

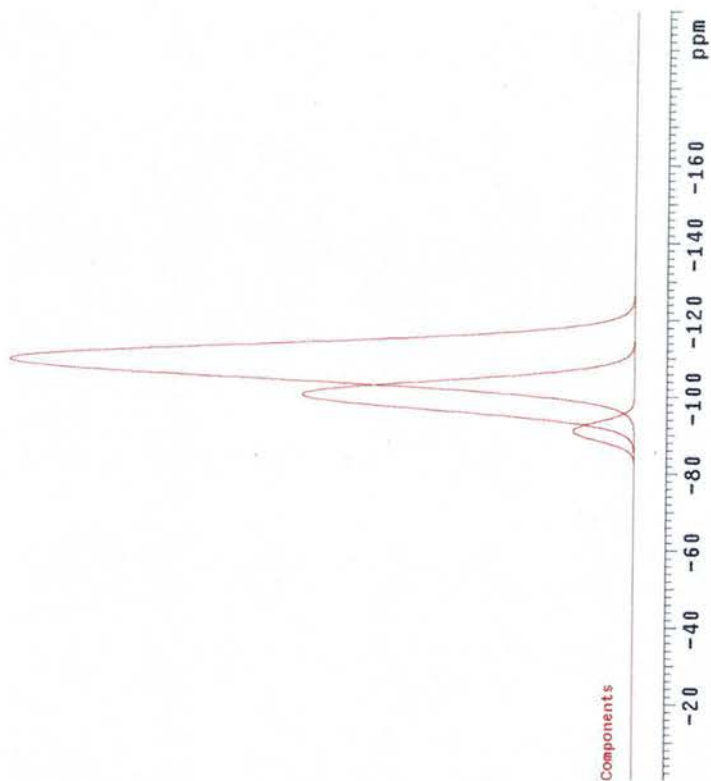
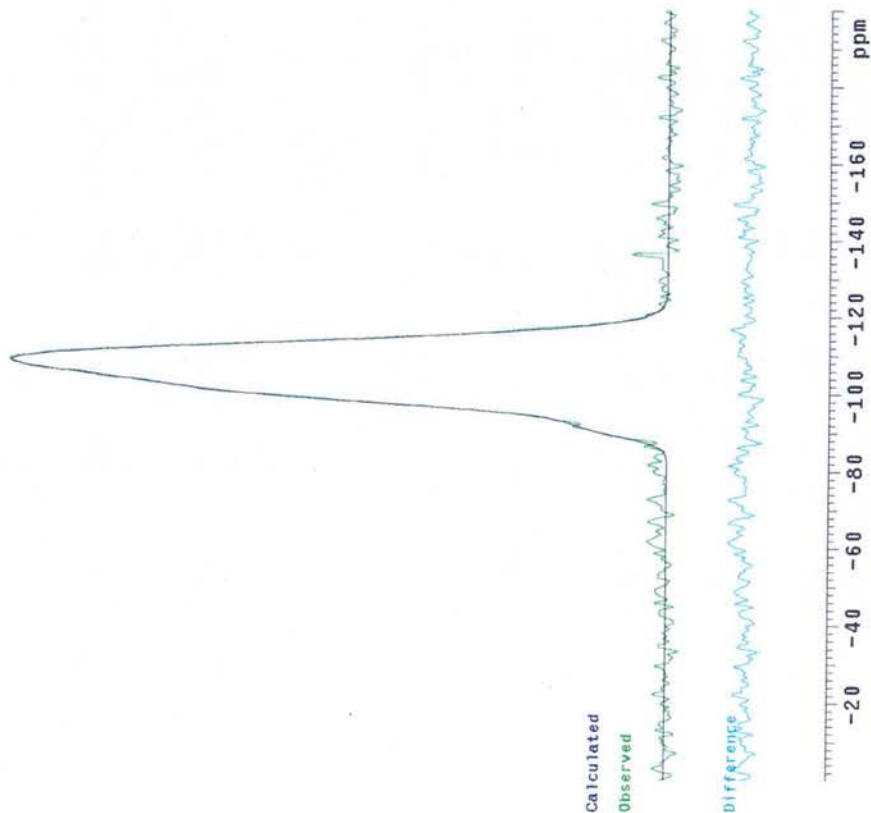
* indicates parameter fixed during fitting

Sample 3

data21/paw28Nov0401.fid

No	ppm	HZ	GF	%
1	-108.7	630.5	1.00*	66.6
2	-100.1	531.6	1.00*	29.9
3	-91.1	344.4	1.00*	3.5

Final chi squared: 2315



Lineshape is $GF \cdot \text{Gaussian} + (1 - GF) \cdot \text{Lorentzian}$

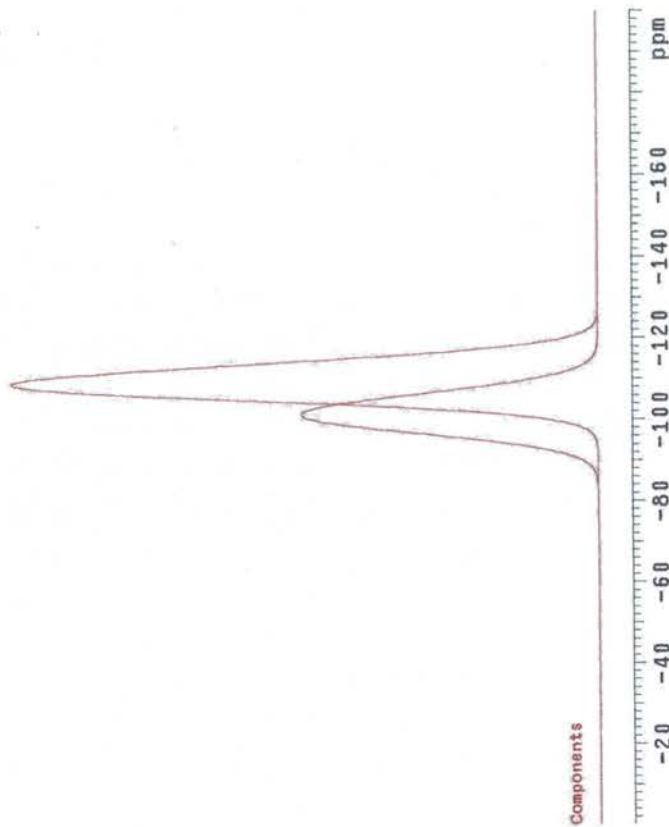
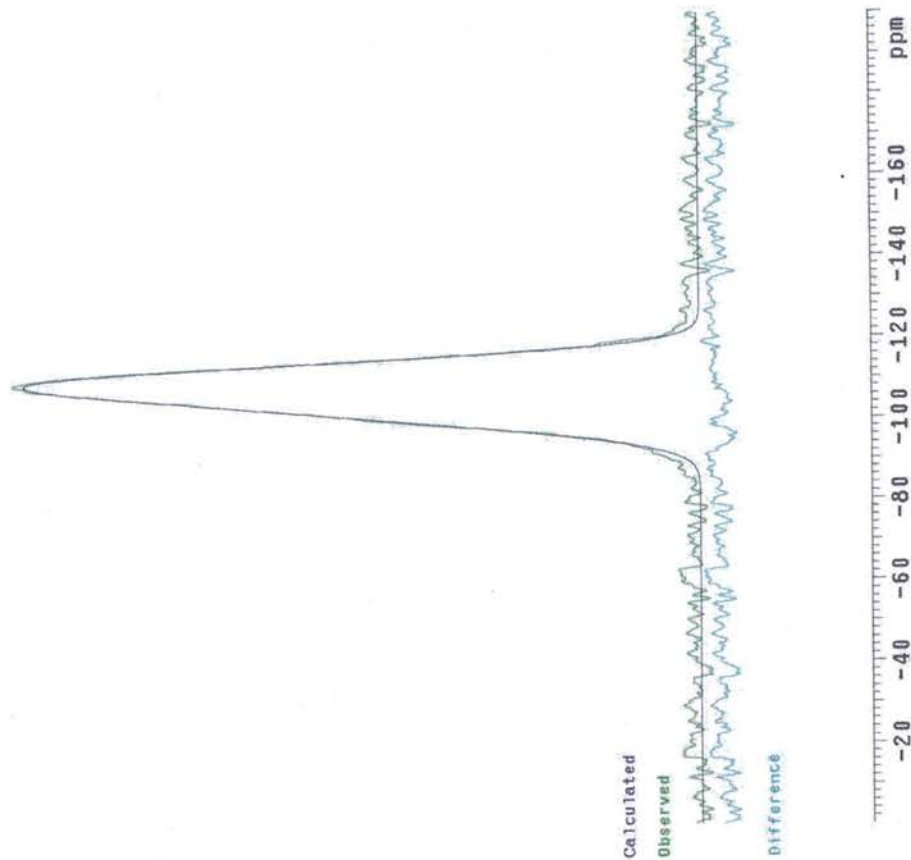
* indicates parameter fixed during fitting

Sample 4

data21/paw29Nov0408.fid

No	ppm	HZ	GF	%
1	-109.8	610.0	1.00*	64.1
2	-101.8	677.8	1.00*	35.9

Final chi squared: 1543



Lineshape is $GF * \text{Gaussian} + (1 - GF) * \text{Lorentzian}$

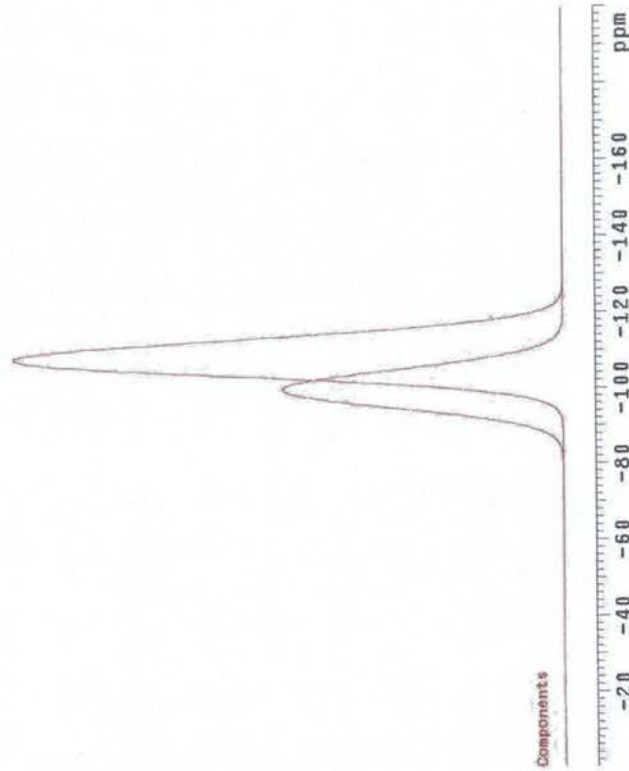
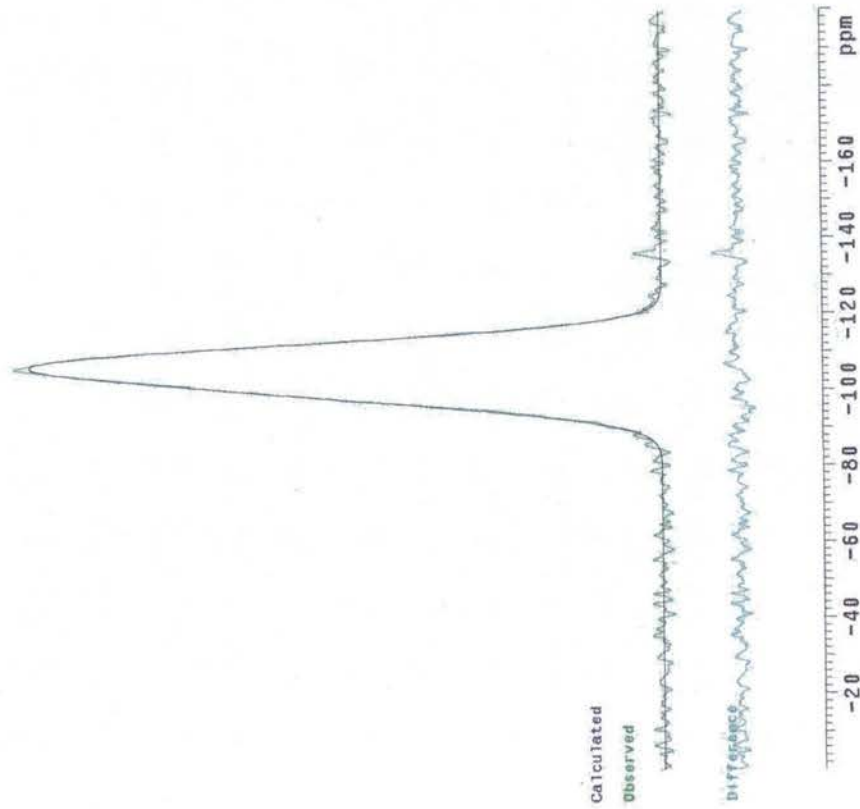
* indicates parameter fixed during fitting

Sample 5

data21/paw50Nov0401.fid

No	ppm	Hz	GF	X
1	-108.5	688.4	1.00*	64.9
2	-100.1	706.3	1.00*	35.1

Final chi squared: 2446



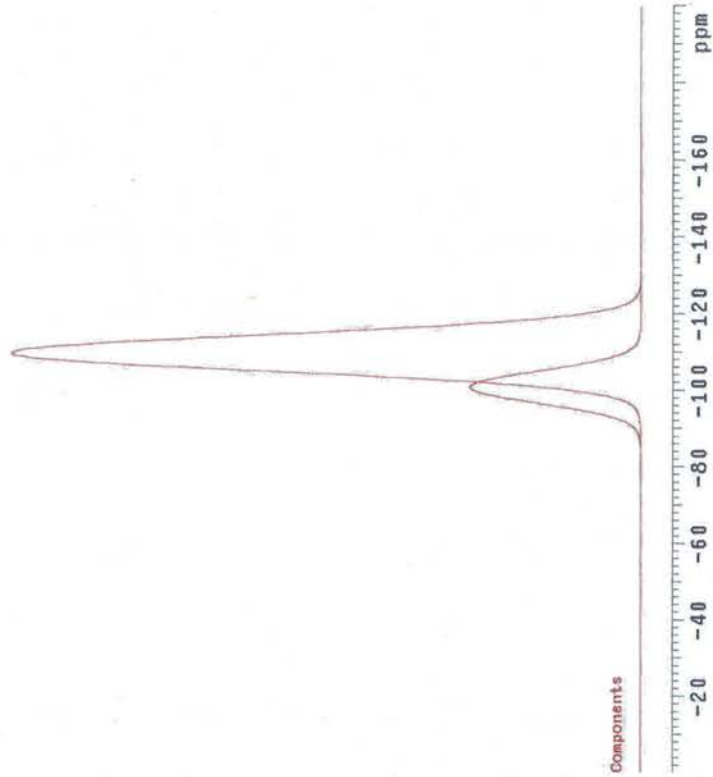
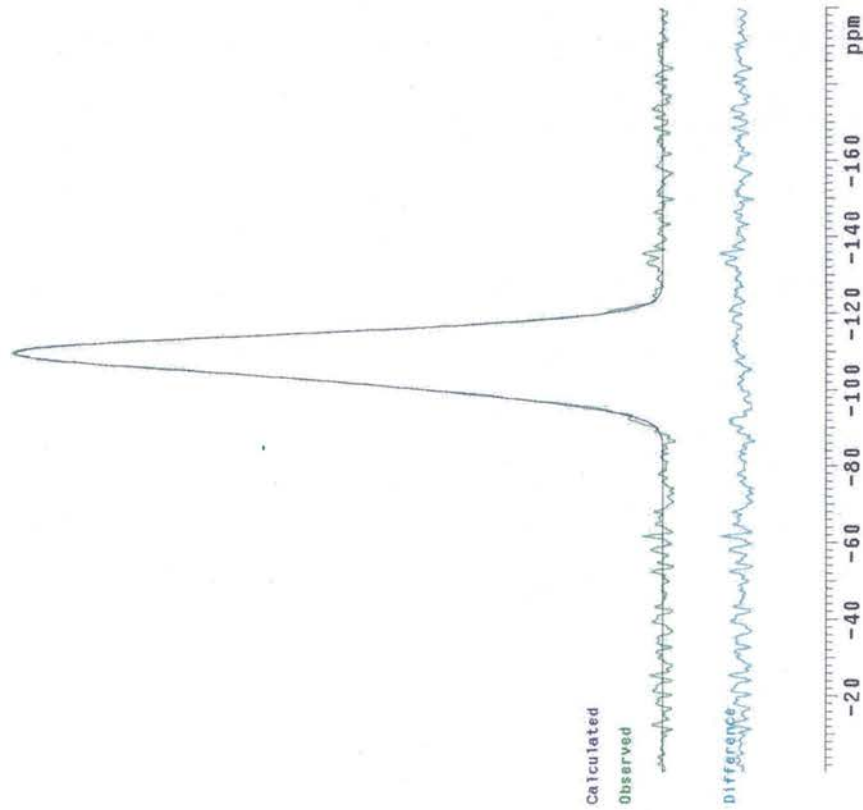
Linehape is $GF \cdot \text{Gaussian} + (1 - GF) \cdot \text{Lorentzian}$
* indicates parameter fixed during fitting

Sample 6

data21/paw30Nov0402

No	ppm	Hz	GF	X
1	-109.8	655.5	1.00*	80.6
2	-101.0	583.1	1.00*	19.4

Final chi squared: 3047



Lineshape is $GF \cdot \text{Gaussian} + (1 - GF) \cdot \text{Lorentzian}$

* Indicates parameter fixed during fitting